

# Characterization of crystalline silicon based on measurements of the photoluminescence emission

Von der Fakultät für Mathematik und Physik  
der Gottfried Wilhelm Leibniz Universität Hannover  
zur Erlangung des Grades

Doktorin der Naturwissenschaften

Dr. rer. nat.

genehmigte Dissertation

von

Dipl.-Phys. Sandra Herlufsen

geboren am 26.10.1979 in Bremerhaven

Referent: Prof. Dr. Jan Schmidt  
Korreferent: Prof. Dr. Michael Oestreich  
Externer Korreferent: Prof. Dr. Daniel Macdonald  
Tag der Promotion: 02.07.2013

# Kurzzusammenfassung

Im Rahmen dieser Arbeit wird die Photolumineszenzemission von Silicium (Si) Wafern bei Raumtemperatur zur Bestimmung der Ladungsträgerlebensdauer eingesetzt. Zu Beginn der Arbeit wird zunächst ein kamera-basierter Photolumineszenzmessplatz für Si-Wafer aufgebaut, welcher die orts aufgelöste Messung eines Signals proportional zur Photolumineszenzemission erlaubt. Anschließend werden zwei unterschiedliche Verfahren zur Bestimmung der Ladungsträgerlebensdauer in Si-Wafern entwickelt.

Als erste Möglichkeit der Ladungsträgerlebensdauerbestimmung mithilfe von Photolumineszenzmessungen wird die Kalibrierung des statischen Photolumineszenzsignals mit einer anderen Methode zur Bestimmung der Lebensdauer umgesetzt. Dafür wird ein kommerziell erhältlicher Photoleitfähigkeitsmessplatz in den Photolumineszenzmessplatz integriert. Auf diese Weise wird eine Messung der Photoleitfähigkeit und der Photolumineszenz unter gleichen Anregungsbedingungen ermöglicht. In dieser Arbeit wird die Abhängigkeit der kalibrierten Photolumineszenz-basierten Lebensdauer messung von der Dotierung der Probe, der Probendicke sowie der Oberflächenbeschaffenheit untersucht. Zudem wird gezeigt, dass die Kalibrierung nur für beliebige Injektions- und Lebensdauerbereiche gültig ist, sofern die Ladungsträger homogen über die Tiefe der Probe verteilt sind. Für die Untersuchung inhomogener Ladungsträgerprofile wird ein verallgemeinerter Zusammenhang zwischen Photolumineszenzemission und Überschussladungsträgerdichte abgeleitet und experimentell verifiziert.

Als zweite Möglichkeit wird ein dynamischer Ansatz zur Bestimmung der Ladungsträgerlebensdauer umgesetzt. Dazu werden vier Lumineszenzaufnahmen zu verschiedenen Zeiten einer rechteckförmigen Anregung aufgenommen. Das Verhältnis dieser vier Aufnahmen hängt nur noch von der Ladungsträgerlebensdauer und der Kameraintegrationszeit ab. In dieser Arbeit kann gezeigt werden, dass der dynamische Ansatz auch für die Untersuchung der Außenseiten von ganzen Si-Blöcken geeignet ist. Die Blockoberflächen liegen typischerweise ohne elektrische Passivierung vor. Aus diesem Grund sind die Blockoberflächen Bereiche mit einer erhöhten Rekombinationswahrscheinlichkeit für die generierten Überschussladungsträger. In dieser Arbeit wird veranschaulicht, dass die dynamische Methode eine starke Abhängigkeit von der Probendicke und der Oberflächenrekombinationsgeschwindigkeit aufweist. Ab einem bestimmten Wert der Probendicke und der Oberflächenrekombinationsgeschwindigkeit ist diese Abhängigkeit jedoch sehr gering und die dynamische Auswertung kann einzig als Funktion der Volumenlebensdauer und der Kameraintegrationszeit durchgeführt werden. Typischerweise überschreiten blockgegossene multikristalline Si-Blöcke die erforderlichen Schwellenwerte für Dicke und Oberflächenrekombinationsgeschwindigkeit und eine Abbildung der Volumenlebensdauer durch die dynamische Photolumineszenzauswertung ist möglich.

Lebensdauer messungen können für eine indirekte Messung der Konzentration rekombinationsaktiven interstitiellen Eisens in Bor-dotierten Si-Wafern verwendet werden. In dieser Arbeit wird das Lebensdauer-basierte Verfahren angewandt, um zwei

Ansätze zur Reduktion der interstitiellen Eisenkonzentration zu untersuchen. Während der Photolumineszenzmessung wird durch die Laseranregung die Trennung von Eisen-Bor-Paaren induziert. Die Zeit, die zur Trennung der Eisen-Bor-Paare benötigt wird, hängt von der interstitiellen Eisenkonzentration und der Beleuchtungsintensität ab. In dieser Arbeit wird gezeigt, dass die Bestimmung der interstitiellen Eisenkonzentration durch eine Messung der Trennungsrates (und der Beleuchtungsintensität) erfolgen kann.

# Abstract

Within the scope of this work, the photoluminescence emission of silicon (Si) wafers at room temperature is used for the determination of the charge carrier lifetime. At the beginning, an experimental setup is constructed that uses a camera as detector and allows the spatially-resolved measurement of a signal proportional to the photoluminescence emission of Si wafers. Then, two different approaches for measuring the carrier lifetime are developed.

The first way of determining the charge carrier lifetime is realized by calibrating the measured steady-state photoluminescence signal with another lifetime technique. For this, a commercially available photoconductance setup is integrated into the photoluminescence setup, enabling the measurement of the photoconductance and the photoluminescence at the same excitation conditions. The dependence of the calibrated photoluminescence-based lifetime measurement on the doping density, sample thickness and surface morphology is analyzed. In addition, it is shown that the calibration is only valid for arbitrary injection and lifetime ranges if the charge carriers are homogeneously distributed as a function of the sample depth. For the investigation of inhomogeneous carrier profiles, a generalized relation between photoluminescence emission and excess carrier density is proposed and experimentally verified.

Another possibility of measuring the carrier lifetime is realized by a dynamic approach. Four photoluminescence images are acquired at different times during a square-wave-shaped excitation. A ratio of these four images depends only on the charge carrier lifetime and the camera integration time. In this work, it is shown that the dynamic approach is also applicable to the investigation of Si bricks. The brick surfaces are typically without an electrical surface passivation. For that reason, the brick surfaces are areas with an increased recombination probability for the generated excess carriers. It is demonstrated that the dynamic approach strongly depends on the sample thickness and the surface recombination velocity. However, this dependence is significantly reduced if exceeding a certain value of the sample thickness and the surface recombination velocity. Then, the dynamic evaluation can be performed only as a function of the bulk lifetime and the camera integration time. Typically, block-casted multicrystalline Si bricks exceed the required threshold values and dynamic bulk lifetime imaging is possible.

On the basis of carrier lifetime measurements, the concentration of recombination-active interstitial iron in boron-doped Si wafers can be indirectly determined. In this thesis, the lifetime-based approach is used to investigate two approaches for reducing the interstitial iron concentration. During the photoluminescence measurement, the splitting of the iron-boron pairs is optically induced by the laser excitation. The time that is required to separate the iron-boron pairs is a function of the interstitial iron concentration and the illumination intensity. It will be shown, that the interstitial iron concentration can be determined from a measurement of the splitting rate (and the illumination intensity).

**Keywords:** charge carrier lifetime, photoluminescence, silicon

**Schlagwörter:** Ladungsträgerlebensdauer, Photolumineszenz, Silicium

---

# Table of Contents

---

<b>Introduction</b>	<b>1</b>
<b>1 Carrier recombination in silicon</b>	<b>3</b>
1.1 Recombination mechanisms in crystalline silicon . . . . .	3
1.1.1 Recombination in the bulk . . . . .	5
1.1.2 Recombination at the surfaces . . . . .	10
1.2 Basic approaches for recombination lifetime measurements . . . . .	12
1.3 Quasi-steady-state photoconductance . . . . .	14
1.3.1 Measurement of the recombination lifetime . . . . .	14
1.3.2 Measurement artifacts . . . . .	16
<b>2 Simulation and measurement of the photoluminescence emission of silicon</b>	<b>21</b>
2.1 Simulation of the photoluminescence signal of a silicon wafer . . . . .	22
2.1.1 Generalized Planck's law . . . . .	22
2.1.2 Radiative recombination coefficient . . . . .	24
2.1.3 Impact of sample geometry on photoluminescence emission . . . . .	26
2.1.4 Time and depth dependence of the excess carrier density . . . . .	29
2.2 Camera-based photoluminescence setup . . . . .	35
2.2.1 Components of the setup . . . . .	35
2.2.2 Setup configurations . . . . .	43
2.2.3 Data acquisition and sensitivity . . . . .	45
<b>3 Carrier lifetime imaging using a photoluminescence setup</b>	<b>49</b>
3.1 Previous work . . . . .	51
3.1.1 Luminescence-based carrier lifetime measurements . . . . .	51

3.1.2	Measurement artifacts . . . . .	53
3.2	Photoconductance-calibrated photoluminescence lifetime imaging (PC-PLI) . . . . .	55
3.2.1	Calibration procedure . . . . .	55
3.2.2	Validity of the PC-PLI calibration for arbitrary lifetime and injection ranges . . . . .	66
3.2.3	Sensitivity analysis . . . . .	75
3.3	Dynamic photoluminescence lifetime imaging (dynamic PLI) . . . . .	77
3.3.1	Principle of dynamic photoluminescence lifetime imaging . . . . .	77
3.3.2	Application of dynamic PL imaging . . . . .	80
3.3.3	Sensitivity analysis . . . . .	82
3.3.4	Steady-state or dynamic lifetime? . . . . .	84
3.3.5	Application of the dynamic PL lifetime technique to multicrystalline silicon bricks . . . . .	88
3.4	Comparison of lifetime imaging techniques . . . . .	97
<b>4</b>	<b>Imaging of the interstitial iron concentration in boron-doped silicon</b>	<b>103</b>
4.1	Previous work . . . . .	104
4.2	Interstitial iron imaging using PC-PLI . . . . .	111
4.2.1	Experimental . . . . .	111
4.2.2	Internal gettering of interstitial iron . . . . .	114
4.3	Dynamic interstitial iron imaging . . . . .	120
4.3.1	Principle of dynamic interstitial iron imaging . . . . .	120
4.3.2	Experimental . . . . .	121
4.3.3	Verification on a deliberately Fe-contaminated FZ-Si wafer . . . . .	123
4.3.4	Application to an mc-Si wafer . . . . .	125
4.3.5	Summary . . . . .	127
<b>5</b>	<b>Summary</b>	<b>129</b>
	<b>Appendix: Camera noise analysis</b>	<b>133</b>
	<b>References</b>	<b>137</b>
	<b>List of publications</b>	<b>151</b>
	<b>Acknowledgment</b>	<b>155</b>
	<b>Curriculum vitae</b>	<b>157</b>

---

# Introduction

---

A solar cell is able to generate an electrical current by being exposed to sunlight. In order to do this efficiently, it is not just important to be able to generate mobile charge carriers, but also to provide the ability to stay mobile until the charge carriers contribute to an electrical current in a circuit outside the cell. A well-suited measure for this ability is the carrier recombination lifetime which is the average time for the existence of a mobile charge carrier.

Most solar cells are fabricated from crystalline silicon (c-Si) with a share of 87.9% of the world-wide cell production in 2011 [1]. It is differentiated between monocrystalline and multicrystalline silicon (mc-Si) with the latter having a market share of 57% in 2011. Monocrystalline Si (mono c-Si) with a share of 30.9% is Czochralski-grown material that has a low density of dislocations and impurities. Multicrystalline Si can be produced at a lower cost but has typically higher concentrations of crystal imperfections and impurities. However, impurities and crystal imperfections may act as recombination sites with the consequence of reduced carrier lifetimes. For that reason, it is highly demanded to monitor the recombination lifetime as a sensitive measure of the absorber quality.

To what extent the cell efficiency is limited by the recombination lifetime depends strongly on the specific solar cell concept. Each concept has a different minimum requirement for the recombination lifetime, depending e.g. on the wafer thickness and the position of the electrical contacts. Hence, it is on the one hand essential to know this requirement e.g. from simulations, and on the other hand, it is indispensable to know the recombination lifetime of the absorber material. Consequently, techniques determining the carrier lifetime are required for choosing the appropriate material for each cell concept.

A broad variety of recombination lifetime measurement techniques have been developed over the years, based on different measurement quantities [2]. For an industrially suited inline control of the wafer quality, a fast and contactless lifetime technique is required. Already in 1963, the band-to-band luminescence emission of Si samples at room temperature was used for carrier lifetime measurements [3]. However, luminescence-based characterization techniques are prevalingly used for the investigation of the Si material quality since Fuyuki et al. [4, 5] and Trupke et al. [6] demonstrated in 2005 and 2006 that the luminescence emission can be measured within seconds using high resolution Si CCD (charge coupled device) cameras. Especially, photoluminescence imaging became a very powerful tool for the investigation of the solar cell base material [7].

## Structure of this thesis

In the first part of this thesis, we present two new techniques for measuring the spatially-resolved recombination lifetime using a photoluminescence-based setup. In the second part of this work, the application of the photoluminescence emission for the contactless determination of the interstitial iron concentration is presented.

**Chapter 1** gives a short review of the main carrier recombination mechanisms in silicon. Furthermore, the conventional approaches for recombination lifetime measurements are discussed.

**Chapter 2** presents the background for one-dimensional modeling of the photoluminescence emission of silicon. The second part of this Chapter describes the components of the experimental setup required for photoluminescence emission measurements.

**Chapter 3** presents two new approaches for measuring the recombination lifetime of silicon wafers using photoluminescence emission as a measure for the optically excited excess carrier density. The first technique evaluates steady-state photoluminescence emission and the second approach analyzes time-dependent photoluminescence emission.

**Chapter 4** demonstrates the applicability of a spatially-resolved photoluminescence-based steady-state lifetime technique to the measurement of the interstitial iron concentration in boron-doped silicon. The technique is applied to evaluate two approaches for the reduction of the interstitial iron concentration. Moreover, a novel method for measuring the interstitial iron concentration is introduced. This approach evaluates the time-dependent photoluminescence emission to determine the interstitial iron concentration from the optical dissociation rate of iron-boron pairs.

**Chapter 5** summarizes the main results achieved in this work.

# CHAPTER 1

---

## Carrier recombination in silicon

---

In this Chapter, a short review of the main carrier recombination mechanisms in crystalline silicon (c-Si) is given. Furthermore, different basic approaches for recombination lifetime measurements are discussed. The quasi-steady-state photoconductance lifetime technique, frequently used in this thesis, is discussed in more detail.

### 1.1 Recombination mechanisms in crystalline silicon

Under thermal equilibrium conditions in the dark, the free<sup>1</sup> carrier concentrations in the valence and conduction bands are determined by the band gap width and the temperature of the semiconductor. The temperature provides the energy required for the excitation of electrons into the conduction band, leaving holes (empty electron states) in the valence band. For the intrinsic semiconductor, the free electron concentration in the conduction band  $n_0$  equals the free hole concentration in the valence band  $p_0$ . The product of both concentrations equals the squared intrinsic carrier concentration  $n_0 p_0 = n_i^2$ . This equilibrium condition is known as mass action law and is also valid for doped semiconductors.

The thermal equilibrium is disturbed if the semiconductor is illuminated by photons with an energy larger than the band gap of Si. In this case, the exciting photons

---

<sup>1</sup>“Free” carriers are the mobile electrons in the conduction band and holes in the valence band that are considered unbound but with an effective mass that takes the location-dependent potential of the crystal lattice into account.

provide the energy required for the transition of electrons from the valence into the conduction band. The carriers excited in addition to the thermally generated ones are defined to be the excess electrons and holes with an equal density  $\Delta n = \Delta p$ . The product of the total free electron and hole concentrations for the disturbed thermal equilibrium is given by

$$np = (n_0 + \Delta n)(p_0 + \Delta p) > n_i^2. \quad (1.1)$$

The excitation process is often referred to as the generation of an electron-hole pair. The reverse process to the generation is the recombination of an electron-hole pair, where the recombination rate  $R$  specifies the recombination events per second and volume element. A new equilibrium state is achieved as soon as the recombination rate  $R$  equals the generation rate  $G$ . With this, the excess carrier density as a function of time becomes, on average, a constant. Then, excess carrier density  $\Delta n$  and recombination rate  $R$  are proportional:

$$\Delta n = R\tau = G\tau, \quad (1.2)$$

with the proportionality constant being the carrier lifetime  $\tau$ . From the carrier lifetime, the diffusion length  $L$  can be calculated if the carrier diffusion coefficient  $D_n$  in the material is known.  $L$  is the average distance that a charge carrier is able to travel within its lifetime  $\tau$  and is given by

$$L = \sqrt{\tau D_n}. \quad (1.3)$$

The re-transition of an excited electron to the valence band, i.e. the recombination of an electron-hole pair, can happen in different ways. It is distinguished between extrinsic recombination, due to impurities and crystallographic imperfections, and intrinsic recombination, unavoidable due to the intrinsic properties of the semiconductor. In multicrystalline (mc) Si and Czochralski-grown (Cz) Si, extrinsic recombination is the dominant recombination channel. In float-zone (FZ) Si, only the intrinsic recombination mechanisms limit the carrier lifetime. If the single recombination paths are independent of each other, a total bulk carrier lifetime  $\tau_b$  is defined by the sum of the single recombination rates  $R$ :

$$\sum_i R_i = \sum_i \frac{\Delta n}{\tau_i} = \frac{\Delta n}{\tau_b}. \quad (1.4)$$

In the next Section, the individual recombination mechanisms in the bulk are discussed. Afterwards, the recombination at the surfaces is included to enable the definition of an effective carrier lifetime of an excited Si sample.

### 1.1.1 Recombination in the bulk

#### Radiative band-to-band recombination

The least probable recombination process in Si is the band-to-band radiative recombination where the electron-hole recombination is accompanied by a photon emission. The reason for the high radiative carrier lifetime is given by the indirect band structure of Si. As a consequence, interaction with the crystal lattice (emission or absorption of a phonon) is required for the band-to-band recombination to account for energy and momentum conservation. However, a three-particle process (electron, hole and at least one phonon) is much less likely than a two-particle process (for a direct semiconductor). A basic approach for the quantitative description of the radiative recombination was given by Roosbroeck and Shockley [8] in 1954. Since a free electron and hole is required for a radiative recombination, they proposed the radiative recombination rate  $R_{\text{rad}}$  to be proportional to the product of the free electron and hole concentrations [8]:

$$R_{\text{rad}} = B_{\text{rad}} \cdot n \cdot p, \quad (1.5)$$

with  $B_{\text{rad}}$  being the radiative recombination coefficient that is a measure for the recombination probability. Using Eq. (1.1) and assuming charge neutrality ( $\Delta n = \Delta p$ ) for a  $p$ -type semiconductor with  $p_0 \approx N_{\text{dop}}$  and  $\Delta n \gg n_0 = n_i^2/p_0$  results in:

$$np = (\Delta n + n_0)(\Delta p + p_0) = \Delta n(\Delta n + N_{\text{dop}}), \quad (1.6)$$

where  $N_{\text{dop}}$  is the doping density. Using Eqs. (1.2) and (1.6) for the calculation of the radiative recombination lifetime from Eq. (1.5) leads us to two limiting cases. At low-level injection (lli) conditions ( $\Delta n \ll N_{\text{dop}}$ ), the band-to-band radiative lifetime  $\tau_{\text{rad}}$  is injection-independent and given by

$$\tau_{\text{rad,lli}} = \frac{1}{B_{\text{rad}} N_{\text{dop}}}, \quad (1.7)$$

whereas for high-level injection (hli) conditions ( $\Delta n \gg N_{\text{dop}}$ ), the radiative lifetime is independent of the doping density:

$$\tau_{\text{rad,hli}} = \frac{1}{B_{\text{rad}} \Delta n}. \quad (1.8)$$

Schlangenotto et al. [9] found that for the correct description of radiative recombination in Si, Coulomb attraction between electrons and holes has to be taken into account. Due to the Coulomb attraction, the electron concentration is increased in the vicinity of a hole and vice versa, which results in an increased recombination probability. However, it is found that the increased recombination probability is reduced at high injection conditions. Altermatt et al. [10, 11] proposed a weakening of the Coulomb enhancement at high injection densities due to a screening of the Coulomb attraction.

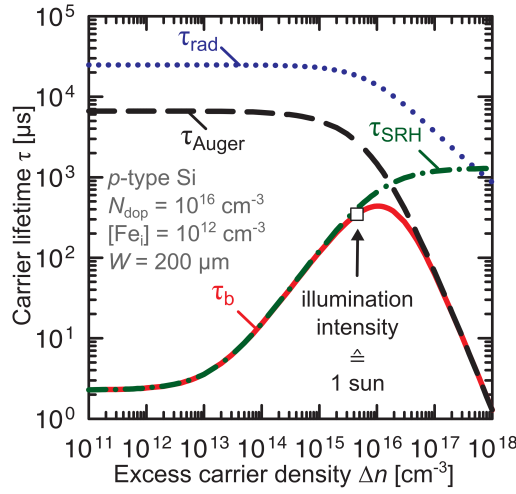


**Figure 1.1:** Calculated bulk lifetime  $\tau_b$  (red solid line) for a p-type Si wafer with a doping concentration of  $10^{16} \text{ cm}^{-3}$  and an impurity concentration (interstitial iron) of  $[\text{Fe}_i] = 10^{12} \text{ cm}^{-3}$  under consideration of radiative, Auger and defect recombination. The empty square shows the injection density for an illumination intensity equivalent to 1 sun ( $\sim 0.1 \text{ W/cm}^2$ ) for a wafer with a thickness of  $W = 200 \text{ }\mu\text{m}$ . In addition, the radiative lifetime  $\tau_{\text{rad}}$  (blue dotted line), the Auger lifetime  $\tau_{\text{Auger}}$  (black dashed line) and the SRH defect lifetime  $\tau_{\text{SRH}}$  (green dashed-dotted line) are presented.

Figure 1.1 shows  $\tau_{\text{rad}}$  as a function of the excess carrier density  $\Delta n$  for a Si wafer with a doping density of  $10^{16} \text{ cm}^{-3}$  (blue dotted line). The photon emission due to radiative band-to-band recombination is the physical quantity of interest in this work. Hence, a detailed description can be found in Section 2.1.

### Band-to-band Auger recombination

Auger recombination describes a recombination process, involving three charge carriers. Thus, the recombination of an electron-hole pair is not accompanied by the emission of a photon; the released energy is transferred to a third charge carrier. This can be an electron in the valence band or a hole in the conduction band. As for the radiative recombination, the Auger recombination rate  $R_{\text{Auger}}$  is proportional to the product of the carrier densities of the involved charge carrier species and thus given by the expression:

$$R_{\text{Auger}} = C_n \cdot n^2 \cdot p + C_p \cdot n \cdot p^2, \quad (1.9)$$

with  $C_n$  and  $C_p$  as the proportionality factors for the two Auger processes, referred to as Auger coefficients. In a p-type Si wafer, the third charge carrier is most likely a hole because of the higher availability. Using Eqs. (1.2) and (1.6) for the calculation of the Auger recombination lifetime from Eq. (1.9) leads us to two limiting cases. At low-level injection (lli) conditions ( $\Delta n \ll N_{\text{dop}}$ ), the band-to-band Auger lifetime

$\tau_{\text{Auger}}$  is injection-independent and given by

$$\tau_{\text{Auger,lli}} = \frac{1}{C_p N_{\text{dop}}^2}, \quad (1.10)$$

whereas at high-level injection (hli) conditions ( $\Delta n \gg N_{\text{dop}}$ ), the Auger lifetime is independent of the doping density:

$$\tau_{\text{Auger,hli}} = \frac{1}{(C_n + C_p)\Delta n^2}, \quad (1.11)$$

assuming a *p*-type Si wafer. Numerous parameterizations for the Auger recombination rate can be found in the literature (e.g. in Refs. 12–17). For the correct description of the Auger recombination rate as a function of injection and doping density, Coulomb enhancement of the recombination rate as well as screening of this Coulomb enhancement at higher injection densities has to be considered. For the calculated Auger lifetime  $\tau_{\text{Auger}}(\Delta n)$  in Fig. 1.1 (black dashed line), a parameterization of Kerr and Cuevas [16] is used that is given by

$$R_{\text{Auger}} = n \cdot p \cdot (1.8 \cdot 10^{-24} \cdot n_0^{0.65} + 6 \cdot 10^{-25} \cdot p_0^{0.65} + 3 \cdot 10^{-27} \cdot \Delta n^{0.8}). \quad (1.12)$$

Recent advances in surface passivation techniques enabled a more precise study of silicon bulk recombination. As a result, Richter et al. [17, 18] proposed recently a new parameterization for Auger recombination.

### Recombination through defect states

Impurities or crystallographic defects in crystalline Si may result in energy levels in the band gap of Si. In that case, the transition of an electron of the conduction band to the valence band can proceed via the defect state in the band gap. The released energy of the electron-hole recombination via a defect state can be transferred differently, e.g. radiatively (defect luminescence), via an Auger process or a process involving the interaction with phonons. A formal description of the recombination rate for a defect with a single fixed energy level in the band gap of a non-degenerate semiconductor was developed by Shockley, Read [19] and Hall [20]. The Shockley-Read-Hall (SRH) net recombination rate  $R_{\text{SRH}}$  of excess electrons and holes was derived from detailed balance considerations and is given by the expression [19, 20]:

$$R_{\text{SRH}} = \frac{np - n_i^2}{\tau_{p,0}(n + n_1) + \tau_{n,0}(p + p_1)}. \quad (1.13)$$

$\tau_{n,0}$  and  $\tau_{p,0}$  are the capture time constants for electrons and holes of the specific impurity:

$$\tau_{n,0} = \frac{1}{[N]v_{\text{th}}\sigma_n} \quad \text{and} \quad \tau_{p,0} = \frac{1}{[N]v_{\text{th}}\sigma_p}, \quad (1.14)$$

where  $v_{th}$  is the thermal velocity of the charge carriers,  $[N]$  is the defect concentration and  $\sigma_n$  and  $\sigma_p$  are the characteristic capture cross sections of the impurity.  $n_1$  and  $p_1$  are defined as the equilibrium carrier concentrations for the case that the impurity energy level coincides with the Fermi level:

$$n_1 = N_C \exp\left(-\frac{(E_C - E_{\text{defect}})}{k_B T}\right) \quad \text{and} \quad p_1 = N_V \exp\left(-\frac{(E_{\text{defect}} - E_V)}{k_B T}\right), \quad (1.15)$$

where  $N_C$  and  $N_V$  are the effective densities of states in the conduction and the valence band.  $E_{\text{defect}}$  is the energy level of the defect and  $E_C$  and  $E_V$  denote the energy levels of the conduction and valence band edges. Assuming charge neutrality ( $\Delta n = \Delta p$ ), the SRH recombination lifetime  $\tau_{\text{SRH}}$  can be calculated from Eqs. (1.2) and (1.13) to

$$\tau_{\text{SRH}} = \frac{\tau_{n,0}(p_0 + p_1 + \Delta n) + \tau_{p,0}(n_0 + n_1 + \Delta n)}{p_0 + n_0 + \Delta n}. \quad (1.16)$$

Defects that serve as recombination centers in general may also act as traps [21]. If this occurs, carriers spend some time trapped at the defect before either recombining or returning to their band of origin. In the SRH recombination model that leads to Eq. (1.16), trapping is not considered. For that reason, Eq. (1.16) is only valid if the impurity concentration is smaller than the generated excess carriers in the sample:  $[N] < \Delta n, \Delta p$  and smaller than the dopant density  $[N] < N_{\text{dop}}$ . More exactly, Macdonald et al. [21] determined a critical impurity concentration  $[N]_{\text{crit}}$  to

$$[N]_{\text{crit}} = \frac{(p_0 + p_1)[n_0 + n_1 + \Delta n + k(p_0 + p_1 + \Delta p)]}{|p_0 - kp_1|}, \quad (1.17)$$

with  $k$  being the ratio of the capture cross sections of electrons and holes:  $k = \sigma_n/\sigma_p$ . For a deep-level defect with an energy level close to the middle of the band gap, i.e.  $n_1, p_1 \ll n_0, p_0$ , and low-level injection conditions, Eq. (1.17) simplifies to

$$[N]_{\text{crit}} = N_{\text{dop}} \frac{\sigma_p}{\sigma_n}. \quad (1.18)$$

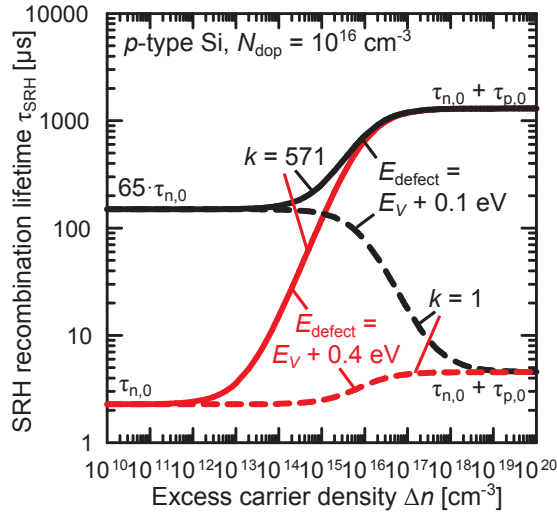
If the simplified SRH model without traps shall be accurate to within 10%, the impurity concentration must be at least one order of magnitude smaller than  $[N]_{\text{crit}}$  [21].

Figure 1.1 shows the SRH recombination lifetime  $\tau_{\text{SRH}}(\Delta n)$  for interstitial iron<sup>2</sup> as an example for a deep-level defect (green dashed-dotted line). The ratio of the capture cross sections for electrons and holes for this specific defect is  $k = \sigma_n/\sigma_p \sim 570$  with the consequence of a strong injection dependence of the recombination lifetime.

Similar to radiative and Auger recombination, limiting cases for SRH recombination at high-level and low-level injection conditions can be derived. For high-level injection (hli) conditions ( $\Delta n \gg N_{\text{dop}}$ ), the SRH lifetime in Eq. (1.16) can be approximated

---

<sup>2</sup> $E_{\text{defect}} = E_V + 0.38 \text{ eV}$  [22],  $\sigma_n = 4 \times 10^{-14} \text{ cm}^2$  [23],  $\sigma_p = 7 \times 10^{-17} \text{ cm}^2$  [23]



**Figure 1.2:** SRH recombination lifetime  $\tau_{\text{SRH}}$  as a function of the injection density  $\Delta n$  for a deep-level defect with  $E_{\text{defect}} = E_V + 0.4$  eV and for a shallow-level defect with  $E_{\text{defect}} = E_V + 0.1$  eV for two different values of  $k = \sigma_n/\sigma_p$ .

by the sum of the two capture time constants:

$$\tau_{\text{SRH, hli}} = \tau_{n,0} + \tau_{p,0}. \quad (1.19)$$

For low-level injection conditions ( $\Delta n \ll N_{\text{dop}}$ ), the SRH lifetime becomes injection-independent and is given by the expression:

$$\tau_{\text{SRH, lli}} = \tau_{p,0} \frac{n_1}{p_0} + \tau_{n,0} \left( 1 + \frac{p_1}{p_0} \right) \quad (1.20)$$

for a  $p$ -type semiconductor. Considering a deep-level defect state with an energy level close to the middle of the band gap, i.e.  $n_1, p_1 \ll n_0, p_0$ , the SRH lifetime equals the fundamental lifetime of the minority carriers  $\tau_{\text{SRH, lli}} = \tau_{n,0}$ . In that case, the electrons available for the recombination limit the recombination process. However, for a shallow-defect state close to the conduction or valence band edges, the low-level injection lifetime can be much higher than the minority carrier lifetime  $\tau_{n,0}$ .

Figure 1.2 shows the SRH lifetime for a deep-level ( $E_{\text{defect}} = E_V + 0.4$  eV) and a shallow-level defect ( $E_{\text{defect}} = E_V + 0.1$  eV) for two different values of  $k = \sigma_n/\sigma_p$ . In both cases, the hli lifetime is given by  $\tau_{\text{SRH, hli}} = \tau_{n,0} + \tau_{p,0}$  as predicted with Eq. (1.19). Figure 1.2 also confirms that for the deep-level defect  $\tau_{\text{SRH, lli}} = \tau_{n,0}$  whereas for the shallow-level defect  $\tau_{\text{SRH, lli}} \neq \tau_{n,0}$ .

The ratio of the hli to the lli lifetime  $h = \tau_{\text{SRH, hli}}/\tau_{\text{SRH, lli}}$  is an important characteristics of an injection-dependent lifetime curve. For a  $p$ -type Si wafer with a deep-level defect, the ratio  $h$  is given by  $h = (\tau_{n,0} + \tau_{p,0})/\tau_{n,0}$ . Thus, an increase of  $k = \sigma_n/\sigma_p$  results in an increased value of  $h$ . In addition,  $h$  will be always larger than 1, i.e. the SRH lifetime of a deep-level defect increases always with increasing injection density.

Considering a shallow-level defect makes it more difficult to predict the shape of the injection-dependent lifetime curve from the ratio of the capture cross sections since  $h$  is additionally a function of the doping density,  $n_1$  and  $p_1$ . Hence,  $h$  can become smaller than 1 with the consequence of a decreasing lifetime with increasing injection density.

### Total bulk lifetime

The total bulk lifetime  $\tau_b$  as calculated using Eq. (1.4) is plotted in Fig. 1.1 as a red solid line. For the specific  $p$ -type Si wafer assumed for the simulation, the recombination via defect levels is dominant at low-level injection conditions ( $\Delta n \ll N_{\text{dop}}$ ), whereas for higher injection densities, the unavoidable Auger recombination limits the carrier lifetime in Si. The empty square shows the calculated data point for which an illumination intensity equivalent to one sun ( $\sim 0.1 \text{ W/cm}^2$ ) is required for a wafer with a thickness of  $W = 200 \text{ }\mu\text{m}$ . Hence, typical injection conditions for the solar cell under working conditions are equal or lower. Thus, a reduction of the defect concentration in the Si bulk material is of interest to lift the lifetime level at low injection levels.

### 1.1.2 Recombination at the surfaces

At the surface, the crystal lattice is disturbed with the result of unsaturated silicon bonds, also known as dangling bonds. These unsaturated bonds result in energy states in the band gap. The main difference to the defect recombination in the bulk is the broad distribution of energy levels in the band gap.

For the thin wafers used for solar cell production with thicknesses typically smaller than the carrier diffusion length, a reduction of the surface recombination is essential. Otherwise, the recombination at the surfaces will limit the overall carrier lifetime. The surface recombination can be either reduced by decreasing the density of interface states or by a reduction of the carrier concentrations at the surface. In this work, the reduction of the unsaturated bonds at the surface is achieved by depositing silicon nitride  $\text{SiN}_x$  [24] or aluminum oxide  $\text{Al}_2\text{O}_3$  [25, 26]. Both layers contain fixed charges with the consequence of additional field effect passivation. The surface recombination analysis is often performed in terms of a surface recombination velocity  $S$  instead of a lifetime since the recombination per unit area instead of a unit volume is considered. The surface recombination velocity is defined as the ratio of the surface recombination rate per second and area  $R_S$  and the excess carrier density at the surface  $\Delta n_S$ :

$$S := \frac{R_S}{\Delta n_S}. \quad (1.21)$$

In the presence of a space charge region, e.g. due to fixed charges in the passivation

layer, an effective surface recombination velocity  $S_{\text{eff}}$  is defined by the expression

$$S_{\text{eff}} := \frac{R_S}{\Delta n_{\text{scr}}}, \quad (1.22)$$

where  $\Delta n_{\text{scr}}$  is the excess carrier density at the edge of the space charge region. For the sake of convenience, we use  $S$  instead of  $S_{\text{eff}}$  as the symbol for the effective surface recombination velocity in this work.

In this work, effective carrier lifetimes are measured that include the impact of the bulk and surface recombination. For a small surface recombination velocity  $S_{\text{eff}}$  on both surfaces of a thin sample<sup>3</sup>, the effective lifetime  $\tau_{\text{eff}}$  is given by the expression [27]

$$\frac{1}{\tau_{\text{eff}}} = \frac{1}{\tau_b} + \frac{2S}{W}, \quad (1.23)$$

where  $W$  is the sample thickness and  $\tau_b$  is the total bulk lifetime. Sproul [27] investigated the accuracy of Eq. (1.23) for lifetime measurements based carrier decay. He found that Eq. (1.23) yields the actual effective lifetime with an deviation of about 4% if  $SW/D_n < 0.25$  [27], i.e. for  $W = 200 \mu\text{m}$  and a minority carrier diffusion coefficient of  $D_n = 28.6 \text{ cm}^2/\text{s}$ , the surface recombination velocity needs to be  $S < 350 \text{ cm/s}$ .

For a large surface recombination velocity, the effective lifetime can be written as [27]

$$\frac{1}{\tau_{\text{eff}}} = \frac{1}{\tau_b} + \frac{\pi^2 D_n}{W^2}. \quad (1.24)$$

In this case, the effective lifetime is limited by the diffusion of the minority carriers to the surfaces. Sproul [27] found that Eq. (1.24) is accurate within a relative uncertainty of 4% for the effective lifetime if  $SW/D_n > 100$  [27], i.e. for the wafer described above  $S$  needs to larger than  $1.4 \times 10^5 \text{ cm/s}$ . For lifetime measurements under steady-state conditions, Cuevas et al. [28] found that the effective lifetime is better described by

$$\frac{1}{\tau_{\text{eff}}} = \frac{1}{\tau_b} + \frac{12D_n}{W^2}. \quad (1.25)$$

---

<sup>3</sup>The wafer is assumed to have large lateral dimensions compared to the thickness of the sample.

## 1.2 Basic approaches for recombination lifetime measurements

In this Section, different approaches for the contactless determination of the carrier recombination lifetime are presented. Lifetime techniques can be basically separated into two groups: steady-state and dynamic approaches. For a steady-state approach, the excess carrier density  $\Delta n$  is evaluated under steady-state conditions, i.e. when generation and recombination of excess carriers are balanced. In that case, the generation rate and the excess carrier density are proportional with the carrier lifetime as proportionality constant:  $\Delta n = \tau_{\text{eff}}G$ . For a dynamic approach, the time-dependent excess carrier density is analyzed in a range where the balance between generation and recombination is disturbed, i.e. directly after the switch-on (or off) of an excitation source. Then, the time-dependent  $\Delta n(t)$  is described by an exponential function with the carrier lifetime as time constant [see Section 2.1.4, Eq. (2.20)].

An illustration of the two basic approaches is presented in Fig. 1.3. Both figures show the time-dependent excess carrier density for two different effective carrier lifetimes of  $\tau_{\text{eff}} = 1$  ms and 0.3 ms for a square-wave-shaped generation rate  $G(t)$ . Clearly visible is the steady-state range where the time-dependent excess carrier density becomes constant. In Fig. 1.3 (a), it is shown that the steady-state signal is related to the effective carrier lifetime. If using a dynamic approach, the time-dependent excess carrier density is analyzed before the steady-state range is reached. In Fig. 1.3 (b), the excess carrier density is normalized to reveal the different time constants of the time-dependent excess carrier density  $\Delta n(t)$ .

A frequently used example for a steady-state lifetime technique is e.g. the quasi-steady-state photoconductance (QSSPC) technique [29] which is presented in more detail in the next Section. An example for a camera-based steady-state approach is the infrared lifetime mapping (ILM) [30] technique. Both techniques require a calibration of the measured signal for the determination of absolute values of the excess carrier density. The relation between the free carrier density and a measured signal of the respective technique is obtained by measuring samples with different known doping concentrations.

However, a calibration of the steady-state signal is not necessarily required. One example for a steady-state approach that works without calibrating the steady-state signal analyzes indirectly the depth-dependent carrier profile. It can be used that the steady-state carrier profile is a function of the carrier lifetime for a setup that provide an inhomogeneous generation profile. Würfel et al. [31] proposed to determine the carrier diffusion length by measuring different intervals of the Si luminescence spectrum. Würfel et al. [31] exploit the dependence of the spectrum's shape on the sample depth due to photon reabsorption. As a consequence, the ratio of two luminescence signals (acquired using two filters with different wavelength-dependent transmittances) can reveal the carrier lifetime [related to the diffusion length via Eq. (1.3)]. Giesecke et al. [32, 33] applied this approach to contactless photoluminescence measurements.

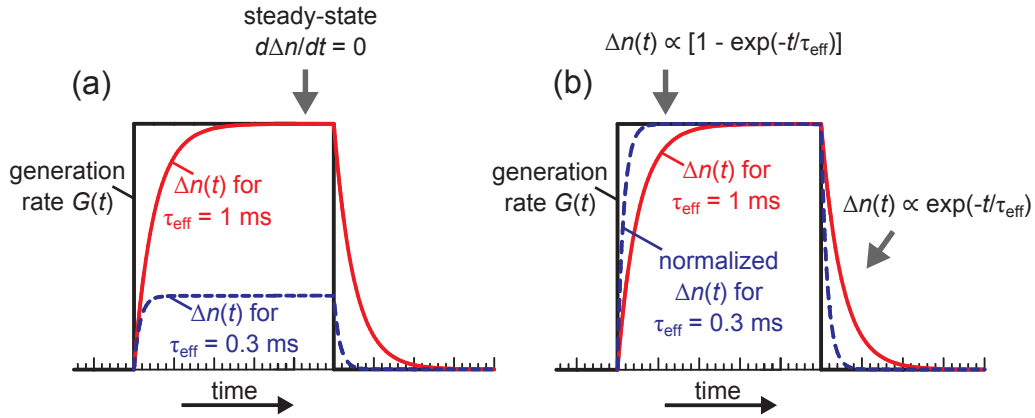


**Figure 1.3:** Time-dependent excess carrier density  $\Delta n$  for a square-wave-shaped generation rate  $G(t)$  as a function of time for the visualization of two fundamentally different approaches for the determination of the effective recombination lifetime  $\tau_{\text{eff}}$  in Si. (a) The steady-state  $\Delta n$  (with  $d\Delta n/dt = 0$ ) is linked with the recombination lifetime by the generation rate  $\tau_{\text{eff}} = \Delta n/G$ . (b)  $\Delta n(t)$  is normalized to the steady-state value to demonstrate that the time constant of  $\Delta n(t)$  corresponds to the recombination lifetime.

However, the PL intensity ratio analysis relies on the precisely modeled signal ratio and the knowledge of the wavelength-dependent properties of the setup. In addition, techniques based on the analysis of the carrier profile are only sensitive for carrier diffusion lengths smaller than the wafer thickness; a requirement that is often not satisfied for today's thin Si wafers and solar cells. However, Trupke et al. [34] could demonstrate the applicability of the so-called “two-filter approach” to thick Si bricks.

A prominent example for a dynamic lifetime measurement technique is the transient photoconductance decay (PCD) approach where the lifetime is extracted from the slope of the time-dependent photoconductance after a pulsed excitation [35–37]. Another example for a dynamic lifetime technique is the light-biased microwave-detected photoconductance-decay (MW-PCD) [38–40] approach. Dynamic techniques have the advantage of being independent of an absolute measurement of the excess carrier density. Hence, a calibration is not required; the measurement of a signal proportional to the excess carrier density is sufficient. However, a basic assumption for the determination of an effective carrier lifetime from the time-dependent  $\Delta n(t)$  is an injection-independent carrier lifetime. Since this is rarely the case (see e.g. Fig. 1.1), the signal variation for the lifetime analysis is kept small to acquire the measurement within a small injection range. The MW-PCD approach is in addition typically used with a bias light since the measured reflected microwave power depends only linearly on the sample conductance (and thus on the carrier density) for a small signal variation. However, for light-biased MW-PCD measurements, the impact of an injection-dependent carrier lifetime was found to be non-negligible. Schmidt et al. [24, 41] introduced the concept of a differential carrier lifetime for transient PCD measurements with additional bias light to account for the impact of an injection-dependent carrier lifetime. The differential lifetime only equals the actual steady-state

carrier lifetime if the lifetime is injection-independent.

In summary, steady-state techniques require either a calibration or a reliable modeling of the measured signal and the carrier distribution. Dynamic techniques get along without a calibration of the measured signal to the excess carrier density but one has to consider the impact of an injection-dependent lifetime on the measured lifetime. In this work, a steady-state and a dynamic lifetime measurement concept are realized using a camera-based photoluminescence setup.

## 1.3 Quasi-steady-state photoconductance (QSSPC)

### 1.3.1 Measurement of the recombination lifetime

The QSSPC technique [29] utilizes the dependence of the photoconductance of a Si sample on its density of excited excess carriers. The steady-state carrier lifetime can be measured over a wide injection range with a single measurement using a photo flash lamp with a decay time constant ( $\sim 2$  ms) much larger than the effective carrier lifetime to be measured. For that reason, steady-state conditions are established in the Si wafer for each illumination intensity (during the decay) to a good approximation. Combined with the knowledge of the photogeneration rate, the effective carrier lifetime of a Si test sample is basically determined using Eq. (1.2). A more generalized approach was proposed by Nagel et al. [37] by taking the impact of the slowly decaying intensity of the flash lamp into account. Thus, the effective carrier lifetime  $\tau_{\text{eff}}$  is calculated using the expression [37]:

$$\tau_{\text{eff}} = \frac{\Delta n(t)}{G(t) - \partial \Delta n(t) / \partial t} \quad (1.26)$$

with  $G(t)$  being the time-dependent photogeneration rate of excess carriers.

The conductance of a Si wafer can be determined using a commercially available QSSPC system (Sinton Consulting, WCT-100), schematically shown in Fig. 1.4 (a). In this setup, the Si sample is placed on top of a radio-frequency (rf) coil which is connected to an rf bridge circuit. Alternating currents in the rf coil with a frequency of  $\sim 10$  MHz induce eddy currents in the Si sample. The eddy currents in the sample are prone to resistivity losses as a function of the sample conductivity. The sample eddy currents are in turn inducing a current in the rf coil with opposite sign. This impact is measured and converted into a voltage which is determined by an external oscilloscope.

The output voltage of the rf bridge circuit is calibrated by measuring samples of different known doping densities. The resulting calibration function is exemplarily shown in Fig. 1.4 (b). The conductance of the wafers is found to be a polynomial function of the output voltage. For the determination of the excess conductance (due

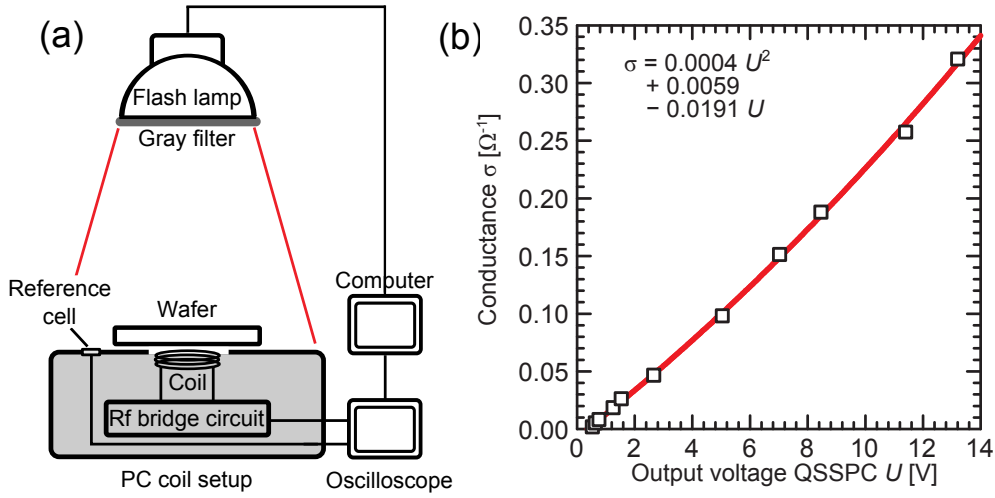


**Figure 1.4:** (a) Schematic of the setup used for quasi-steady-state photoconductance lifetime measurements. (b) Calibration function of the rf bridge circuit: Conductance  $\sigma$  of Si samples of different dopant densities versus the output voltage of the QSSPC setup  $U$  if measuring the samples without optical excitation.

to the illumination), the background conductance (in the dark) is measured and used as a baseline for measurements of the excess conductance. An example measurement of a  $p$ -type mc-Si wafer is presented in Fig. 1.5 (a). The black curve represents the output voltage of the QSSPC due to the time-dependent excitation of excess carriers. The exciting illumination intensity  $I_{\text{exc}}$  is measured using a reference solar cell under short-circuit conditions. It is used that the short circuit current of the cell is over a wide range proportional to the illumination intensity  $I_{\text{sc}} \propto I_{\text{exc}}$ . The measured  $I_{\text{exc}}$  is plotted in Fig. 1.5 (a) as a red dashed line.

The excess conductance  $\Delta\sigma$  (due to the illumination) and hence, the excess carrier density  $\Delta n$  of a sample of thickness  $W$  is given by

$$\Delta\sigma = q(\Delta n\mu_n + \Delta p\mu_p)W \Rightarrow \Delta n = \frac{\Delta\sigma}{qW(\mu_n + \mu_p)}, \quad (1.27)$$

assuming  $\Delta n = \Delta p$  and a homogeneous distribution of excess carriers in the sample. It is further considered that the electron and hole mobilities  $\mu_n$  and  $\mu_p$  are themselves a function of doping and excess carrier density. Using an empirical mobility model (e.g. from Ref. 42 or 43), the excess carrier density can be self-consistently determined from the excess photoconductance (see e.g. Ref. 44, p. 53).

The time-dependent photogeneration rate  $G(t)$  is derived from the measured illumination intensity  $I_{\text{exc}}$  under consideration of the optical properties of the Si sample. Knowing the current density of the reference cell under one sun illumination  $J_{\text{sc},1\text{sun}}$ , the photogeneration rate is calculated using the expression

$$G(t) = \frac{I_{\text{exc}}(t)J_{\text{sc},1\text{sun}}A}{q}, \quad (1.28)$$

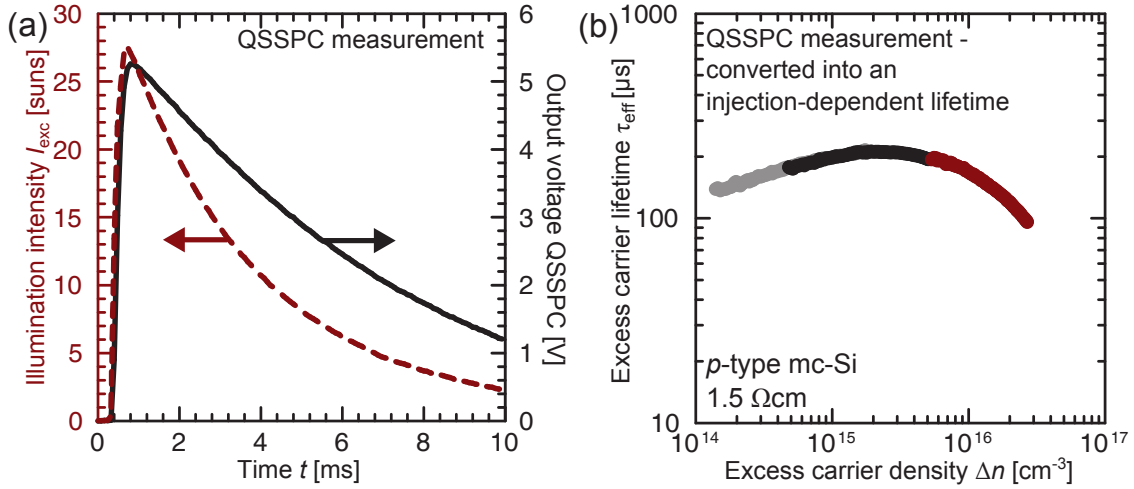


**Figure 1.5:** (a) Measured illumination intensity of the flash lamp as a function of time (red dashed line) and measured output voltage of the QSSPC for a p-type mc-Si wafer (black line). (b) Injection-dependent effective carrier lifetime  $\tau_{\text{eff}}$  as a function of the excess carrier density  $\Delta n$  calculated from (a) using Eqs. (1.26) to (1.28).

where the factor  $A$  accounts for differences in the optical properties between the reference cell and the test sample. Figure 1.5 (b) shows the injection-dependent effective carrier lifetime (red data points) that is calculated from the data of Fig. 1.5 (a) by using Eqs. (1.26) to (1.28). Additionally, two more QSSPC measurements are shown (gray and black data points) that were acquired using gray filters in front of the flash lamp.

### 1.3.2 Measurement artifacts

For the validity of Eq. (1.27), it is required that  $\Delta n = \Delta p$ . Additionally, it is assumed that the free carriers are homogeneously distributed throughout the Si wafer. If the made assumptions are not fulfilled, a deviation between the measured and the actual lifetime is expected and one speaks of a measurement artifact. In this Section, two measurement artifacts of PC measurements are presented.

#### Minority carrier trapping

For photoconductance-based lifetime measurements, anomalously high lifetimes have been observed at low injection levels [45, 46]. For mc-Si and Cz-Si wafers, the difference between the measured apparent lifetime and the actual recombination lifetime was attributed to trapping of electrons in shallow trap states. Macdonald and Cuevas [45] explained the increasing lifetime with decreasing injection density by applying the Hornbeck-Haynes model [47] to their data. An illustration of the essential features of the Hornbeck-Haynes model can be found in Fig. 1.6 (a). In the Hornbeck-Haynes

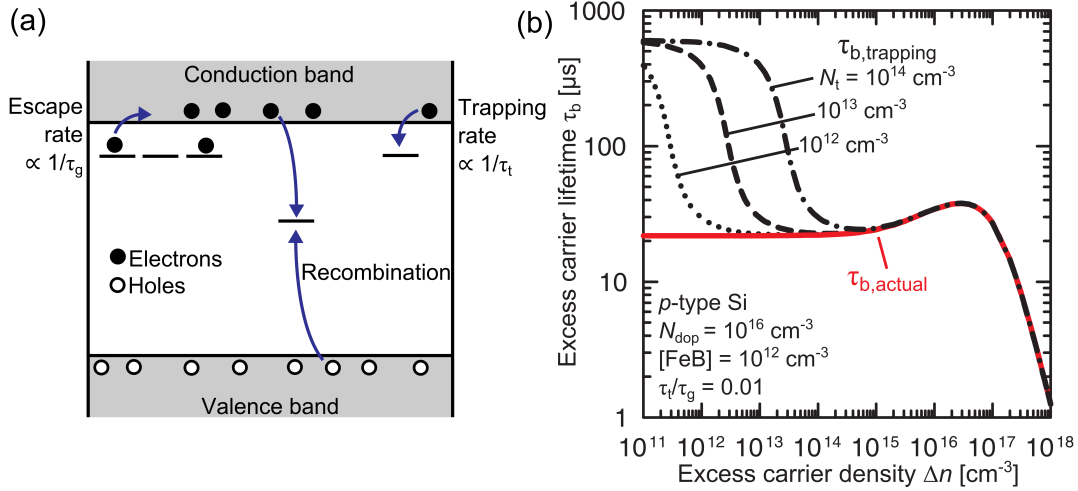


**Figure 1.6:** (a) Energy band diagram that illustrates the recombination of electron-hole pairs via deep-level defect states and the trapping of electrons by shallow-level defect states (based on Fig. 2 in Ref. 45). (b) Actual bulk lifetime  $\tau_{b,actual}$  as expected for a *p*-type Si wafer with a doping density of  $10^{16} \text{ cm}^{-3}$  and an impurity (FeB pairs) concentration of  $[FeB] = 10^{12} \text{ cm}^{-3}$  as a function of the excess carrier density (red solid line). Calculated apparent carrier lifetime  $\tau_{b,trapping}$  as measured with a photoconductance-based setup as a function of the apparent excess carrier density for different trap densities  $N_t$  (black lines).

model, it is assumed that electron-hole recombination occurs via a deep-level defect center (close to the middle of the Si band gap). An additional shallow-level defect center (close to the conduction band in *p*-type Si) is assumed to trap electrons from the conduction band but does not serve as a recombination center. As a consequence, the density of excess electrons in the conduction band is not affected by the traps. For steady-state conditions, the density of excess electrons is only determined by the recombination lifetime via the deep state. This is different for the excess holes in the valence band since each excess electron in a trap state is accompanied by an excess hole in the valence band. Thus, the number of excess holes is unbalanced to the excess electrons recombining via the deep defect state:  $\Delta n \neq \Delta p$ . As a result, a major assumption for the usage of Eq. (1.27) is violated and the excess conductance in the presence of trapped electrons (with a density of  $n_t$ ) is given by [45]:

$$\Delta\sigma_t = qW [\mu_n \Delta n + \mu_p (\Delta p + n_t)]. \quad (1.29)$$

According to the Hornbeck-Haynes model, the density of trapped electrons  $n_t$  can be expressed as a function of the trap density  $N_t$ :

$$n_t = \frac{N_t \Delta n}{\Delta n + N_t \tau_t / \tau_g} \quad (1.30)$$

with  $\tau_t$  being the mean time before an electron is trapped (when all traps are empty) and  $\tau_g$  being the mean time spent in a trap. Calculating  $\Delta\sigma_t$  in relation to the excess

photoconductance without any traps [Eq. (1.27)] yields [45]:

$$\Delta\sigma_t = \Delta\sigma \left( 1 + \frac{n_t}{\Delta n} \frac{\mu_p}{\mu_p + \mu_n} \right). \quad (1.31)$$

From Eq. (1.31) it can be concluded that if  $\Delta n < n_t$ , the excess conductance and thus the measured excess carrier density and steady-state carrier lifetime increases as a function of the ratio  $n_t/\Delta n$ . Figure 1.6 (b) shows a modeled carrier lifetime  $\tau_{b,\text{actual}}$  as expected for a *p*-type Si wafer with a doping density of  $10^{16} \text{ cm}^{-3}$  and an impurity (FeB pairs<sup>4</sup>) concentration of  $[\text{FeB}] = 10^{12} \text{ cm}^{-3}$  as a function of the excess carrier density. Additionally, the apparent lifetime  $\tau_{b,\text{trapping}}$  as measured by a photoconductance-based setup is calculated for different trap densities  $N_t$ . As expected from Eq. (1.31), the apparent lifetime increases strongly with decreasing excess carrier density.

Note that lifetime measurements based on free carrier emission [30] are similarly affected by trapping of minority carriers as are PC-based lifetime measurements [50].

### Depletion region modulation

Another measurement artifact of photoconductance-based lifetime measurement is known as depletion region modulation (DRM) effect [51]. The DRM effect was demonstrated for PC measurements on samples having a space charge region as e.g. samples with deposited corona charges on an oxidized Si surface [51], with a *p*-*n* junction [52, 53] or samples with a  $\text{SiN}_x$  passivation layer that contains fixed charges [54].

For the measurement of the excess conductance  $\Delta\sigma$ , the conductance in the dark  $\sigma_{\text{dark}}$  is subtracted from the conductance measured under illumination  $\sigma_{\text{ill}}$ :

$$\Delta\sigma = \sigma_{\text{ill}} - \sigma_{\text{dark}} \quad (1.32)$$

with

$$\sigma_{\text{ill}} = q[(N_{\text{dop}} + \Delta n)\mu_p + \Delta n\mu_n]W \quad \text{and} \quad \sigma_{\text{dark}} = qN_{\text{dop}}\mu_p W, \quad (1.33)$$

assuming that  $\Delta n = \Delta p$  and  $n_0 \ll p_0 \approx N_{\text{dop}}$  for a *p*-type Si wafer. Inserting Eq. (1.33) into (1.32) yields the excess conductance as given by Eq. (1.27). For the validity of Eq. (1.27), it is assumed that the mobile excess carriers are homogeneously distributed throughout the Si wafer. In the presence of a space charge region, this assumption is not fulfilled since this region is empty of mobile excess carriers.

In addition, the optical excitation of a sample with a space charge region changes the width of the space charge region  $W_{\text{scr}}$  due to accumulated excess carriers at the edges of the space charge region. Thus,  $W_{\text{scr}}$  modulates with the illumination intensity  $I_{\text{exc}}$ . As a result, the conductance under illumination  $\sigma_{\text{ill}}$  and the conductance in the dark

---

<sup>4</sup> $E_{\text{defect}} = E_C - 0.26 \text{ eV}$  [48, 49],  $\sigma_n = 5 \times 10^{-15} \text{ cm}^2$  [49],  $\sigma_p = 3 \times 10^{-15} \text{ cm}^2$  [49]

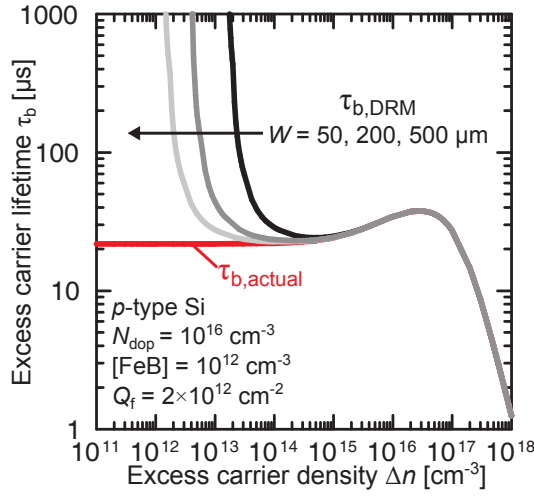


**Figure 1.7:** Actual bulk lifetime  $\tau_{b,actual}$  as expected for a *p*-type Si wafer with a doping density of  $10^{16} \text{ cm}^{-3}$  and an impurity (FeB pairs) concentration of  $[\text{FeB}] = 10^{12} \text{ cm}^{-3}$  as a function of the excess carrier density  $\Delta n$ . Calculated apparent carrier lifetime  $\tau_{b,DRM}$  as measured in the presence of a space charge region with a photoconductance-based setup as a function of the apparent excess carrier density for different thicknesses  $W$ .

$\sigma_{\text{dark}}$  are given by:

$$\begin{aligned} \sigma_{\text{ill}} &= q[(N_{\text{dop}} + \Delta n)\mu_p + \Delta n\mu_n](W - W_{\text{scr}}(I_{\text{exc}})) \quad \text{and} \\ \sigma_{\text{dark}} &= qN_{\text{dop}}\mu_p(W - W_{\text{scr}}(I_{\text{exc}} = 0)). \end{aligned} \quad (1.34)$$

Using Eqs. (1.32) and (1.34), the excess conductance for a sample with a space charge region  $\Delta\sigma_{\text{scr}}$  is calculated to

$$\Delta\sigma_{\text{scr}} = q\Delta n(\mu_n + \mu_p)[W - W_{\text{scr}}(I_{\text{exc}})] + q\mu_p N_{\text{dop}}[W_{\text{scr}}(I_{\text{exc}} = 0) - W_{\text{scr}}(I_{\text{exc}})]. \quad (1.35)$$

With increasing illumination and excess carrier density, the width of the space charge region decreases and the impact of the second summand of the right hand side of Eq. (1.35) increases. However, the first summand scales with the excess carrier density. As a consequence, the second summand only dominates the measured excess conductance for excess carrier densities much lower than the doping density ( $\Delta n \ll N_{\text{dop}}$ ).

Figure 1.7 (b) shows a modeled carrier lifetime  $\tau_{b,actual}$  as expected for a *p*-type Si wafer with a doping density of  $10^{16} \text{ cm}^{-3}$  and an impurity (FeB pairs<sup>5</sup>) concentration of  $[\text{FeB}] = 10^{12} \text{ cm}^{-3}$  as a function of the excess carrier density. Additionally, the apparent lifetime  $\tau_{b,DRM}$  as measured with a photoconductance-based setup is modeled for a sample that has a space charge region due to fixed charges at the surfaces. Using the device simulation program PC1D v5.8, we modeled the cumulative excess conductance for the *p*-type wafer with a charge density of  $Q_f = 2 \times 10^{12} \text{ cm}^{-3}$  at the surfaces. From Eq. (1.35) it can be derived that the impact of the space charge region on

<sup>5</sup> $E_{\text{defect}} = E_C - 0.26 \text{ eV}$  [48, 49],  $\sigma_n = 5 \times 10^{-15} \text{ cm}^2$  [49],  $\sigma_p = 3 \times 10^{-15} \text{ cm}^2$  [49]

the measurement of the apparent carrier lifetime is strongly influenced by the wafer thickness. Figure 1.7 (b) shows the calculated apparent lifetime for three thicknesses  $W$  demonstrating the increasing DRM impact with decreasing wafer thickness.

In summary, the photoconductance-based lifetime measurement is prone to measurement artifacts in the presence of traps or a space charge region. Both artifacts manifest themselves in anomalously high lifetimes at low injection conditions.

## CHAPTER 2

---

# Simulation and measurement of the photoluminescence emission of silicon

---

Luminescence is defined as the photon emission as a result of electronic excitation in a device or material, excluding any photon emission that is purely the result of the temperature of the material [55, p. 602]. The luminescence emission is mostly distinguished by the source of input energy. Since 2005, electro- and photoluminescence [5, 6] are frequently used for the analysis of the electrical properties of silicon (Si) wafers and solar cells. The luminescence emission of a semiconductor is caused by the transition of an excited electron from the conduction band to an empty state (or hole) in the valence band, releasing the energy difference as a photon. Electroluminescence is generated by charge carrier injection via contacts at a different electrical potential. Hence, this form of luminescence stimulation is only applicable for samples where carriers can be electrically injected, e.g. via a  $p$ - $n$  junction or a Schottky contact. On the contrary, photoluminescence allows the contactless investigation of Si solar cells and wafers since the charge carriers are generated by optical excitation.

For the interpretation of the measured photoluminescence signal in terms of the material properties, modeling of the photoluminescence signal is indispensable. In this Chapter, a one-dimensional model for the simulation of the stationary and time-dependent photoluminescence emission of a Si wafer is presented. Finally, the technical components of a photoluminescence setup, required for the measurement of a signal proportional to the photoluminescence emission of a Si sample, are introduced.

## 2.1 Simulation of the photoluminescence signal of a silicon wafer

First, the modification of Planck's law for thermal emission to the generalized Planck equation for luminescence emission of semiconductors is briefly discussed. A more detailed description can be found in Ref. 56. The radiative recombination of electron-hole pairs in Si is discussed in terms of wavelength and carrier concentration. Afterwards, a simple model for the impact of the sample geometry on the photoluminescence emission of a Si wafer is presented. Since the photoluminescence emission depends on the spatial distribution of charge carriers in the Si sample, we present a one-dimensional model for the time- and depth-dependent carrier distribution in a Si wafer under optical excitation.

### 2.1.1 Generalized Planck's law

The photon flux, emitted from a perfect absorber or "black body" due to its temperature, is described by Planck's law of radiation [57]. The emitted photon flux  $d\Phi_\gamma$  of the black body per energy interval  $d(\hbar\omega)$  (integrated over all directions in space) is derived from the product of the density of allowed states with the Bose-Einstein occupation function for photons<sup>1</sup> [56]:

$$d\Phi_\gamma(\hbar\omega) = \frac{(\hbar\omega)^2}{\pi^2\hbar^3(c/n_{\text{Si}})^2} \left[ \exp\left(\frac{\hbar\omega}{k_B T}\right) - 1 \right]^{-1} d(\hbar\omega). \quad (2.1)$$

Kirchhoff found from detailed balance<sup>2</sup> considerations that the thermal emission of a non-black body  $\Phi_{\text{non-bb}}$  with an absorptivity of  $a < 1$  can be derived from the black-body emission  $\Phi_{\text{bb}}$  ( $a = 1$  for a black body), defined by Eq. (2.1), using  $\Phi_{\text{non-bb}} = a \cdot \Phi_{\text{bb}}$ . The absorptivity  $a$  is a function of the sample geometry and depends on the absorption coefficient  $\alpha$  of the material. A major assumption for the validity of Planck's law is a thermal equilibrium of the body of interest with its surroundings.

It has been found that these considerations are also valid for radiative band-to-band transitions of semiconductors [58–60]. Although an excited semiconductor is not generally in an equilibrium state, it can be considered being in thermal equilibrium. If the semiconductor is e.g. optically excited, the carrier distribution is directly after the excitation determined by the excitation spectrum. However, shortly after the excitation, the carriers have already again established a state of minimum free energy due to collisions with the crystal lattice (exchange of phonons). Since the emission and absorption rates of phonons are much higher than for the photons, the semiconductor is in thermal equilibrium with respect to the relatively high lifetimes of the excited

<sup>1</sup> $\hbar = \frac{h}{2\pi}$ : reduced Planck constant,  $c$ : speed of light in vacuum,  $\omega = 2\pi\frac{c}{\lambda}$ : angular frequency,  $n_{\text{Si}}$ : refractive index of Si,  $k_B$ : Boltzmann constant,  $T$ : temperature

<sup>2</sup>At equilibrium, each elementary process should be equilibrated by its reverse process.

electrons. As a consequence, the carrier energy distribution of the excited semiconductor is still correctly described by a Fermi-distribution but shifted by the so-called quasi-Fermi energy.

The radiative transition of an excited electron to an empty state in the valence band is accompanied by the emission of a photon. Würfel [58] introduced the chemical potential of photons  $\eta_\gamma$  similar to the chemical potential of a material gas. Since the electrochemical energy of the excited electrons and holes can be completely converted into the energy of the emitted photons,  $\eta_\gamma$  is given by the sum of the electrochemical potentials of the excited electrons and holes [58]. The sum equals the chemical energy of the excited electron-holes pairs which is well-defined by the difference of the quasi-Fermi energies. For that reason, it is possible to relate the chemical potential of photons and thus, the emitted photon flux, to the carrier distributions in the excited semiconductor. With  $\eta_\gamma$  as a measure for the excited carrier concentration, Würfel [58] introduced the generalized Planck equation for the emitted photon flux  $\Phi_\gamma$  of an excited semiconductor that is not purely the result of the temperature of the material:

$$d\Phi_\gamma(\hbar\omega) = \frac{a(\hbar\omega)(\hbar\omega)^2}{\pi^2\hbar^3(c/n_{\text{Si}})^2} \left[ \exp\left(\frac{\hbar\omega - \eta_\gamma}{k_B T}\right) - 1 \right]^{-1} d(\hbar\omega). \quad (2.2)$$

The chemical potential is  $\eta_\gamma = 0$  for thermal radiation and  $\eta_\gamma > 0$  for non-thermal radiation of the excited semiconductor. Equation (2.2) is valid for  $\hbar\omega - \eta_\gamma > k_B T$ . Herrmann and Würfel [61] state that the luminescent radiation cannot contain all photon energies as can be read from Eq. (2.2). It can exist only above the energy threshold of  $k_B T + \eta_\gamma$ . Interestingly, this condition is fulfilled by a semiconductor due to the band gap of the material [61].

In this work, the simulated spectra of emitted photons are expressed as a function of the photon wavelength  $\lambda$ . Therefore, the energy interval  $d(\hbar\omega)$  in Eq. (2.2) is transferred into a wavelength interval  $d\lambda$ :

$$\frac{d(\hbar\omega)}{d\lambda} = \frac{d(hc/\lambda)}{d\lambda} = -\frac{hc}{\lambda^2} \Rightarrow d(\hbar\omega) = -\frac{hc}{\lambda^2} d\lambda. \quad (2.3)$$

The negative sign expresses the reduction of wavelength with increasing photon energy. Additionally, the photon distribution function is replaced by the Boltzmann distribution since it is expected that  $\hbar\omega - \eta_\gamma \gg k_B T$  at 300 K for the carrier densities and the wavelength range investigated in this work, resulting in

$$d\Phi_\gamma(\lambda) = \frac{a(\lambda) 8\pi c n_{\text{Si}}^2}{\lambda^4} \exp\left(\frac{-(hc/\lambda - \eta_\gamma)}{k_B T}\right) d\lambda. \quad (2.4)$$

As mentioned above, the chemical potential of photons  $\eta_\gamma$  can be related to the carrier densities in the semiconductor via the difference of the quasi-Fermi energies

of electrons in the conduction band  $\epsilon_{Fc}$  and holes in the valence band  $\epsilon_{Fv}$ :

$$\eta_\gamma = \epsilon_{Fc} - \epsilon_{Fv}. \quad (2.5)$$

In non-equilibrium, the product of the free carrier densities is larger than the product of the equilibrium concentrations  $n_i^2$  [Eq. (1.1)]. The non-equilibrium state can be described by the difference of the quasi-Fermi energies with

$$np = n_i^2 \exp\left(\frac{\epsilon_{Fc} - \epsilon_{Fv}}{k_B T}\right) = n_i^2 \exp\left(\frac{\eta_\gamma}{k_B T}\right). \quad (2.6)$$

Using Eq. (2.6), the emitted photon flux due to band-to-band recombination  $d\Phi_\gamma(\lambda)$  [Eq. (2.4)] can be related to the carrier densities in the Si sample:

$$d\Phi_\gamma(\lambda) = \frac{a(\lambda) 8\pi c n_{Si}^2}{\lambda^4} \exp\left(\frac{-hc/\lambda}{k_B T}\right) \frac{np}{n_i^2} d\lambda. \quad (2.7)$$

Combining Eqs. (2.7) and Eq. (1.6) results in the functional dependence of the emitted photon flux on the excess carrier density:

$$d\Phi_\gamma(\lambda) = \frac{a(\lambda) 8\pi c n_{Si}^2}{\lambda^4} \exp\left(\frac{-hc/\lambda}{k_B T}\right) \frac{[\Delta n N_{dop} + \Delta n^2]}{n_i^2} d\lambda. \quad (2.8)$$

### 2.1.2 Radiative recombination coefficient

The photoluminescence emission of an excited semiconductor is frequently described by the radiative recombination coefficient  $B_{rad}$  as proportionality constant between the radiative recombination rate  $R_{rad}$  and the product of the carrier densities [Eq. (1.5)]. From Eq. (2.7), the radiative recombination rate  $R_{rad}$  is derived using the Lambert-Beer absorption law, which states that the annihilation of photons is related to the absorption coefficient  $\alpha$ . In case of band-to-band photon absorption, this annihilation is proportional to the generation rate of electron-hole pairs  $G_{eh}$  [56, p. 62]:

$$d\Phi_\gamma/dz = -\alpha\Phi_\gamma = G_{eh}. \quad (2.9)$$

For equilibrium conditions, the generation rate of electron-hole pairs  $G_{eh}$  due to absorption of photons equals the radiative recombination rate  $G_{eh} = R_{rad}$ . Additionally, the absorptivity  $a$  has to cancel out since the recombination rate is defined independent of the sample geometry. Hence, using Eq. (2.7) we obtain:

$$dR_{rad} = \frac{\alpha}{a} d\Phi_\gamma(\lambda) = \frac{\alpha(\lambda) 8\pi c n_{Si}^2}{\lambda^4} \exp\left(\frac{-hc/\lambda}{k_B T}\right) \frac{np}{n_i^2} d\lambda. \quad (2.10)$$

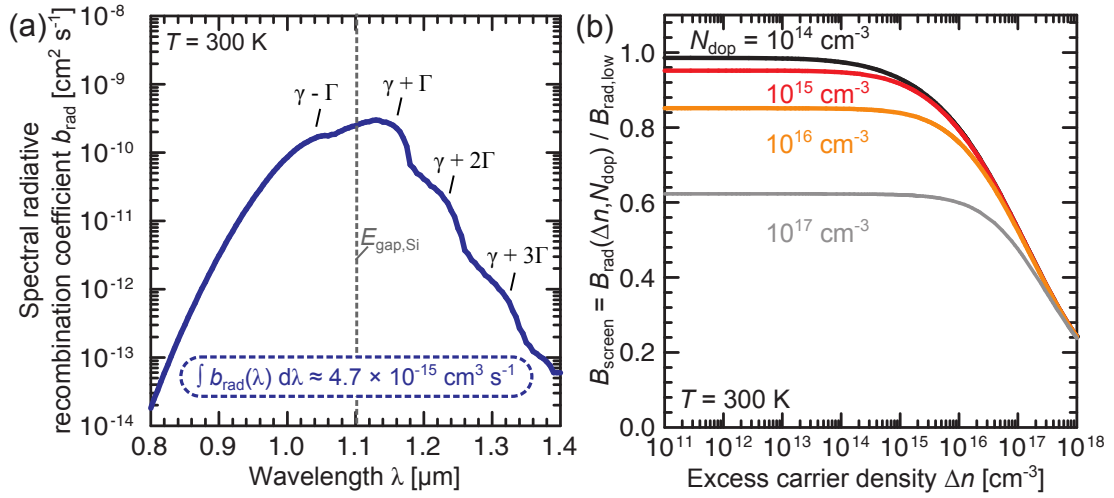


**Figure 2.1:** (a) Spectral radiative recombination coefficient  $b_{\text{rad}} = \frac{dB_{\text{rad}}}{d\lambda}$  as a function of the photon wavelength [Eq. (2.11)]. (b) Scaled radiative recombination coefficient  $B_{\text{screen}} = \frac{B_{\text{rad}}(\Delta n, N_{\text{dop}})}{B_{\text{rad,low}}}$  as a function of the excess carrier density  $\Delta n$  for different doping densities  $N_{\text{dop}}$  after a parameterization of Altermatt et al. [10].

Comparing Eqs. (2.10) and (1.5) yields the dependence of  $B_{\text{rad}}$  on wavelength, temperature, and the absorption coefficient:

$$dB_{\text{rad}}(\lambda, T) = \frac{\alpha(\lambda, T) 8\pi c n_{\text{Si}}^2}{\lambda^4} \exp\left(\frac{-hc/\lambda}{k_B T}\right) \frac{1}{n_i^2} d\lambda = b_{\text{rad}} d\lambda. \quad (2.11)$$

The spectral radiative recombination coefficient  $b_{\text{rad}} = \frac{dB_{\text{rad}}}{d\lambda}$  is displayed in Fig. 2.1 (a). The visible shoulders correspond to the emission of photons with absorption and emission of a variable number of phonons (e.g.  $\gamma + \Gamma$  indicates that one photon and one phonon are simultaneously emitted) [62]. The integral radiative recombination coefficient is calculated to  $B_{\text{rad}}(300 \text{ K}) = 4.7 \times 10^{-15} \text{ cm}^3 \text{ s}^{-1}$  as in Ref. 62 (using the wavelength-dependent band-to-band absorption coefficient of Ref. 63). This relatively low value reflects the low probability of radiative recombination in an indirect semiconductor such as Si. For comparison, for gallium arsenide as a direct semiconductor,  $B_{\text{rad}}$  was determined to be  $1.3 \times 10^{-10} \text{ cm}^3 \text{ s}^{-1}$  [64], which is about five orders of magnitude higher than for Si.

As already mentioned in Section 1.1, the radiative recombination rate of Si was found to be enhanced due to the Coulomb attraction of electrons in the conduction band and holes in the valence band. However, for high excess carrier densities, Altermatt et al. [10, 11] found a decrease of the radiative recombination rate with increasing density of free carriers. They found a good agreement between simulation and experiment by assuming a screening of the Coulomb enhancement by the increased carrier density. Altermatt et al. [10] modeled the relative dependence of  $B_{\text{rad}}(\Delta n, N_{\text{dop}})$  in comparison

to a value of  $B_{\text{rad}}$  for low carrier densities ( $\Delta n, N_{\text{dop}} < 10^{14} \text{ cm}^{-3}$ ):

$$B_{\text{screen}} := \frac{B_{\text{rad}}(\Delta n, N_{\text{dop}})}{B_{\text{rad,low}}}, \quad (2.12)$$

with  $B_{\text{rad,low}}$  being the value determined from Trupke et al. [62] to  $B_{\text{rad,low}} = 4.7 \times 10^{-15} \text{ cm}^3\text{s}^{-1}$ . The scaled radiative recombination coefficient  $B_{\text{screen}}$  as a function of the carrier density is displayed in Fig. 2.1 (b) for different doping densities.

We conclude that the variation of  $B_{\text{rad}}$  as a function of excess carrier density and doping density due to Coulomb screening is expected to be  $< 20\%$  if investigating excess carrier densities below  $10^{16} \text{ cm}^{-3}$  and doping densities in the range  $10^{15} \text{ cm}^{-3} < N_{\text{dop}} < 10^{16} \text{ cm}^{-3}$ .

### 2.1.3 Impact of sample geometry on photoluminescence emission

The photoluminescence photon flux given by Eq. (2.8) emits equally in all directions in space. In this Section, the impact of the sample geometry on the photon flux as emitted from a Si wafer surface is analyzed. Due to the large lateral dimensions of the sample and laterally homogeneous sample properties, a one-dimensional treatment of the PL emission is sufficient.

From Kirchhoff's law, it is known that the absorptivity equals the emissivity in any solid angle and energy (or wavelength) interval. In this work, the emissivity is specified by the escape fraction for luminescence photons  $\eta_{\text{esc}}$ . For the calculation of the average PL emission from a unit area of a Si sample, the PL photon flux [Eq. (2.8)] is integrated over depth:

$$\Phi_{\gamma}(\lambda) = \int \int \eta_{\text{esc}}(\lambda, z) b_{\text{rad}}(\lambda) [\Delta n(z) N_{\text{dop}} + (\Delta n(z))^2] dz d\lambda. \quad (2.13)$$

If using an experimental setup for the measurement of the PL emission (for details see Section 2.2), it has to be considered that the detector sensitivity as well as the transmission of filters and lenses are typically a function of the photon wavelength. Hence, the measured PL intensity signal  $I_{\text{PL}}$  is given by

$$I_{\text{PL}} = \frac{\Omega}{2\pi} \int \int \eta_{\text{esc}}(\lambda, z) b_{\text{rad}}(\lambda) [\Delta n(z) N_{\text{dop}} + (\Delta n(z))^2] f_{\text{setup}}(\lambda) dz d\lambda, \quad (2.14)$$

with  $f_{\text{setup}}(\lambda)$  incorporating all wavelength-dependent quantities of the PL setup. The luminescence photons are considered being emitted into the half space between the sample surface and the detector. However, only a fraction of these PL photons are actually detected. Photons have to be emitted inside a solid angle  $\Omega = A_{\text{lens}}/g^2$  to be detected ( $A_{\text{lens}}$ : area of the used lens for imaging of the photons onto the detector,

g: object distance between sample and lens)<sup>3</sup>.

With the PL setup used in this work a signal proportional to the net luminescence emission is detected. From the actual PL signal, a dark signal (without optical excitation) is subtracted which accounts for detector offsets but also for luminescence due to thermally generated free carriers. However, the thermally generated photon flux is proportional to  $n_i^2$ , whereas the photoluminescence photon flux is proportional to the product of free carriers  $np = (\Delta n + n_0)(\Delta p + p_0)$ . Thus, for a doping density of  $N_{\text{dop}} \approx p_0 \gg n_i$  and an excess carrier density of  $\Delta n \gg n_0$ , the subtraction of the thermally generated photon flux is negligible for the modeling of the measured PL signal.

For the description of a stationary or a time-dependent photoluminescence signal, the time- and position-dependent excess carrier density  $\Delta n(z, t)$  is determined in Section 2.1.4. The escape fraction  $\eta_{\text{esc}}(\lambda)$  is discussed in more detail in the following Section.

### Escape fraction $\eta_{\text{esc}}(\lambda, z)$

The escape fraction for luminescence photons  $\eta_{\text{esc}}$  describes the fraction of photons that is able to leave the Si sample, whereby the sample geometry is taken into account. A fraction of the generated PL emission is re-absorbed in the Si. This fraction is a function of the position of the PL generation and of the photon wavelength. The Lambert-Beer absorption law  $I_T(z)/I_0(z=0) = \exp(-\alpha(\lambda)z)$  is applied to determine the transmitted PL intensity fraction  $I_T(z)/I_0(z=0)$  over a distance  $z$  with  $\alpha$  being the wavelength-dependent absorption coefficient of Si.

After traveling through the sample, the PL photons meet the interface of the sample with the surrounding medium. For perpendicular incidence of the light, the wavelength-dependent transmittance  $T(\lambda) = 1 - R(\lambda)$  of the interface is calculated from the two refractive indices of the adjacent media (e.g. Si and air):

$$T(\lambda) = 1 - R(\lambda) = 1 - \frac{[n_{\text{Si}}(\lambda) - n_{\text{air}}(\lambda)]^2}{[n_{\text{Si}}(\lambda) + n_{\text{air}}(\lambda)]^2}. \quad (2.15)$$

The escape fraction  $\eta_{\text{esc}}(\lambda, z)$  for the generated photons, emitted from one sample surface, is calculated by considering the transmittance at the front interface with  $T_f(\lambda)$  for the photons traveling in the front direction and one reflection at the rear side with  $R_r(\lambda)$  for the photons traveling in the rear direction (according to Ref. 31):

$$\eta_{\text{esc}}(z, \lambda) = \frac{1}{2n_{\text{Si}}^2} T_f(\lambda) [\exp(-\alpha(\lambda)z) + R_r(\lambda) \exp(-\alpha(\lambda)(2W - z))]. \quad (2.16)$$

<sup>3</sup>In this work, g is variable but has to be about 70 cm to image a complete wafer with an edge length of 15.6 cm with the lens used in this work. The lens area is about  $A_{\text{lens}} \approx 3.8 \text{ cm}^2$ . For this specific case only  $\sim 0.01\%$  of the emitted luminescence photons are detected.

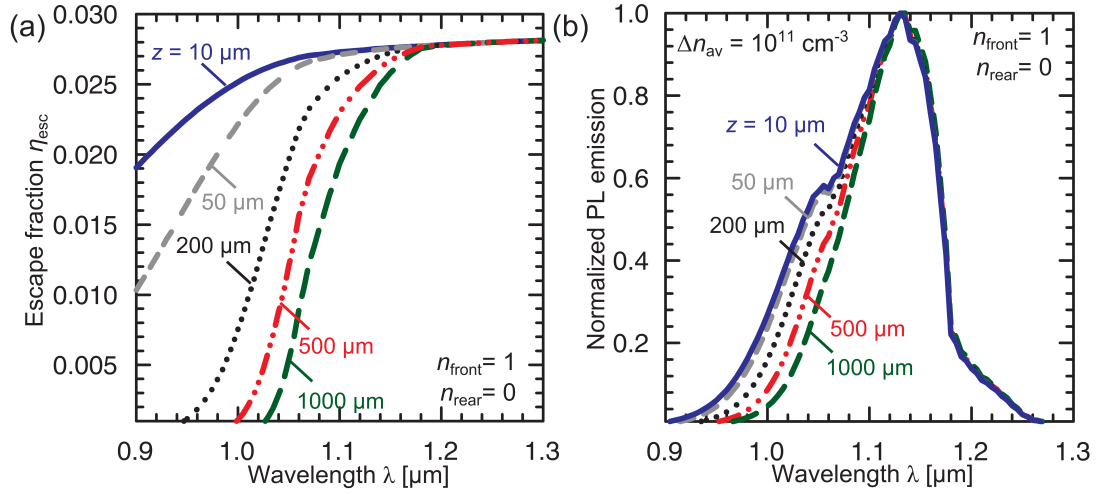


**Figure 2.2:** (a) Escape fraction  $\eta_{\text{esc}}$  of luminescence photons as a function of photon wavelength  $\lambda$  from different depths  $z$  of a Si wafer with a thickness of  $W = 200 \mu\text{m}$  and planar surfaces. Additionally, the escape fraction of luminescence photons from the rear side of two samples with  $W = 500 \mu\text{m}$  and  $W = 1000 \mu\text{m}$  is shown. (b) Impact of the escape fraction on the shape of the PL spectrum from different depths of a Si wafer.

The factor  $1/2$  is due to the fact that half of the photons travels towards the rear and the other half towards the front side of the wafer. According to Snell's law, photons have to have an incidence angle  $< \arcsin(\frac{n_{\text{air}}}{n_{\text{Si}}}) \approx 16^\circ$  relative to the surface normal to leave the sample. Otherwise, the photons are totally reflected at the interface. Thus, the fraction of the isotropic emission that is able to leave the Si sample is only a function of the refractive indices of both media and is found to be  $\frac{1}{2n_{\text{Si}}}$  [65, 66].

Figure 2.2 (a) presents the PL escape fraction  $\eta_{\text{esc}}$  as a function of the photon wavelength  $\lambda$  for different depths  $z$ . Due to the reabsorption of PL photons, the escape fraction decreases with decreasing wavelength for increasing depths of PL generation (since the absorption coefficient of Si decreases as a function of wavelength in the investigated range). Figure 2.2 (b) shows the corresponding emitted normalized PL spectra from the different depths.

If modeling the PL emission of samples with rough surfaces, e.g. a textured surface, the angle-dependent reflectivity at the sample-air interface has to be considered for the calculation of the escape fraction  $\eta_{\text{esc}}(z, \lambda)$ . The escape fraction is expected to be increased compared to a sample with planar surfaces since a reflected photon changes his incidence angle for each encounter with the rough interface. Hence, the overall probability of hitting the surface with an incidence angle that leads not to total reflection is increased. A detailed description can be found in Ref. 67.

### 2.1.4 Time and depth dependence of the excess carrier density

For the modeling of the photoluminescence emission emitted from a Si sample, the information of the carrier distribution in the wafer is required due to Eq. (2.13). In this Section, only a short review of the theory of the carrier transport in a semiconductor is given. A more detailed description can be found e.g. in Ref. 68 (p. 49) and Ref. 55 (p. 62). A one-dimensional description of the carrier transport is sufficient due to the large lateral sample dimensions and the homogeneous excitation over the complete wafer area. For that reason, it is expected that the lateral diffusion of charge carriers is negligible and net diffusion occurs only into the depth of the Si wafer. Based on the continuity equation for excess carriers, the depth- and time-dependent excess carrier density is derived for different boundary conditions.

#### Continuity equation

The continuity equation for the excess carrier concentration  $\Delta n$ , derived from charge conservation, can be written as [55]:

$$\frac{\partial \Delta n(z, t)}{\partial t} = G(z, t) - \frac{\Delta n(z, t)}{\tau_b} - \mu_a E \frac{\partial \Delta n(z, t)}{\partial z} + D_a \frac{\partial^2 \Delta n(z, t)}{\partial z^2}, \quad (2.17)$$

with  $D_a = (n + p)/(n/D_p + p/D_n)$  being the ambipolar diffusion coefficient and  $\mu_a$  the ambipolar mobility  $\mu_a = (n - p)/(n/\mu_p + p/\mu_n)$ . The excess carriers are created with the generation rate  $G(z, t)$  and they have an injection-independent bulk carrier lifetime  $\tau_b$  with a recombination rate  $R(z, t) = \Delta n(z, t)/\tau_b$ . The third term on the right-hand side of Eq. (2.17) stems from the drift current and the fourth term from the diffusion current of the excess carriers.

#### Time-dependent excess carrier density $\Delta n(t)$

If it can be assumed that the carriers are generated spatially homogeneous and in addition mobility, lifetime and doping are homogeneous across the semiconductor, no currents due to drift or diffusion are expected. Thus, the last two terms in Eq. (2.17) are negligible. As a consequence, the dynamics of the excess carrier density is reduced to its time dependence:

$$\frac{d\Delta n(t)}{dt} = G(t) - \frac{\Delta n(t)}{\tau_b}. \quad (2.18)$$

If a square-wave-modulated generation of excess carriers is applied,  $G(t)$  is ideally described by a step function:

$$G(t) = \begin{cases} G_0 & \text{if } 0 < t < T/2, \\ 0 & \text{if } T/2 < t < T, \end{cases} \quad (2.19)$$

with the period  $T$ . With the initial conditions  $\Delta n(t = 0) = 0$  for  $0 < t < T/2$  and  $\Delta n(t = T/2) = G_0\tau_b$  for  $T/2 < t < T$ , the solution of Eq. (2.18) is:

$$\Delta n(t) = \begin{cases} G_0\tau_b [1 - \exp(-t/\tau_b)] & \text{if } 0 < t < T/2, \\ G_0\tau_b \exp(-(t - T/2)/\tau_b) & \text{if } T/2 < t < T. \end{cases} \quad (2.20)$$

Figure 1.3 shows Eq. (2.20) for two different bulk carrier lifetimes as a function of time. For a real excitation source, the assumption of a step function is not valid anymore and Eq. (2.18) has to be solved e.g. for a light source with exponential switching characteristics as in Ref. 69 (p. 78).

### Time- and depth-dependent excess carrier density $\Delta n(z, t)$

At low-level injection conditions, i.e.  $\Delta n \ll N_{\text{dop}}$ , the electric field  $E$  in Eq. (2.17) is negligible and the ambipolar diffusion coefficient can be replaced by the diffusion coefficient of the minority carriers  $D_n$ . As a consequence, the continuity equation simplifies to the diffusion equation:

$$\frac{\partial \Delta n(z, t)}{\partial t} = G(z, t) - \frac{\Delta n(z, t)}{\tau_b} + D_n \frac{\partial^2 \Delta n(z, t)}{\partial z^2}. \quad (2.21)$$

We solve Eq. (2.21) for a time-dependent square-wave-shaped excitation source following the approach of Refs. 70 and 71. First, the time-dependent diffusion equation (2.21) is solved for a pulsed excitation source using a separation approach [71]:

$$\Delta n_{\text{puls}}(z, t) = \exp(-t/\tau_b) \sum_k [A_k \cos(a_k z) + B_k \sin(a_k z)] \exp(-a_k^2 D_n t), \quad (2.22)$$

with  $A_k$ ,  $B_k$  and  $a_k$  being coefficients that are determined by the boundary conditions. We solve the diffusion equation for a sample of thickness  $W$  with equal surface recombination velocities  $S$  on both wafer surfaces. Hence, the boundary conditions are given by the expressions

$$\begin{aligned} D_n \frac{\partial \Delta n(z, t)}{\partial z} \Big|_{z=-\frac{W}{2}} &= S \Delta n \left( -\frac{W}{2}, t \right), \\ -D_n \frac{\partial \Delta n(z, t)}{\partial z} \Big|_{z=\frac{W}{2}} &= S \Delta n \left( \frac{W}{2}, t \right). \end{aligned} \quad (2.23)$$

Combining the boundary conditions of Eq. (2.23) with the general solution of Eq. (2.22) yields a transcendental equation for the  $a_k$ 's:

$$a_k = \frac{2}{W} \arctan\left(\frac{S}{D_n a_k}\right) + k \frac{\pi}{W}, \quad (2.24)$$

which can be solved graphically or numerically. Furthermore, the coefficients  $A_k$  and  $B_k$  are related by  $A_k = B_k b_k$  with the additional coefficient

$$b_k = -\frac{D_n a_k \cos(a_k W/2) + S \sin(a_k W/2)}{D_n a_k \sin(a_k W/2) - S \cos(a_k W/2)}. \quad (2.25)$$

In this work, the time- and position-dependent excess carrier density  $\Delta n(z, t)$  needs to be calculated for the analysis of thick Si samples with thicknesses  $W > 1$  mm. For this specific case, the coefficient  $B_k$  is determined in a simplified form, neglecting all terms multiplied with  $\exp(-W\alpha_{\text{exc}})$  since the absorption length  $L_a = 1/\alpha_{\text{exc}}$  of the excitation wavelength  $\alpha_{\text{exc}}$  is much smaller than the thickness  $W$  of the brick; hence,  $\exp(-W\alpha_{\text{exc}}) \ll 1$ . As a consequence,  $B_k$  is found to be

$$B_k = \frac{2a_k \alpha_{\text{exc}}^2 (1 - R_{\text{exc}}) \varphi_{\text{exc}} [(b_k + \frac{a_k}{\alpha_{\text{exc}}}) \cos(a_k \frac{W}{2}) + (b_k \frac{a_k}{\alpha_{\text{exc}}} - 1) \sin(a_k \frac{W}{2})]}{[b_k^2 (a_k W + \sin(a_k W)) + (a_k W - \sin(a_k W))](\alpha_{\text{exc}}^2 + a_k^2)}. \quad (2.26)$$

The average excess carrier density  $\Delta n_{\text{puls,av}}$  is given by the expression

$$\Delta n_{\text{puls,av}}(t) = \frac{1}{W} \int_{-W/2}^{W/2} \Delta n_{\text{puls}}(z, t) dz = \sum_k B_k b_k \frac{\sin z_k}{z_k} \exp(-t/t_k) = \sum_k H_k \exp(-t/t_k) \quad (2.27)$$

with the amplitudes  $H_k$  and the time constants  $t_k$ . The decay time constants  $t_k$  are effective time constants with regard to the recombination in the bulk and at the surfaces:

$$t_k = \left( \frac{1}{\tau_b} + a_k D_n \right)^{-1}. \quad (2.28)$$

The average excess carrier density  $\Delta n_{\text{arb,av}}$  for an arbitrary-shaped generation profile  $G(t)$  is extracted from the pulse solution by convolution [70]:

$$\Delta n_{\text{arb,av}}(t) = \int_0^t \Delta n_{\text{puls,av}}(\tau) G(t - \tau) d\tau. \quad (2.29)$$

For an ideal square-wave-shaped excitation source with instantaneous switching characteristics [as defined in Eq. (2.19)], the solutions are:

$$\Delta n_{\text{av}}(t) = \begin{cases} \sum_k H_k t_k [1 - \exp(-t/t_k)] & \text{if } 0 < t < T/2, \\ \sum_k H_k t_k \exp(-t/t_k) [\exp(T/2/t_k) - 1] & \text{if } T/2 < t < T. \end{cases} \quad (2.30)$$

Note that the value of  $a_k$  increases monotonously, which means that the decay time constants  $t_k$  decrease with increasing  $k$ . As a consequence, the impact of the fast decay modes quickly decreases and  $\Delta n_{\text{av}}(t)$  is well-described by a mono-exponential decay curve with the effective carrier lifetime  $\tau_{\text{eff}} = t_{k=0}$  as decay time constant.

### Depth-dependent excess carrier density $\Delta n(z)$

If only the depth dependence of the excess carrier density is of interest, Eq. (2.21) simplifies by setting  $\partial\Delta n/\partial t = 0$ , leading to the one-dimensional stationary diffusion equation (valid for low-level injection conditions  $\Delta n \ll N_{\text{dop}}$ ):

$$D_n \frac{\partial^2 \Delta n}{\partial z^2} - \frac{\Delta n(z)}{\tau_b} + G(z) = 0. \quad (2.31)$$

Duggan and Scott [72] solved the stationary diffusion equation for two different surface recombination velocities at the front and rear side  $S_{\text{front}}$  and  $S_{\text{rear}}$  and a photogeneration rate<sup>4</sup> of  $G(z) = \varphi_{\text{exc}}(1 - R_{\text{exc}})\alpha_{\text{exc}} \exp(-z\alpha_{\text{exc}})$ . Then, the general solution of Eq. (2.31) is given by:

$$\Delta n(z) = A \exp\left(-\frac{z}{L}\right) + B \exp\left(\frac{z}{L}\right) + C \exp\left(-\frac{z}{L_a}\right), \quad (2.32)$$

with  $A$  and  $B$  being a function of  $S_{\text{front}}$ ,  $S_{\text{rear}}$ ,  $D_n$  and  $L = \sqrt{\tau_b D_n}$  and  $C$  being defined by the parameters of the generation profile [72].  $L_a = 1/\alpha_{\text{exc}}$  is the absorption length (or penetration depth) of the exciting photons.

### The average excess carrier density

If using the PL emission as a measure for the excess carrier density, there is in principal no access to the depth-dependent profile of the excess carriers but to the integral over depth. An average carrier density  $\Delta n_{\text{av}}$  is thus defined as:

$$\Delta n_{\text{av}} := \frac{\int \Delta n(z) dz}{W}. \quad (2.33)$$

For thick samples or diffusion lengths  $L < W$  and an inhomogeneous generation profile  $G(z)$ , the average excess carrier density  $\Delta n_{\text{av}}$  as defined by Eq. (2.33) deviates strongly from the local  $\Delta n(z)$ . For that reason, Bowden and Sinton [73] proposed a weighting of the depth-dependent carrier density with itself:

$$\Delta n_{\text{av,w}} = \frac{\int [\Delta n(z)]^2 dz}{\int \Delta n(z) dz}. \quad (2.34)$$

This leads in accordance with  $W = \frac{\int \Delta n(z) dz}{\Delta n_{\text{av}}}$  [Eq. (2.33)] to the definition of an effective thickness:

$$W_{\text{eff}} := \frac{\int \Delta n(z) dz}{\Delta n_{\text{av,w}}} = \frac{[\int \Delta n(z) dz]^2}{\int [\Delta n(z)]^2 dz}. \quad (2.35)$$

---

<sup>4</sup> $\varphi_{\text{exc}}$ : exciting photon flux,  $R_{\text{exc}}$ : reflection of the Si sample at the excitation wavelength,  
 $\alpha_{\text{exc}}$ : absorption coefficient of Si at the excitation wavelength

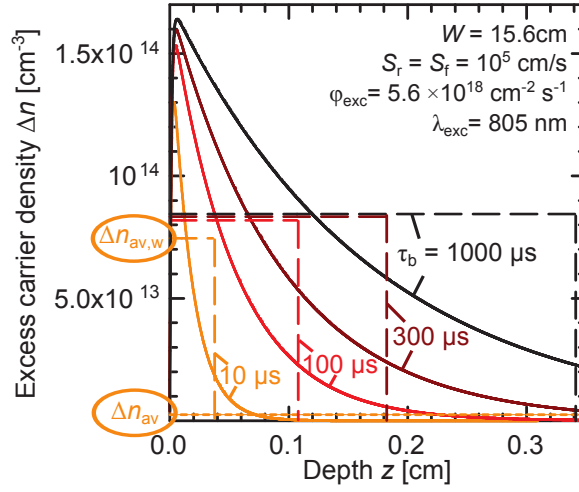


**Figure 2.3:** Excess carrier density  $\Delta n$  (solid lines) as a function of depth  $z$  for different bulk carrier lifetimes  $\tau_b$  for a thick Si brick with  $W = 15.6$  cm for an exciting photon flux of  $\varphi_{exc} = 5.6 \times 10^{18} \text{ cm}^{-2} \text{ s}^{-1}$ . Additionally, the effective thickness  $W_{eff}$  and the weighted average excess carrier density  $\Delta n_{av,w}$  are marked by dashed lines. For the example with  $\tau_b = 10 \mu\text{s}$ , the average excess carrier density is  $\Delta n_{av} \approx 2.5 \times 10^{12} \text{ cm}^{-3}$  (lower dotted line) and the weighted average excess carrier density is calculated to be  $\Delta n_{av,w} \approx 7.5 \times 10^{13} \text{ cm}^{-3}$ .

The effective thickness  $W_{eff}$  can be regarded as a measure for the spreading of the excess carriers into the sample depth.

Figure 2.3 shows the carrier density profiles in a thick Si brick with  $W = 15.6$  cm and a high surface recombination velocity of  $S = 10^5$  cm/s for different bulk lifetimes  $\tau_b$  (solid lines), calculated using Eq. (2.32). Additionally, the effective thickness  $W_{eff}$  [Eq. (2.35)] and the weighted average excess carrier density  $\Delta n_{av,w}$  [Eq. (2.34)] are marked by dashed lines at the abscissa and ordinate.

For the example with  $\tau_b = 10 \mu\text{s}$ , the average excess carrier density is  $\Delta n_{av} \approx 2.5 \times 10^{12} \text{ cm}^{-3}$  (lower dotted line) and the weighted average excess carrier density  $\Delta n_{av,w} \approx 7.5 \times 10^{13} \text{ cm}^{-3}$  is thirty times higher. As can be understood by comparison with  $\Delta n(z)$ , the actual local excess carrier density is much higher than the average excess carrier density. Hence, we consider the weighted average excess carrier density as a much more meaningful figure of merit.

For a thick Si brick with unpassivated surfaces (large  $S$ ), it was found that the weighted average carrier density  $\Delta n_{av,w}$  is not a function of the lifetime anymore if the diffusion length  $L$  is much larger than the penetration depth  $L_a = 1/\alpha_{exc}$  of the exciting photons [73, 74]:

$$\Delta n_{av,w} = \frac{N_{exc} L_a}{2D_n}, \quad (2.36)$$

with  $N_{exc} = \varphi_{exc}(1 - R_{exc})$  being the number of exciting photons per second and area. In that case, the main variation of the carrier profile with bulk lifetime is the depth

distribution. Thus, the effective thickness is a function of the diffusion length [73]:

$$W_{\text{eff}} = 2(L + L_a). \quad (2.37)$$

Figure 2.3 demonstrates the constant average excess carrier density for  $L \gg L_a$  by the horizontal dashed lines, which are in agreement for lifetimes  $> 100 \mu\text{s}$  ( $L \approx 500 \mu\text{m}$ ) for an absorption length of  $L_a \approx 12 \mu\text{m}$ .

## 2.2 Camera-based photoluminescence setup

For the measurement of the photoluminescence (PL) emission of a Si sample, an excitation source for the electron-hole pair generation and an appropriate detector for the PL photons are required. In this Chapter, the different components of the PL setup are presented, namely (i) a Si CCD and an InGaAs CMOS camera as detectors, (ii) two lasers and an LED<sup>5</sup> array as excitation sources, and (iii) interference and absorption filters with a high optical density for the separation of the luminescence emission from the excitation light. In this Section, the components of the PL setup are explained with respect to the special requirements needed for measurements of the stationary PL signal and for measurements of the time-dependent PL signal. Figure 2.4 shows the actual PL setup used in this work.

### 2.2.1 Components of the setup

#### Detectors: Si CCD versus InGaAs CMOS camera

Throughout this study, a silicon charge-coupled device (Si CCD, Hamamatsu Photonics, model: C9100-13) and an indium gallium arsenide complementary metal-oxide semiconductor (InGaAs CMOS, Xenics, model: Cheetah) camera are used for the investigation of the Si material. In this Section, the focus is not on explaining the functionality of the detectors (see e.g. Ref. 55) but to emphasize the main differences between the two detectors which are relevant for this work.

The applied detectors in this work utilize the photoelectric effect for the detection of the luminescence photons with a semiconductor as photosensitive material. An important characteristic of a photon detector is its quantum efficiency. This parameter quantifies the ability to convert the incoming photons into signal electrons and is always specified as a function of the energy (or wavelength) of the photons to be detected. The quantum efficiency is one of the main differences between a detector with Si or InGaAs as photosensitive material and is shown for both detectors in Fig. 2.5 (a).

With the InGaAs CMOS detector, the complete luminescence spectrum of Si can be captured, whereas using the Si CCD, the quantum efficiency is strongly decreasing with increasing wavelength for wavelengths larger than 1000 nm. As a consequence, the actual detected PL spectrum looks quite different if using a Si CCD or an InGaAs CMOS detector, as can be seen at the modeled, normalized PL spectra in Fig. 2.5 (b). The peak wavelengths are shifted by about 125 nm. In addition, the peak PL intensities are expected to differ by almost two orders of magnitude. Since Si CCDs were dominating the vision applications until the late 1990s [75], this technology is already well-engineered. That may explain why Si CCDs are mainly used for the investigation

---

<sup>5</sup>LED: light emitting diode

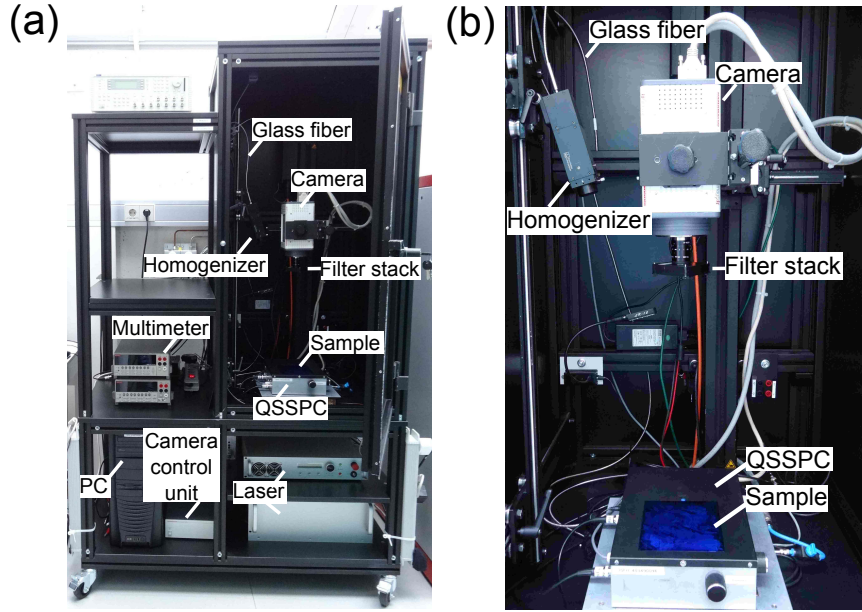


**Figure 2.4:** (a) Image of the actual PL setup used in this work. (b) Enlarged view of the interior of the dark box. The laser that is utilized for the excitation of the luminescence emission is stored outside the black box. The laser light is guided through a glass fiber into the homogenizer optics. The exciting light is widened to the size of a Si wafer (up to  $16 \times 16 \text{ cm}^2$ ). In the shown setup configuration, the Si wafer lies on top of a QSSPC setup (presented in Section 1.3) that is used for the calibration of the PL signal (as will be shown in Section 3.2). A voltage proportional to the photoconductance of the wafer is monitored by a multimeter. The luminescence emission is detected by a Si CCD camera that is mounted above the sample. The filter stack required for the blocking of the reflected excitation light is positioned between detector and sample.

of the spatially resolved luminescence detection [5, 6] although only a fraction of the PL spectrum is detected.

The spatial resolution of the Si CCD camera is generated by exposing an array of  $512 \times 512$  light-sensitive detectors to the incoming light. The single detectors are referred to as camera pixels. The InGaAs CMOS camera provide an array of  $512 \times 640$  camera pixels. The fraction of the sensitive area per pixel is as important as the quantum efficiency of the sensor pixels. For the Si CCD camera used in this work the light-sensitive area of the pixels is well-optimized to 100% since the semiconductor substrate is thinned and the illumination takes place from the rear side with the electrodes at the front side (not facing the PL source).

Another important difference between the Si CCD and the InGaAs camera, specially relevant to time-dependent PL measurements, is related to the read-out mechanism of the detectors. A CCD camera consists of an array of light-sensitive coupled MIS (metal-insulator-semiconductor) capacitors. If photons are absorbed in the photo-active region, electrical charges are collected proportionally to the incoming light intensity. The read-out in CCD cameras occurs via a shift register where the collected charges are transferred through the potential wells of the neighboring pixels,

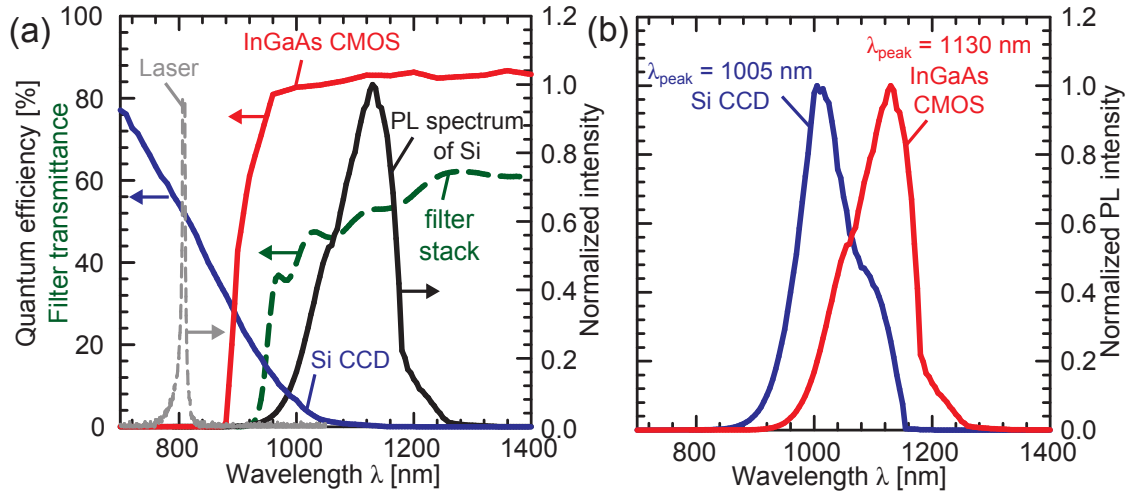


**Figure 2.5:** (a) Quantum efficiencies (manufacturer information) of the used cameras (Si CCD and InGaAs CMOS) and a simulated normalized PL spectrum of a passivated Si wafer with a thickness of  $200 \mu\text{m}$ , a bulk lifetime of  $1 \text{ ms}$  and a surface recombination velocity of  $S = 10 \text{ cm/s}$ . Additionally, a laser spectrum is shown and the transmittance of the filter stack used for the suppression of the reflected excitation signal. (b) Normalized PL intensity of a Si wafer if detected with a Si CCD camera and with an InGaAs CMOS detector.

controlled by the respective gate voltages. The Si CCD, used in this work, shifts all collected charge carriers parallel into another pixel frame (full-frame transfer) where the read-out via shift register takes place. At the same time of the read-out in the second pixel frame, the frame facing the PL source is already again able to collect signal electrons.

The full-frame transfer architecture allows fast read-out rates. However, the disadvantage for applications with short integration times is the occurrence of the so-called smearing. This effect is due to the fact that the pixels continue to receive light as signal charges are passed through them [55] if there is no mechanical shutter in front of the detector. These smearing effects are limited to the time necessary for transfer of image integration data to the storage array and is about  $32 \text{ ms}$  for the Si CCD camera used in this work. As a consequence, the Si CCD is not suitable for the acquisition of PL images with integration times  $t_{\text{int}} \lesssim 32 \text{ ms}$  if detecting a time-dependent signal. CCD sensors are also affected by blooming effects that result from an unintentional transfer of charge carriers into adjacent device structures with the consequence of a reduced image contrast [76].

Opposed to the coupled pixel structure of the CCD sensor, each pixel of a CMOS camera contains its own photo-detector and active amplifier. Since each pixel has its own read-out mechanism, the image detected by a CMOS detector is free of any blooming or smearing effects [75]. Another advantage of the application of an InGaAs detector for PL measurements is the weak sensitivity in the wavelength range of the exciting illumination, reducing the necessity of a strong optical blocking (see p. 43, Section: Filters). However, the restriction of the Si CCD to shorter wavelengths may

be interpreted as an advantage over the InGaAs camera since at smaller wavelengths the influence of optical blurring effects is strongly reduced and the images possess higher contrasts. For comparison, the absorption length of the PL photons in Si at a wavelength of 1005 nm ( $\lambda_{\text{peak}}$  of the Si CCD PL spectrum) is only  $\sim 180 \mu\text{m}$  whereas at 1130 nm ( $\lambda_{\text{peak}}$  of the InGaAs CMOS PL spectrum) the absorption length is already  $\sim 6700 \mu\text{m}$ .

An important property of a photon detector is its noise characteristics. The knowledge of this noise reveals how accurately the measured quantity can be determined. The last Section of this Chapter will shortly compare the noise behavior of the PL setup using a Si CCD and an InGaAs CMOS detector [see also the Appendix (p. 133)].

### Response time of the InGaAs CMOS detector

For the dynamic PL lifetime imaging approach [see Section 3.3], it is required to detect PL photons at well-defined time intervals during a modulated excitation. For the image acquisition at a specific time interval, both cameras have a trigger mode available. Since the Si CCD camera is prone to smearing effects for camera integration times in the order of milliseconds, the InGaAs camera is used for this application. In the trigger mode, the image acquisition is started by sending a voltage to the camera. For the InGaAs CMOS, the change in voltage is actually decisive and one can choose between a rising voltage or a falling voltage edge as a starting point for the triggered image acquisition.

For the quantitative evaluation of the measured PL signal at a certain time interval, the knowledge of the response time (time between trigger signal and start of image capture) of the detector is required. For the determination of the response time, the known switching behavior of an LED array with a central wavelength of 850 nm is used. Since the spectrum of the LEDs is relatively broad ( $\text{FWHM}^6 \approx 35 \text{ nm}$ ), the emission of the LED array is still detectable by the InGaAs camera. For a homogeneous illumination of the CMOS sensor, the LED light is diffused by a sheet of paper. The LED array as well as the camera receive the same square-wave-modulated trigger input.

The switch-on behavior of the LEDs follows an exponential function as demonstrated in Fig. 2.6 (a) with a blue line. The square-wave-shaped trigger signal is shown as a gray line. The response time  $t_{\text{response}}$  is the time between the trigger release (as soon as the trigger voltage changes) and the actual image acquisition. However, an additional delay time  $t_{\text{delay}}$  can be set to increase the time between trigger release and image acquisition. The length of the signal acquisition is given by the camera integration time  $t_{\text{int}}$ .

For the measurement of the response time  $t_{\text{response}}$ , we measure the LED emission as a function of the additional delay time  $t_{\text{delay}}$  for a camera integration time of

---

<sup>6</sup>FWHM: full width at half maximum

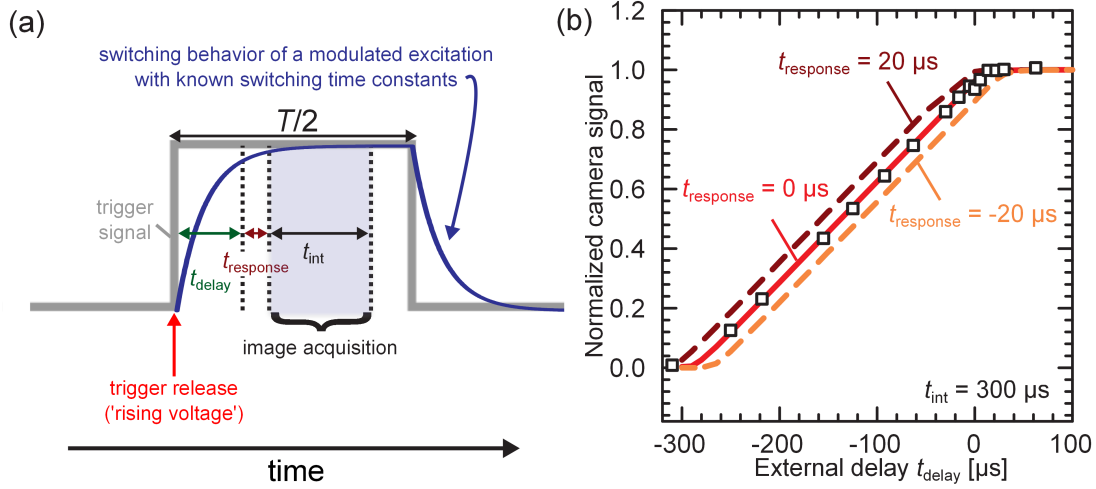


**Figure 2.6:** (a) Pulse of a square-wave-modulated LED illumination of period  $T$ . The gray line is the trigger signal provided by a frequency generator. The non-instantaneous switching behavior of the LED array is described by exponential functions (blue line). The response time  $t_{\text{response}}$  is the time between trigger release and actual image acquisition. However, an additional delay time  $t_{\text{delay}}$  can be set. The length of the signal acquisition is given by the camera integration time  $t_{\text{int}}$ . (b) Normalized camera signal as a function of the delay time  $t_{\text{delay}}$ . The response time  $t_{\text{response}}$  of the InGaAs detector is determined by shifting (variation of the delay time  $t_{\text{delay}}$ ) the image acquisition window (with the width  $t_{\text{int}}$ ). The red solid line is calculated from the switching time constants of the LED array assuming an instantaneous reaction of the camera ( $t_{\text{response}} \approx 0$ ). The dashed lines are calculated assuming a response time of  $t_{\text{response}} = \pm 20 \mu\text{s}$ .

$t_{\text{int}} = 300 \mu\text{s}$ . The result is shown in Fig. 2.6 (b) as open symbols<sup>7</sup>.

The response time is determined by comparing the modeled signal variation as a function of  $t_{\text{delay}}$  with the actual camera-detected LED signal. For this, the integral over the camera integration time is calculated using the known switching time constants of the LEDs. The signal variation is calculated by taking different starting times of the image acquisition into account since  $t_{\text{delay}} + t_{\text{response}}$  is varying. Figure 2.6 (b) shows the measured and the calculated normalized camera signal for three different response times  $t_{\text{response}}$  as a function of the delay time  $t_{\text{delay}}$ . The measured values are normalized to a measurement at a constant LED emission (steady-state conditions) since only the time dependence of the measured signal is of interest. The actual response time is determined to be  $(-1 \pm 3) \mu\text{s}$ . The specified uncertainty is derived from the standard deviation of the measured signal. The manufacturer specification of  $t_{\text{response}} = (320 \pm 25) \text{ ns}$  lies well within the measured range of the response time.

Unfortunately, the InGaAs CMOS camera displays a measurement artifact if using the trigger mode. For the sensor design of the used camera, the read-out has been optimized for fast frame rates which requires steep clock signals. As a consequence,

<sup>7</sup>It was actually not possible to set negative delay times at the CMOS camera. The negative delay times in Fig. 2.6 (b) are calculated from the actual set delay times  $t_{\text{delay,set}}$  and the period  $T$  with  $t_{\text{delay}} = T - t_{\text{delay,set}}$ .

an interference pattern is build up over the sensor area due to parasitic charges inside the single pixels<sup>8</sup>. However, the pixels influenced by parasitic charges are found to be at well-defined positions. Since the parasitic charges are interpreted as an additional input signal, these pixels cannot be used for the PL evaluation. The pixels containing inaccurate information are replaced by the average information of surrounding artifact-free pixels. Since about half of the pixels of the sensor are influenced by the interference pattern, the resolution is reduced by half.

### Excitation sources

For the optical excitation of the band-to-band photoluminescence of a Si wafer, an excitation source providing photons with an energy larger than the band gap of Si<sup>9</sup> is required. We used three different excitation sources in this work.

For the monochromatic illumination, a gallium arsenide (GaAs) diode laser (Jenoptik unique-mode, JUM30k/400/20) with a central wavelength (CWL) of 808 nm is used. For Si, this CWL corresponds to an absorption length of  $\sim 13 \mu\text{m}$ . The maximum continuous wave (cw) output power of the laser is 30 W. In order to obtain an optical excitation of the entire wafer area, the laser beam is widened and homogenized by a fiber-coupled beam homogenizer (custom-made made product, Bayerisches Laserzentrum GmbH), leading to a homogeneity of  $\pm 10\%$  over an area of  $16 \times 16 \text{ cm}^2$ . The second monochromatic illumination source is a high power diode laser with a CWL of 805 nm (LIMO - Lissotschenko Mikrooptik, LIMO80-F400-DL808-FP-A) and a cw output power of 80 W. The third illumination source is a custom-made LED array of 924 LEDs (Osram, SFH 4550). In this case, the spatially homogeneous excitation deviating by  $\pm 10\%$  over an area of  $18 \times 18 \text{ cm}^2$  is obtained by using a diffusion disc between LEDs and investigated sample.

Within the scope of this work, the illumination intensity is expressed in the unit suns. The unit one sun is equivalent to an intensity of  $0.1 \text{ W/cm}^2$  and is defined in accordance to the sunlight spectrum passing the earth's atmosphere (AM1.5G). If the spectrum is integrated over all energies, it results in a total photon flux of  $4.1 \times 10^{17} \text{ cm}^{-2}\text{s}^{-1}$ . However, only about 2/3 of the photons have sufficient energy to create electron-hole pairs in Si. Since the exciting photons of the excitation sources as used in this work have an energy of  $\sim 1.5 \text{ eV}$  well-above the band gap of Si, it is assumed that each photon that is not reflected at the sample surface generates one electron-hole pair. Thus, in this work, one sun is defined to be equivalent to a photon flux of  $2.78 \times 10^{17} \text{ cm}^{-2}\text{s}^{-1}$ . At the excitation wavelength of 808 nm this corresponds to an intensity of  $0.07 \text{ W/cm}^2$ .

<sup>8</sup>personal communication with the manufacturer

<sup>9</sup>1.1242 eV at 300 K [77], equivalent to a wavelength of 1103 nm (in air)

## Filters

The main challenge for the construction of a PL setup is the separation of the small amount of PL photons from the large amount of the exciting photons that are reflected at the front side of the Si sample. By a simple one-dimensional simulation of the quotient of the signal to be blocked and the signal to be measured, we estimate the required specification of an optical filter in front of the PL detector.

The PL signal  $I_{\text{PL}}$  of a Si wafer is calculated using Eq. (2.14)<sup>10</sup> by considering the specifications of the actual PL setup as used in this work. As an excitation source, a laser with a central wavelength of 808 nm is used. A Si charge-coupled device (Si CCD) detector has a much higher sensitivity at the excitation wavelength compared to the sensitivity in the wavelength range of the PL emission. The reflected laser photons that are detected are calculated from the product of the exciting photon flux  $\varphi_{\text{exc}}$  times the reflectivity of the Si wafer surface  $R_{\text{front}}$  taking additionally the wavelength-dependent sensitivity of the detector and the lenses into account. Figure 2.7 shows the calculated ratio of the reflected laser photons that are detected and the PL signal. If 1% laser photons are tolerated in the detected PL signal, the required blocking can be read from Fig. 2.7 by multiplication  $\varphi_{\text{exc}}R_{\text{front}}/I_{\text{PL}}$  with 100. For example, for a PL measurement of the modeled Si wafer with  $\Delta n_{\text{av}} = 10^{13} \text{ cm}^{-3}$ , the optical filter has to attenuate the incoming exciting illumination by at least eleven orders of magnitude (if using our Si CCD camera for the detection).

Since the measured PL signal depends on the free carrier concentration, the required degree of blocking decreases with increasing excess carrier density. The dashed green line shows the minimum requirement of blocking without the consideration of any specific detector or lenses, revealing the large difference between required excitation and actual photoluminescence emission. Since the PL signal depends strongly on the specific optical parameters of the setup components and the sample, Fig. 2.7 shall only serve as an estimate of the required blocking.

At the beginning of this work, a single thick (2 cm) absorbing glass filter (RG850, Schott-Glass) is used for the separation of excitation and luminescence light. The manufacturer specifies the filter with an optical density<sup>11</sup> of  $\text{OD} \approx 17$  at the excitation wavelength of 808 nm.

A spectral photometer (Varian, CARY 5000) was used for the determination of the wavelength-dependent filter transmittance, e.g. required for the modeling of the detected PL emission with Eq. (2.14). However, the PL setup itself was used to verify the filter utility for the blocking approach since the CARY 5000 only allows the accurate measurement of attenuations of five to six orders of magnitude. The filter blocking was tested by comparing the measured camera signal of an illuminated as-cut wafer

<sup>10</sup>For the simulation of the PL signal, a Si wafer with a thickness of  $W = 200 \text{ }\mu\text{m}$  and a doping density of  $N_{\text{dop}} = 4 \times 10^{15} \text{ cm}^{-3}$  is assumed for an exciting photon flux of  $\varphi_{\text{exc}} = 8.3 \times 10^{16} \text{ cm}^{-2}\text{s}^{-1}$ .

<sup>11</sup>The optical density is defined as the logarithmic of the ratio of the light intensity  $I_0$ , falling onto the filter and the light intensity  $I_t$ , transmitted through the filter:  $\text{OD} := \log_{10}(I_0/I_t)$ .

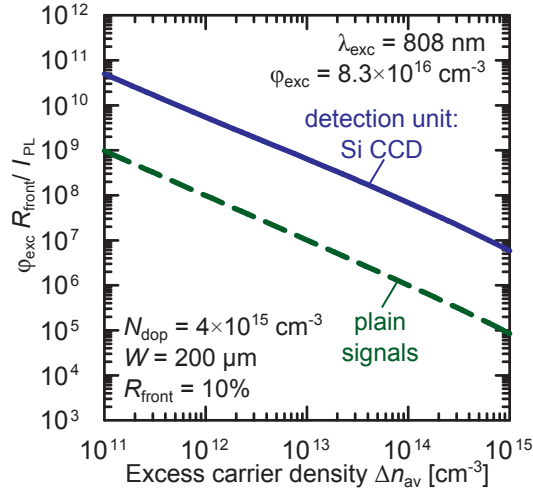


**Figure 2.7:** Calculated ratio of reflected excitation light  $\varphi_{exc}R_{front}$  and PL signal  $I_{PL}$  as measured with our front-illuminated PL setup and a front reflectivity of the Si sample of  $R_{front} = 10\%$ . The ratio is calculated as a function of the excess carrier density  $\Delta n_{av}$  in the Si wafer. The exciting photon flux is kept constant at  $\varphi_{exc} = 8.3 \times 10^{16} \text{ cm}^{-2}\text{s}^{-1}$ . The blue solid line shows the ratio  $\varphi_{exc}R_{front}/I_{PL}$  if using a Si CCD detector and the green dashed line shows the plain ratio for the actual amount of photons without considering any specific setup.

with a low PL signal ( $I_{ascut}$ ) to the measured camera signal of reflected excitation light at the rear side of a solar cell with full-area screen-printed aluminum coating ( $I_{alu}$ , with the aluminum facing the detector). The test criterion was given by the signal ratio  $I_{ascut}/I_{alu}$ . The best suited filter has to have the highest ratio  $I_{ascut}/I_{alu}$  since then the fraction of reflected excitation illumination of the camera signal is expected to be lowest. An additional test criterion is the absolute wafer signal  $I_{ascut}$ . If two filters have the same ratio  $I_{ascut}/I_{alu}$ , the best suited filter is recognized from the highest absolute wafer signal  $I_{ascut}$ . However, with the presented filter test, we were not able to determine the absolute optical density of the tested filters but we could compare different filter combinations with respect to their blocking ability.

Due to the strong absorption of photons within the RG850 filter, the filter itself emits light [32] because it contains nanocrystallites of II-IV semiconducting compounds [78]. Even though in most cases this parasitic light emission is negligibly small it may disturb the measurement significantly for wafers with very low PL emission. For that reason, two additional interference filters were placed on both sides of the absorption glass filter. One is placed between the luminescent sample and the RG850 to reflect a large amount of the exciting photons before entering the RG850 and the other one is placed between the RG850 and the detector for the blocking of the parasitic light generated within the RG850.

In the course of this work, the thick absorbing glass filter RG850 was replaced by an interference filter with an optical density of  $OD \approx 14$  at the excitation wavelength and a higher transmittance in the wavelength range of the luminescence emission. As a consequence, a slightly higher ratio  $I_{ascut}/I_{alu}$  and a much higher absolute PL signal

(increase by  $\sim 50\%$ ) could be achieved. The transmittance of the final filter stack of three interference filters is displayed in Fig. 2.5 (a).

For PL measurements with the InGaAs CMOS camera the requirements for blocking are much lower compared to the Si CCD camera since the InGaAs detector has a low sensitivity at the CWL of the laser [see Fig. 2.5 (a)]. The filter test described above reveals that a single interference filter is sufficient.

If excitation and detection of luminescence takes place from opposite sides of the wafer, the Si wafer itself serves as a filter for the exciting photons. In this work, this concept was realized by using an LED array as measuring table for Si wafers [see Fig. 2.8 (b)]. However, if using the InGaAs camera and the broad spectrum of an LED array, additional blocking of the long wavelength photons is still required due to the decreasing absorption coefficient with increasing photon wavelength. Giesecke et al. [32] implemented the rear side illumination for a PL setup with a Si CCD camera and laser excitation by placing a mirror behind the Si sample.

An additional bandpass filter (custom-made product, bk-Interferenzoptik) is positioned in front of the homogenization optics [green filter in Fig. 2.8 (a)] since the sharp laser line is weakly superimposed by a broad spectrum due to spontaneous emission from the GaAs laser diode. Since the bandpass filter contains absorbing layers, its application requires caution if using high laser output power. In order not to damage the filter, it is mounted at the exit of the homogenization optics where the laser output beam is already widened ( $\sim 1\text{ cm}^2$ ) and the intensity is thus reduced.

### 2.2.2 Setup configurations

Two different configurations of the PL setup are used in this work. A schematic of both formations is shown in Fig. 2.8. The basic experimental setup for a PL measurement comprises an excitation source with a homogenization optics, a camera, lenses, various filters, a motor-driven linear unit for the vertical movement of the camera, and a computer for the data acquisition and evaluation. Using such a basic setup, a quantity proportional to the luminescence of the Si sample is detectable.

To avoid the detection of ambient light, the detection unit and the sample stage are mounted in a dark box ( $1290\text{ cm} \times 700\text{ cm} \times 690\text{ cm}$ ). All metallic parts of this box are anodized (blackened) to minimize the detection of reflected stray light. The side-walls of the box consist of black polyvinyl chloride plastic (SIMONA, Simocel-Color black 6 mm). For the imaging of the spatial distribution of the emitted luminescence of the Si sample onto the detector chip, a lens [Pentax, C3516-M (KP)] with a focal length of  $f = 35\text{ mm}$  and an aperture of 1.6 is used.

The first configuration of the PL setup enables the measurement of the PL signal and the photoconductance (PC) under the same excitation conditions and is shown in Fig. 2.8 (a). For the PC measurement a commercially available quasi-steady-state photoconductance (QSSPC) system (Sinton Consulting, WCT-100) is used [see Sec-

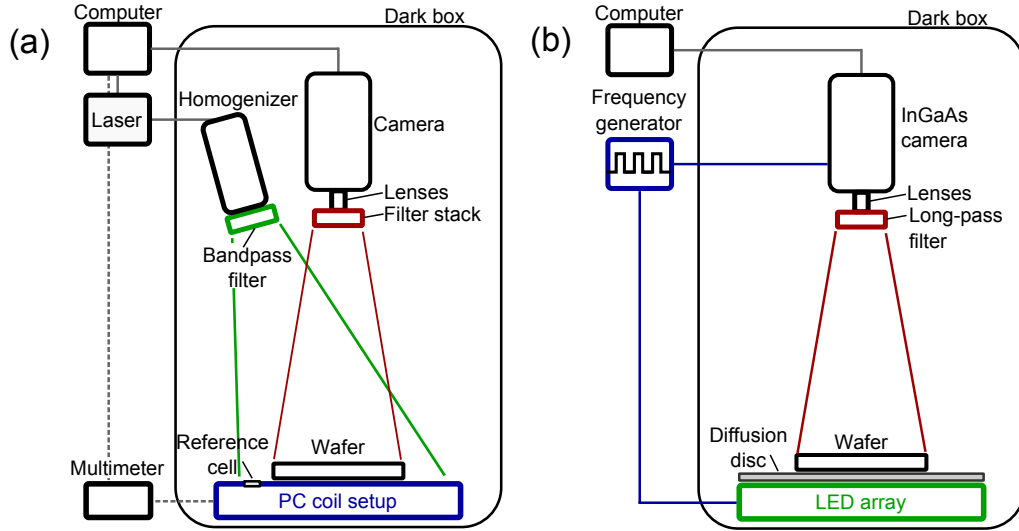


**Figure 2.8:** (a) Experimental setup for calibrated PL lifetime imaging (see Section 3.2). The image acquisition is performed at the same excitation conditions as the photoconductance measurement. (b) Schematic of the experimental setup for dynamic PL lifetime imaging (see Section 3.3).

tion 1.3]. In the setup shown in Fig. 2.8 (a), the QSSPC system is directly implemented into the PL setup. The Si sample is placed on top of the radio-frequency (rf) coil of the QSSPC setup, which is connected to a calibrated rf bridge circuit. The output voltage of this bridge is proportional to the photoconductance of the sample and is determined by an external multimeter (Keithley, DMM 2701).

The investigated Si sample is illuminated by one of the diode cw lasers in combination with the homogenization optics (at an angle of  $\sim 15^\circ$ ) from the same side as the detection of the PL signal takes place. The camera is mounted vertically above the sample and can be adjusted in height by a motor-driven linear unit to adjust the PL image resolution. The excitation photon flux  $\varphi_{\text{exc}}$  is measured by a calibrated short-circuited Si solar cell which is already implemented in the QSSPC system. The voltage drop over a resistor with a resistance of  $0.33 \Omega$  is determined via an external multimeter (Keithley, DMM 2701). The average photogeneration rate  $G_{\text{av}}$  in the Si wafer of thickness  $W$  is then calculated using the expression

$$G_{\text{av}} = \frac{\varphi_{\text{exc}}(1 - R_{\text{front}})}{W}, \quad (2.38)$$

where  $R_{\text{front}}$  is the reflectivity at the front side of the sample under test. The high energy of the exciting photons with respect to the band gap of Si and the resulting small penetration depth of  $\sim 13 \mu\text{m}$  justifies the approximation that all non-reflected photons generate an electron-hole pair in a wafer with a thickness of  $W > 100 \mu\text{m}$ . The front reflectivity is typically small, e.g. for a planar Si surface with a  $60 \text{ nm SiN}_x$  coating (refractive index  $n = 2.4$ )  $R_{\text{front}} \approx 0.1$  at  $\lambda_{\text{exc}} = 808 \text{ nm}$ .

The second setup configuration is used for the dynamic approach of determining the carrier lifetime (see Section 3.3) and is shown in Fig. 2.8 (b). As pointed out before (see p. 37), only the InGaAs detector is suitable for this approach since short camera integration times of the order of magnitude of the charge carrier lifetime are required. For the excitation of excess carriers, we use the LED array with the sample placed above the LEDs. Thus, the Si sample itself serves as an additional filter for the exciting photons. For a spatially homogeneous illumination, a diffusion disc is placed between the LEDs and the investigated sample. For the precisely timed image acquisition and switching of the excitation source, a square-wave-shaped trigger signal is synchronously sent to the camera and the LED array.

### 2.2.3 Data acquisition and sensitivity

#### Data acquisition

The PL image acquisition process is controlled by a computer software based on the programming system LabVIEW (National Instruments). For the acquisition of the spatially resolved PL signal, two images are acquired: one with the excitation source in operating mode and the other one with the excitation source switched off. The second image is called dark image and is subtracted from the PL image to account for remaining stray light and camera offsets. For an improved signal-to-noise ratio (SNR),  $N$  images at the same setup configuration are acquired and an average PL signal

$$I_{\text{PL}} := \frac{1}{N} \sum_{i=1}^N I_{\text{PL},i} \quad (2.39)$$

is calculated for each pixel. The SNR of the acquired average PL signal  $I_{\text{PL}}$  is defined as

$$\text{SNR} := \frac{I_{\text{PL}}}{v} \quad \text{with} \quad v := \frac{\sigma_t}{\sqrt{N}}, \quad (2.40)$$

with the standard error or noise  $v$  calculated from the standard deviation  $\sigma_t$  of  $N$  measurements. Hinken [79] found from simulations of the SNR as a function of the total measurement time  $N \times t_{\text{int}}$  that an increase of the integration time  $t_{\text{int}}$  results in a higher SNR than averaging more often if considering the same total measurement time.

A non-uniformity correction (NUC) of the acquired images is necessary to correct for inhomogeneities of the lateral sensitivity of the camera sensor and the inhomogeneous transmission of the used optics. The NUC image is acquired using a homogeneous luminescence light source as proposed in Ref. 79. The image is acquired with the lenses set out of focus to obtain a homogeneous illumination of the camera sensor. As a homogeneous light source, the electroluminescence (EL) of a back-contacted monocrystalline Si solar cell at open-circuit conditions is used. The detected NUC

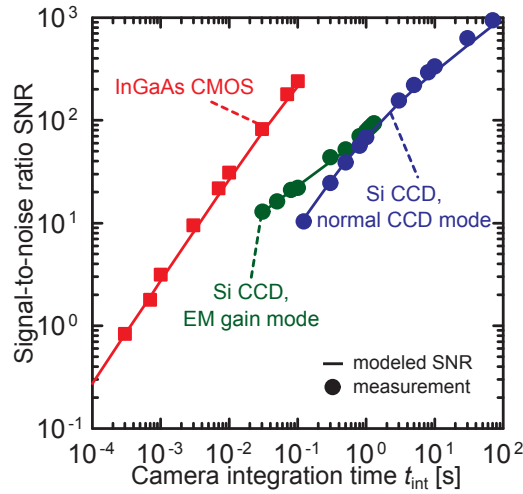


**Figure 2.9:** Calculated (lines) and measured (symbols) signal-to-noise ratio SNR as a function of the camera integration time  $t_{\text{int}}$  for a Si CCD with full-frame transfer read-out electronics (EM gain and normal CCD mode - this work) and an InGaAs CMOS camera (data from Ref. 80). The measured electroluminescence signal stems from a solar cell hold at a voltage of 550 mV. The measured signals result from 20 averages at the same setup configurations. The lines are calculated using an analytical expression for the SNR that is presented in the Appendix (Eq. A.7).

image is normalized to the mean value of all pixels and contains values between 0.55 and 1.2. In order to correct the detected images for the optical measurement artifact, each acquired PL image is divided by the NUC image.

### Noise analysis

The signal-to-noise ratio SNR is determined for the Si CCD camera as a function of the camera integration time  $t_{\text{int}}$ . For the Si CCD, two different modes are available, the normal CCD mode and the EM gain mode that uses an additional electron multiplication amplifier. Equation (2.40) is used for the calculation of the SNR and the result is shown as filled circles in Fig. 2.9. For comparison, the SNR for the InGaAs CMOS camera (data from Ref. 80) is shown in the same graph. The measured signal corresponds to an electroluminescence spectrum emitted from a solar cell operating at an applied voltage of 550 mV. Equal measurement conditions are used to allow a comparison of the two detectors. We used the same optics (lenses and filters), the same position of the solar cell image within the sensor and the same luminescence intensity for all data in Fig. 2.9.

From Fig. 2.9 it can be concluded that the EM gain mode of the Si CCD is only superior if small camera integration times  $t_{\text{int}}$  are required. Otherwise, a longer  $t_{\text{int}}$  in the normal CCD mode enables the same SNR.

Since the InGaAs CMOS detector is able to measure the complete luminescence spectrum, a higher SNR is already obtained for much smaller  $t_{\text{int}}$  as for the Si CCD camera.

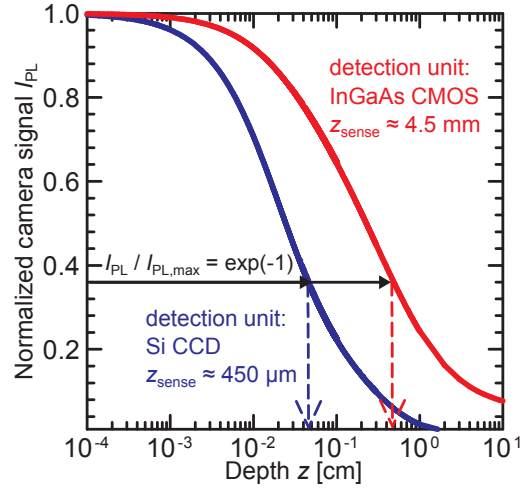


**Figure 2.10:** Calculated normalized PL emission  $I_{PL}$  as a function of the depth  $z$  in a Si sample, assuming a homogeneous photon generation throughout the wafer, for a Si CCD and an InGaAs CMOS detector. The characteristic depth  $z_{sense}$  of the two detectors differs by about one order of magnitude.

However, the same SNR can be acquired with a Si CCD camera if a longer integration time is chosen. Even higher SNRs are possible by using the Si CCD since the InGaAs camera is limited by a maximum possible camera integration time of  $\sim 0.2$  s (due to a large dark current).

In addition, the SNR is modeled by using an analytical expression with the experimentally determined noise components of each detector. The modeled SNR is presented in Fig. 2.9 as solid lines and is in a good agreement with the measured SNR. A short review of the different noise sources and the analytical expression for the SNR can be found in the Appendix (p. 133).

The knowledge of the noise behavior of the PL setup is used to determine the general sensitivity of the lifetime techniques that are developed in this work.

### Depth-dependent sensitivity

If investigating thick samples or even Si bricks as in Section 3.3.5, the depth-dependent sensitivity  $f_{sense}(z)$  of the PL setup is of great interest. For the PL setup used in this work  $f_{sense}(z)$  can be described by an exponential function with the characteristic depth  $z_{sense}$  (in accordance with Refs. 81 and 82):

$$f_{sense}(z) = f_{max} \exp(-z/z_{sense}), \quad (2.41)$$

with  $f_{max}$  being the sensitivity at the wafer front side. We determine the characteristic depth  $z_{sense}$  from simulations of a depth-dependent PL signal  $I_{PL}$  assuming a homogeneous carrier distribution.  $I_{PL}$  is plotted in Fig. 2.10 as a function of the

sample depth  $z$ . If using the InGaAs detector, we determine a characteristic depth of  $z_{\text{sense}} \approx 4.5$  mm. If using a Si CCD detector, the characteristic depth is determined to be one order of magnitude lower with  $z_{\text{sense}} \approx 0.45$  mm. The value of  $z_{\text{sense}}$  is mainly determined by the reabsorption of the luminescence photons and is hence linked with the wavelength-dependent sensitivity of the used detector.

# CHAPTER 3

---

## Carrier lifetime imaging using a photoluminescence setup

---

As presented in the previous Chapter, excess carrier density and photoluminescence (PL) emission of an optically excited silicon (Si) sample are related due to the dependence of the rate of radiative recombination on the densities of free carriers. Hence, the excess carrier density can be determined from a measurement of the photoluminescence emission of a Si sample. The steady-state recombination lifetime is then given by the ratio of the photogeneration rate and the excess carrier density.

In Fig. 3.1, the PL signal  $I_{\text{PL}}$ , calculated using Eq. (2.14), is shown as a function of the bulk lifetime  $\tau_b$  for a Si wafer of thickness  $W = 300 \mu\text{m}$  and a low surface recombination velocity of  $S = 10 \text{ cm/s}$ . A pronounced sensitivity to the bulk lifetime is clearly visible. Additionally, the PL signal is calculated for a thin Si wafer ( $W = 300 \mu\text{m}$ ) and a thick Si brick ( $W = 15.6 \text{ cm}$ ) with a high surface recombination velocity of  $S = 10^5 \text{ cm/s}$ . In the latter two cases, the overall PL signal is reduced since the excess carrier density is reduced due to the increased recombination at the surfaces. For the thin Si wafer, the excess carrier density and hence the PL signal is dominated by the recombination at the surfaces for bulk carrier lifetimes above  $10 \mu\text{s}$ . Interestingly, for the thick Si brick the PL signal still depends on the bulk lifetime up to lifetimes in the range of milliseconds.

The first Section of this Chapter briefly outlines the status of carrier lifetime imaging using photoluminescence measurements published at the beginning of this work. In the second Section, we present a first approach for relating the photoluminescence

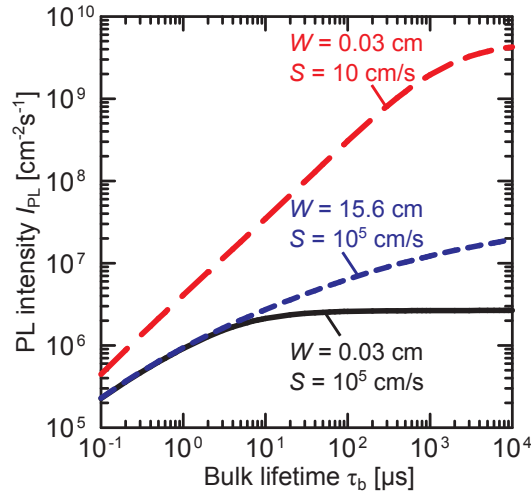


**Figure 3.1:** Photoluminescence signal  $I_{PL}$  as a function of the bulk carrier lifetime  $\tau_b$  for a thin wafer of thickness  $W = 300 \mu\text{m}$  and a low surface recombination velocity of  $S = 10 \text{ cm/s}$ . Additionally, the PL signal is calculated for a thin wafer and a brick ( $W = 15.6 \text{ cm}$ ) with a high surface recombination velocity of  $S = 10^5 \text{ cm/s}$ . A Si CCD camera is assumed as detector. The illumination intensity was set to  $0.01 \text{ suns}$  ( $0.7 \text{ mW/cm}^2$ ).

emission to the excess carrier density. The detected PL signal is calibrated by integrating an inductively-coupled coil-detecting photoconductance measurement system into a camera-based PL setup. In addition, we investigated the dependence of the calibration on doping density, thickness of the wafer and surface morphology. Furthermore, the impact of the carrier lifetime on the calibration parameter is demonstrated. Moreover, we propose a modified calibration relation that takes the influence of an inhomogeneous carrier density profile for high-level injection conditions into account.

Unfortunately, the calibration procedure relies on the precise knowledge of the dopant density of the sample, the wafer thickness and the validity of the underlying carrier mobility model. Thus, a calibration-free approach enabling fast carrier lifetime imaging with a high spatial resolution is of great advantage. A calibration-free analysis can be realized by evaluating the time dependence of a physical quantity related to the excess carrier density [see Section 1.2]. In 2008, Ramspeck et al. [83] introduced the dynamic infrared lifetime mapping (dynamic ILM) technique on the basis of measurements of the free carrier emission using an infrared camera.

In the third Section, we present the adaption of the dynamic ILM approach to dynamic camera-based photoluminescence (dynamic PL) measurements. The main advantages of PL measurements compared to ILM measurements are: (a) PL measurements are less influenced by measurement artifacts such as trapping or depletion region modulation [84] and (b) they can be easily performed at room temperature.

Moreover, we present the application of the dynamic PL technique to Si bricks. In the limiting case of high surface recombination velocities, we demonstrate that not only the effective carrier lifetime but the bulk lifetime of the brick is accessible. The

investigation of the bulk lifetime of a Si brick prior to the sawing into wafers is highly preferable since it allows a first quality check of the silicon brick and its crystallization process. After sawing the brick into thin wafers, the bulk lifetime can only be extracted after an effective surface passivation or to a minor degree by modeling the relation between bulk and effective lifetime [85, 86]. We demonstrate that the exact knowledge of the surface recombination velocity or the thickness of the sample is not required for the determination of the bulk carrier lifetime of thick Si samples if using dynamic PL lifetime imaging.

In the fourth Section, the PL-based techniques are compared with PC-based techniques (light-biased microwave-detected photoconductance-decay (MW-PCD) [38], quasi-steady-state photoconductance (QSSPC) [29], transient photoconductance decay (PCD) [35–37]) and with the dynamic ILM lifetime imaging technique [83].

## 3.1 Previous work

### 3.1.1 Luminescence-based carrier lifetime measurements

In 1952, Haynes and Briggs [87, 88] reported the detection of radiation due to the recombination of free holes and electrons in silicon at room temperature. They applied current pulses to a Si  $p$ - $n$  junction and detected the electroluminescence (EL) using a spectrometer.

In 1963, Uchida [3] already used the luminescence to determine the recombination lifetime of induced charge carriers. He evaluated the time-dependent EL signal from a forward-biased Si  $p$ - $n$  junction under pulsed carrier injection. Uchida was the first who actually took a photograph from the luminescence of a Si sample and visualized its spatial distribution by imaging it with a tube on a phosphor screen.

In 1977, Dziewior and Schmid [12] determined the coefficients for the description of Auger recombination in Si. They measured the minority carrier lifetime by detecting the decay of a spatially integrated band-to-band PL signal after a pulsed excitation.

In 1988, Penner [89] used a high-speed camera with a Si cathode as image converter for the investigation of the inhomogeneous current distribution in an mc-Si solar cell. He also proposed using the EL image for the determination of the carrier lifetime. In the same journal, Bohnert et al. [90] reported on time-resolved PL spectroscopy measurements for the determination of a position-dependent carrier lifetime for the cross-section of a silicon diode.

In 1999, Tarasov et al. [91] mapped the band-to-band PL of an mc-Si wafer at room temperature using a spectrometer. They found a good correlation with a minority carrier lifetime mapping, obtained with a laser-microwave reflection technique.

In 2003, Trupke et al. [92] pointed out that Si is able to be an efficient light emitter

with efficiencies up to several percent if the carrier recombination at the surfaces is significantly reduced. In 2004, Trupke et al. [93] presented first results of transient and quasi-steady-state PL measurements of a passivated high-resistivity *n*-type Si wafer. Trupke et al. [93, 94] related the spatially integrated luminescence signal of a Si wafer, detected by a Si photodiode, to the excess carrier density from a photoconductance measurement at the same illumination conditions. This approach enabled them to measure the injection-dependent carrier lifetime down to an excess carrier density of only  $10^9 \text{ cm}^{-3}$  [94]. In the same year, Trupke et al. [95] proposed the quasi-steady-state photoluminescence (QSS-PL) technique for carrier lifetime measurements. The QSS-PL technique determines the carrier lifetime from a spatially integrated PL measurement [95], evaluating self-consistently the increasing and decreasing PL signal due to a modulated excitation.

In 2006, Brüggemann and Reynolds [96] determined the carrier lifetime of surface-passivated crystalline Si wafers with modulated PL measurements at room temperature. They extracted the minority carrier lifetime directly from the phase information of the modulated PL, detected spatially integrated with an InGaAs photodiode.

In 2005, Fuyuki et al. [4, 5] acquired electroluminescence images using a cooled Si CCD camera for the investigation of the inhomogeneous luminescence distribution of an mc-Si solar cell. In 2006, Trupke et al. [6] presented photoluminescence imaging on silicon wafers using a Si CCD camera. He correlated the luminescence signal with the carrier lifetime by calibrating the PL signal to the excess carrier density using the previously presented QSS-PL technique [95].

Since then camera-based PL imaging is known as a contactless and non-destructive measurement technique for the spatially resolved analysis of the quality of Si wafers. Since measurement conditions close to solar cell operating conditions can be adjusted, it is valuable to monitor the processing of solar cells at any stage of fabrication as no electrical contacts are required. In 2006, Abbott et al. [97] used PL imaging for process control during the manufacturing of high-efficiency Si solar cells. In 2007, Sugimoto et al. [98] used the PL imaging technique to study the passivation of a Si wafer by immersion into hydrofluoric acid (HF).

The et al. [99] proposed in 2007 the calibration of the PL imaging technique with the carrier density imaging CDI/ILM [30] technique. Macdonald et al. [100, 101] used PL imaging for the determination of the spatial distribution of the interstitial iron concentration, calibrating the PL signal with an external QSSPC [29] measurement. Würfel et al. [31] introduced a technique for the determination of the charge carrier diffusion length based on the ratio of two EL images, acquired with two different short-pass filters.

### 3.1.2 Measurement artifacts

Bardos et al. [84] presented in 2006 a study concerning measurement artifacts that are well-known for photoconductance (PC) measurement; namely trapping [45, 46] and the depletion region modulation effect [51, 53]. These measurement artifacts prevent the reliable measurement of the injection-dependent carrier lifetime at low injection densities (see Section 1.3.2). Due to the PL signal dependence on the product of the free carrier densities instead of the sum as for PC measurements, PL-based lifetime measurements are only minor influenced by these measurement artifacts.

#### Minority carrier trapping

We consider the simple Hornbeck-Haynes model [47] (see Section 1.3.2) for the investigation of the trapping impact on PL-based lifetime measurements. The measured PL signal is related to the rate of radiative recombination and thus, to the product of the carrier densities [see Eqs. (1.5) and (1.6)]. Without traps, the PL signal  $I_{\text{PL}}$  is expected to be proportional to the product of excess carrier density  $\Delta n$  and doping density  $N_{\text{dop}}$ :

$$I_{\text{PL}} \propto \Delta n N_{\text{dop}}, \quad (3.1)$$

assuming low-level injection conditions ( $N_{\text{dop}} \gg \Delta n$ ). Thus, the PL signal in the presence of traps  $I_{\text{PL,t}}$  is expected to be proportional to

$$I_{\text{PL,t}} \propto \Delta n (N_{\text{dop}} + n_t), \quad (3.2)$$

where  $n_t$  is the density of trapped electrons. As a consequence, the ratio of the measured signal in the presence of traps to the measured signal without traps is given by [84]

$$\frac{I_{\text{PL,t}}}{I_{\text{PL}}} = \frac{N_{\text{dop}} + n_t}{N_{\text{dop}}}. \quad (3.3)$$

For the PC measurement, the ratio of trap density to excess carrier density is decisive for the overestimation of the measured signal [see Eq. (1.31)], but for the PL signal, the ratio with the doping density determines a possible overestimation of the measured PL signal. For a measurement-artifact-free PL-based lifetime measurement, the trap density has to be smaller than the doping density ( $n_t \ll N_{\text{dop}}$ ). Thus, the trapping impact on the PL measurement is independent of the injection density, allowing the PL-based lifetime measurement down to low excess carrier densities.

#### Depletion region modulation

In 2004, Trupke et al. [93] proposed the small impact of depletion region modulation on PL-based lifetime measurements for samples having a space-charge region. Trupke and Bardos [94] demonstrated the reduced impact compared to PC-based lifetime

measurements by comparing the injection-dependent lifetime of two *p*-type Si wafers, one with a phosphorus diffusion and the other one with a boron diffusion on both sides.

As discussed in Section 1.3.2, the variation of the space charge region width  $W_{\text{scr}}$  as a function of the illumination intensity  $I_{\text{exc}}$  causes a difference between actual and apparent carrier lifetime for PC-based lifetime measurements. For PL-based lifetime measurements, the measured signal is related to the rate of radiative recombination and thus, to the product of the carrier densities [see Eq. (1.5)]. Typically, a net luminescence signal  $I_{\text{PL}}$  is acquired by subtracting a signal measured in the dark  $I_{\text{PL,dark}}$  from a signal measured under illumination  $I_{\text{PL,ill}}$ :

$$I_{\text{PL}} = I_{\text{PL,ill}} - I_{\text{PL,dark}} \propto B_{\text{rad}} (np - n_i^2). \quad (3.4)$$

However, for typical doping densities with  $N_{\text{dop}} > 10^{13} \text{ cm}^{-3}$ ,  $I_{\text{PL,dark}}$  is negligible compared to  $I_{\text{PL,ill}}$  since  $n_i^2 \ll np \approx \Delta n N_{\text{dop}}$ . Thus, the net luminescence signal  $I_{\text{PL,scr}}$  for a sample with a space charge region is proportional to the expression

$$I_{\text{PL,scr}} \propto B_{\text{rad}} \cdot n p \cdot [W - W_{\text{scr}}(I_{\text{exc}})], \quad (3.5)$$

where  $W$  is the thickness of the sample and  $W_{\text{scr}}$  is the thickness of the space charge region. Hence, the difference between the wafer thickness and thickness of the space charge region determines the impact of the DRM effect on PL-based lifetime measurements. Since typically  $W \gg W_{\text{scr}}$ , the DRM effect is negligible for PL-based lifetime measurements. For PC-based lifetime measurements, the difference between the space charge region width in the dark and under illumination was found to be decisive for excess carrier densities much lower than the doping density [see Eq. (1.35)].

## Reabsorption

Another measurement artifact of PL-based lifetime measurements is caused by reabsorption of generated luminescence photons. One way to relate the PL emission to the excess carrier density and carrier lifetime is by calibrating the PL emission to absolute values of the excess carrier density. This calibration procedure requires assumptions about the relation of the average PL emission to the average excess carrier density (averaged over the wafer depth). Due to reabsorption, the assumption of a proportionality between average excess carrier density and average PL emission is not valid for arbitrary shapes of the carrier density profile. However, Trupke [102] demonstrated that for realistic variations<sup>1</sup> of the carrier density profile the maximal influence of reabsorption on the measured PL signal is below 20%. A more detailed analysis of the impact of reabsorption on calibrated PL-based lifetime measurement is presented in Section 3.2.2.

<sup>1</sup>Trupke [102] varied the carrier lifetime between 1  $\mu\text{s}$  and 50  $\mu\text{s}$  in a wafer with a thickness of 300  $\mu\text{m}$ .

## 3.2 Photoconductance-calibrated photoluminescence lifetime imaging (PC-PLI)

The most obvious way to convert the PL signal in relative units of the used detector into absolute values of the actual carrier lifetime is by comparison with another lifetime technique. This comparison is regarded as the calibration of the PL signal.

In this Section, the detected PL signal is calibrated to the excess carrier density by integrating an inductively-coupled coil-detecting photoconductance (PC) measurement system [29] into a camera-based PL setup. The captured PL image is calibrated by measuring the photoconductance of the Si wafer in the same setup under identical excitation conditions.

Firstly, we introduce the photoconductance-calibrated photoluminescence lifetime imaging (PC-PLI) technique. An example is given by the measurement of an mc-Si wafer. Afterwards, we investigate the sensitivity of the PC-PLI approach on the assumed detection area of the PC setup. Since the Si samples of interest are mostly varying in doping density, thickness and surface texture, the PC-PLI calibration is investigated as a function of these parameters. Additionally, we investigate the impact of the depth-dependent carrier distribution on the PL calibration. As a consequence of this investigation, we propose a generalized calibration that is valid for arbitrary depth profiles. A last Section presents the general sensitivity of the PC-PLI technique with respect to the PL setup used in this work.

If not otherwise stated, sample preparation includes an acidic (mc-Si) or alkaline (FZ-Si) damage etching, an RCA cleaning [103] and a surface passivation (PECVD silicon nitride  $\text{SiN}_x$  or atomic-layer-deposited aluminum oxide  $\text{Al}_2\text{O}_3$ ) on both surfaces of the wafers.

### 3.2.1 Calibration procedure

The rate of radiative recombination  $R_{\text{rad}}$  is proportional to the product of the electron and the hole carrier densities  $n \cdot p$  (see Section 1.1). Expressed in terms of the excess carrier density  $\Delta n$ , the resulting photoluminescence flux  $\Phi_\gamma$  [Eq. (2.8)] is typically written as a second-order polynomial in  $\Delta n$  [95, 99, 104, 105]:

$$\Phi_\gamma \propto R_{\text{rad}} = B_{\text{rad}}np \approx B_{\text{rad}}(\Delta n N_{\text{dop}} + \Delta n^2), \quad (3.6)$$

where  $B_{\text{rad}}$  is the radiative recombination coefficient [Eq. (2.11)] and  $N_{\text{dop}}$  is the doping density. The PL signal  $I_{\text{PL}}$  of a Si wafer, measured with an appropriate detector, is typically assumed to be proportional to the emitted photon flux  $\Phi_\gamma$  [95, 99, 104, 105]:

$$I_{\text{PL}} \propto \Phi_\gamma. \quad (3.7)$$

With this assumption, basically one single measurement of the PL signal  $I_{\text{PL}}$  and the excess carrier density  $\Delta n$  under identical excitation conditions in the same setup is sufficient to obtain the calibration relation due to Eq. (3.6), assuming  $B_{\text{rad}}$  being constant<sup>2</sup>. The limits of the assumption (3.7) are discussed in Section 3.2.2.

Using the PC-PLI setup described in Section 2.2.2 for the calibration, the excess carrier density is determined from a calibrated steady-state photoconductance (SSPC) measurement of the Si sample under test. With the PC setup, a quantity proportional to the average excess carrier density

$$\Delta n_{\text{av}} := \frac{1}{W} \int \Delta n(z) dz \quad (3.8)$$

is acquired where  $W$  is the thickness of the sample. Using  $I_{\text{PL}}$  instead of  $\Phi_{\gamma}$  and  $\Delta n_{\text{av,SSPC}}$  instead of  $\Delta n$  yields the PL calibration factor

$$C_{\text{PL}} = \frac{I_{\text{PL}}}{\Delta n_{\text{av,SSPC}} N_{\text{dop}} + \Delta n_{\text{av,SSPC}}^2}, \quad (3.9)$$

assuming  $B_{\text{rad}}$  being independent of the free carrier density and included in the calibration factor.  $C_{\text{PL}}$  is a specific function of the setup configuration (camera, optical filters, lenses) and sample properties (thickness, surface properties). In Section 3.2.2, we show that the calibration factor  $C_{\text{PL}}$  is also affected by the depth-dependent carrier distribution.

In practice, the PL signal is often measured as a function of the illumination intensity resulting in  $I_{\text{PL}}$  as a function of  $\Delta n_{\text{av,SSPC}}$ . In this case, a second-order polynomial fit is applied to the data using

$$I_{\text{PL}} = a_{\text{PL}} \Delta n_{\text{av,SSPC}} + C_{\text{PL}} \Delta n_{\text{av,SSPC}}^2, \quad (3.10)$$

where  $a_{\text{PL}} := C_{\text{PL}} N_{\text{dop}}$  is the linear calibration factor. This procedure allows to become independent of the exact value of the doping density<sup>3</sup>.

For the calibration, the PL signal  $I_{\text{PL}}$  has to be averaged over the detection area of the SSPC setup to enable the comparison of  $I_{\text{PL}}$  and  $\Delta n_{\text{av,SSPC}}$ . This area is assumed to be the cross section of the SSPC measurement coil (circular area with a diameter of  $\sim 1.85$  cm). Cuevas et al. [107] found that the QSSPC setup, as used for the PC measurement in our PC-PLI setup, measures the arithmetic mean of a spatially distributed carrier lifetime. Thus, the PL signal  $I_{\text{PL}}$  for the calibration relation is determined by an arithmetic mean of the camera pixels displaying the detection area of the PC setup.

<sup>2</sup> $B_{\text{rad}}$  can be regarded as independent of the free carrier density with an uncertainty  $< 20\%$  if  $\Delta n < 10^{16} \text{ cm}^{-3}$  and  $N_{\text{dop}}$  is between  $10^{15} \text{ cm}^{-3}$  and  $10^{16} \text{ cm}^{-3}$  (see Fig. 2.1).

<sup>3</sup>Otherwise,  $N_{\text{dop}}$  has to be obtained from four-point-probe [106] or photoconductance measurements [2].

If  $C_{\text{PL}}$  is known, the detected PL signal  $I_{\text{PL}}$  of each camera pixel can be converted into absolute values of the average excess carrier density  $\Delta n_{\text{av}}$  of the Si wafer under test using the expression:

$$\Delta n_{\text{av}}(I_{\text{PL}}) = \frac{-N_{\text{dop}}}{2} + \frac{1}{2} \sqrt{4 \frac{I_{\text{PL}}}{C_{\text{PL}}} + N_{\text{dop}}^2}. \quad (3.11)$$

For low-level injection conditions ( $\Delta n \ll N_{\text{dop}}$ ), Eqs. (3.10) and (3.11) can be further simplified to

$$I_{\text{PL}} = C_{\text{PL}} N_{\text{dop}} \Delta n_{\text{av}} = a_{\text{PL}} \Delta n_{\text{av}} \Rightarrow \Delta n_{\text{av}}(I_{\text{PL}}) = \frac{I_{\text{PL}}}{a_{\text{PL}}}, \quad (3.12)$$

using the doping-dependent linear calibration factor  $a_{\text{PL}}$ . Finally, the effective lifetime  $\tau_{\text{eff}}$  of the excess charge carriers in a Si wafer under steady-state illumination conditions is calculated from the ratio of the average photogeneration rate  $G_{\text{av}}$  [Eq. (2.38)] and the average excess carrier density  $\Delta n_{\text{av}}$  applying Eq. (1.2):

$$\tau_{\text{eff}} = \frac{\Delta n_{\text{av}}(I_{\text{PL}})}{G_{\text{av}}}. \quad (3.13)$$

### Example for the PC-PLI calibration

In this Section, the PC-PLI calibration procedure is presented by means of an injection-dependent lifetime measurement of a  $\text{SiN}_x$ -passivated  $1.8 \Omega\text{cm}$   $p$ -type mc-Si wafer ( $N_{\text{dop}} = 8 \times 10^{15} \text{ cm}^{-3}$ ) and a  $\text{SiN}_x$ -passivated  $1.1 \Omega\text{cm}$   $p$ -type FZ-Si wafer ( $N_{\text{dop}} = 1.3 \times 10^{16} \text{ cm}^{-3}$ ). Figure 3.2 (a) shows the injection-dependent lifetime  $\tau_{\text{eff}}(\Delta n_{\text{av}})$  for both samples, measured with the SSPC setup (open circles) and with the PC-PLI technique (filled symbols).

The impact of the measurement artifacts described above (Section 1.3.2) of the PC-based lifetime measurements can be seen in Fig. 3.2 (a) by the increase of the carrier lifetime at low injection densities. Accordingly, the calibration function has to be determined for injection densities higher than the artifact-affected injection range.

Figure 3.2 (b) shows the measured PL signal  $I_{\text{PL}}$  in units of the detector (counts per second: cts/s) averaged over the coil detection area versus the excess carrier density  $\Delta n_{\text{av,SSPC}}$  obtained from the steady-state photoconductance measurement for the mc-Si wafer of Fig. 3.2 (a). A PL image of the mc-Si wafer is displayed in Fig. 3.2 (b) where the position of the detection unit of the PC setup is marked with a yellow circle. In order to determine the relation between the PL signal and the excess carrier density, the measured data are fitted to a second-order polynomial in accordance with Eq. (3.10).

The obtained calibration parameter  $a_{\text{PL}}$  and  $C_{\text{PL}}$  are used for the conversion of the measured PL signal of each pixel into the excess carrier density and then into a

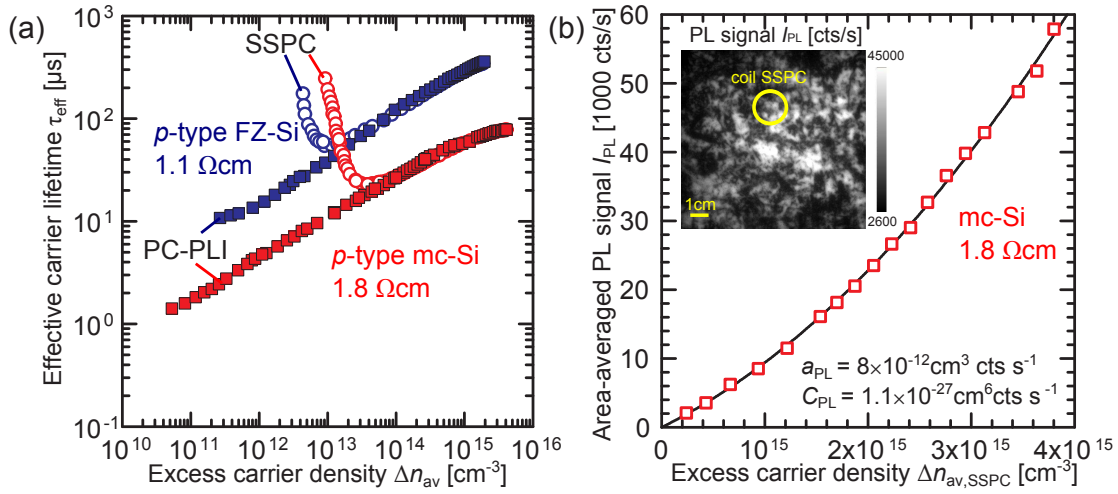


**Figure 3.2:** (a) Injection-dependent effective lifetime  $\tau_{\text{eff}}(\Delta n_{\text{av}})$  measured using the SSPC setup (open squares) and the PC-PLI setup (filled circles) for a 1.8  $\Omega\text{cm}$  p-type mc-Si wafer with a thickness of 200  $\mu\text{m}$  and for a 1.1  $\Omega\text{cm}$  p-type FZ-Si wafer with a thickness of 303  $\mu\text{m}$ . (b) PC-PLI calibration curve  $I_{\text{PL}} = a_{\text{PL}} \Delta n_{\text{av,SSPC}} + C_{\text{PL}} \Delta n_{\text{av,SSPC}}^2$  for the mc-Si wafer of (a). The inset shows an example PL image of the mc-Si wafer. The yellow circle marks the detection area of the coil of the PC setup that is used for averaging of the PL signal  $I_{\text{PL}}$ .

carrier lifetime using Eq. (3.13). The PC-PLI lifetime values shown in Fig. 3.2 (a) are the arithmetic means over the area of the imaged Si wafer that displays the SSPC detection region.

Since the PL measurement is only minor affected by minority carrier trapping and the DRM effect (see Section 3.1.2), the injection-dependent lifetime is reliably measurable down to low excess carrier densities of  $\Delta n_{\text{av}} = 10^{11} \text{ cm}^{-3}$ . In principle, even lower excess carrier densities are measurable. However, this would require much longer measurement times since the latter is inversely proportional to the injection density (see Section 3.2.3).

A comparison of a PC-PLI lifetime image with a light-biased microwave-detected photoconductance-decay (MW-PCD, Semilab, WT-2000) lifetime mapping is exemplarily shown in Fig. 3.3 for the same mc-Si wafer as presented in Fig. 3.2. Both lifetime distributions are measured at a steady-state illumination intensity of 0.3 suns ( $\sim 21 \text{ mW/cm}^2$ ). The step width of the MW-PCD setup is set at 250  $\mu\text{m}$ , which leads to a total acquisition time of 17 hours for the mapping shown in Fig. 3.3 (b). For the PC-PLI setup the resolution is 245  $\mu\text{m}$ . The total measurement time of the single PL image shown in Fig. 3.3 (a) is 3.2 s. For a better quantitative verification, a histogram of both lifetime distributions is presented in Fig. 3.3 (c).

Both lifetime mappings are qualitatively in good agreement. With the MW-PCD technique a broader distribution of lifetime values is measured. Thus, deviations between the two lifetime techniques are determined in the low- as well as in the high-lifetime range of the distribution. However, the mean values of the complete lifetime images

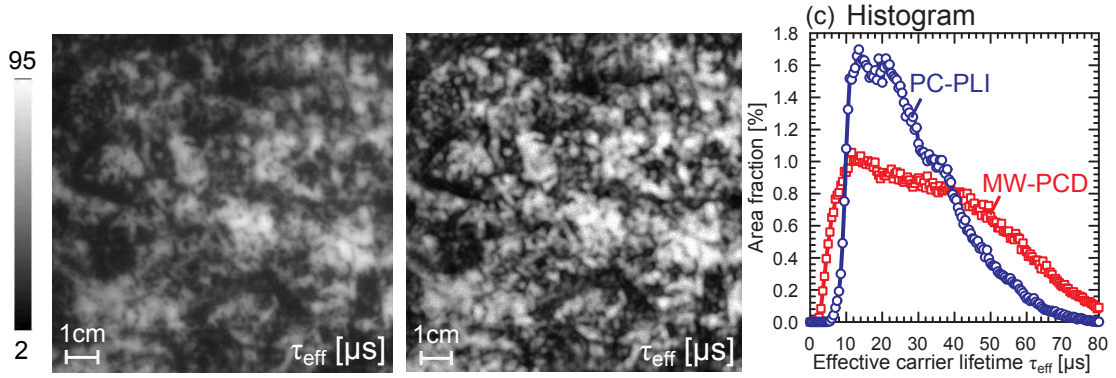


**Figure 3.3:** (a) PC-calibrated PL lifetime image of a  $10 \times 10 \text{ cm}^2$  p-type  $1.8 \Omega\text{cm}$  mc-Si wafer measured at an illumination intensity of  $21 \text{ mW/cm}^2$  ( $\sim 0.3$  suns) and (b) for comparison an MW-PCD lifetime mapping of the same wafer. (c) Histogram of the lifetime distributions of (a) and (b).

are similar with  $\tau_{\text{av}} = 31 \mu\text{s}$  (PC-PLI) and  $\tau_{\text{av}} = 34 \mu\text{s}$  (MW-PCD). One reason for deviations of the two lifetime distributions could be the fact that in the case of the light-biased MW-PCD mapping differential lifetimes are measured [41], whereas the PC-PLI determines actual lifetimes. A differential lifetime of up to 50% larger than the actual lifetime is estimated from the injection-dependent carrier lifetime in Fig. 3.2 (a). Another possible reason for deviations in the low-lifetime range is a different impact of reabsorption on the PL measurement [102] (see Section 2.1.3). However, for the lowest carrier lifetimes of the mc-Si wafer in Fig. 3.3 (b) ( $\tau \approx 2 \mu\text{s}$ ), the impact due to reabsorption on the PL calibration is estimated to be only  $\sim 10\%$ .

### Sense region of the photoconductance setup

For the calibration of the PL signal with a photoconductance measurement, the PL signal has to be averaged over the sensitive area of the detection coil of the PC setup. Earlier experiments of Berge [44] indicated a pronounced sensitivity limited to the coil area. In his investigations, Berge scanned the detection area with small-area conductive samples.

Especially for wafers with an inhomogeneous lateral distribution of the recombination properties, the size of the chosen area for averaging is expected to have a strong impact on the PC-PLI calibration. In this work, this impact is studied on an mc-Si wafer by varying the size of the averaging area for calculating  $I_{\text{PL}}$ . The maximal possible sensitive area is given by the opening of the PC setup with a diameter of 3.85 cm. The detection coil itself has a diameter of only 1.85 cm.

For the investigation, an mc-Si wafer is chosen with areas of high and low carrier lifetimes with dimensions in the order of the SSPC coil. Exemplarily, Fig. 3.4 (a) shows a PL image of the mc-Si wafer for an illumination intensity of 0.87 suns ( $\sim 60 \text{ mW/cm}^2$ ). The linear PC-PLI calibration parameter  $a_{\text{PL}}$  [Eq. (3.12)] is acquired in three different

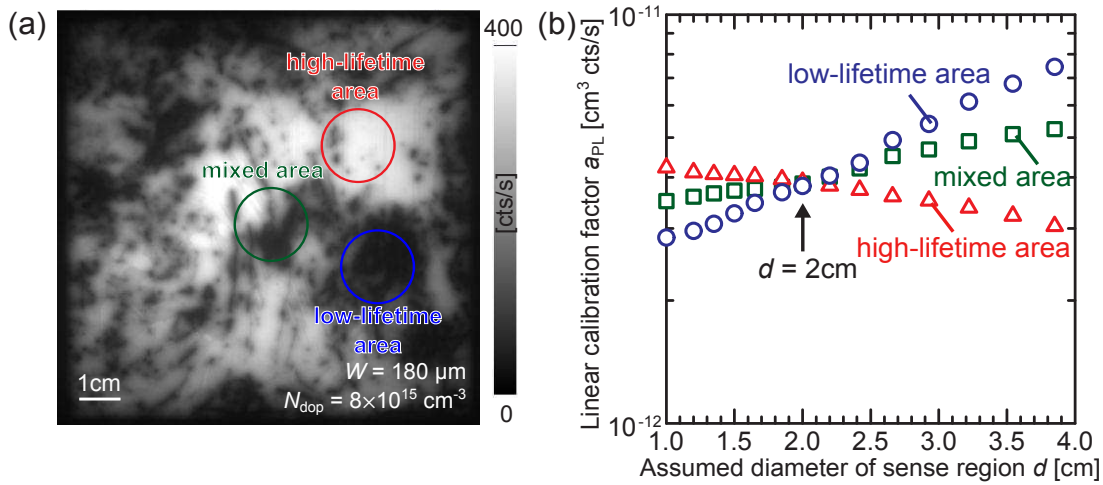


**Figure 3.4:** (a) Photoluminescence image of a  $10 \times 10 \text{ cm}^2$  *p*-type Si wafer with a doping density of  $N_{\text{dop}} = 8 \times 10^{15} \text{ cm}^{-3}$  and a thickness of  $W = 180 \mu\text{m}$  for an illumination intensity of  $60 \text{ mW/cm}^2$  ( $\sim 0.87$  suns). For the three marked areas, SSPC and PL measurements are performed as a function of the illumination intensity. (b) The linear calibration factor  $a_{\text{PL}}$  for the three marked areas of (a) as a function of the diameter  $d$  of the circular area used for averaging of the PL signal.

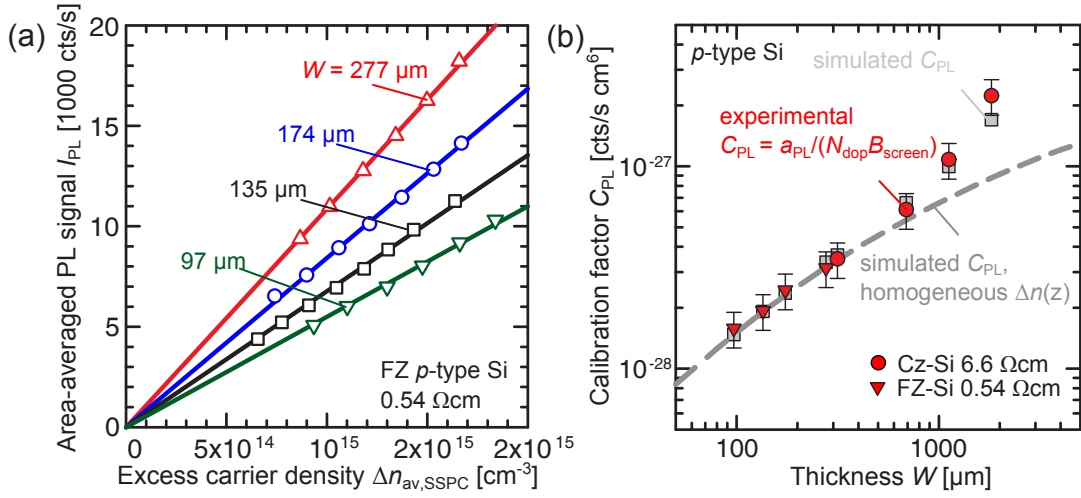
regions of the mc-Si wafer as a function of the size of the chosen averaging area for calculating  $I_{\text{PL}}$ . Two of the chosen wafer areas exhibit a nearly homogeneous distribution of the PL signal and differ by about one order of magnitude in signal amplitude. A third region is chosen with a mixed distribution of high and low PL signals. All three areas are marked in Fig. 3.4 (a).

Figure 3.4 (b) shows the linear calibration factor  $a_{\text{PL}}$  as a function of the diameter of the circular area for averaging. The diameter was varied in  $\sim 10\%$  steps between 1 cm and the maximum possible diameter of 3.85 cm. The calibration parameters for the three regions are in agreement for a diameter of  $(2 \pm 0.2)$  cm, which is close to the actual coil diameter of 1.85 cm.

It can be concluded that for the investigated mc-Si wafer almost the same PL calibration parameters (with a deviation  $\leq 10\%$ ) are determined for regions with different lifetime distributions if the PL signal is averaged over the coil area.

### PC-PLI calibration as a function of the wafer thickness

The impact of the wafer thickness on the PL signal is investigated by performing the PC-PLI calibration as a function of the wafer thickness for two sets of wafers: four *p*-type  $\text{SiN}_x$ -passivated  $0.54 \Omega\text{cm}$  FZ-Si wafers with thicknesses ranging from 97 to 277  $\mu\text{m}$  and four *p*-type  $\text{SiN}_x$ -passivated  $6.6 \Omega\text{cm}$  Cz-Si wafers with thicknesses ranging from 315 to 1820  $\mu\text{m}$ . Fig. 3.5 (a) shows exemplarily the PC-PLI calibrations for the  $0.54 \Omega\text{cm}$  FZ-Si wafers. The PC-PLI calibration is carried out at low-level injection



**Figure 3.5:** (a) Area-averaged PL signal  $I_{PL}$  as a function of the average excess carrier density  $\Delta n_{av,SSPC}$  for four  $\text{SiN}_x$ -passivated p-type FZ-Si wafers with different sample thicknesses. The lines stem from a linear regression of the data to determine the linear calibration factor  $a_{PL}$  from  $I_{PL} = a_{PL}\Delta n_{av,SSPC}$ . (b) Experimentally determined calibration factor  $C_{PL} = a_{PL}/(N_{dop}B_{screen})$  for two sets of wafers with different sample thicknesses (red circles: 6.6  $\Omega\text{cm}$  Cz-Si, red squares: 0.54  $\Omega\text{cm}$  FZ-Si). The dashed line shows the expected dependence of  $C_{PL}(W)$  if the excess carriers are homogeneously distributed in the Si wafer and the gray squares mark the simulated values for the same  $(\Delta n_{av}, \tau_{eff})$  pairs as the measurements.

conditions. Hence, only the linear calibration factor  $a_{PL}$  is determined [Eq. (3.12)].

To compare both sets of wafers, the doping-independent calibration factor  $C_{PL}$  is calculated. Since the difference in the doping concentrations of the two wafer sets is more than one order of magnitude, the correction factor  $B_{screen}$  [Eq. (2.12)] is additionally considered:  $C_{PL} = a_{PL}/(N_{dop}B_{screen})$ . According to the parameterization of Altermatt et al. [10], the PL signal is expected to be reduced by  $\sim 18\%$  for the FZ-Si wafers compared to the Cz-Si wafers due to a reduced probability of radiative recombination for the wafers with the higher doping density.

In Fig. 3.5 (b), the thickness dependence of the calibration factor  $C_{PL}$  is presented for the two sets of wafers (red filled symbols). The calibration factor  $C_{PL}$  increases with thickness since the integral number of excess carriers increases with thickness for the same average excess carrier concentration. However, the calibration factor is expected to scale not directly with the thickness of the wafer. The slope of  $C_{PL}(W)$  is expected to decrease with increasing thickness due to an increasing fraction of reabsorbed photons. The dashed line shows the simulated  $C_{PL}(W)$ , calculated using Eq. (2.14), for a homogeneous distribution of excess carriers and demonstrates the expected impact of reabsorption on the PC-PLI calibration.

However, we observe a deviation between the modeled  $C_{PL}(W)$  and the experimental results for the three thickest samples in Fig. 3.5 (b). This deviation can be explained by the impact of the excess carrier distribution on the PC-PLI calibration. The depth distribution of the excess carriers is quite inhomogeneous in the thick samples since

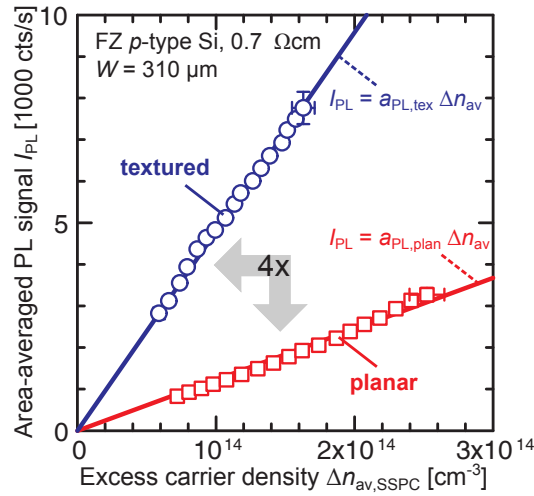


**Figure 3.6:** Area-averaged PL signal  $I_{PL}$  as a function of the excess carrier density  $\Delta n_{av,SSPC}$  for two FZ-Si wafers with different surface morphologies (textured and planar). The solid lines stem from a linear regression to the data. The ratio of the two linear calibration factors is found to be  $a_{PL,tex}/a_{PL,plan} \approx 3.9$ .

the absorption length of the exciting illumination is only  $\sim 13 \mu\text{m}$  and the diffusion length is smaller than the wafer thickness. Therefore, we modeled the calibration factor for the same  $(\Delta n_{av}, \tau_{eff})$  pairs as the actual measurement. The result is shown in Fig. 3.5 (b) as gray squares and is in a better agreement with the experimental data.

The question arises if different samples can be measured with the same calibration relation, saving the efforts for the calibration of each single sample itself. From this experiment, it can be concluded that small variations in the wafer thickness are in fact tolerable. The same PC-PLI calibration can be applied with an error  $< 10\%$  if the thickness variations are in the range  $(200 \pm 20) \mu\text{m}$ . If only small thickness variations are present,  $C_{PL}(W)$  can be approximated by a linear dependence. If determining the PC-PLI calibration for a thickness of  $200 \mu\text{m}$ , the calibration parameter can be linearly scaled with the thickness in a range of  $(200 \pm 50) \mu\text{m}$  with an uncertainty of below  $10 \%$ .

### PC-PLI calibration for a planar and a textured wafer

A different surface morphology (e.g. a textured surface) is expected to have a pronounced impact on the PL signal due to an increased escape probability of the luminescence photons. In Fig. 3.6, the PC-PLI calibrations for a planar  $\text{SiN}_x$ -passivated  $0.7 \Omega\text{cm}$  FZ-Si wafer and a textured  $\text{SiN}_x$ -passivated  $0.7 \Omega\text{cm}$  FZ-Si wafer are presented. The random uprights pyramids on the surface of the textured wafer were generated by exposing the RCA cleaned Si wafer to an alkaline etch solution of potassium hydroxide (KOH) and isopropyl alcohol.

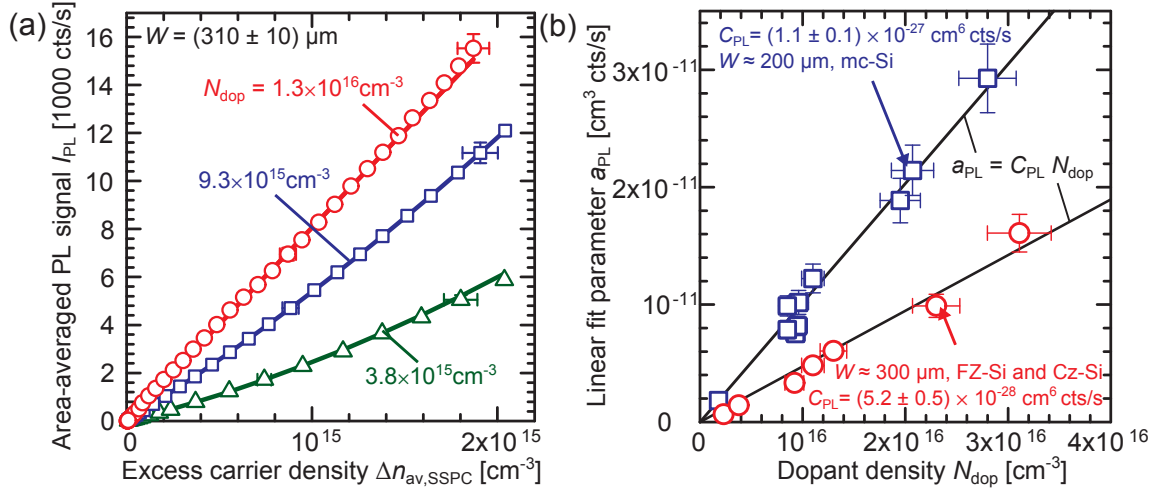


**Figure 3.7:** (a) Area-averaged PL signal  $I_{PL}$  as a function of the excess carrier density  $\Delta n_{av,SSPC}$  for FZ-Si wafers of different dopant densities  $N_{dop}$ . (b) Linear calibration parameter  $a_{PL}$ , obtained from a linear regression, as a function of the dopant density  $N_{dop}$  for different FZ-Si wafers and a Cz-Si wafer (red circles). The PC-PLI calibration factor  $C_{PL}$  is found from the slope of a linear regression to  $C_{PL} = (5 \pm 1) \times 10^{-28} \text{ cm}^3 \text{ cts/s}$ . Additionally, the linear calibration factor  $a_{PL}$  is shown for mc-Si wafers of different dopant densities (blue squares). The PC-PLI calibration factor for the mc-Si is found to be  $C_{PL} = (11 \pm 1) \times 10^{-28} \text{ cm}^3 \text{ cts/s}$ .

From the comparison of the two measurements, it can be concluded that the ratio of the two linear PC-PLI calibration factors of the textured and the planar Si wafer is  $a_{PL,tex}/a_{PL,plan} \approx 3.9$ . Thus, the textured wafer exhibits an about four times larger escape probability for the generated luminescence photons. Hence, the surface morphology has a strong impact on the PC-PLI calibration. If comparing the results with a simulation, assuming a textured surface for the calculation of the escape fraction  $\eta_{esc}$  in Eq. (2.14) as in Ref. 67, a similar ratio of  $\sim 4.3$  is determined.

### PC-PLI calibration for different doping densities

A set of six  $p$ -type FZ-Si wafers and one  $p$ -type Cz-Si wafer of different dopant densities  $N_{dop}$  ranging between  $(1.5 - 30) \times 10^{15} \text{ cm}^{-3}$  with a thickness of  $W = (310 \pm 10) \mu\text{m}$  are investigated. Additionally, ten  $p$ -type mc-Si wafers with doping concentrations in the range of  $(8 - 28) \times 10^{15} \text{ cm}^{-3}$  and a thickness of  $W = (200 \pm 30) \mu\text{m}$  and one  $n$ -type mc-Si wafer with a doping concentration of  $1.8 \times 10^{15} \text{ cm}^{-3}$  and a thickness of  $320 \mu\text{m}$  are examined.

Figure 3.7 (a) shows the PL signal  $I_{PL}$  versus the excess carrier density  $\Delta n_{av,SSPC}$  exemplarily for three of the investigated FZ-Si wafers. In Fig. 3.7 (b), the linear fit parameter  $a_{PL}$  is plotted as a function of the dopant density  $N_{dop}$ . In order to allow for a comparison of the linear calibration factor at a fixed thickness, the small differences in the wafer thicknesses are considered by assuming a linear relation between thickness

and calibration factor as proposed in the last Section<sup>4</sup>. The experimentally determined PC-PLI calibration factors of the mc-Si wafers are adjusted to a thickness of  $W = 200 \mu\text{m}$  and for the monocrystalline silicon (mono c-Si) to  $W = 300 \mu\text{m}$ .

As expected from Eq. (3.12), a linear dependence is obtained with the slope being the calibration constant  $C_{\text{PL}}$ . The difference in  $B_{\text{rad}}$  due to its dependence on the dopant density is estimated to be  $< 20\%$  (see Section 2.1.2) and is considered in the error bars in Fig. 3.7 (b).

Interestingly, different calibration factors are obtained for mono c-Si and mc-Si wafers. The difference between the two different kinds of wafers is approximately a factor of two. In contrast, it was expected that the mono c-Si wafers exhibit higher calibration factors than the mc-Si wafers (for the same doping concentration) due to the larger thickness.

The mc-Si wafers, investigated in this work, are typically treated with an acidic isotropic etch (CP4, consisting of  $\text{HNO}_3$ ,  $\text{CH}_3\text{COOH}$  and  $\text{HF}$  [108]) with the purpose of removing the saw damage. An isotropic etching is required since the crystal orientation of the various grains of the multicrystalline structure is different. CP4 is also known for etching preferably along dislocations [108], resulting in etch pits along these crystal imperfections that are always present in mc-Si. For mono c-Si, anisotropic alkaline etch solutions can be used due to the uniform crystal orientation of the surface. In addition, mono c-Si wafers receive sometimes a chemical-mechanical polishing with the result of much smoother surfaces than the mc-Si wafers with a surface roughness  $\approx 1 \mu\text{m}$  [109].

As shown in the last Section for the textured sample, the surface roughness has a strong impact on the PL emission. Since both materials have experienced different surface treatments before the deposition of the  $\text{SiN}_x$  or  $\text{Al}_2\text{O}_3$  surface passivation, both surfaces are expected to have different surface roughnesses. For that reason, we conclude that the different PC-PLI calibration factors for mono c-Si and mc-Si reflects the different surface morphologies of the wafers.

As a consequence of the doping-dependent calibration factor, the question arises if the doping density can be extracted from the PC-PLI calibration. By fitting the measured data independently of the dopant density, the doping concentration should be given by the ratio of the fit parameter  $a_{\text{PL}}$  and  $C_{\text{PL}}$ . For that reason, we applied a second-order polynomial least square fit to the PC-PLI measurements of Fig. 3.7 (b) if injection densities close to the respective doping density were reached. The doping density was then calculated from the ratio of the fit parameter. A comparison of  $N_{\text{dop}}$  from four-point-probe measurements [106] with the ratio of the fit parameters  $a_{\text{PL}}/C_{\text{PL}}$  in Fig. 3.8 shows a good agreement (deviations are below 10%).

<sup>4</sup>Only for the *n*-type mc-Si wafer with the low doping density, a complete modeling of the thickness impact on the PL signal was performed using Eq. (2.14) to convert the experimentally determined calibration factor for a thickness of  $320 \mu\text{m}$  to a thickness of  $200 \mu\text{m}$  allowing the comparison of the PC-PLI measurements at a constant wafer thickness.

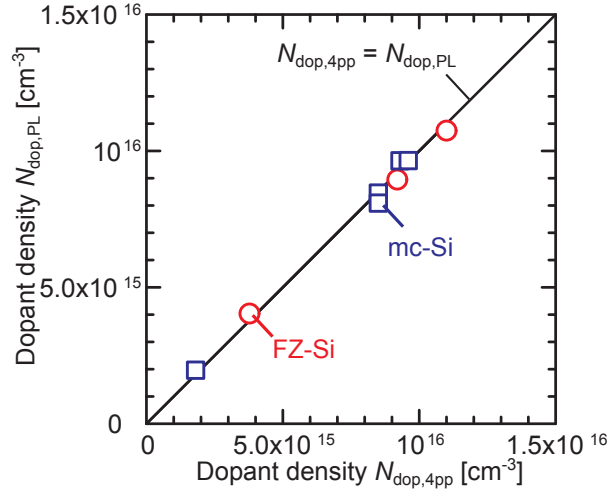


**Figure 3.8:** Comparison of the doping density  $N_{\text{dop},4pp}$  from four-point-probe measurements [106] with the doping density from the ratio of the PC-PLI calibration parameters  $N_{\text{dop},PL} = a_{PL}/C_{PL}$ .

However, the value of the doping density is already required for the determination of the average excess carrier density  $\Delta n_{\text{av,SSPC}}$  from the photoconductance measurement since the carrier mobility is a function of the doping density. In order to estimate the impact of the doping-dependent mobility, PL and PC measurements are modeled as a function of the doping density.

The PC-PLI measurements are simulated for excess carrier concentrations between  $\Delta n_{\text{av}} = 10^{13} \text{ cm}^{-3}$  and  $10 \times N_{\text{dop}}$  and dopant densities between  $N_{\text{dop}} = 10^{13} \text{ cm}^{-3}$  and  $10^{17} \text{ cm}^{-3}$  using Eqs. (2.14) and (1.27) and the mobility model of Ref. 43. The doping density is determined from the ratio of the modeled calibration parameters but with different doping densities as input parameter for the mobility model.

As a result of the simulation, we conclude that the doping density is determined by the ratio of  $a_{PL}/C_{PL}$  with an uncertainty  $\leq 10\%$  if the actual doping density is  $N_{\text{dop}} \leq 5 \times 10^{15} \text{ cm}^{-3}$ . For higher doping densities, the variation of the mobility with doping density increases more strongly and the accuracy of the doping density as input parameter for the mobility model becomes more important.

### 3.2.2 Validity of the PC-PLI calibration for arbitrary lifetime and injection ranges

In this Section, the validity of the presented PC-PLI calibration procedure for arbitrary lifetime and injection ranges is discussed. If measuring an injection-dependent carrier lifetime or the spatially distributed carrier lifetime of an mc-Si wafer, various values of the carrier lifetime have to be determined accurately with the same calibration relation at arbitrary injection levels.

In practice, the calibration parameter  $C_{\text{PL}}$  is obtained from measurements at high excitation levels and is then applied to the entire excess carrier density range of interest. The reasons for this procedure are twofold. On the one hand, measurement artifacts of the PC technique such as trapping or depletion region modulation (see Section 1.3.2) may restrict the calibration to injection ranges close to the doping density. On the other hand, one may use a calibration previously determined on a similar wafer at a different injection level.

In this Section, it will be demonstrated that the simple calibration relation  $I_{\text{PL}} = C_{\text{PL}} (\Delta n_{\text{av}} N_{\text{dop}} + \Delta n_{\text{av}}^2)$  is only valid for arbitrary lifetime and injection ranges if the excess carriers are homogeneously distributed throughout the depth in the Si sample.

At first, the PC-PLI calibration is investigated at low-level injection conditions as a function of the carrier lifetime to study the impact of reabsorption. Next, the PC-PLI calibration is studied as a function of the carrier lifetime for different injection conditions. Then, a modified calibration relation is derived, which is valid for arbitrary carrier profiles.

Afterwards, we verify the impact of the depth-dependent carrier distribution on the PL calibration and the validity of the generalized calibration relation by investigating two Si wafers with considerably different bulk lifetimes. Finally, an iterative correction procedure is proposed, which reduces the deviations due to an inhomogeneous carrier density profile of calibrated PL-based lifetime measurements significantly.

#### Impact of reabsorption on the PC-PLI calibration at low-level injection conditions ( $\Delta n \ll N_{\text{dop}}$ )

The fraction of reabsorbed photons from the originally generated luminescence depends on the covered path length of the photons in the excited Si sample. Hence, the fraction of the reabsorbed photons is a function of the shape of the depth-dependent carrier density profile as shown by Trupke [102]. The short absorption length of the exciting photons of the PL setup used in this work results in a strong variation of the depth-dependent carrier distribution for carrier lifetimes with  $L = \sqrt{\tau D_n} < W$ . As a consequence, the fraction of reabsorbed photons is smaller for  $L < W$  compared to a carrier profile with  $L > W$  due to the different photon path lengths towards the surface facing the detector.

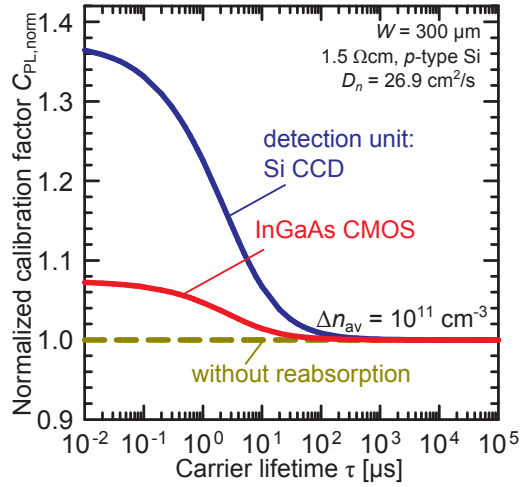


**Figure 3.9:** Variation of the calibration factor  $C_{PL}$  as a function of the carrier lifetime  $\tau$  if detecting the PL signal with a Si CCD (blue line) or an InGaAs CMOS (red line) camera. For comparison, the dashed line shows  $C_{PL}(\tau)$  if reabsorption is neglected. The values are normalized to  $C_{PL}$  for a homogeneous carrier profile at a high carrier lifetime ( $\tau > 10^3 \mu\text{s}$ ). The average excess carrier density  $\Delta n_{av}$  is set at  $10^{11} \text{ cm}^{-3}$  for all carrier lifetimes. The temperature is set at  $T = 300 \text{ K}$ , the excitation wavelength is chosen to be  $\lambda_{exc} = 808 \text{ nm}$  and the surface recombination velocity is set at  $S = 0 \text{ cm/s}$ .

To study the impact of reabsorption on the PC-PLI calibration, the calibration factor  $C_{PL}$  is calculated as a function of the carrier lifetime using Eqs. (3.8) and (3.9)<sup>5</sup>. We keep the excess carrier density  $\Delta n_{av}$  constant at low-level injection for all carrier lifetimes. Hence, the exciting photon flux is varied for this simulation.

The calibration factor  $C_{PL}$  is calculated for a  $1.5 \Omega\text{cm}$   $p$ -type Si sample without surface recombination ( $S = 0 \text{ cm/s}$ ). Thus, the effective lifetime  $\tau_{\text{eff}}$  equals the bulk lifetime  $\tau_b$ . The optical properties (absorption coefficient, refractive index) for the calculation of the PL signal  $I_{PL}$  are taken from Green and Keevers [63]. Since reabsorption is a function of the photon wavelength, the simulation is performed for two detectors with different spectral sensitivities (Si CCD and InGaAs CMOS - see Fig. 2.5). The exciting photons are modeled with a wavelength of  $808 \text{ nm}$ , resulting in an absorption length of  $\sim 13 \mu\text{m}$  in Si.

Figure 3.9 shows the normalized calibration factor  $C_{PL, \text{norm}}$  as a function of the carrier lifetime  $\tau$  for low-level injection conditions ( $\Delta n_{av} = 10^{11} \text{ cm}^{-3}$ ). The calibration factor  $C_{PL}$  is normalized to a value calculated for a large carrier lifetime ( $\tau > 10^3 \mu\text{s}$ ), guaranteeing a homogeneous carrier distribution throughout the Si sample. The normalization allows the presentation of the maximum possible variation of the calibration factor. For a valid application of the PC-PLI calibration factor [Eq. (3.9)] to Eq. (3.11) for arbitrary injection levels and lifetimes, a constant  $C_{PL}(\tau)$  is required.

Figure 3.9 shows that for carrier lifetimes below  $100 \mu\text{s}$ ,  $C_{PL, \text{norm}}$  increases strongly

<sup>5</sup>The carrier density profile  $\Delta n(z)$  is modeled with Eq. (2.32) and the PL signal  $I_{PL}$  with Eq. (2.14).

if using a Si CCD camera for the detection of the PL signal (upper blue line). The variation is smaller if an InGaAs camera is used (middle red line) since the fraction of detected long-wave photons is larger for the InGaAs detector compared to the Si CCD camera. As a result, the fraction of reabsorbed photons is smaller for the InGaAs detector since the absorption probability decreases with increasing wavelength (see Fig. 2.2). For very low lifetimes  $\tau < 0.1 \mu\text{s}$ , the calculated calibration factor is approximating a constant value for both types of detectors since the shape of the carrier density profile is limited by the generation profile. In addition, we calculated  $C_{\text{PL}}$  without considering the effect of reabsorption. As expected, the calibration factor  $C_{\text{PL}}(\tau)$  is constant if reabsorption is not included (lower dashed line).

An increase in  $C_{\text{PL}}$  corresponds to an increased  $I_{\text{PL}}$  [Eq. (3.10)] and thus to an overestimation of the excess carrier density (and carrier lifetime) with Eq. (3.11). Figure 3.9 shows, that for a lifetime of  $1 \mu\text{s}$ ,  $C_{\text{PL,norm}}$  deviates from the value for a homogeneous carrier distribution by  $\sim 22\%$  with the result of an overestimation of the carrier lifetime of  $\sim 22\%$  to  $\sim 1.22 \mu\text{s}$ .

The variation of  $C_{\text{PL}}$  due to reabsorption is expected to depend on the thickness of the sample and the diffusivity since these parameters are affecting the shape of the excess carrier profile  $\Delta n(z)$ . For thinner samples, the deviation caused by reabsorption is decreasing. The carrier density profile is also affected by the spectral distribution of the exciting illumination. For longer excitation wavelengths, the carriers are excited deeper in the wafer and are able to spread more uniformly with the consequence of a lower reabsorption impact on the PC-PLI calibration.

In summary, we confirmed the results of Trupke [102] who concluded that reabsorption has only a low impact ( $< 20\%$ ) on PL-based lifetime measurements for realistic variations of lifetime and injection density. Only for thick samples and low carrier lifetimes, reabsorption has to be considered for an accurate lifetime determination. However, the impact of reabsorption can be corrected for by using the calculated  $C_{\text{PL}}(\tau)$  as a transfer function since the influence of reabsorption is only a function of the shape of the carrier profile and not of the injection density.

With the transfer function  $C_{\text{PL}}(\tau)$ , the actual lifetime  $\tau_{\text{actual}}$  is determined from the measured lifetime  $\tau_{\text{meas}}$  using the correction factor  $\varepsilon$ :

$$\tau_{\text{actual}} = \frac{\tau_{\text{meas}}}{\varepsilon(\tau_{\text{meas}})} \quad \text{with} \quad \varepsilon(\tau_{\text{meas}}) = \frac{C_{\text{PL}}(\tau_{\text{meas}})}{C_{\text{PL}}(\tau_{\text{cal}})} \quad (3.14)$$

where  $\tau_{\text{cal}}$  is the carrier lifetime for which the PC-PLI calibration factor  $C_{\text{PL}}$  is experimentally determined.

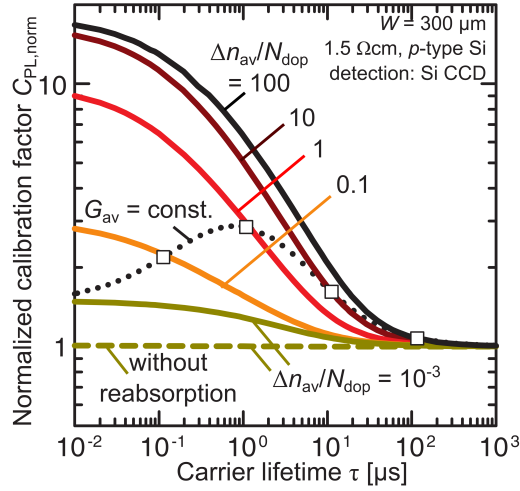


**Figure 3.10:** Calibration factor  $C_{PL} = I_{PL}/(\Delta n_{av}^2 + N_{dop}\Delta n_{av})$  as a function of the carrier lifetime  $\tau$  for different injection levels  $\Delta n/N_{dop}$ . The values are normalized to  $C_{PL}$  for a homogeneous carrier profile for a high carrier lifetime ( $\tau > 10^3 \mu\text{s}$ ). The dotted line shows the variation of the calibration factor  $C_{PL}$  if the photogeneration rate is constant (here:  $G_{av} = 8.2 \times 10^{21} \text{ cm}^{-3} \text{ s}^{-1}$ ) and the injection level is varying. Solid lines (and the dotted line) are calculated taking reabsorption into account. For reference, reabsorption was omitted for the calculation of the dashed line. The temperature is set at  $T = 300 \text{ K}$ , the excitation wavelength is chosen to be  $\lambda_{exc} = 808 \text{ nm}$  and the surface recombination velocity is set at  $S = 0 \text{ cm/s}$ .

### Variation of the PC-PLI calibration factor for high-level injection conditions ( $\Delta n \gg N_{dop}$ )

In this Section, the variation of the calibration factor  $C_{PL}$  is not only analyzed as a function of the carrier lifetime but also as a function of the injection density. The procedure for the calculation of  $C_{PL}$  is similar as in the last Section (for Fig. 3.9). Deviating from that, the depth-dependent carrier density profile is numerically calculated from the stationary one-dimensional diffusion equation [Eq. (2.31)] since the injection-dependent ambipolar diffusion coefficient  $D_a$  has to be considered at high-level injection conditions. For the calculation of the ambipolar diffusion coefficient, the mobility model of Klaassen et al. is used [42]. Figure 3.10 shows the normalized calibration factor  $C_{PL, \text{norm}}$  as a function of carrier lifetime  $\tau$  for injection levels from  $\Delta n_{av}/N_{dop} = 10^{-3}$  up to 100.

Figure 3.10 shows that for excess carrier densities close and above the doping density,  $C_{PL, \text{norm}}$  increases strongly with decreasing carrier lifetime  $\tau$  for  $\tau < 100 \mu\text{s}$ . For low-level injection conditions (lowest solid line with  $\Delta n_{av}/N_{dop} = 10^{-3}$ ), the variation of  $C_{PL, \text{norm}}$  is only caused by reabsorption (the same data as in Fig. 3.9). However, for higher injection densities ( $\Delta n \geq 0.1 N_{dop}$ ), the variation of  $C_{PL}(\tau)$  becomes additionally a function of the excess carrier density.

An increase in  $C_{PL}$  corresponds to an increased  $I_{PL}$  [Eq. (3.10)] and thus to an overestimation of the excess carrier density (and carrier lifetime) with Eq. (3.11). The

maximum possible overestimation of the carrier lifetime is given by  $\sim \sqrt{C_{\text{PL, norm}}}$  for the case of true high injection conditions. Figure. 3.10 shows that for a lifetime of 1  $\mu\text{s}$  and high injection conditions,  $C_{\text{PL, norm}}$  deviates from the value for a homogeneous carrier distribution by a factor of  $\sim 6.5$  with the result of an overestimated carrier lifetime of  $\sqrt{6.5} \mu\text{s} \approx 2.5 \mu\text{s}$ .

Figure 3.10 also shows the variation of  $C_{\text{PL, norm}}$  for a measurement at a constant photogeneration rate (dotted line). This would be the experimental situation for a single PL measurement of an mc-Si wafer with laterally inhomogeneous recombination properties. In this case,  $C_{\text{PL, norm}}$  decreases with decreasing  $\tau$  as  $\Delta n$  is approaching low-level injection conditions.

We also performed simulations assuming a finite recombination at the wafer surfaces with an additional impact on the shape of the carrier profile. However, it turned out that for surface recombination velocities below 100 cm/s virtually no difference ( $< 5\%$ ) in the calculated variations of  $C_{\text{PL}}$  was found.

For high-level injection conditions, it is expected that the probability of radiative recombination is reduced due to screening effects [10] [see Section 2.1.2]. As a consequence,  $C_{\text{PL}}(\tau)$  is expected to be reduced for large excess carrier densities  $\Delta n(z) \gg 10^{15} \text{ cm}^{-3}$ . For example, at an average injection level of  $\Delta n_{\text{av}}/N_{\text{dop}} = 10$  and a carrier lifetime of 1  $\mu\text{s}$  in the scenario shown in Fig. 3.10, screening is expected to reduce the normalized calibration factor by  $\sim 30\%$ .

In this Section, strong variations of the PC-PLI calibration factor were predicted as a function of the carrier lifetime for high-level injection conditions. In the next Section, a generalized PC-PLI calibration relation is derived which is valid for arbitrary carrier density profiles.

### Generalized PC-PLI calibration relation for arbitrary carrier density profiles

The luminescence signal  $I_{\text{PL}}$  detected by an appropriate sensor was found to be [Eq. (2.14)]:

$$I_{\text{PL}} = \frac{\Omega}{2\pi} \int \int b_{\text{rad}}(\lambda) f_{\text{setup}}(\lambda) \eta_{\text{esc}}(z, \lambda) [\Delta n(z) N_{\text{dop}} + [\Delta n(z)]^2] dz d\lambda \quad (3.15)$$

where  $b_{\text{rad}}(\lambda)$  is the spectral coefficient of radiative recombination. The wavelength-dependent properties of the PL setup (transmittance of filters and lenses, efficiency of the detector) are lumped into  $f_{\text{setup}}(\lambda)$ . The escape fraction for luminescence photons  $\eta_{\text{esc}}(z, \lambda)$  accounts for reabsorption of PL photons within the Si sample.

However, at this point, reabsorption is regarded negligible [ $\eta_{\text{esc}}(z, \lambda) = 1$ ], allowing the splitting of the luminescence integral [Eq. (3.15)] into a wavelength- and a depth-

dependent integral:

$$I_{\text{PL}} = \frac{\Omega}{2\pi} \int b_{\text{rad}}(\lambda) f_{\text{setup}}(\lambda) d\lambda \left[ N_{\text{dop}} \int \Delta n(z) dz + \int [\Delta n(z)]^2 dz \right]. \quad (3.16)$$

In order to account for inhomogeneous carrier density profiles in Si blocks and wafers, Bowden et al. [73] proposed to use an effective thickness  $W_{\text{eff}}$  instead of the physical thickness  $W$  of the Si sample (see Section 2.1.4). The effective thickness

$$W_{\text{eff}} := \frac{[\int \Delta n(z) dz]^2}{\int [\Delta n(z)]^2 dz} \quad (3.17)$$

can be regarded as a measure for the spreading of the excess carriers into the Si wafer.

In this work, we insert the definition of the effective thickness  $W_{\text{eff}}$  [Eq. (3.17)] into Eq. (3.16) to account for inhomogeneous carrier profiles. As a consequence, the integrand of the last integral in Eq. (3.16) changes from quadratic to linear:

$$I_{\text{PL}} = \frac{\Omega}{2\pi} \int b_{\text{rad}}(\lambda) f_{\text{setup}}(\lambda) d\lambda \left[ N_{\text{dop}} \int \Delta n(z) dz + \frac{1}{W_{\text{eff}}} \left[ \int \Delta n(z) dz \right]^2 \right]. \quad (3.18)$$

As a last step, the integral of the excess carrier density over depth is substituted by the average excess carrier density

$$\Delta n_{\text{av}} := \frac{\int \Delta n(z) dz}{W}, \quad (3.19)$$

since this is the measured quantity when calibrating the PL signal with a photoconductance-based setup. Inserting  $\Delta n_{\text{av}}$  in Eq. (3.18) yields the expression

$$I_{\text{PL}} = C_{\text{PL}} \left[ N_{\text{dop}} \Delta n_{\text{av}} + \Delta n_{\text{av}}^2 \frac{W}{W_{\text{eff}}} \right], \quad (3.20)$$

with  $C_{\text{PL}} = \frac{\Omega W}{2\pi} \int b_{\text{rad}}(\lambda) f_{\text{setup}}(\lambda) d\lambda$  being the PL calibration factor.

With Eq. (3.20), we introduce a generalized PL calibration relation that is valid for inhomogeneous depth-dependent excess carrier density profiles, assuming reabsorption as a comparably small disturbance. It will be shown below that reabsorption can be taken into account by applying an iterative correction procedure.

The quadratic term in Eq. (3.20) does not affect the PL signal if  $\Delta n_{\text{av}} \frac{W}{W_{\text{eff}}} \ll N_{\text{dop}}$ . Therefore, the previously used calibration relation Eq. (3.10) is correct under low-level injection conditions ( $\Delta n_{\text{av}} \ll N_{\text{dop}}$ ) or if the thickness of the wafer equals the effective thickness  $W = W_{\text{eff}}$ , which is equivalent to a homogeneous depth-independent

carrier distribution. The correction factor  $(W_{\text{eff}})^{-1}$  accounts for the fact that

$$\int [\Delta n(z)]^2 dz \neq \left[ \int \Delta n(z) dz \right]^2 \quad (3.21)$$

for inhomogeneous carrier profiles.

### Experimental verification

For the verification of the impact of the depth-dependent carrier distribution on the PC-PLI calibration, two different boron-doped  $\text{SiN}_x$ -passivated  $4 \times 5 \text{ cm}^2$  Czochralski-grown (Cz) Si wafers with different bulk carrier lifetimes, a thickness of  $W \approx 685 \text{ }\mu\text{m}$  and a doping density of  $N_{\text{dop}} = 10^{15} \text{ cm}^{-3}$  are used.

The PL measurements are performed using the PC-PLI setup described in Section 2.2.2. For the excitation of the excess carriers a high power diode laser with a central wavelength of 805 nm is used. A high illumination intensity is needed to reach injection densities close to the doping density at low carrier lifetimes. Therefore, we decrease the excited area of the Si wafer to  $3 \times 3 \text{ cm}^2$  and apply illumination intensities of up to  $7 \text{ W/cm}^2$  ( $\sim 100$  suns). Since the temperature of the Si wafer is an important parameter regarding the reabsorption of luminescence photons as well as the carrier lifetime, the sample is mounted on a peltier-cooled, temperature-controlled plane table using a vacuum pump. The temperature of the sample was set at  $T = 303 \text{ K}$ .

One of the Cz-Si wafers (sample A) exhibit an effective lifetime of  $\tau_{\text{eff}} \approx 1 \text{ ms}$  at an average excess carrier density of  $\Delta n_{\text{av}} = 10^{15} \text{ cm}^{-3}$  [see inset of Fig. 3.11 (a)]. The injection-dependent lifetime is measured using the PC-PLI setup. Fig. 3.11 (a) shows the quadratic dependence of the measured PL signal  $I_{\text{PL}}$  versus the average excess carrier density  $\Delta n_{\text{av,SSPC}}$ .

The effective thickness  $W_{\text{eff}}$  in the lifetime range shown in Fig. 3.11 (a) and used for the calibration equals the physical thickness of the wafer  $W$ . Therefore, Eq. (3.10) is valid for this calibration. This can be verified by investigating the fit parameter of a second-order polynomial  $I_{\text{PL}} = a\Delta n_{\text{av}} + b\Delta n_{\text{av}}^2$  to the calibration data shown in Fig. 3.11 (a) as a solid line. Since Eq. (3.10) is valid, the ratio of the fit parameter yields the known doping density of the wafer:  $a/b = N_{\text{dop}} = 9.6 \times 10^{14} \text{ cm}^{-3}$ . The calibration factor equals the fit parameter  $b = C_{\text{PL}} = 7.3 \times 10^{-28} \text{ cm}^6 \text{ cts/s}$ .

Figure 3.11 (b) shows the injection-dependent lifetime of the second Cz-Si wafer (sample B), determined with a QSSPC setup (see Section 1.3), as a black solid line. The carrier lifetimes are about two orders of magnitude lower compared to sample A. For the determination of the carrier lifetime from PL measurements, the calibration factor of sample A is used since the samples have the same optical properties. To estimate the impact of the carrier depth distribution on the PL calibration, Eq. (3.10) is used for the conversion of the PL signal into the excess carrier density and the

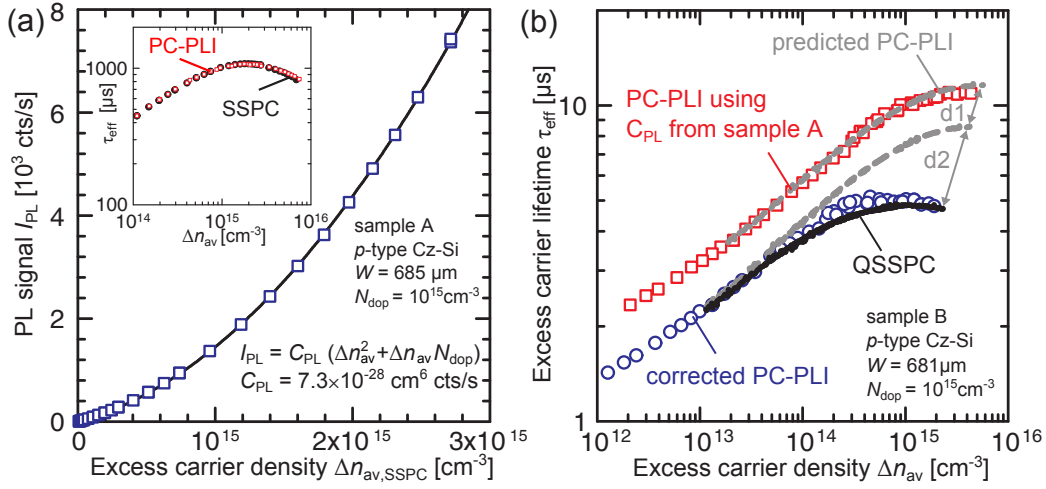


**Figure 3.11:** (a) PL calibration  $I_{PL}(\Delta n_{av,SSPC})$  for a  $p$ -type  $\text{SiN}_x$ -passivated  $4 \times 5 \text{ cm}^2$  Cz-Si wafer (sample A). The inset shows the injection-dependent carrier lifetime  $\tau_{eff}$  as measured with the PC-PLI setup. (b) Injection-dependent carrier lifetime of sample B as measured with a QSSPC setup (black line) at a temperature of  $T \approx 303 \text{ K}$  and from calibrated PL measurements (red squares), using the calibration of sample A. The open, blue circles show the calibrated PL lifetime if using our proposed iterative correction procedure (see Fig. 3.12). The upper dashed gray line is calculated from the QSSPC lifetime, predicting the PC-PLI lifetime based on the impact of the inhomogeneous carrier density profile. The lower dashed gray line shows the predicted PC-PLI lifetime if reabsorption is neglected. Hence, it can be distinguished between the impact of reabsorption [distance  $d1$ ] and the impact due to Eq. (3.21) [distance  $d2$ ].

excess carrier lifetime. The result of the calibrated PL lifetime measurement is shown in Fig. 3.11 (b) as red squares. Clearly visible is the deviation between the injection-dependent lifetime of the QSSPC measurement and the calibrated PL measurement.

Since we are able to quantify the influence of an inhomogeneous carrier density profile by using the effective thickness, a correction of our experimental data is possible. As the carrier lifetime is the parameter to be determined, the effective thickness is not initially known from the PL measurement. We iteratively approach the true value of the carrier lifetime by self-consistent variations, as sketched in Fig. 3.12 (a). A first estimate of the average excess carrier density is made by means of Eq. (3.20), assuming  $W_{eff} = W$ . From this first result, a rough estimate of the carrier lifetime  $\tau_{eff}$  is made using  $\tau_{eff} = \Delta n_{av}/G_{av}$ . Using the estimated  $\tau_{eff}$ , we determine an improved value of the effective thickness  $W_{eff}$ . These steps are repeated until the obtained  $\tau_{eff}$  value of the carrier lifetime is virtually not changing anymore (until a certain minimum difference  $\delta$  is reached). We chose a stop criterion of  $\delta = 0.01 \tau_{eff}$ .

In a second phase, the impact of reabsorption is included in the correction procedure. Since reabsorption only depends on the shape of the carrier distribution and not on the actual value of the injection density, a simple correction factor  $\varepsilon$  is suffi-

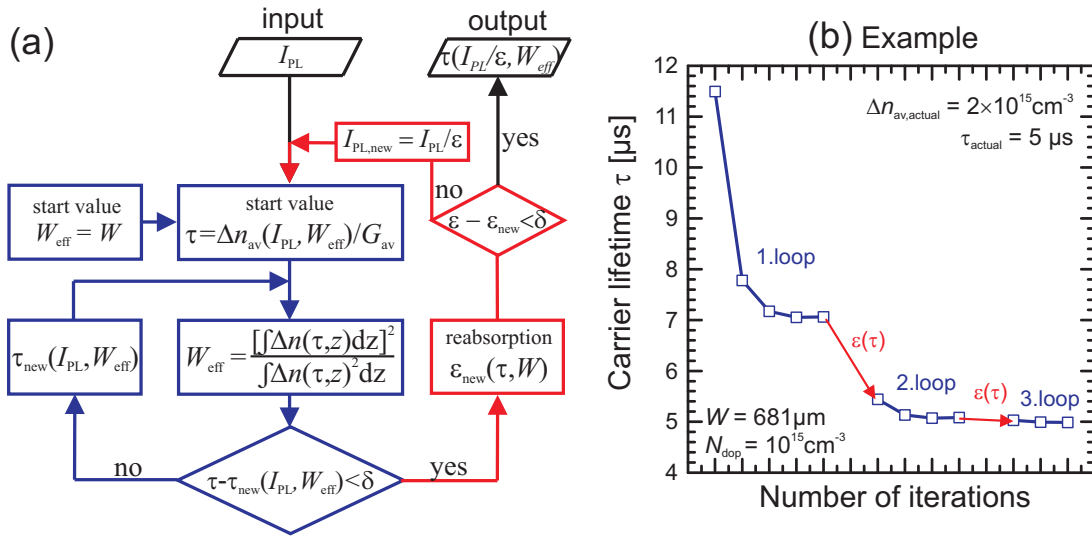


**Figure 3.12:** (a) Flow chart for the illustration of the self-consistent correction of the PC-PLI calibration. The blue marked loop corrects the impact of the carrier distribution on the PL calibration by calculating self-consistently the effective thickness. The red marked loop considers the different influence of reabsorption for different shapes of the carrier density profile. (b) Example for the correction loop for the last data point of the calibrated PL measurement of sample B [Fig. 3.11 (b)].

cient as proposed in Eq. (3.14)<sup>6</sup>. Subsequently, the previously described loop for the determination of the effective thickness  $W_{eff}$  is executed again.

Our proposed correction procedure is applied to the PL measurements of sample B, using the calibration factor of sample A. The result is plotted as blue circles in Fig. 3.11 (b) and is in agreement with the QSSPC measurement.

If a correction of the calibrated PL data is not performed, it is recommended to determine the calibration factor in the same lifetime and injection range as the PL measurement of interest.

The difference between the non-corrected PC-PLI lifetime (red squares) and the QSSPC measurement (black line) is determined by reabsorption and the wrongly considered average excess carrier density in the calibration function. In order to show how large the impact of each effect is, we modeled the expected non-corrected PC-PLI lifetime from the QSSPC measurement. The predicted PC-PLI lifetime is shown as the upper dashed gray line in Fig. 3.11 (b). As expected, measured and modeled PC-PLI lifetimes are in good agreement. Additionally, the PC-PLI lifetime is calculated from the QSSPC lifetime without considering reabsorption. This second modeled calibrated lifetime is shown as the lower dashed gray line in Fig. 3.11 (b) and enables the separation of the different influences on the PL calibration due to an inhomogeneous carrier depth distribution.

<sup>6</sup>A slight dependence of the carrier distribution on the injection conditions is expected due to the injection-dependent diffusion properties.

The distance  $d_1$  marks the impact of reabsorption on the PL calibration and the distance  $d_2$  labels the impact of the wrongly considered average excess carrier density [expressed by the factor  $\frac{W}{W_{\text{eff}}}$  in Eq. (3.20)]. At low-level injection conditions ( $\Delta n < 10^{14} \text{ cm}^{-3}$ ), reabsorption is the only reason for the deviation between calibrated PL and QSSPC measurement; whereas for high-level injection conditions, the integral-based deviation increases with injection level.

### 3.2.3 Sensitivity analysis

There is basically no lower limit for the determination of the excess carrier density with PL imaging regarding the sensitivity of the detector. The limit is rather given by the maximal available time for the measurement. For that reason, the total acquisition time, using a Si CCD or an InGaAs detector, is calculated for the investigation of the detection limit of the PL setup used in this work. However, most detector manufacturers specify an upper limit for the camera integration time  $t_{\text{int}}$  for which detector linearity is guaranteed (for the Si CCD used in this work:  $t_{\text{int,max}} = 120 \text{ min}$ ). For the calculation of the detection limit, a Si wafer with planar surfaces, a thickness of  $170 \text{ }\mu\text{m}$  and a doping density of  $10^{14} \text{ cm}^{-3}$  is assumed. The PL signal as a function of the excess carrier density is calculated with Eq. (2.14). The signal-to-noise ratio SNR for the measured signal is calculated using the analytical expression given in the Appendix (Eq. A.7).

Figure 3.13 shows the total acquisition time for a signal-to-noise ratio of  $\text{SNR} = 40$ . This is found to appear noiseless to the human eye and is equivalent to a relative uncertainty of the PL signal of  $1/\text{SNR} = 2.5\%$ . The total acquisition time is calculated from the product of the number of averages  $N$  and the camera integration time  $t_{\text{int}}$  [ $N \times t_{\text{int}}$ ] needed to achieve a SNR of 40. The camera integration time is increased until the detector has filled 90% of its capacity or the SNR of 40 is reached. If the SNR is still lower as required, although the detector is almost filled, the number of averaged images is increased. This procedure was found to be best to minimize the required total acquisition time for a given SNR [79].

We define a detection limit for the excess carrier density by restricting the total measurement time per image to one hour. As a consequence, the detection limit is  $\Delta n_{\text{av}} \approx 10^{13} \text{ cm}^{-3}$  for a FZ-Si wafer with a thickness of  $W = 170 \text{ }\mu\text{m}$  and a doping density of  $N_{\text{dop}} = 10^{14} \text{ cm}^{-3}$ . Increasing the doping density decreases the lower detection limit. The same wafer with a doping density of  $N_{\text{dop}} = 10^{16} \text{ cm}^{-3}$  has a detection limit of  $\Delta n_{\text{av}} \approx 10^{11} \text{ cm}^{-3}$ . An increase of the wafer thickness also decreases the total acquisition time if measuring the same average excess carrier density.

A reduction of the total measurement time is also achieved by averaging over the pixels of the sensitive area of the detector. If averaging over  $4 \times 4$  pixels, the detection limit is already reduced by about one order of magnitude, assuming a homogeneous

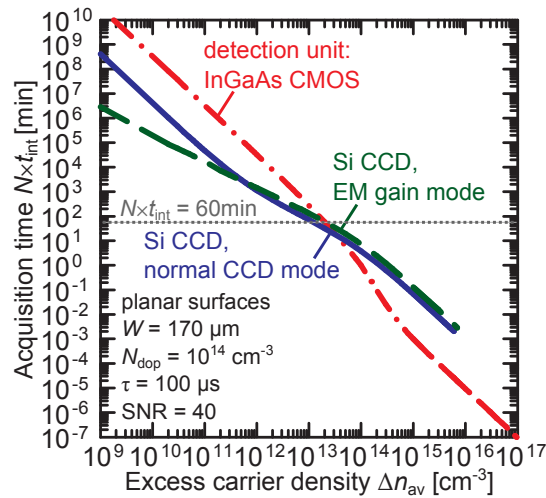


**Figure 3.13:** Total acquisition time  $N \times t_{int}$  as a function of the average excess carrier density  $\Delta n_{av}$  for the two different detectors used in this work: the Si CCD camera in the two available modes (normal, EM gain) and the InGaAs CMOS detector. A required signal-to-noise ratio SNR of 40 is set for the simulation of the PL signal of a passivated FZ-Si wafer with a thickness of  $W = 170 \mu\text{m}$ , a carrier lifetime of  $100 \mu\text{s}$  and a doping density of  $N_{dop} = 10^{14} \text{cm}^{-3}$ .

PL signal on all  $4 \times 4$  pixels. Averaging  $100 \times 100$  pixels of the PL image of such an homogeneous wafer might allow measurements of excess carrier densities down to  $\sim 7 \times 10^8 \text{cm}^{-3}$  in one hour. In 2005, Trupke et al. [94] demonstrated the high sensitivity of the PL detection for lifetime measurements by measuring excess carrier densities down to  $10^9 \text{cm}^{-3}$  on a  $1 \Omega\text{cm}$  ( $N_{dop} = 1.5 \times 10^{16} \text{cm}^{-3}$ ) FZ-Si wafer of thickness  $W = 260 \mu\text{m}$  using a silicon diode as detector. They used a low-noise preamplifier and the measurement took about one hour.

An upper limit exists due to the minimal possible camera integration time. For the Si CCD camera and the simulation scenario of Fig. 3.13, we determine an upper limit of  $\Delta n_{av} = 4 \times 10^{16} \text{cm}^{-3}$ . For the InGaAs CMOS camera, the limit is about one order of magnitude higher. However, this limitations may be easily solved using an appropriate neutral density filter in front of the camera. Practically, the upper limit is rather given by the maximum available photogeneration rate.

From Fig. 3.13, the appropriate detector (mode) at each injection level can be deduced for the given wafer properties. At high injection densities, the Si CCD camera in the normal CCD mode allows slightly shorter measurement times than the EM gain mode. The EM gain mode is only useful at very low PL intensities. For samples of higher doping concentrations or thicker samples, the crossing point of the Si CCD modes is found to be at lower injection densities. The InGaAs CMOS camera allows very fast measurements at high injection densities, however, at lower injection densities, the camera is limited by the dark current that is filling the detector. Therefore, an increase of the SNR for the lower injection densities can be only realized by increasing the number of averages  $N$ .

### 3.3 Dynamic photoluminescence lifetime imaging (dynamic PLI)

In the previous Section, the determination of the carrier lifetime was implemented by calibrating the steady-state PL signal with a photoconductance measurement. However, the photoconductance measurement itself is calibrated and relies on the knowledge of the dopant density of the sample, the wafer thickness and the validity of the underlying carrier mobility model.

In this Section, a calibration-free lifetime technique is presented that is based on the evaluation of the time dependence of the PL signal. Advantages of the dynamic approach over the steady-state lifetime technique are the independence of the knowledge of doping density, wafer thickness and mobility. Additionally, the dynamic approach is not affected by inhomogeneous sample optics (e.g. thickness variations, an inhomogeneous surface morphology) or inhomogeneous optics in the setup (e.g. an inhomogeneous filter transmission). Since a measurement of the photoconductance is not required anymore, even partly metalized, structured samples or solar cells can be measured. Basically, we adapt the dynamic infrared lifetime mapping (dynamic ILM) approach of Ramspeck et al. [83] to dynamic camera-based photoluminescence (dynamic PLI) measurements. The main advantages of PL measurements compared to ILM measurements are: (a) PL measurements are weakly influenced by measurement artifacts such as trapping or depletion region modulation [84] (see Sections 1.3.2 and 3.1.2) and (b) they can be easily performed at room temperature.

At first, the basic principle of the dynamic imaging approach and the adaption of the dynamic ILM approach to dynamic PL measurements is presented, followed by an exemplary measurement of an mc-Si wafer. Then, the general sensitivity to the effective carrier lifetime is investigated as a function of the camera integration time, considering the specific noise behavior of the used detector. One Section is about the impact of an injection-dependent carrier lifetime on the dynamic lifetime. Furthermore, the dynamic PL technique is applied to bulk carrier lifetime measurements of Si bricks.

#### 3.3.1 Principle of dynamic photoluminescence lifetime imaging

If the equilibrium of excess carriers in an optically excited Si sample is disturbed e.g. by switching a light source off or on, the excess carriers tend to reach a new equilibrium state. Solving the continuity equation has led to an exponential time dependence for the excess carrier density  $\Delta n_{av}$  with the effective lifetime  $\tau_{eff}$  as time constant [Eqs. (2.20) and (2.30)]. For that reason, the lifetime is often extracted directly from the time-dependent  $\Delta n_{av}(t)$  as e.g. for photoconductance decay [2, 35, 38] or photoluminescence decay [3, 12, 90] measurements.

Figure 3.14 shows the carrier density  $\Delta n_{av}(t)$  for a Si wafer with a bulk carrier lifetime

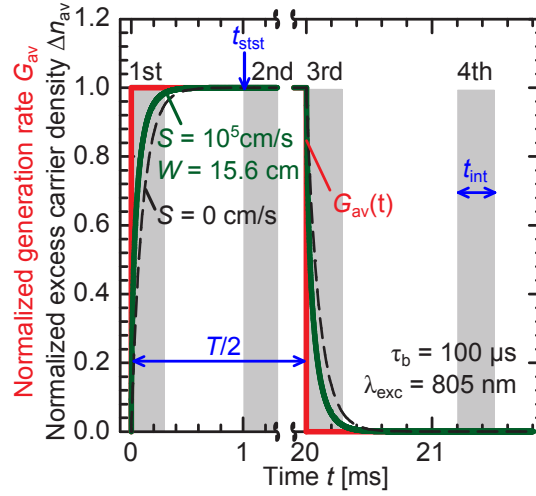


**Figure 3.14:** Time-dependent behavior of the excess carrier density  $\Delta n_{av}$  and the photogeneration rate  $G_{av}$  for a square-wave-modulated excitation. The gray bars mark the times of the image acquisition as required for the dynamic lifetime evaluation [Image1 to Image4 in Eq. (3.24)].  $\Delta n_{av}$  is calculated for a sample with  $S = 0$  cm/s and additionally for an unpassivated brick with  $W = 15.6$  cm and  $S = 10^5$  cm/s. The period of the square-wave-shaped modulation is  $T = 40$  ms ( $f = 25$  Hz). The bulk lifetime was set at  $\tau_b = 100$   $\mu$ s and the excitation wavelength at 805 nm.

of 100  $\mu$ s and a surface recombination velocity  $S = 0$  cm/s (dashed black line) together with the photogeneration rate  $G_{av}(t)$  for a square-wave-modulated excitation (red line).

However, instead of evaluating the complete time dependence of  $\Delta n_{av}(t)$ , it is basically sufficient to analyze the ratio of two PL images for the lifetime determination [83]. The first image is captured directly after switching on the light source and the second is captured for steady-state conditions of  $\Delta n_{av}(t)$ . The simple ratio of these two images only depends on the camera integration time  $t_{int}$  and the carrier lifetime  $\tau_{eff}$  for a linear relation between  $\Delta n_{av}$  and measured signal as shown in Ref. 83 for dynamic ILM measurements. However, for the quadratic dependence of the PL signal on  $\Delta n$ :

$$I_{PL} \propto \Delta n N_{dop} + \Delta n^2, \quad (3.22)$$

the simple ratio of two PL images becomes a function of the doping density  $N_{dop}$  and the photogeneration rate  $G_{av}$  since both parameters could not be reduced from the PL image ratio due to the specific dependence of the PL signal on  $\Delta n$ .

For that reason, we follow the extended approach of Ramspeck et al. [83] who considered not only the increase of  $\Delta n_{av}(t)$  after the switch-on of an excitation source, but also the decrease of  $\Delta n_{av}(t)$  after the light source is switched off. We introduce

an image ratio  $P$  that contains four instead of two PL images:

$$P = \frac{\text{Image1} - \text{Image3}}{\text{Image2} - \text{Image4}} = \frac{\int_0^{t_{\text{int}}} I_{\text{PL}}(t) dt - \int_{T/2}^{T/2+t_{\text{int}}} I_{\text{PL}}(t) dt}{\int_{t_{\text{stst}}}^{t_{\text{stst}}+t_{\text{int}}} I_{\text{PL}}(t) dt}. \quad (3.23)$$

where  $T$  is the period of the modulated excitation and  $t_{\text{stst}}$  is the time when recombination and generation of electron-hole pairs are balanced and the steady-state is reached. We calculate  $P$  for the PL signal dependence on  $\Delta n$  [Eq. (3.22)] for a square-wave-shaped excitation source with instantaneous switching characteristics:

$$P = \frac{\text{Image1} - \text{Image3}}{\text{Image2} - \text{Image4}} = \frac{t_{\text{int}} + 2\tau_{\text{eff}} \exp(-t_{\text{int}}/\tau_{\text{eff}}) - 2\tau_{\text{eff}}}{t_{\text{int}}}. \quad (3.24)$$

Note that despite of the quadratic dependence of the PL signal on  $\Delta n_{\text{av}}$ ,  $P$  has the same  $\tau_{\text{eff}}$  dependence as obtained for the linear relation between infrared emission and  $\Delta n$  in Ref. 83. The most important step in the calculation of Eq. (3.24) is the reduction of the image ratio by the factor  $N_{\text{dop}}\tau_{\text{eff}} + G_0\tau_{\text{eff}}^2$  that leads to the cancellation of  $N_{\text{dop}}$  and  $G_0$ . For that reason, the carrier lifetime can still be determined from the measurement of  $P$  for a known camera integration time but without the knowledge of any wafer parameters. The carrier lifetime is determined at each PL image pixel by comparing the experimentally determined ratio  $P$  with the calculated values.

In Fig. 3.14, the four PL images, required for the experimental determination of  $P$ , are marked by the gray bars with the width as the camera integration time  $t_{\text{int}}$ . The increasing  $\Delta n_{\text{av}}(t)$  is recorded in the first image and the decreasing  $\Delta n_{\text{av}}(t)$  in the third image. For the numerator of  $P$  in Eq. (3.23) the difference between the first and third image is calculated. The denominator results from the difference between the steady-state signal of the second image and the background signal (dark image) of the fourth image.

Figure 3.15 shows  $P$  as a function of the carrier lifetime  $\tau_{\text{eff}}$  for different camera integration times  $t_{\text{int}}$ . Clearly visible is the pronounced sensitivity of the ratio  $P$  to the effective carrier lifetime. If the camera integration time  $t_{\text{int}}$  is much larger than the effective carrier lifetime  $t_{\text{int}} \gg \tau_{\text{eff}}$ , it can be seen that the sensitivity [in that case: the slope of  $P(\tau_{\text{eff}})$ ] decreases. The same behavior can be observed for the case that  $t_{\text{int}} \gg \tau_{\text{eff}}$ . Obvious, the best sensitivity can be achieved if the camera integration time is in the order of the lifetime. A more detailed analysis of the sensitivity of the dynamic PL technique is presented in Section 3.3.3.

The details of the experimental setup for the dynamic technique are described in Section 2.2.2. Technical challenges regarding the implementation of the dynamic PLI technique are described in Section 2.2.1.

It can be concluded that we were able to transfer the dynamic ILM approach [83] to PL imaging. However, if the dynamic PL lifetime technique shall be independent of sample doping, thickness and reflectivity for arbitrary injection levels, a PL image

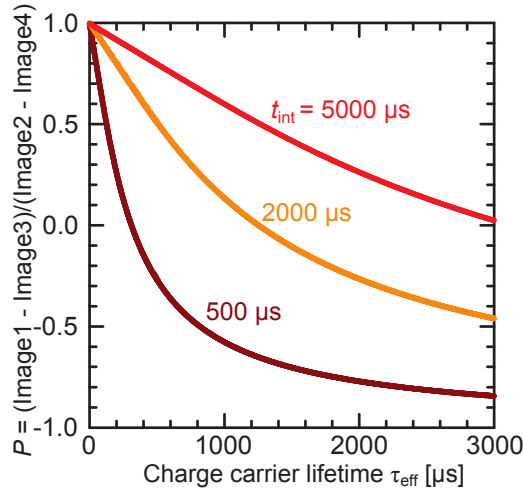


**Figure 3.15:** Ratio  $P$  from Eq. (3.24) as a function of the carrier lifetime  $\tau_{\text{eff}}$  for different camera integration times  $t_{\text{int}}$ .

ratio of four images (including one dark image) instead of just two images is required. However, it has generally proven to be advantageous using four instead of two images since the impact of an injection-dependent lifetime on the dynamic lifetime evaluation is strongly reduced as demonstrated in Ref. [110] for ILM measurements and in Section 3.3.4 of this work for PL measurements.

### 3.3.2 Application of dynamic PL imaging

In order to demonstrate the applicability of the dynamic PL imaging technique, we investigate a  $10 \times 10 \text{ cm}^2$   $1.5 \text{ } \Omega\text{cm}$   $\text{SiN}_x$ -passivated  $p$ -type mc-Si wafer with a thickness of  $211 \text{ } \mu\text{m}$ . Figure 3.26 (a) [Section 3.4] shows a dynamic PL image of the investigated wafer at an illumination intensity of 0.5 suns ( $\sim 34 \text{ mW/cm}^2$ ). The total measurement time is 32 s (8 s per image) for a modulation frequency of 25 Hz and 200 measurement periods for each image. The camera integration time for the single PL image is set at  $t_{\text{int}} = 1 \text{ ms}$ . For comparison, the carrier lifetime of the same wafer is measured using the light-biased MW-PCD technique at a bias light intensity of 0.5 suns. The total acquisition time for the MW-PCD lifetime mapping is 90 min for a step width of  $250 \text{ } \mu\text{m}$ . The result of this measurement is shown in Fig. 3.26 (c).

Comparing both measurements by linescans, a good agreement in the regions of high lifetimes and deviations in regions of lower lifetimes are observed [see Fig. 3.27]. The increased lifetimes determined in the low-lifetime regions of the dynamic PL measurement are expected to result from carrier diffusion and internal reflection of luminescence photons from regions of strong to regions of low PL emission. Ramspeck et al. [110] observed a similar behavior for their dynamic ILM measurements and called the effect blurring. They proposed that blurring has a stronger impact on the dynamic evaluation than on steady-state measurements. For that reason, Ramspeck

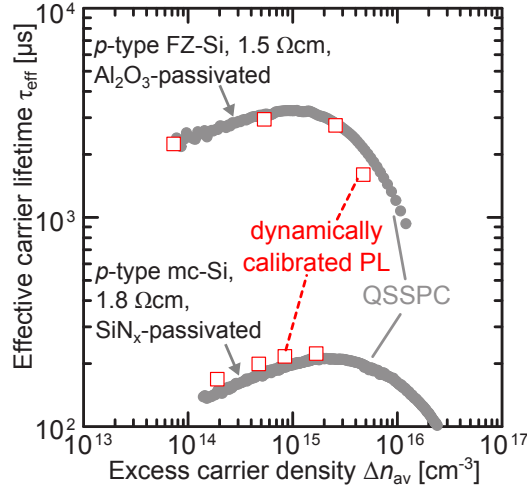


**Figure 3.16:** Injection-dependent effective lifetime  $\tau_{\text{eff}}$  measured with dynamic PL lifetime imaging (open squares) and QSSPC (gray circles) for a p-type  $\text{Al}_2\text{O}_3$ -passivated FZ-Si wafer and a p-type  $\text{SiN}_x$ -passivated mc-Si wafer.

et al. [110] suggested to calibrate the steady-state image (2nd image in Fig. 3.14) using the dynamic lifetime image in a weakly blurred high-lifetime region of the wafer. In Fig. 3.26 (b), the result of this dynamically calibrated steady-state lifetime image is shown. In Fig. 3.27, linescans of the three images are compared and a good quantitative agreement between the dynamically calibrated lifetime and the lifetime values from the MW-PCD lifetime mapping is obtained.

We have performed additional comparative measurements by using the QSSPC lifetime technique (see Section 1.3) for injection-dependent carrier lifetime measurements. A  $10 \times 10 \text{ cm}^2$   $\text{Al}_2\text{O}_3$ -passivated FZ-Si wafer and the mc-Si wafer shown in Fig. 3.26 are investigated. The results from the QSSPC measurement are presented in Fig. 3.16 together with data points extracted from dynamic PL lifetime images by averaging over the detection area ( $\sim 2.7 \text{ cm}^2$ ) of the QSSPC setup in the center of the wafer. To obtain the information of the excess carrier density  $\Delta n_{\text{av}} = \tau_{\text{eff}} G_{\text{av}}$  from the dynamic PL lifetime image, the information of wafer thickness and reflectivity of the wafer is required to calculate the average photogeneration rate  $G_{\text{av}}$  according to Eq. (2.38). Both lifetime techniques are in agreement.

### 3.3.3 Sensitivity analysis

The ratio  $P$  from Eq. (3.24) only depends on the carrier lifetime  $\tau_{\text{eff}}$  and the camera integration time  $t_{\text{int}}$ . Therefore, the integration time is an important parameter for the sensitivity of the dynamic PL lifetime technique. In this Section, the impact of the noise behavior of the InGaAs detector<sup>7</sup> on the lifetime determination with Eq. (3.24) is analyzed. A relative uncertainty  $\Delta\tau_{\text{eff}}/\tau_{\text{eff}}$  is calculated that reflects the dependence of  $P$  on  $\tau_{\text{eff}}$  and  $t_{\text{int}}$ .

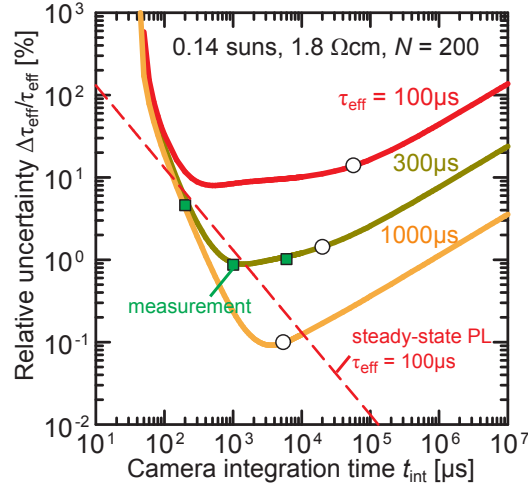
The expected PL signal for a fixed pair of  $\tau_{\text{eff}}$  and  $t_{\text{int}}$  is calculated for all four images using Eq. (3.22) and inserted into Eq. (3.23). A relative uncertainty  $\Delta\tau_{\text{eff}}/\tau_{\text{eff}}$  is calculated by determining the carrier lifetime from the PL signal ratio by taking the statistical error due to the noise behavior of the used detector into account. The noise of the InGaAs camera used in this work is analyzed [Section 2.2.3, Fig. 2.9] and yields a  $1/t_{\text{int}}$  dependence for the relative statistical uncertainty  $\Delta I_{\text{PL}}/I_{\text{PL}}$  in the investigated range ( $10^2 < t_{\text{int}} < 10^5 \mu\text{s}$ ).

Figure 3.17 shows the uncertainty in  $\tau_{\text{eff}}$  as a function of the camera integration time  $t_{\text{int}}$  for carrier lifetimes of 100, 300 and 1000  $\mu\text{s}$ . The assumed number of averages  $N$  for each image is 200. The photogeneration rate  $G_{\text{av}}$  is calculated for an illumination intensity of  $\sim 0.14$  suns ( $\sim 10 \text{ mW}/\text{cm}^2$ ) and a wafer thickness of 200  $\mu\text{m}$  and is the same for all three lifetimes. Hence, average excess carrier density and PL signal decrease with decreasing carrier lifetime. In contrast to the PC-PLI technique, an increasing camera integration time is not necessarily decreasing the relative uncertainty.

Importantly, a minimum in the relative uncertainty at each carrier lifetime is observed. For increasing ( $t_{\text{int}} > \tau_{\text{eff}}$ ) and decreasing ( $t_{\text{int}} < \tau_{\text{eff}}$ ) camera integration times, the uncertainty increases due to the decreasing difference between numerator and denominator in Eq. (3.23). The optimum camera integration time for each carrier lifetime for the modeled scenario is best chosen to be about three times larger as the effective carrier lifetime. This estimate is only valid for the specific detector noise considered for the simulation. For an mc-Si wafer with spatially distributed lifetime values, a compromise has to be accepted for the choice of the best suitable  $t_{\text{int}}$ . For the simulated scenario, lifetimes down to  $\tau_{\text{eff}} = 100 \mu\text{s}$  can be determined with an uncertainty  $< 10\%$  by choosing a camera integration time between 240 and 8000  $\mu\text{s}$ .

Then, the total measurement time is  $t_{\text{total}} = 32 \text{ s}$  (8 s per image). By increasing the number of averages  $N$  to 1000 ( $t_{\text{total}} = 160 \text{ s}$ ), an effective carrier lifetime of 50  $\mu\text{s}$  can be measured with a relative uncertainty of  $\sim 13\%$ . By additionally increasing the illumination intensity to 1 sun ( $\sim 70 \text{ mW}/\text{cm}^2$ ), an effective carrier lifetime of 20  $\mu\text{s}$  can be measured with a relative uncertainty of  $\sim 14\%$ . An improvement of the signal-noise-ratio for a given scenario (illumination intensity, effective lifetime) is only

<sup>7</sup>As pointed out before, the Si CCD detector used in this work is not suitable for the dynamic PLI approach (see Section 2.2.1 p. 37). For short camera integration times in the order of the charge carrier lifetime as required for the dynamic technique, the Si CCD images show a smearing of the pixel information to adjacent pixels.



**Figure 3.17:** Relative uncertainty  $\frac{\Delta\tau_{\text{eff}}}{\tau_{\text{eff}}}$  of the dynamic PL lifetime imaging technique for different carrier lifetimes  $\tau_{\text{eff}}$  as a function of the camera integration time  $t_{\text{int}}$ . The uncertainty is calculated at a constant photogeneration rate and 200 averages per image. The open circles mark the integration time which leads to a saturated detector. The dashed line shows the uncertainty of the steady-state PL measurement.

achieved by increasing the number of averages.

In order to reduce the impact of blurring, we have proposed above to calibrate the steady-state PL image with the dynamic PL lifetime image. The uncertainty of the steady-state measurement is plotted in Fig. 3.17 for an effective carrier lifetime of  $100 \mu\text{s}$  (dashed line). The noise-to-signal ratio is only limited by the noise behavior of the InGaAs detector and decreases with increasing  $t_{\text{int}}$ .

We have shown that for each carrier lifetime an optimal camera integration time exists for minimizing the uncertainty in the measured dynamic carrier lifetime. The optimal camera integration time is about three times the effective carrier lifetime if considering the specific noise behavior of the InGaAs detector used in this work.

### 3.3.4 Steady-state or dynamic lifetime?

A major assumption for the correct determination of a carrier lifetime from a time-dependent quantity proportional to the excess carrier density is the injection independence of the carrier lifetime. If the carrier lifetime varies with injection density, the time-dependent excess carrier density  $\Delta n(t)$  does not obey the simple mono-exponential relation as calculated in Section 2.1.4 [Eq. (2.20)]. As a consequence, it is expected that the carrier lifetime determined from a time-dependent signal proportional to  $\Delta n$  deviates from the steady-state carrier lifetime.

One way to reduce the impact of an injection-dependent lifetime is the narrowing of the evaluated injection range as e.g. for transient PCD measurements [35–37]. However, this cannot be applied to the dynamic PL lifetime analysis. Using the dynamic PLI approach, a large injection range is detected since the camera integration time is typically chosen larger than the effective carrier lifetime ( $t_{\text{int}} > \tau_{\text{eff}}$ ) [see Section 3.3.3 above].

Ramspeck et al. [110] investigated the impact of an injection-dependent lifetime on the dynamic ILM analysis. They concluded that the dynamic ILM lifetime evaluation is only slightly influenced by an injection-dependent lifetime with deviations below 30%. For their analysis, Ramspeck et al. assumed an injection dependence as it is typically observed in the presence of impurities in *p*-type Si (increasing carrier lifetime with increasing excess carrier density).

The reason for the small impact of a strong injection dependence is the consideration of not only the decay of the carrier density, as it is common for PCD measurements, but also the increase of the carrier density directly after switching on an excitation source. An injection-dependent lifetime would only influence the numerator of the image ratio  $P$  [Eq. (3.23)]. We conclude that the variation of the measured signal due to the injection dependence has to be equal for the first image (Image1) and the third image (Image3):

$$[\text{Image1} - \text{Image3}]_{\tau(\Delta n) = \tau_{\text{stst}}} = [\text{Image1} - \text{Image3}]_{\tau(\Delta n)} \quad (3.25)$$

to obtain the same ratio  $P$  as for the actual steady-state carrier lifetime  $\tau_{\text{stst}}$ .

In the following, the injection dependence typical for intrinsic Auger recombination at high injection densities (decreasing carrier lifetime with increasing excess carrier density) is considered for the dynamic lifetime evaluation. Additionally, special attention is paid to the impact of the chosen camera integration time.

Figure 3.18 (a) shows an injection-dependent carrier lifetime that is only limited by intrinsic recombination processes<sup>8</sup>. The time-dependent excess carrier density  $\Delta n(t)$  is numerically calculated for a square-wave-shaped generation rate  $G(t)$  under consideration of the injection-dependent carrier lifetime  $\tau(\Delta n)$ . Then, a dynamic lifetime

<sup>8</sup>The Auger recombination is calculated using Eq. (1.12) and the radiative recombination is calculated using Eqs. (1.5) and (2.12)

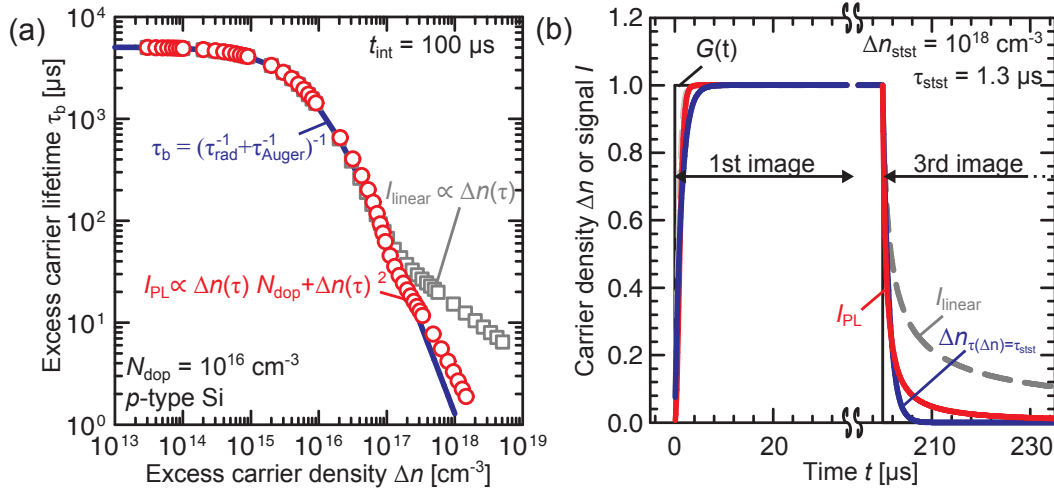


**Figure 3.18:** (a) Calculated injection-dependent bulk carrier lifetime  $\tau_b(\Delta n)$  of a p-type Si wafer limited only by radiative and Auger recombination (blue line). The open symbols show the  $\tau_b(\Delta n)$  as obtained with the dynamic approach for a camera integration time of  $100 \mu\text{s}$ . The gray squares were calculated assuming a linear relationship between signal and excess carrier density. The red circles show the dynamic lifetime results if using the PL signal as a measure for the excess carrier density. (b) Time-dependent signal  $I$  for a modulated generation rate  $G(t)$  and an injection-dependent carrier lifetime as shown in (a) for a steady-state excess carrier density of  $\Delta n_{\text{stst}} = 10^{18} \text{ cm}^{-3}$  and a steady-state carrier lifetime of  $\sim 1.3 \mu\text{s}$ . The blue line shows the time-dependent excess carrier density  $\Delta n_{\tau(\Delta n)=\tau_{\text{stst}}}$  for an injection-independent lifetime ( $\tau_{\text{stst}}$ ).

evaluation is simulated by integrating the expected signals over the camera integration time for the three signal images that are required for the dynamic lifetime technique [Image1, Image2, and Image3 of Eq. (3.23)] (at first for a fixed camera integration time of  $t_{\text{int}} = 100 \mu\text{s}$ ). Two scenarios are chosen, (i) a signal  $I_{\text{linear}}$  proportional to  $\Delta n$  as for ILM measurements and (ii) a PL signal with  $I_{\text{PL}} \propto N_{\text{dop}}\Delta n + \Delta n^2$ .

The modeled dynamic lifetimes are shown in Fig. 3.18 (open symbols) and reveal that the dynamic and the actual lifetime differ only considerably for excess carrier densities above  $10^{17} \text{ cm}^{-3}$ . However, due to the small lifetimes for  $\Delta n > 10^{17} \text{ cm}^{-3}$ , very high illumination intensities of more than 100 suns are required to achieve the high injection densities. Hence, for realistic measurement conditions with illumination intensities below 100 suns, the impact of the injection-dependent lifetime is negligible for a camera integration time of  $100 \mu\text{s}$ .

Nevertheless, Fig. 3.18 (b) demonstrates the reason for the deviation between the actual and the dynamic lifetime above an injection density of  $10^{17} \text{ cm}^{-3}$ . As pointed out before, the impact of an injection-dependent lifetime on the PL signal of Image1 and Image3 has to be the same to measure the actual steady-state carrier lifetime with the dynamic approach [Eq. (3.25)]. Figure 3.18 (b) shows  $\Delta n(t)$  for the injection-dependent lifetime of Fig. 3.18 (a) for a steady-state excess carrier density of  $\Delta n_{\text{stst}} = 10^{18} \text{ cm}^{-3}$  and a steady-state carrier lifetime of  $\sim 1.3 \mu\text{s}$ . If we compare the areas below the signal curves  $I_{\text{linear}}(t)$  and  $I_{\text{PL}}(t)$  with  $\Delta n_{\tau(\Delta n)=\tau_{\text{stst}}}(t)$ , we see that Eq. (3.25) is

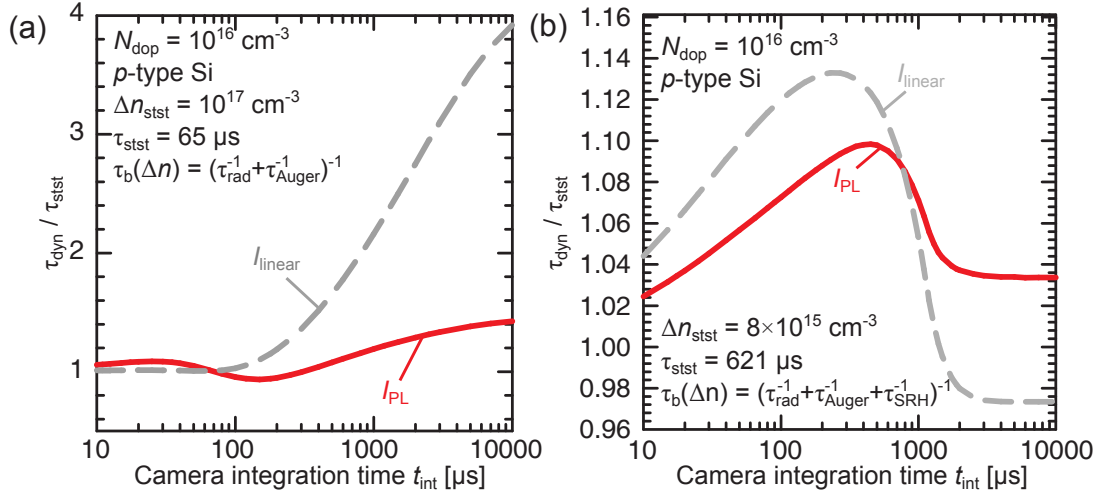


**Figure 3.19:** Relation between the dynamic carrier lifetime  $\tau_{\text{dyn}}$  and the actual steady-state carrier lifetime  $\tau_{\text{stst}}$  as a function of the camera integration time  $t_{\text{int}}$  for different injection-dependent carrier lifetimes. (a) Auger and radiative recombination are assumed for the modeled dynamic carrier lifetime as in Fig. 3.18 (a). (b) SRH recombination limits the carrier lifetime used for modeling the dynamic lifetime as a function of  $t_{\text{int}}$  (defect concentration  $[N] = 10^{11} \text{ cm}^{-3}$ , energy level  $E_{\text{defect}} = E_C + E_g/2$ , capture cross section electrons  $\sigma_n = 4 \times 10^{-14} \text{ cm}^2$ , asymmetry factor  $k = 100$  (see Section 1.1.1)).

not fulfilled.

For the third image, the area below the signal curve  $I_{\text{linear}}$  is strongly increased due to the injection-dependent lifetime whereas for the first image, the injection-dependent lifetime has only a small impact. The third image is strongly influenced by the large carrier lifetimes at low injection conditions [see Fig. 3.18 (a)]. The impact of the large carrier lifetimes at low injection densities is smaller for the first image of the dynamic evaluation (Image1) due to the varying slope of the exponential function describing  $\Delta n(t)$  [Eq. (2.20)]. This slope is large in the beginning of the exponential function and small in the range close to the steady-state signal [close to zero for the decreasing  $\Delta n(t)$ ].

We found that the impact of the injection dependent lifetime is smaller for the quadratic relation between signal and excess carrier density. In that case, the difference between Image1 and Image3 is normalized to a much higher signal at high-level injection ( $\propto \Delta n_{\text{stst}} N_{\text{dop}} + \Delta n_{\text{stst}}^2$  instead of  $\propto \Delta n_{\text{stst}} N_{\text{dop}}$ ). Thus, the normalization reduces the impact of the injection-dependent lifetime on the time-dependent signal  $I(t)$ .

Using a constant bias light during the dynamic PL image acquisition would suppress the strong impact of the long lifetimes at low injection densities for the signal of the third image of the dynamic evaluation for the example in Fig. 3.18. As a result the difference between dynamic and actual lifetime would be reduced. Another approach for minimizing the impact of an injection-dependent carrier lifetime is the appropriate choice of the detection interval i.e. the camera integration time.

Figure 3.19 (a) shows the deviation of the dynamic lifetime from the actual steady-state carrier lifetime as a function of the camera integration time  $t_{\text{int}}$  for the case of an Auger recombination limited lifetime. The ratio of the dynamic to the actual lifetime increases with increasing camera integration time since the impact of the high carrier lifetimes at low injection increases [see Fig. 3.18 (b)].

Figure 3.19 (b) shows the difference between the dynamic and the actual lifetimes for an injection-dependent carrier lifetime that increases with increasing injection density [calculated using the Shockley-Read-Hall Eq. (1.16)]. Similar to the simulations of Ramspeck et al. [110] for dynamic ILM measurements, we found only a minor impact [deviations below  $< 10\%$  for the calculated  $\tau(\Delta n)$ ] on the determination of the actual steady-state carrier lifetime with dynamic lifetime imaging.

In summary, the impact of an injection-dependent carrier lifetime is only significant for very high excess carrier densities and large camera integration times. By an appropriate choice of the camera integration time, the deviation between the measured dynamic lifetime and the actual steady-state lifetime can be significantly reduced. Importantly, we found that for the quadratic dependence of the PL signal on the excess carrier density, the impact of an injection-dependent lifetime is much smaller than for the linear dependence of the ILM signal to the excess carrier density. Further advantages of PL measurements over ILM measurements are: (a) PL measurements are weakly influenced by measurement artifacts such as trapping or depletion region modulation [84] (see Sections 1.3.2 and 3.1.2) and (b) they can be easily performed at room temperature.

### 3.3.5 Application of the dynamic PL lifetime technique to multicrystalline silicon bricks

The advantage of investigating a Si brick over measuring as-cut wafers is the smaller influence of the surface recombination on the effective lifetime. In Fig. 3.1, we demonstrate the high sensitivity of the measured signal to the bulk carrier lifetime despite the recombination at the surfaces if using a photoluminescence setup for measuring a quantity proportional to the excess carrier density.

In 2009, Trupke et al. [74] calibrated the PL signal of a Si brick with a photoconductance measurement. In contrast to the PC-PLI technique presented in Section 3.2 a different PC setup is required with illumination and detection from the same side of the brick. In addition, the PL signal has to be corrected for the typical height-dependent variations of the doping density since the PL signal depends on the doping concentration [Eq. (3.22)]. In 2010, Trupke et al. demonstrated the applicability of the “two-filter method” of Würfel et al. [31] (see p. 12) to Si bricks.

In this Section, the dynamic PL technique is adapted for the investigation of Si bricks. It is demonstrated that the exact knowledge of the surface recombination velocity or the thickness of the sample is not required for the determination of the bulk carrier lifetime of thick Si samples. Additionally, the sensitivity of the dynamic PL technique is analyzed with respect to the information depth.

#### Calculation of the ratio $P$ for thick samples with finite surface recombination

For the evaluation of the time-dependent PL signal of a silicon brick with recombination at the surfaces, we solve the time- and position-dependent diffusion equation to obtain  $\Delta n(z, t)$  [Eq. (2.30)]. For the dynamic PLI technique, a ratio of four PL images acquired at different times during a square-wave-shaped excitation [Eq. (3.23)] has to be calculated.

Since the PL signal  $I_{\text{PL}}$  is proportional to the product of the doping density and excess carrier density for low-level injection conditions  $I_{\text{PL}} \propto \Delta n N_{\text{dop}}$ , the ratio  $P$  is obtained by integration of  $\Delta n(t)$  [Eq. (2.30)] over the camera integration time  $t_{\text{int}}$ . Thus, for a square-wave-shaped excitation source [Eq. (2.19)],  $P$  is found to be:

$$\begin{aligned}
 P &= \frac{\text{Image1} - \text{Image3}}{\text{Image2} - \text{Image4}} = \frac{\int_0^{t_{\text{int}}} \Delta n(t) dt - \int_{T/2}^{T/2+t_{\text{int}}} \Delta n(t) dt}{\int_{t_{\text{stst}}}^{t_{\text{stst}}+t_{\text{int}}} \Delta n(t) dt} \\
 &= \frac{\sum_k H_k t_k t_{\text{int}} - 2 \sum_k H_k t_k^2 + 2 \sum_k H_k t_k^2 \exp(-t_{\text{int}}/t_k)}{\sum_k H_k t_k t_{\text{int}}}, \quad (3.26)
 \end{aligned}$$

with the  $t_k$ 's being the decay time constants of  $\Delta n(t)$  [Eq. (2.30)]. The  $H_k$ 's summarize all terms which are independent of time or bulk lifetime and are known as the amplitudes of the modes describing the time-dependent excess carrier density.

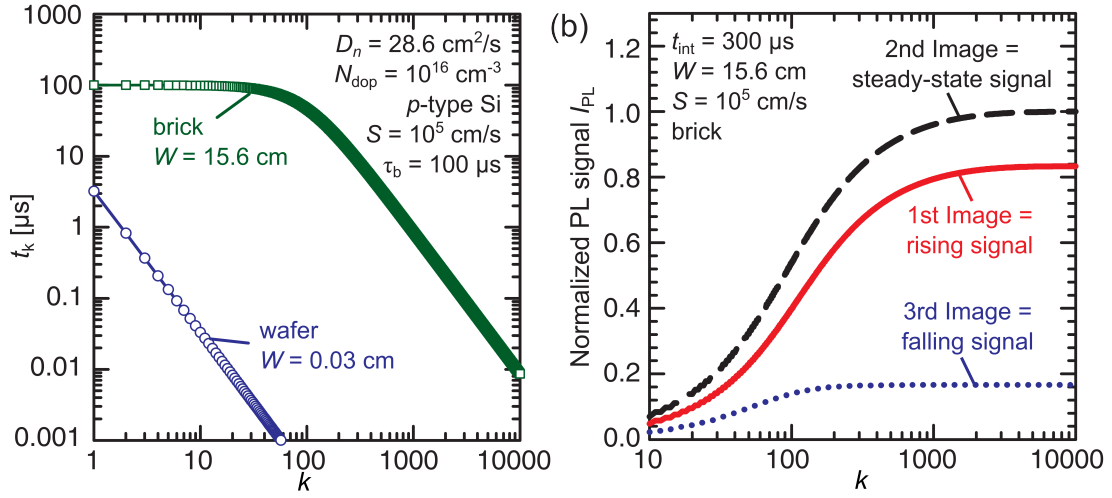


**Figure 3.20:** (a) The time constants  $t_k$  as a function of the numerator  $k$  for an unpassivated Si brick with a thickness of 15.6 cm and an unpassivated Si wafer with a thickness of 300 μm. The surface recombination velocity of both samples is assumed to be  $S = 10^5$  cm/s. (b) Integrated PL signal as a function of the numerator  $k$  for the three images of the dynamic PL evaluation for the thick unpassivated Si brick.

Fortunately, the dependence of the doping density cancels out in Eq. (3.26) since the ratio of PL images is evaluated. The assumption of low-level injection is valid since high-level injection conditions are hardly reached due to the spreading of the charge carriers into the brick and the high recombination at the front surface.

The decay time constants  $t_k$ 's [Eq. (2.28)] are a function of the bulk lifetime  $\tau_b$ , the sample thickness  $W$ , the diffusion coefficient of the minority carriers  $D_n$  and of the surface recombination velocity  $S$ :

$$t_k = \left( \frac{1}{\tau_b} + a_k D_n \right)^{-1} \quad \text{with} \quad a_k = \frac{2}{W} \arctan\left(\frac{S}{D_n a_k}\right) + k \frac{\pi}{W}. \quad (3.27)$$

In general, the transcendental equation for the  $a_k$ 's in Eq. (3.27) has to be solved numerically or graphically. However, for large values of the surface recombination velocity, the arctangent in Eq. (3.27) equals  $\pi/2$  and allows an algebraic expression for the determination of the modes  $t_k$ :

$$t_k = \left( \frac{1}{\tau_b} + \frac{\pi^2}{W^2} (1+k)^2 D_n \right)^{-1}. \quad (3.28)$$

Equation (3.28) is valid if  $S$  and  $D_n$  are chosen to fulfill  $\arctan(S/(D_n a_k)) = \pi/2$  and the value of  $W$  still leads to a result of  $a_k$  that fits the condition of a large argument of the arctangent. Therefore, Eq. (3.28) can be used with an accuracy of 99% for the  $t_k$ 's if:

$$\frac{SW}{D_n(1+k)} > 70\pi. \quad (3.29)$$

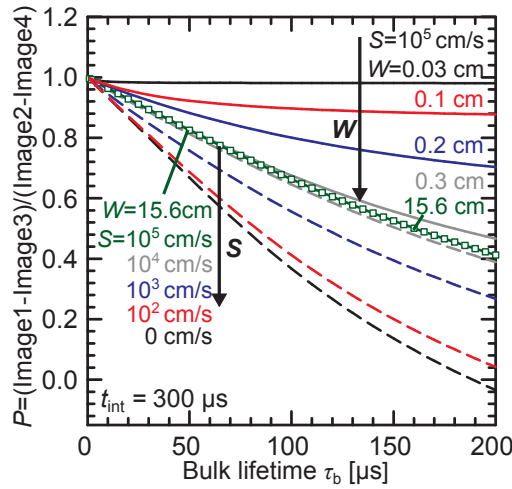


**Figure 3.21:** Ratio  $P$  from Eq. (3.26) as a function of the bulk lifetime  $\tau_b$  for unpassivated samples ( $S = 10^5$  cm/s) with different thicknesses  $W$  (solid lines) and for a Si brick ( $W = 15.6$  cm) with different surface recombination velocities  $S$  (dashed lines). The open symbols present the ratio  $P$  for a brick with  $W = 15.6$  cm and  $S = 10^5$  cm/s.

For a passivated wafer (e.g.  $W = 300$   $\mu\text{m}$ ) with a low surface recombination velocity (e.g.  $S \sim 10$  cm/s), the first mode  $t_{k=0}$  is close to the bulk lifetime and higher order modes ( $k > 0$ ) decay much faster than  $t_{k=0}$ . Therefore, their contribution to the time dependence of the excess carrier concentration  $\Delta n(t)$  is negligible. The same holds for thin wafers with a high surface recombination velocity [111, 112]. In general, the thinner the wafer, the faster the decay curve approaches the shape described solely by the principal mode with  $k = 0$  [112]. If the time-dependent  $\Delta n(t)$  is only determined by the principal mode, Eq. (3.26) can be transformed into Eq. (3.24) with  $t_{k=0} = \tau_{\text{eff}}$  since the term  $H_{k=0}t_{k=0}$  cancels out.

However, for a brick with a thickness well above that of a typical wafer ( $W > 1$  mm), the higher modes have a considerable impact on  $\Delta n(t)$ . Figure 3.20 (a) shows the time constants  $t_k$  as a function of the numerator  $k$  for an unpassivated brick and wafer.

For a typical mc-Si brick with  $W = 15.6$  cm and  $S = 10^5$  cm/s, Eq. (3.29) is fulfilled and the decay time constants  $t_k$  are easily calculated and inserted in Eq. (3.26). In Fig. 3.20 (b), we demonstrate the impact of the modes on the integrated signal as a function of the numerator  $k$ . From Fig. 3.20 (b), we found that  $\sim 5000$  modes have a considerable impact on the time-dependent  $\Delta n(t)$ . Thus, 5000 modes are considered for the calculation of the ratio  $P$  for an unpassivated brick with  $W = 15.6$  cm and  $S = 10^5$  cm/s.

Figure 3.14 shows additionally to the passivated sample ( $S = 0$  cm/s) the time-dependent excess carrier concentration  $\Delta n(t)$  for an unpassivated brick ( $S = 10^5$  cm/s) with a typical thickness of 15.6 cm. In comparison to  $\Delta n(t)$  for the passivated sample, it is visible that  $\Delta n(t)$  of the brick is only minor influenced by the surface recombination at the front side.

In Fig. 3.21, the ratio  $P$  is evaluated with respect to the bulk lifetime as a function of the sample thickness  $W$ , assuming a Si sample with unpassivated surfaces ( $S = 10^5$  cm/s). Additionally, the ratio  $P$  is analyzed for different surface recombination velocities. As can be seen in Fig. 3.21, the ratio  $P$  is virtually independent of the thickness  $W$  for values larger than  $\sim 0.3$  cm in the lifetime range shown. Furthermore, it can be concluded that the exact knowledge of the surface recombination velocity is not required for an unpassivated brick if the surface recombination velocity is larger than  $S \approx 10^4$  cm/s. The ratio  $P$  shows also no dependence on the diffusion coefficient  $D_n$  [not shown].

Since an mc-Si brick has typically a thickness larger than 0.3 cm and a surface recombination velocity larger than  $10^4$  cm/s, the dynamic PL lifetime evaluation is well suited for the investigation of Si bricks.

### Calculation of the ratio $P$ for a real light source with non-instantaneous switching characteristics

For a real light source with non-instantaneous switching characteristics, Eq. (2.29) has to be calculated for the time-dependent photogeneration rate

$$G(t) = \begin{cases} G_0 \exp(-t/\tau_{\text{rise}}) & \text{if } 0 < t < T/2, \\ G_0 [1 - \exp(-(t - T/2)/\tau_{\text{fall}})] & \text{if } T/2 < t < T, \end{cases} \quad (3.30)$$

with the time constant  $\tau_{\text{rise}}$  that describes the switch-on behavior of the excitation source, and with the time constant  $\tau_{\text{fall}}$  that characterizes the switch-off behavior. The time-dependent excess carrier density is calculated from the pulse solution  $\Delta n_{\text{puls,av}}$  [Eq. (2.27)] by convolution using Eq. (2.29). For  $0 < t < T/2$ , the solution is

$$\Delta n(t) = \sum_k H_k t_k \left[ (1 - \exp(-t/t_k)) + \frac{\tau_{\text{rise}}}{\tau_{\text{rise}} - t_k} [\exp(-t/t_k) - \exp(-t/\tau_{\text{rise}})] \right]. \quad (3.31)$$

For the specific case that  $t_k = \tau_{\text{rise}}$ , the solution becomes

$$\Delta n(t) = \sum_k H_k [t_k - t_k \exp(-t/t_k) - t \exp(-t/t_k)]. \quad (3.32)$$

For  $T/2 < t < T$ , the solution is

$$\Delta n(t) = \sum_k H_k t_k \exp(-(t - T/2)/t_k) - \sum_k H_k t_k \frac{\tau_{\text{fall}}}{\tau_{\text{fall}} - t_k} [\exp(-(t - T/2)/t_k) - \exp(-(t - T/2)/\tau_{\text{fall}})]. \quad (3.33)$$

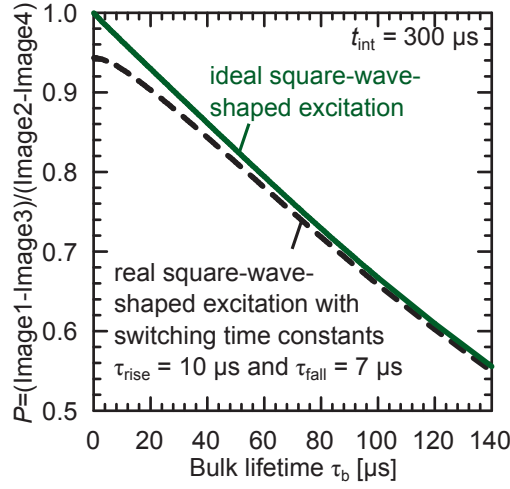


**Figure 3.22:** Ratio  $P$  from Eq. (3.26) as a function of the bulk lifetime  $\tau_b$  for an ideal light source with instantaneous switching characteristics (green solid line) and for a real light source with the switching time constants (black dashed line)  $\tau_{rise}$  and  $\tau_{fall}$  [see Eq. (3.30)].

For the case that  $t_k = \tau_{fall}$ , the solution is found to be

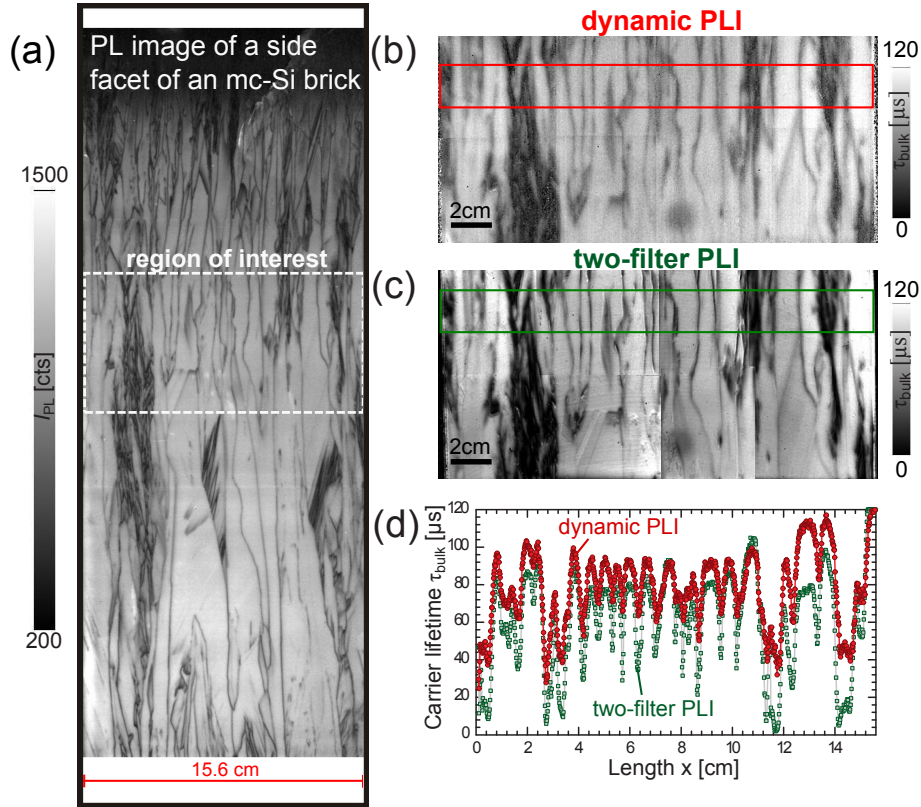
$$\Delta n(t) = \sum_k H_k [t_k \exp(-(t - T/2)/t_k) + t \exp(-(t - T/2)/t_k)]. \quad (3.34)$$

Figure 3.22 demonstrates the impact of the real switching characteristics on the image ratio  $P$  as a function of the bulk lifetime. We used for the calculation of  $P$  [Eq. (3.26)] the solutions Eqs. (3.31) to (3.34) and the switching time constants of the high power diode laser that is used for the dynamic PL lifetime imaging of the Si brick (see next Section). If the switching characteristics are not considered, the measured dynamic lifetime will be overestimated for lifetimes below and in the order of the switching time constants.

### Experimental verification

The applicability of the dynamic PL approach for the investigation of Si bricks is demonstrated by determining the bulk lifetime of a typical mc-Si brick with a thickness of 15.6 cm and polished surfaces. In Fig. 3.23 (a), a PL image from one side facet of an mc-Si brick is shown in digital units of the camera [counts/s]. Since the PL setup used in this work (Section 2.2.2) was not designed for measuring Si bricks, the PL information from the upper and lower edge is missing.

The excess carriers in the brick are generated by a high power diode laser with a central wavelength of  $\lambda_{exc} = 805$  nm. For a sufficiently high PL signal of the Si brick, the illumination intensity was increased to  $\sim 30$  suns ( $\sim 2$  W/cm<sup>2</sup>) by decreasing the illumination area to  $\sim 4.5 \times 4.5$  cm<sup>2</sup>. The average excess carrier density in unpassivated Si bricks is typically not a function of the lifetime anymore if the diffusion length  $L$  is



**Figure 3.23:** (a) PL image of a side facet of an mc-Si brick in relative units of the camera. Since the PL setup used in this work was not especially designed for measuring Si bricks, the PL information from the upper and lower edge is missing. (b) Dynamic PL lifetime image of a section of the side facet from (a). The brick was illuminated with an intensity of  $\sim 30$  suns ( $\sim 2 \text{ W/cm}^2$ ). A camera integration time for the single image of  $300 \mu\text{s}$  was used and 5000 images were averaged. (c) Lifetime image from the two-filter technique [34] for the same excitation conditions as the dynamic PLI measurement of (b). (d) Comparison of dynamic PLI and two-filter PLI by a linescan, averaged over the pixel rows of the areas marked in (b) and (c) with a red and green square.

much larger than the absorption length of the exciting photons  $L_a \ll L$  [Eq. (2.36)]. Since the absorption length for a wavelength of 805 nm is only  $L_a \approx 12 \mu\text{m}$ , the average carrier density is estimated from Eq. (2.36) to be  $\Delta n_{av} \sim 10^{14} \text{ cm}^{-3}$  for steady-state conditions of the presented measurement. The period of the square-wave-shaped modulation was set at  $T = 40 \text{ ms}$  and the camera integration time was chosen to be  $t_{int} = 300 \mu\text{s}$ . We acquired eight dynamic PL lifetime images from different positions of the Si brick with a resolution of  $\sim 280 \mu\text{m}$  per pixel. Figure 3.23 (b) shows the dynamic PL lifetime image that is the result of merging the eight measured images. The merged image displays an area of the brick side facet that has a size of  $15.6 \times 8.6 \text{ cm}^2$ .

For comparison, we applied the two-filter technique of Trupke et al. [34] to the same area. We found a pronounced sensitivity of the PL signal ratio to the bulk lifetime if using a short-pass filter with an edge wavelength of 1030 nm and a long-pass filter

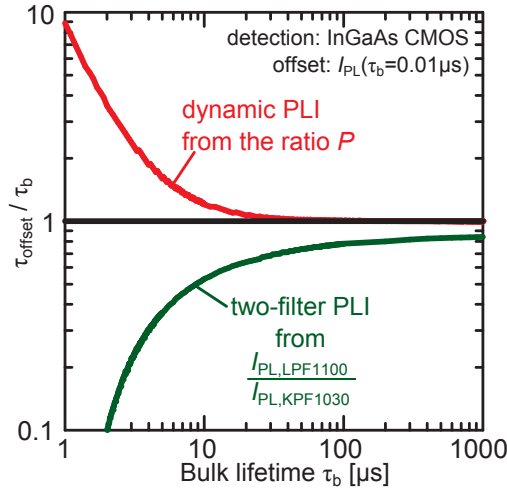


**Figure 3.24:** Impact of a PL signal offset (e.g. due to the unintended detection of stray light or blurring in the low-lifetime regions) on the measured carrier lifetime  $\tau_{offset}$  for the dynamic PLI technique and for the two-filter technique [34]. The PL signal offset is equivalent to the PL signal for a carrier lifetime  $0.01 \mu\text{s}$ .

with an edge wavelength of 1100 nm. Figure 3.23 (c) shows the result of the two-filter approach that is obtained by comparing the experimentally acquired image ratio (dividing the images obtained with the two edge filters) with a calculated loop-up table.

For a better quantitative comparison of the two lifetime techniques, a linescan from both images is shown in Fig. 3.23 (d), averaged over the pixel rows marked in Figs. 3.23 (b) and 3.23 (c) with a red and green square. With the two-filter technique, we obtain slightly lower values compared to the dynamic PLI lifetime image.

We exclude the impact of blurring [110] as possible explanation for the deviation of the two lifetime images since the steady-state PL image (not shown) exhibits the same dynamic range as the dynamic lifetime image. Since blurring is expected to have a much stronger impact on the dynamic evaluation than on the steady-state measurement [110], a difference between the signal distributions of the steady-state image compared to the dynamic lifetime image is expected.

Figure 3.24 demonstrates the impact of a PL signal offset due to the unintended detection of stray light or blurring in the low-lifetime regions. The dynamic lifetime and the two-filter lifetime are modeled under consideration of an additional offset with respect to the actual bulk lifetime:  $\tau_{offset}/\tau_b$ . As offset, the PL signal corresponding to a carrier lifetime of  $\tau_b = 0.01 \mu\text{s}$  is chosen. The first thing to notice is the opposite direction of  $\tau_{offset}/\tau_b$  for both lifetime techniques in the presence of unintended offset light. Secondly, the strong impact on the two-filter technique even for higher carrier lifetimes is clearly visible. Hence, unintentional detected stray light may be responsible for the measured deviations between the dynamic PLI lifetime and the two-filter lifetime.

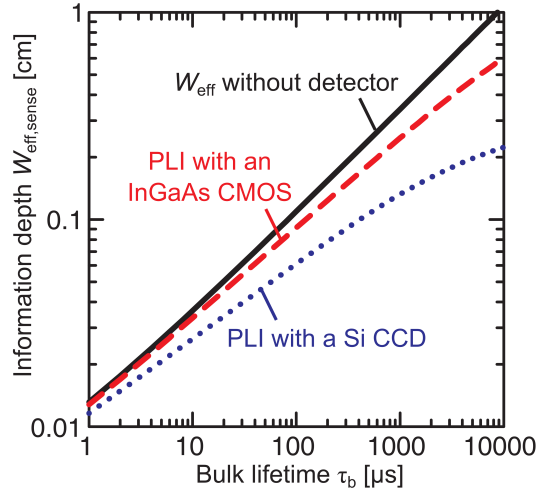


**Figure 3.25:** Effective thickness  $W_{\text{eff}}$  as a function of the bulk lifetime  $\tau_b$ , with and without consideration of the sense depth  $z_{\text{sense}}$  of a PLI setup using an InGaAs CMOS or a Si CCD detector, an excitation wavelength of  $\lambda_{\text{exc}} = 805 \text{ nm}$  for an unpassivated brick with  $W = 15.6 \text{ cm}$ ,  $S = 10^5 \text{ cm}^2/\text{s}$ ,  $D_n = 28.6 \text{ cm}^2/\text{s}$ .

The reason for the smaller impact of offset light on the dynamic PLI technique is the cancellation of the additional offset for the numerator of the ratio  $P$  [see Eq. (3.26)]. Whereas for the ratio of the two PL signals, obtained with the two different edge filters, both contributing signals (numerator and denominator) are influenced by the additional offset signal. Especially for our experimental setup with the InGaAs detector and the two chosen edge filters, we measure a large ratio if comparing the signals obtained with the two edge filters. As a consequence, a small offset can already have a massive effect.

### Information depth of the dynamic PL technique on Si bricks

If investigating a thick Si brick, one question of interest is concerning the accessible information depth of the chosen lifetime technique. The depth-dependent sensitivity  $f_{\text{sense}}$  of the used PL setup was shown to be of exponential form with the characteristic depth  $z_{\text{sense}}$  (Si CCD:  $z_{\text{sense}} = 0.45 \text{ mm}$ , InGaAs CMOS:  $z_{\text{sense}} = 4.5 \text{ mm}$ , see Fig. 2.10). However, the actual information depth of the PL lifetime measurement is not only a function of the sensitivity of the used detector but also of the depth distribution of the excess carriers. The latter one is determined by the lifetime of the carriers, their diffusivity and by the excitation wavelength of the used setup.

The depth-dependent carrier distribution can be linked with  $z_{\text{sense}}$  by calculating an effective thickness [Eq. (2.35)] but considering additionally  $f_{\text{sense}}(z)$  as recently done for QSSPC measurements [82]. The effective thickness  $W_{\text{eff,sense}}$  is calculated by weighting the excess carrier density with the depth-dependent sensitivity of the used

setup [73, 82]:

$$W_{\text{eff,sense}} = \frac{[\int \Delta n(z) f_{\text{sense}}(z) dz]^2}{\int [\Delta n(z) f_{\text{sense}}(z)]^2 dz}. \quad (3.35)$$

Considering the general sensitivity of the PL setup for the calculation of the effective thickness yields a quantity that can be regarded as the information depth of the PL measurement. Figure 3.25 shows the effective thickness  $W_{\text{eff,sense}}$  as a function of the bulk lifetime  $\tau_b$  if using a Si CCD or an InGaAs CMOS detector. Additionally, the detector-independent effective thickness [Eq. (2.35)] is calculated (black line).

For a bulk lifetime below 100  $\mu\text{s}$ , the actual information depth is below 1 mm (for  $D_n = 28.6 \text{ cm}^2/\text{s}$ ,  $\lambda_{\text{exc}} = 805 \text{ nm}$  and  $S = 10^5 \text{ cm/s}$ ). From Fig. 3.25, it can be concluded that the information depth is only weakly limited by the detector sensitivity for  $\tau_b < 100 \mu\text{s}$  if using an InGaAs CMOS detector for the lifetime measurement. The information depth is rather limited by the excitation conditions and the bulk quality of the Si brick.

## Summary

The applicability of the dynamic PLI lifetime technique to Si bricks is demonstrated. An analytical expression for the ratio  $P$  is derived under consideration of the impact of surface recombination, allowing the determination of the bulk lifetime for thick Si bricks. From simulations with varying surface recombination velocities  $S$  and for different thicknesses  $W$  of the sample, it can be concluded that the exact knowledge of both parameters is not required for the application of the dynamic PLI technique to Si bricks if  $S > 10^4 \text{ cm/s}$  and  $W > 0.3 \text{ cm}$ . Since the ratio of PL images is analyzed, the dynamic PLI lifetime technique is independent of the doping density at low-level injection conditions and therefore well suited for the investigation of Si bricks. Additionally, the accessible information depth of the PLI technique is analyzed and found to be limited by the excitation conditions and the bulk quality of the Si brick for bulk carrier lifetimes below  $\sim 100 \mu\text{s}$ .

## 3.4 Comparison of lifetime imaging techniques

In this Section, different lifetime techniques are compared by investigating a 1.5  $\Omega\text{cm}$   $\text{SiN}_x$ -passivated mc-Si wafer with a size of  $10 \times 10 \times 0.0211 \text{ cm}^3$ . The PC-PLI approach (Section 3.2) is performed using an InGaAs CMOS as well as a Si CCD camera. The obtained PC-PLI lifetime images are compared with results of the dynamic PLI (Section 3.3.2) and the dynamic infrared lifetime mapping (ILM)<sup>9</sup> technique [83]. Additionally, the lifetime measurements are compared to a light-biased microwave-detected photoconductance-decay (MW-PCD)<sup>10</sup> (Semilab, WT-2000) lifetime mapping [38] as well as to spatially integrated QSSPC (Section 1.3) and transient PCD<sup>11</sup> [35–37] measurements. The QSSPC and transient PCD measurements are performed with the WCT-100 from Sinton Consulting. The sample temperature is room temperature (298 K) or slightly higher (up to 303 K) except for the dynamic ILM technique (343 K).

Figure 3.26 shows a comparison of the results of the spatially resolved lifetime imaging techniques. For a better quantitative comparison linescans, marked in Fig. 3.26 (a) with a red line, are shown for all images in Fig. 3.27. A comparison of area-averaged injection-dependent carrier lifetime measurements is shown in Fig. 3.28. For the camera-based techniques, an arithmetic mean of the pixels is calculated over the area that displays the detection area of the PC measurements [marked in Fig. 3.26 (f) with a red circle].

### General image comparison

The lifetime images are qualitatively in good agreement. The dynamic PL (a), dynamic ILM (d) and the MW-PCD (c) lifetime images look more blurred than the steady-state images (b), (e), and (f). The dynamic lifetimes images are expected to look blurred due to the impact of carrier diffusion and internally reflected photons from adjacent regions that have a strong impact on the time-dependent dynamic analysis [110].

The MW-PCD lifetime mapping appear especially different in the border regions of high and low lifetime areas. We expect that the blurred edges originate from the point-by-point acquisition of the lifetime mapping (laser spot size  $\sim 1 \text{ mm}^2$ ). The step width is set at  $250 \mu\text{m}$  (similar to the spatial resolution of the camera-based approaches) but the detection area is supposed to be larger ( $\sim 1 \text{ cm}^2$  [113]). Thus,

<sup>9</sup>For the dynamic ILM technique, the square-wave-modulated (frequency 40 Hz) illumination source is an LED array with a central wavelength of 950 nm. The camera integration time for the single image is set at 400  $\mu\text{s}$ .

<sup>10</sup>For the MW-PCD technique, a laser with a central wavelength of 904 nm is used for the pulsed excitation (pulse length 200 ns). The white bias light is set at 0.5 suns. The microwave frequency is  $\sim 10.4 \text{ GHz}$ . The step width is set at  $250 \mu\text{m}$ .

<sup>11</sup>For the transient PCD measurements with the QSSPC setup, the decay time constant of the flash lamp is  $\sim 80 \mu\text{s}$ .

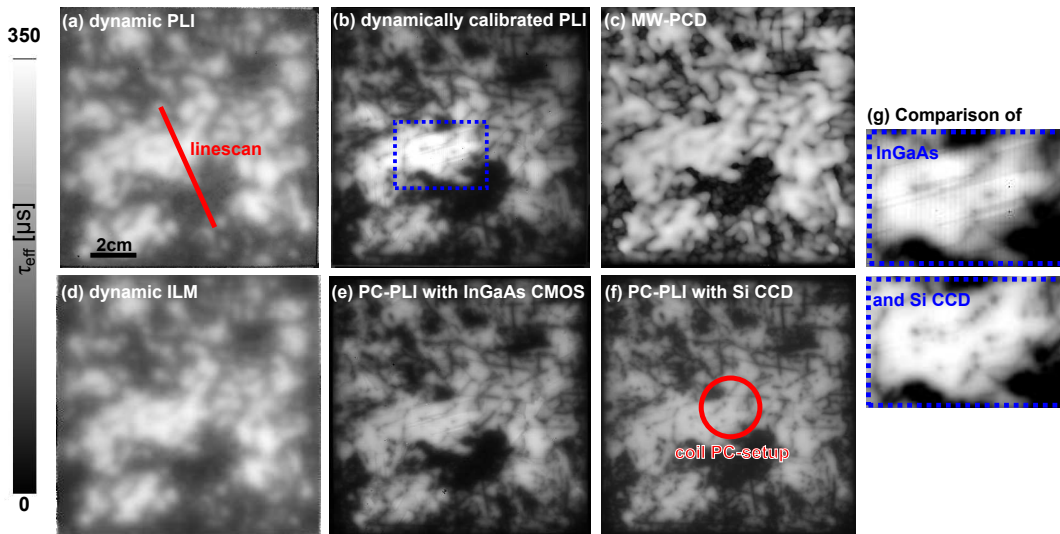


**Figure 3.26:** Comparison of different lifetime imaging techniques by investigating a  $\text{SiN}_x$ -passivated mc-Si wafer at an illumination intensity of 0.5 suns ( $\sim 34 \text{ mW/cm}^2$ ). All measurements were performed at room temperature except for the dynamic ILM measurement (at 343 K). (a) Dynamic PL lifetime image. (b) A steady-state PL image is calibrated using the dynamic PL image in a high-lifetime region. (c) MW-PCD lifetime mapping. (d) Dynamic ILM lifetime image, recorded at a sample temperature of 343 K. (e) PC-PLI lifetime image acquired with an InGaAs CMOS camera. (f) PC-PLI lifetime image acquired with a Si CCD camera. (g) Comparison of the lifetime distributions of a section in the middle of the wafer [blue rectangle in (b)] if using a Si CCD or an InGaAs detector (different scale).

the spatial resolution of the MW-PCD lifetime mapping is actually smaller than for the camera-based techniques.

The strongest deviation of measured lifetime values is visible for the dynamic PL and ILM lifetime images compared to the PC-PLI lifetime images and the MW-PCD lifetime mapping in the regions of low lifetimes. It is expected that carrier diffusion and internal reflections of luminescence photons are responsible for the overestimation of the carrier lifetime in these regions. Ramspeck et al. [110] suggested to use the dynamic lifetime in a region of high signal to calibrate the steady-state image. The result of such a dynamically calibrated PLI is shown in Fig. 3.26 (b). It is obvious that this image is in a much better agreement with the PC-PLI and MW-PCD lifetime distributions.

However, the steady-state lifetime image is stronger affected by sample inhomogeneities, e.g. different surface roughnesses of the various grains of the mc-Si wafer. This impact is visible e.g. for the region with the highest intensity in the middle of the wafer, marked with a blue rectangle. An enlarged image of this region with a different scale is shown in Fig. 3.26 (g) comparing the lifetime distributions if using a Si CCD camera or an InGaAs detector. The image obtained with the InGaAs camera reveals a sharp-edged structure that is not visible in the image acquired with the Si CCD camera. The region is imaged differently due to the different spectral sensitivities of

the detectors (see Fig. 2.5). The long-wavelength photons detected with the InGaAs detector travel longer distances in the Si wafer since they have a lower reabsorption probability. As a consequence, the probability of escaping photons far away from the generation position increases with increasing wavelength, enhancing the impact of optical artifacts as exemplified by the region shown in Fig. 3.26 (g).

### Comparison of PC-PLI using a Si CCD and an InGaAs CMOS camera

The area-averaged injection-dependent lifetimes are in agreement if comparing the PC-PLI measurement with the Si CCD and with the InGaAs CMOS camera in Fig. 3.28. Comparing the lifetime distributions of Figs. 3.26 and 3.27 yields a good agreement in the high lifetime regions. However, the PC-PLI lifetimes in the “dark” regions of the wafer (Fig. 3.26) are only half as large for the measurement performed with the InGaAs detector compared to the measurement with the Si CCD camera.

As can be derived from Fig. 3.9 (a), the impact of reabsorption on the PC-PLI calibration is expected to be below 10% in the measured lifetime range ( $\tau > 10 \mu\text{s}$ ) and thus, reabsorption cannot explain the difference by a factor of two. On the contrary, the impact of internal reflections (generated in a high-lifetime region but detected in the low-lifetime region) is expected to be higher for the InGaAs than for the Si CCD-detected lifetime measurement (due to the different spectral sensitivities of the detectors).

Another explanation for the observed difference might be the overestimation of the linear calibration factor for the measurement with the InGaAs detector due to the enhanced PL emission of the artifact-influenced bright region in the middle of the wafer ( $a_{\text{PL}} = I_{\text{PL}}/\Delta n$ ). In consequence of the overestimated  $a_{\text{PL}}$ , the excess carrier density is underestimated in the low-lifetime regions ( $\Delta n = I_{\text{PL}}/a_{\text{PL}}$ ).

### Comparison of dynamic PLI and dynamic ILM

The dynamic ILM and the dynamic PLI lifetime image show nearly the same result although recorded at different temperatures (dynamic ILM at  $\sim 70^\circ\text{C}$ , dynamic PLI at  $\sim 30^\circ\text{C}$ ).

Ramspeck [69, p. 180] expected a different impact of blurring for the PL and the ILM measurements due to the different spectral ranges of the detected signals [(4 - 5)  $\mu\text{m}$  for dynamic ILM and (0.9 - 1.3)  $\mu\text{m}$  for dynamic PLI]. Blurring is caused by the impact of regions with a high PL signal on regions with a low signal. The reason is given on the one hand by lateral diffusion of charge carriers from regions of low recombination activity to regions with a high recombination activity. On the other hand, luminescence photons that are generated in the high-signal region may reach the low-signal region due to internal reflections. In the latter case, three parameters are decisive for the blurring impact. The first one is the absorption length of the PL

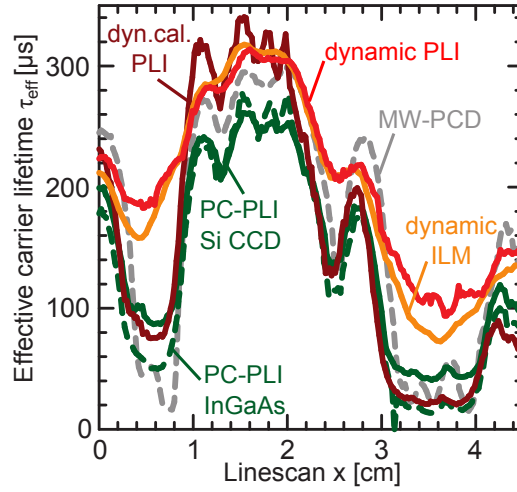


**Figure 3.27:** Comparison of linescans for all lifetime images of Fig. 3.26. The position of the linescan is marked by the red line in Fig. 3.26 (a).

photons, the second one is the surface roughness and the third one is the distance of the low signal to the high signal regions.

Interestingly, the absorption length for dynamic ILM and dynamic PL measurements is in the same order of magnitude if comparing the values for the peak wavelengths of the respective spectrum. For ILM measurements, the free carrier absorption coefficient<sup>12</sup> is considered for  $\lambda_{\text{ILM}} \approx 5 \mu\text{m}$ , yielding an absorption length of  $L_{\text{ILM}} \approx 1.5 \text{ cm}$  at an injection density of  $10^{14} \text{ cm}^{-3}$  down to  $L_{\text{ILM}} \approx 0.6 \text{ cm}$  for an injection density of  $10^{16} \text{ cm}^{-3}$  (for a  $1.5 \Omega\text{cm}$   $p$ -type Si wafer). The absorption length for the peak wavelength  $\lambda_{\text{peak}} \approx 1130 \text{ nm}$  of the band-to-band luminescence spectrum<sup>13</sup> (if detected with an InGaAs detector) is  $L_{\text{b2b}} \approx 0.7 \text{ cm}$ .

The similar ranges of the absorption length may explain the similarity between the dynamic ILM and the dynamic PL lifetime images. However, we suggest a thorough investigation of the blurring impact on dynamic PL and dynamic ILM measurements by comparing blurring of samples with different diffusion lengths and different surface roughnesses.

### Comparison with area-averaged PC techniques

In Fig. 3.28, the transient PCD measurement lies slightly above the QSSPC measurement. Cuevas et al. [107] demonstrated the overestimation of high lifetimes if detecting an inhomogeneous lifetime distribution with area-averaged transient PCD measurements. The areas of high lifetimes dominate the decay of the transient curve since their contribution is larger and longer.

<sup>12</sup>The free carrier absorption coefficient is calculated using a parameterization of Schroder et al. [114].

<sup>13</sup>The absorption coefficient of Green and Keevers [63] is used for the calculation of the band-to-band absorption length.

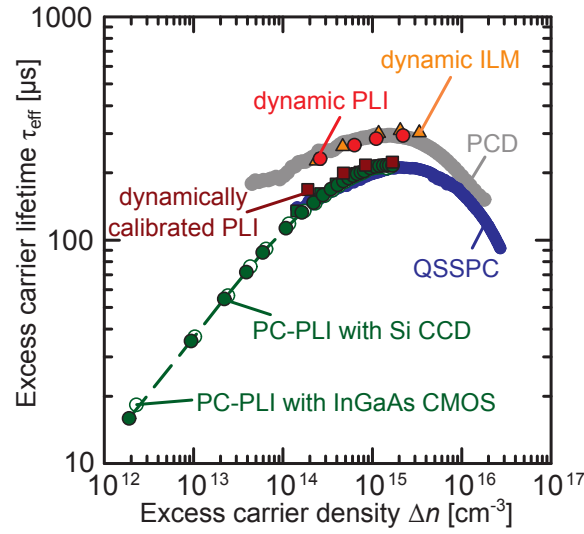


**Figure 3.28:** Injection-dependent effective lifetime  $\tau_{\text{eff}}$  measured with different lifetime techniques. The lifetime techniques, presented in Fig. 3.26 are compared with a QSSPC and a PCD measurement.

We observe a good agreement of the steady-state measurements QSSPC, PC-PLI with the dynamically calibrated steady-state PL lifetime measurements. The good agreement of the PCD measurements with the dynamic lifetimes are expected to be coincidental since different reasons are expected to result in a deviation from the actual carrier lifetime (dynamic PLI/ILM: blurring, PCD: underestimation of the low lifetimes due to their weak signal contribution and fast decay).



# CHAPTER 4

---

## Imaging of the interstitial iron concentration in boron-doped silicon

---

Iron is one of the most abundant lifetime-limiting contaminants in multicrystalline silicon (mc-Si) as used by the photovoltaic industry [115]. It introduces deep levels in the silicon (Si) band gap and has a large diffusivity at elevated temperatures which can result in a fast contamination of large areas.

For the analysis and monitoring of interstitial iron in Si, it is essential to be able to accurately determine its concentration. Compared to the total amount of atoms in one cubic centimeter pure Si of about  $5 \times 10^{22} \text{ cm}^{-3}$ , only low concentrations of the impurity in the range of  $(10^{10} - 10^{14}) \text{ cm}^{-3}$  have to be measured. Istratov et al. [115] compared the sensitivity of various techniques for the determination of iron in Si and found the lifetime-based techniques to be most sensitive. The lifetime-based techniques exploit the defect reaction of the positively charged interstitial iron  $\text{Fe}_i^+$  with a shallow, negatively charged acceptor  $\text{A}_s^-$  on a substitutional site such as boron, gallium or indium [23, 116–118]:



Unfortunately, the interstitial iron is activated under illumination and is particularly recombination active under typical injection conditions of the solar cell.

Section 4.1 gives a short overview of previous lifetime-based techniques for the determination of the interstitial iron concentration published at the beginning of this

work. Additionally, the previous work on the reaction kinetics of the association and dissociation process of iron boron (FeB) pairs in Si is shortly summarized. In Section 4.2, we use calibrated PL lifetime measurements to investigate the interstitial iron concentration in multicrystalline silicon (mc-Si) wafers. In the last Section, we introduce a new dynamic approach for determining the interstitial iron concentration in boron-doped Si wafers. The dynamic  $\text{Fe}_i$  approach enables the identification of the  $\text{Fe}_i$  concentration without measuring absolute values of the carrier lifetime and without knowing the recombination properties of  $\text{Fe}_i$  and FeB in Si.

## 4.1 Previous work

In this Section, previous work on (i) the measurement of the interstitial iron concentration via carrier lifetime measurements and (ii) the dynamics of the association and dissociation process of iron-boron pairs is reviewed. The Section does not claim to give a complete review of the present knowledge of iron in silicon. A more comprehensive overview is given in the review articles of Istratov et al. [115, 119, 120].

### **Lifetime-based determination of the interstitial iron concentration in boron-doped silicon**

In 1986, Kittler et al. [116] demonstrated on the basis of electron-beam induced current (EBIC) diffusion length measurements that the determination of the diffusion length is sufficient to determine the interstitial iron concentration in deliberately contaminated boron-doped Cz-Si samples. The diffusion length  $L$  or alternatively the carrier lifetime  $\tau$  has to be measured in two different states, namely (i) when the  $\text{Fe}_i$  is bound to boron (B) dopant atoms to form iron-boron (FeB) pairs and (ii) after complete dissociation of the FeB pairs. Due to the different recombination properties of the iron in these two states, the  $\text{Fe}_i$  concentration can be deduced from the difference of the inverse effective lifetimes in the paired state ( $\tau_{\text{FeB}}$ ) and in the isolated state ( $\tau_{\text{Fe}_i}$ ) [23, 116, 117]:

$$[\text{Fe}_i] = C_{\text{SRH}} \left( \frac{1}{\tau_{\text{Fe}_i}} - \frac{1}{\tau_{\text{FeB}}} \right), \quad (4.2)$$

with  $C_{\text{SRH}}$  being a prefactor which depends on the doping concentration  $N_{\text{dop}}$  and the excess carrier concentration  $\Delta n$  [117]. The basis for the lifetime-based technique is the inverse proportionality of the SRH recombination lifetime to the defect concentration [see Eq. (1.16)]. An important prerequisite for the application of Eq. (4.2) to the determination of the  $\text{Fe}_i$  concentration is the assumption that other recombination channels do not change their influence on the effective lifetime during the dissociation process. Only then, the participation of other recombination paths cancels out by subtracting the inverse lifetimes. However, the  $[\text{Fe}_i]$  technique is most sensitive if the

interstitial iron is the dominant recombination center.

In most experiments, the bonding of the FeB pairs is typically realized by storing the sample in the dark at room temperature. For sufficiently long storing periods, it is expected that all  $\text{Fe}_i$  atoms are bound to  $\text{B}_s$  to form FeB pairs [121]. Kittler et al. [116] achieved the dissociated state of the  $\text{Fe}_i$  by electrically injecting charge carriers into their Si samples, exploiting an effect that had been observed by Kimerling and Benton [122].

In 1990, Zoth and Bergholz [23] used measurements of the surface photovoltage (SPV) for the determination of the diffusion length of their deliberately Fe-contaminated Cz- and FZ-Si samples. They dissociated the FeB pairs by an anneal treatment at 210°C for 3 min. No specific sample preparation (no contacts, no surface passivation) is needed for the SPV technique. One drawback may be the requirement of a sample thickness much larger than the diffusion length [2]. The SPV measurements are typically carried out at very low injection densities ( $\Delta n \approx 10^{10} \text{ cm}^{-3}$ ), which allow the assumption of an injection-independent prefactor  $C_{\text{SRH}}$ . In 1993, Lagowski et al. [123] were able to measure  $\text{Fe}_i$  concentrations down to  $\sim 10^9 \text{ cm}^{-3}$  using the SPV technique.

In 2004, Macdonald et al. [117] used the QSSPC technique for the determination of the  $\text{Fe}_i$  concentration. They realized the splitting of the FeB pairs by exposing the samples to white light of  $0.1 \text{ W/cm}^2$  for 5 min. Since the QSSPC technique is in the low injection range often influenced by measurement artifacts [see Section 1.3] the evaluable injection range lies mostly in the mid to high injection regime and an adjustment from the constant  $C_{\text{SRH}}$  to the injection- and doping-dependent prefactor  $C_{\text{SRH}}$  [117] was required:

$$C_{\text{SRH}}(\Delta n, N_{\text{dop}}) = \left( \frac{1}{[N]\tau_{\text{Fe}_i, \text{SRH}}(\Delta n, N_{\text{dop}})} - \frac{1}{[N]\tau_{\text{FeB}, \text{SRH}}(\Delta n, N_{\text{dop}})} \right)^{-1}, \quad (4.3)$$

using the definition of the SRH lifetime [Eq. (1.16)] with  $[N]$  being the impurity concentration.

The advantage of the QSSPC lifetime measurement for  $[\text{Fe}_i]$  measurements lies in the fast acquisition of the lifetime over a wide injection range. The disadvantage of the technique is the low spatial resolution. As Cuevas et al. [107] demonstrated, the measured lifetime is the arithmetical mean over the sense region of the QSSPC setup. If having two adjacent regions with  $\text{Fe}_i$  concentrations differing by about one order of magnitude, a lifetime measurement would only yield 33% of the arithmetic mean of the  $\text{Fe}_i$  concentrations. For an accurate determination of the mean value of a distributed  $\text{Fe}_i$  concentration, the QSSPC technique would need to measure the harmonic mean of the lifetime distribution.

Since the recombination lifetime and the defect density in mc-Si are typically inhomogeneously distributed, imaging techniques for the determination of the  $\text{Fe}_i$  concentration are of great interest. In 1992, Lagowski et al. [124] presented  $[\text{Fe}_i]$  mappings using the SPV technique. In 2001, Palais et al. [125, 126] generated mappings of the

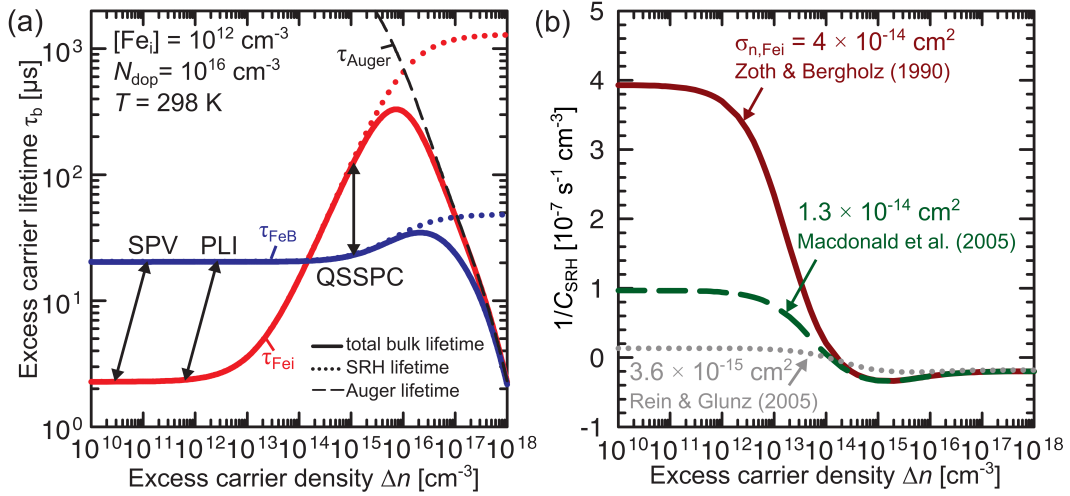


**Figure 4.1:** (a) Expected bulk carrier lifetimes  $\tau_b$  as a function of the excess carrier density  $\Delta n$  in a B-doped Si wafer with  $[\text{Fe}_i] = 10^{12} \text{ cm}^{-3}$ . The total bulk lifetime (solid line) is modeled for the  $\text{Fe}_i$  bound to the boron and in the dissociated state taking into account Auger [Eq. (1.12)] (dashed line) and SRH recombination [Eq. (1.16)] (dotted lines). Typical injection ranges for PL, QSSPC and SPV measurements are indicated by the arrows. The tilted lines show the measurement techniques that are typically operating at a fixed generation rate. The illustration is drawn based on Fig. 1 in Ref. 101. (b) The inverse prefactor  $C_{\text{SRH}}$  [Eq. (4.3)] as a function of the excess carrier density  $\Delta n$  for different electron capture cross sections  $\sigma_n$  in the presence of  $\text{Fe}_i$  (recombination parameter from Zoth and Bergholz [23], Rein and Glunz [128], Macdonald et al. [101]).

$\text{Fe}_i$  concentration from MW-PCD lifetime mappings, determining the prefactor  $C_{\text{SRH}}$  from comparison with deep level transient spectroscopy (DLTS) measurements of the  $\text{Fe}_i$  concentration. In 2005, Henze et al. [127] presented  $[\text{Fe}_i]$  imaging on Ga-doped mc-Si wafer using ILM measurements. In 2007, Macdonald [100, 101] used photoluminescence imaging for the spatially resolved generation of  $[\text{Fe}_i]$  images.

Since ILM or PL images are acquired at a fixed generation rate, the injection density is different for the PL measurements in the dissociated and associated state of the interstitial iron. As a consequence, Macdonald proposed calculating the prefactor  $C_{\text{SRH}}$  [Eq. (4.3)] in consideration of the two different injection densities at each pixel of the PL image. As a consequence, it is additionally required that the impact of other recombination paths is the same for the two different injection densities of the lifetime measurement with the  $\text{Fe}_i$  bound to the boron and in the dissociated state.

The prominent lifetime-based techniques for the determination of the  $\text{Fe}_i$  concentration and their typical injection ranges are displayed in Fig. 4.1 (a). We use the recombination parameters, listed in Tab. 4.1, for the calculation of the SRH recombination lifetime. The tilted lines show the different injection densities for the lifetime measurement with the  $\text{Fe}_i$  bound to the boron and in the dissociated state. Clearly seen is the cross-over point (COP) of the injection-dependent lifetimes where the recombination lifetime is equal in the both states of the interstitial iron. The COP is found to depend on temperature and doping density [48, 49]. For doping densities be-

tween  $N_{\text{dop}} = (0.1 - 70) \times 10^{15} \text{ cm}^{-3}$ , the COP is between  $\Delta n = (0.4 - 3) \times 10^{14} \text{ cm}^{-3}$  at a temperature of  $T \approx 304 \text{ K}$  [48, 49]. The characteristic COP can be used as an identifier for the presence of  $\text{Fe}_i$  in boron-doped Si samples [49].

Figure 4.1 (b) shows the injection-dependent prefactor  $C_{\text{SRH}}(\Delta n, N_{\text{dop}})$  as proposed by Macdonald et al. [117] [Eq. (4.3)].  $C_{\text{SRH}}$  is calculated for some recombination property sets taken from Refs. 23, 128 and 101. These sets differ mainly in the electron capture cross section in the presence of interstitial iron  $\sigma_{n,\text{Fe}_i}$  which strongly influences the recombination lifetime at low-level injection conditions. If using these sets for the  $[\text{Fe}_i]$  determination, the difference in the calculated  $[\text{Fe}_i]$  can directly be taken from Fig. 4.1 (b) since  $[\text{Fe}_i]$  scales with  $C_{\text{SRH}}$  [Eq. (4.2)].

From Fig. 4.1 (a) it becomes evident why lifetime measurements at low-level injection conditions are widely assumed to be favorable for the determination of the interstitial iron concentration with Eq. (4.2). Due to the expected injection independence of the carrier lifetime in the low-level injection range, an uncertainty of the measured carrier lifetime has a smaller impact on the  $[\text{Fe}_i]$  determination. However, the systematic error due to the unprecise knowledge of  $\sigma_{n,\text{Fe}_i}$  is already up to one order of magnitude.

**Table 4.1:** Recombination parameters of interstitial iron and iron-boron pairs in boron-doped c-Si.  $E_{\text{defect}}$  is the defect's energy level in the band gap of Si,  $\sigma_n$  and  $\sigma_p$  are the capture cross sections for electrons and holes.

	$E_{\text{defect}}$ [eV]	$\sigma_n$ [cm <sup>2</sup> ]	$\sigma_p$ [cm <sup>2</sup> ]
<b>Fe<sub>i</sub></b>	$E_V + 0.38$ [22]	$4 \times 10^{-14}$ [23]	$7 \times 10^{-17}$ [23]
<b>FeB</b>	$E_C - 0.26$ [48, 49]	$5 \times 10^{-15}$ [49]	$3 \times 10^{-15}$ [49]

## Reaction kinetics of the association and dissociation process of FeB pairs in Si

The re-pairing and dissociation of FeB pairs can be characterized by corresponding rates:  $R_{\text{rep}}$  and  $R_{\text{diss}}$ . A simple differential equation that described the time-dependent behavior of the FeB pair concentration can be written down if assuming that the reaction [Eq. (4.1)] is fully reversible and the interstitial iron does not precipitate. Furthermore, it is required that the boron concentration is much larger than the interstitial iron concentration [119]. The derivative in time of the FeB pair concentration due to the dissociation or association process is then given by the expression:

$$\frac{d[\text{FeB}]}{dt} = -R_{\text{diss}}[\text{FeB}] + R_{\text{rep}}[\text{Fe}_i]. \quad (4.4)$$

Using further that the total number of interstitial is given by the sum of FeB pairs and interstitial iron  $[\text{Fe}_i]_{\text{total}} = [\text{FeB}] + [\text{Fe}_i]$  and that the relative number of FeB pairs

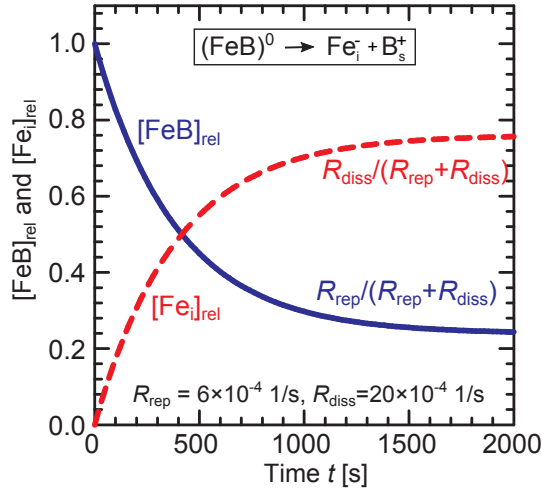


**Figure 4.2:** Time-dependent behavior of the relative FeB and  $Fe_i$  concentration during optical excitation, starting with 100% associated FeB pairs. The parameter used for the calculation based on Eq. (4.6) are:  $[Fe_i] = 4 \times 10^{12} \text{ cm}^{-3}$ ,  $N_{dop} = 1.5 \times 10^{16} \text{ cm}^{-3}$ , illumination intensity: 0.2 suns ( $\sim 14 \text{ mW/cm}^2$ ),  $W = 200 \text{ }\mu\text{m}$ ,  $T = 298 \text{ K}$ .  $R_{rep}$  and  $R_{diss}$  are calculated using Eqs. (4.7) and (4.9).

is defined as  $[FeB]_{rel} := [FeB]/[Fe_i]_{total}$  results in [119]:

$$\frac{d[FeB]_{rel}}{dt} = -[FeB]_{rel} (R_{diss} + R_{rep}) + R_{rep}. \quad (4.5)$$

The solution of the differential equation (4.5) is of exponential form:

$$[FeB]_{rel}(t) = \frac{R_{diss}}{R_{rep} + R_{diss}} \exp(-(R_{rep} + R_{diss})t) + \frac{R_{rep}}{R_{rep} + R_{diss}}, \quad (4.6)$$

with the time constant being the inverse of the sum of re-pairing and dissociation rate.

Figure 4.2 shows the time-dependent characteristics of the relative FeB and  $Fe_i$  concentration of an illuminated sample as expected from Eq. (4.6). The saturation value for both functions is determined by the relative association or dissociation rate with respect to the sum of both rates.

The association reaction is driven by the Coulomb attraction between the positively-charged interstitial iron  $Fe_i^+$  and the negatively-charged substitutional boron  $B_s^-$ . Kimerling and Benton [122] performed capacitance transient spectroscopy measurements on Schottky barrier structures on iron-contaminated FZ-Si wafers. Their measurements revealed that the association reaction is suppressed if the  $Fe_i$  is not charged. They realized the neutral  $Fe_i$  state by applying a reverse bias to their Schottky barrier structure. As a consequence, the Fermi level is shifted above the  $Fe_i$  donor level and the positively charged interstitial iron is occupied with an electron and thus neutralized. The reduced concentration of FeB pairs was directly verified by their DLTS

measurements.

The re-pairing of FeB pairs is a diffusion-controlled pairing reaction as described by Reiss et al. [129]. If the  $\text{Fe}_i$  is randomly distributed in the Si wafer and the fixed boron dopant is present in a much higher concentration, i.e.  $[\text{B}] \gg [\text{Fe}_i]$ , the association rate of FeB pairs  $R_{\text{rep}}$  can be written as [129, 130]:

$$R_{\text{rep}} = \tau_{\text{rep}}^{-1} = \frac{4\pi q^2 D [\text{B}]}{\varepsilon \varepsilon_0 k_B T} = \frac{1}{A} \frac{[\text{B}]}{T} \exp\left(\frac{-E_{\text{ass}}}{k_B T}\right), \quad (4.7)$$

with  $E_{\text{ass}}$  being the activation energy for the association process<sup>1</sup>.  $E_{\text{ass}}$  is expected to be equal to the migration enthalpy of  $\text{Fe}_i^+$  in Si and describes the barrier height for the  $\text{Fe}_i^+$  diffusing to the  $\text{B}_s^-$ . The migration enthalpy is found to be  $E_{\text{mig}} = 0.68$  eV [131] and  $E_{\text{mig}} = 0.67$  eV [119]. From temperature-dependent lifetime or diffusion length measurements, the activation energy of the FeB pairing was found to be e.g.  $E_{\text{ass}} = 0.68$  eV [123] and  $E_{\text{ass}} = 0.66$  eV [130] which is in a good agreement with the migration enthalpy. With measurements of the doping-dependent re-pairing rate obtained from carrier lifetime or diffusion length measurements, the prefactor  $A$  was determined to be between  $(4.2 \text{ and } 5.7) \times 10^5 \text{ cm}^{-3}\text{K}^{-1}$  [23, 130, 132].

The dissociation of the FeB pairs as reverse process to the association can be achieved by increasing the temperature or by injecting charge carriers (optically or electrically). Measurements of the paired fraction as a function of temperature has yielded the quantitative relation [121, 122]:

$$\frac{[\text{FeB}]}{[\text{Fe}_i]} = [\text{B}]K = [\text{B}]10^{-23} \exp\left(\frac{E_b}{k_B T}\right) \quad (4.8)$$

with  $K$  being the equilibrium constant of this law of mass action and  $E_b = 0.65$  eV being the binding energy.

Graff and Pieper [133] demonstrated the dissociation of FeB pairs by injecting carriers through illumination with white light. Kimerling and Benton [122] showed that the dissociation rate scales with injection density by electrically injecting minority carriers. They concluded from their results that the dissociation process is a recombination-enhanced reaction. Kimerling and Benton found a reduced activation energy of the dissociation process of  $E_{\text{diss}} = 0.09$  eV due to charge carrier injection. For a recombination-enhanced reaction it is expected that the released energy due to the recombination process is converted into vibrational energy of the  $\text{Fe}_i$ . The vibrational energy of the defect reduces the energy necessary to reach the next-neighbor position and in this way facilitates the dissociation of the FeB pair.

Lagowski et al. [123] investigated the dissociation process of FeB pairs with respect to optical dissociation and found an accelerated photodissociation with increasing

<sup>1</sup> $\varepsilon$ : dielectric constant of Si,  $\varepsilon_0$ : vacuum permittivity,  $k_B$ : Boltzmann constant,  $D$ : diffusivity of  $\text{Fe}_i$  in Si

illumination intensity. Another result of the experiments of Lagowski et al. arose from measurements of the dissociation rate for different excitation wavelengths. They found that the threshold photon energy equals the band gap of silicon which supports the assumption of a recombination-enhanced dissociation process.

Geerligs and Macdonald [134] investigated the dynamics of the FeB pair dissociation induced by illumination with halogen lamps and revealed a quadratic dependence of the dissociation rate  $R_{\text{diss}}$  on the average photogeneration rate  $G_{\text{av}}$  and an inverse proportionality on the square of the interstitial iron concentration  $[\text{Fe}_i]$  [134]:

$$R_{\text{diss}} = C_{\text{diss}} \frac{G_{\text{av}}^2}{[\text{Fe}_i]^2}, \quad (4.9)$$

with a proportionality constant  $C_{\text{diss}}$  that Geerligs and Macdonald [134] determined to be  $C_{\text{diss}} = 5 \times 10^{-15}$  s. Since for a steady-state carrier lifetime measurement, the generation rate equals the recombination rate, they determined a quadratic dependence on the recombination rate. The origin of the squared dependencies in Eq. (4.9) is presently not fully understood. Geerligs and Macdonald suggested a two-electron capture event with the result of a negatively-charged or neutralized  $\text{Fe}_i$ .

## 4.2 Interstitial iron imaging using PC-PLI

In the beginning of this Section, we describe the procedure of measuring the interstitial iron concentration  $[\text{Fe}_i]$  with photoconductance-calibrated PL lifetime imaging. Secondly, two examples are given for the application of the lifetime-based  $[\text{Fe}_i]$  determination. The first example demonstrates the  $[\text{Fe}_i]$  measurement over the ingot height of a deliberately iron-contaminated mc-Si ingot. The second example monitors the  $\text{Fe}_i$  concentration during a long-time anneal at a low-temperature with the result of a pronounced  $[\text{Fe}_i]$  reduction due to internal gettering.

### 4.2.1 Experimental

The samples investigated in this Chapter have a  $\text{SiN}_x$  (PECVD) surface passivation on both sides of the wafer to increase the sensitivity to variations of the bulk lifetime. All measurements are performed with the PC-PLI setup described in Section 2.2.2.

In this work, the bonding of the  $\text{Fe}_i$  to the substitutional boron  $\text{B}_s$  is accelerated by placing the sample on a hotplate at  $50^\circ\text{C}$  for about 30 min. Due to the increased mobility of the interstitial iron at the elevated temperature, the association time is strongly reduced [Eq. (4.7)], resulting in a complete FeB pair bonding after 30 min for doping concentrations above  $10^{16} \text{ cm}^{-3}$ .

By now, the splitting of the FeB pairs was reached by heating [23], illumination [117, 133] or electrical injection of charge carriers [116, 122]. For Si wafers, only the first two approaches are applicable. Macdonald et al. [117] emphasized the advantages of the optical over thermal dissociation. The thermal dissociation requires elevated temperatures. However, it is difficult to prevent the pairing of the FeB pairs during cooling. Optical dissociation can be achieved within a short time and without noteworthy heating. In this work, the PL signal of the fully dissociated state is measured after exposing the wafer to about 15 flashes of a photo flash lamp with an intensity of  $\sim 100 \text{ W/cm}^2$ . All PL measurements are performed at a sample temperature of  $25^\circ\text{C}$  if not otherwise stated.

For the achievement of a sufficient signal-to-noise ratio of the PL images, a certain measurement time is required during which the Si wafer with the FeB pairs is exposed to the laser illumination. As a consequence, a fraction of the FeB pairs will be separated during the PL measurement. Hence, the measured PL signal is not reflecting the signal for complete FeB pair association. We correct for the impact of the PL measurement on the FeB concentration by recording a sequence of PL images. Figure 4.3 shows an exemplary measurement of a deliberately contaminated FZ-Si wafer with an interstitial iron concentration of  $[\text{Fe}_i] = 2.5 \times 10^{12} \text{ cm}^{-3}$  at an illumination intensity of 0.5 suns ( $\sim 34 \text{ mW/cm}^2$ ). The PL signal is obtained by averaging over the pixels which image about  $2 \text{ cm}^2$  of the Si wafer. The data of the PL sequence are adjusted to an exponential function according to Eq. (4.6). The intersection with the

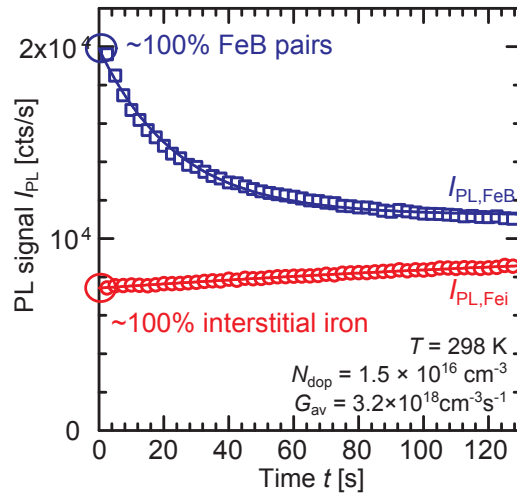


**Figure 4.3:** Time-dependent PL signals, beginning with 100%  $[Fe_i]$  ( $I_{PL,Fe_i}$ ) and 100%  $[FeB]$  ( $I_{PL,FeB}$ ), respectively. The deliberately contaminated FZ sample ( $[Fe_i] = 2.5 \times 10^{12} \text{ cm}^{-3}$ ) was illuminated with a photon flux equivalent to 0.5 suns ( $\sim 34 \text{ mW/cm}^2$ ).

ordinate yields the PL signal expected for the case of 100% FeB pairing. If only few data points are available, a linear regression is sufficient.

The  $[Fe_i]$  measurement is performed at low-level injection (lli) since the SRH recombination lifetime is expected to be injection-independent at lli (see Fig. 4.1). Another reason for the measurement at lli is the squared dependence of the dissociation rate on the illumination intensity or photogeneration rate [see Eq. (4.9)]. A disadvantage of this approach is the long measurement time required for a PL measurement at lli conditions. In addition, the PL measurement of the Si wafer with the dissociated  $Fe_i$  requires correction for long measurement times since the fraction of re-associated FeB pairs is not negligible anymore. In Fig. 4.3, a slight increase due to the re-association of FeB pairs can be observed (lower curve). As a consequence, the PL signal of the Si wafer with all  $Fe_i$  being dissociated is obtained by linear regression.

For the PC-PLI calibration, a PC measurement of the Si wafer of interest is needed. However, PC measurements are often influenced by measurement artifacts at the lli injection conditions required for the  $[Fe_i]$  measurement (see Section 1.3.2). Thus, the PL calibration has to be performed at higher injection densities. Due to the strong injection dependence of the recombination lifetime in the presence of  $Fe_i$  [see Fig. 4.1 (a)], the lifetime values under high- and low-level injection conditions are expected to differ strongly. As a consequence, it is necessary to consider the impact of reabsorption on the PC-PLI calibration.

As presented in Section 3.2.2, the impact of reabsorption on the carrier lifetime is for most relevant cases below 20% ( $\tau > 1 \mu\text{s}$ ). Figure 4.4 shows the deviation in the  $Fe_i$  concentration that results from calibrated PL measurements taking the impact of reabsorption into account. For the simulation it is assumed that the PL signal is calibrated at an injection density of  $10^{16} \text{ cm}^{-3}$  for a carrier lifetime of  $300 \mu\text{s}$ .

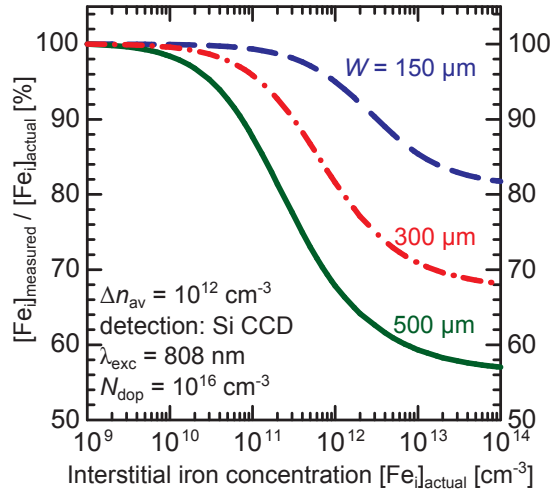


**Figure 4.4:** Impact of reabsorption on the lifetime-based determination of the interstitial iron concentration with calibrated PL measurements for different wafer thicknesses  $W$ . The surface passivation is assumed to be perfect with  $S = 0$  cm/s.

This combination yields a homogeneous carrier distribution in a Si wafer with a thickness  $W < 600$   $\mu\text{m}$ . The lifetimes for the  $\text{Fe}_i$  determination are evaluated at an average excess carrier density of  $\Delta n_{\text{av}} = 10^{12}$   $\text{cm}^{-3}$ . Figure 4.4 shows the ratio of the measured  $[\text{Fe}_i]$  compared to the actual  $[\text{Fe}_i]$  for different wafer thicknesses  $W$ . It can be concluded that the impact of reabsorption on the  $[\text{Fe}_i]$  determination increases with increasing wafer thickness. For thin Si wafers with  $W = 150$   $\mu\text{m}$ , the modeled deviation is below 20 % for  $\text{Fe}_i$  concentrations below  $10^{14}$   $\text{cm}^{-3}$ . If a more exact value of the  $[\text{Fe}_i]$  is required, the correction procedure proposed in Section 3.2.2 can be used for the correct determination of the carrier lifetime. However, in most cases only the order of magnitude is of interest if investigating the  $\text{Fe}_i$  content.

In 2009, Schubert et al. [135] discussed the impact of an inhomogeneous carrier density profile onto the measurement of the  $\text{Fe}_i$  concentration if using an integral-based technique such as QSSPC, ILM or PL. The investigation of Schubert et al. [135] is focused on the difference between the local excess carrier density and the average excess carrier density that is actually measured. If the difference is sufficiently large, the prefactor  $C_{\text{SRH}}$  [Eq. (4.3)] is wrongly calculated. However, the correction procedure presented in Section 3.2.2 allows not only the correct determination of the carrier lifetime but also of the average excess carrier density.

### 4.2.2 Internal gettering of interstitial iron

In solar-grade boron-doped block-cast mc-Si, the total iron concentration is in the range of  $5 \times 10^{13} \text{ cm}^{-3}$  to  $10^{15} \text{ cm}^{-3}$  [136–138]. Macdonald et al. [137] showed that in their mc-Si wafers only  $\sim 1\%$  of the iron is present in the interstitial form. The remainder of the iron was found to be present in precipitates, which are lower in density and hence reduce the lifetime less effectively [139, 140].

As a consequence of their high recombination activity, a reduction of the  $\text{Fe}_i$  concentration would improve the bulk material quality of the solar cell material. External gettering, such as segregation gettering during phosphorus diffusion, is frequently applied during the solar cell fabrication process to effectively reduce the  $\text{Fe}_i$  concentration. An internal getter approach for the reduction of the  $\text{Fe}_i$  concentration is the transformation into a less recombination-active form, e.g. through the clustering of the  $\text{Fe}_i$  into precipitates.

In the following, the PC-PLI lifetime technique is used to investigate the impact of two different internal gettering approaches on deliberately contaminated mc-Si wafers. In the first experiment, copper and iron are added to the melt before the casting of the mc-Si ingot with the prospect of co-precipitation of iron and copper (Cu). The carrier lifetime and the  $\text{Fe}_i$  concentration are measured on wafers of different ingot heights. The second experiment investigates the  $\text{Fe}_i$  concentration of a single mc-Si wafer as a function of time during a long-term annealing at  $450^\circ\text{C}$ .

#### Height-dependent investigation of the $\text{Fe}_i$ concentration of mc-Si ingots

In 2007, Buonassisi et al. [141] found co-precipitates of iron, copper and nickel in Si samples after slowly cooling the samples from  $1200^\circ\text{C}$ . They proposed the existence of liquid droplets with a high copper concentration during the cooling process. These droplets may locally getter metallic impurities via solid-liquid segregation [141].

Three ingots with additional (i) 20 ppma Fe, (ii) 20 ppma Fe and 20 ppma Cu, and (iii) 20 ppma Cu were casted in a small furnace (base area:  $270 \times 177 \text{ mm}^2$ , height: 210 mm) at Deutsche Solar AG [142]. The impurities were added directly to the feedstock. We investigate the wafers of these ingots using PC-calibrated PL lifetime imaging (PC-PLI, Section 3.2).

Lifetime images of the Si wafers with the  $\text{Fe}_i$  bound to the boron and in the dissociated state are acquired and converted into  $[\text{Fe}_i]$  images using Eq. (4.2) and the recombination parameters of Tab. 4.1. Figure 4.5 presents the arithmetical mean of the carrier lifetime  $\tau_{\text{FeB}}$  (with the  $\text{Fe}_i$  bound to the boron) and the  $\text{Fe}_i$  concentration over an area in the middle of the wafer ( $7.5 \times 7.5 \text{ cm}^2$ ). The error bars are calculated from error propagation using the statistical uncertainty of the lifetime measurements. The illumination intensity was set at  $4 \text{ mW/cm}^2$  (0.06 suns) with the result of an average excess carrier density well below  $10^{12} \text{ cm}^{-3}$  for the ingots with additional Fe

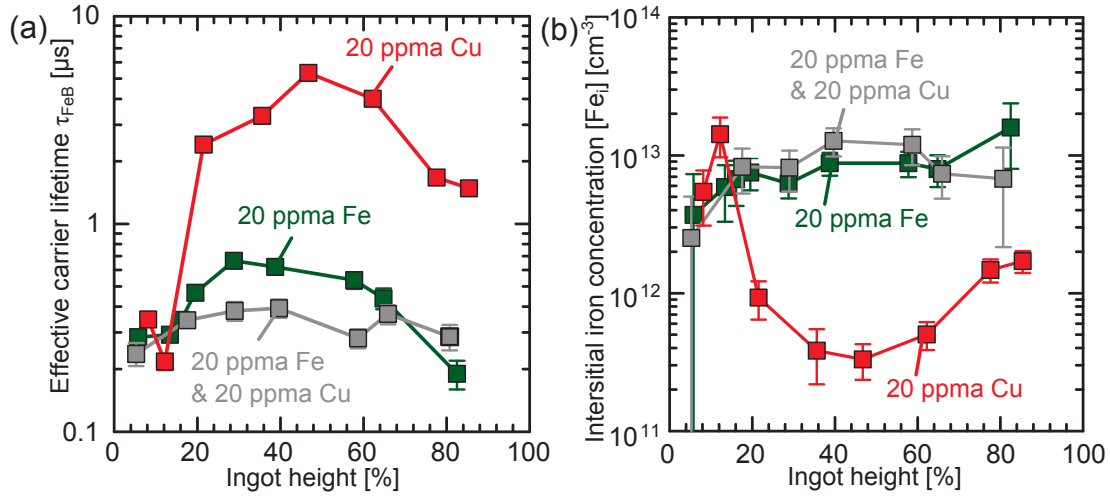


**Figure 4.5:** Measurements of the carrier lifetime and the  $Fe_i$  concentration on  $SiN_x$ -passivated wafers from different ingots as a function of the ingot height. The total ingot height is 21 cm. The different ingots are deliberately contaminated with iron and copper in different concentrations (ppma: parts per million atoms). (a) Effective carrier lifetime  $\tau_{FeB}$ , measured at a constant photogeneration rate with the  $Fe_i$  bound to the boron at low-level injection conditions. (b) The  $Fe_i$  concentration  $[Fe_i]$  is determined from calibrated lifetime measurements (PC-PLI) using Eq. (4.2).

content. For the ingot only with additional Cu, the average excess carrier density is still below  $4 \times 10^{12} cm^{-3}$ .

The  $Fe_i$  concentration of the ingot with additional 20 ppma Fe and 20 ppma Cu is not reduced compared to the ingot with additional 20 ppma Fe. Thus, we conclude that the presence of additional copper (in the added concentration) does not reduce the  $Fe_i$  content in our mc-Si ingots. The experiment of Buonassisi et al. [141] could not be adapted to the mc-Si that were casted for our experiment.

Figure 4.5 (b) shows a typical U-shaped distribution for the  $Fe_i$  concentration of the ingot with additional Cu (and without additional Fe). At the top of the ingot, the  $Fe_i$  concentration increases due to the segregation into the molten Si, whereas at the bottom of the ingot  $[Fe_i]$  probably increases due to in-diffusion from the crucible after solidification [137]. As a consequence, the  $Fe_i$  concentration is lowest in the middle of the ingot.

For the two ingots with higher additional iron content,  $[Fe_i]$  is almost constant at a high level of  $\sim 8 \times 10^{12} cm^{-3}$  to  $\sim 10^{13} cm^{-3}$  as a function of the ingot height. A similar study from Kvande et al. [143] with additional 53 ppm wt ( $\sim 27$  ppma) has resulted in a comparable  $[Fe_i]$  level throughout the ingot. However, the high  $[Fe_i]$  level is not compatible with the solubility limit at the low temperatures during the ingot cooling ( $\sim 10$  h from  $1300^\circ C$  to  $600^\circ C$ ) but has been reported before [143, 144]. Macdonald et al. [144] assumed a supersaturated state for the  $Fe_i$  down to temperatures of  $650^\circ C$ . They proposed an energetic barrier for the formation of precipitates in the investigated temperature range.

### Internal gettering of interstitial iron at low temperature

Recently, low-temperature annealing up to 500°C was explored [145, 146] for the reduction of the  $\text{Fe}_i$  concentration in mc-Si by internal gettering. On FZ-Si wafers, Henley and Ramappa [147] investigated the reduction of the  $\text{Fe}_i$  concentration as a function of annealing temperature and proposed the formation of heterogeneously distributed, spherical iron silicide precipitates. They assumed that during the quenching of their FZ-Si samples, a lattice defect structure is formed that provides preferred nucleation sites [147]. Henley and Ramappa [147] found that maximum precipitation occurs in the temperature interval of (500 - 600)°C. In mc-Si, it is expected that during low-temperature annealing the precipitates form at extrinsic defect sites such as grain boundaries and dislocations [137]. The segregation to these defects is driven by the reduced free energy for metal atoms at distorted lattice sites compared to the undisturbed lattice sites [137].

In this work, the internal gettering of an mc-Si wafer is investigated using calibrated PL lifetime imaging. Before and during the annealing of an mc-Si sample, lifetime images of the mc-Si wafer with the  $\text{Fe}_i$  bound to the boron and in the dissociated state are acquired and converted into  $[\text{Fe}_i]$  images using Eq. (4.2) and the recombination parameters of Tab. 4.1.

The boron-doped  $\text{SiN}_x$ -passivated mc-Si wafer has a thickness of 228  $\mu\text{m}$ , a doping density of  $2.4 \times 10^{16} \text{ cm}^{-3}$  and stems from the top region of an ingot ( $\sim 80\%$  of the total ingot height) that is deliberately contaminated with iron. Figure 4.6 (a) shows carrier lifetime images before the anneal, after 10 minutes and after 4 hours of annealing at a temperature of 450°C in atmosphere. Only a section of  $6.5 \times 6.5 \text{ cm}^2$  of the wafer is imaged (original wafer size:  $15.6 \times 15.6 \text{ cm}^2$ ) to increase the spatial resolution. We use a weak illumination intensity of  $5.5 \text{ mW/cm}^2$  (0.08 suns) for the PL measurement to achieve average excess carrier densities below  $2 \times 10^{12} \text{ cm}^{-3}$ . Figure 4.6 (b) shows the  $\text{Fe}_i$  concentration images that are calculated from the calibrated lifetime images.

The carrier lifetime image before the annealing shows lifetimes below 1  $\mu\text{s}$  at an injection density below  $9 \times 10^{11} \text{ cm}^{-3}$ . The low lifetime value reflects the impact of a high content of various impurities that are expected in this ingot region. We observe two kinds of line-like defects with an increased recombination activity [appearing as dark lines in the first image of Fig. 4.6 (a)]. One kind [exemplarily labeled A in Fig. 4.6 (a)] exhibits so-called denuded zones, i.e. areas of increased lifetime in the direct vicinity. The denuded zones indicate the occurrence of internal gettering during the ingot cooling. This behavior is attributed to grain boundaries and dislocations [148, 149]. The clustered appearance of a second type of dark lines [exemplarily labeled B] is attributed to dislocation clusters [150]. However, we observe no denuded zones for the dark lines of type B. For type A, the  $\text{Fe}_i$  concentration is comparably low in the first image of Fig. 4.6 (b), whereas type B is hardly visible.

Interestingly, this behavior changes during the anneal. After 4 h annealing at 450°C, the clustered recombination active lines of type B are clearly visible in the lifetime

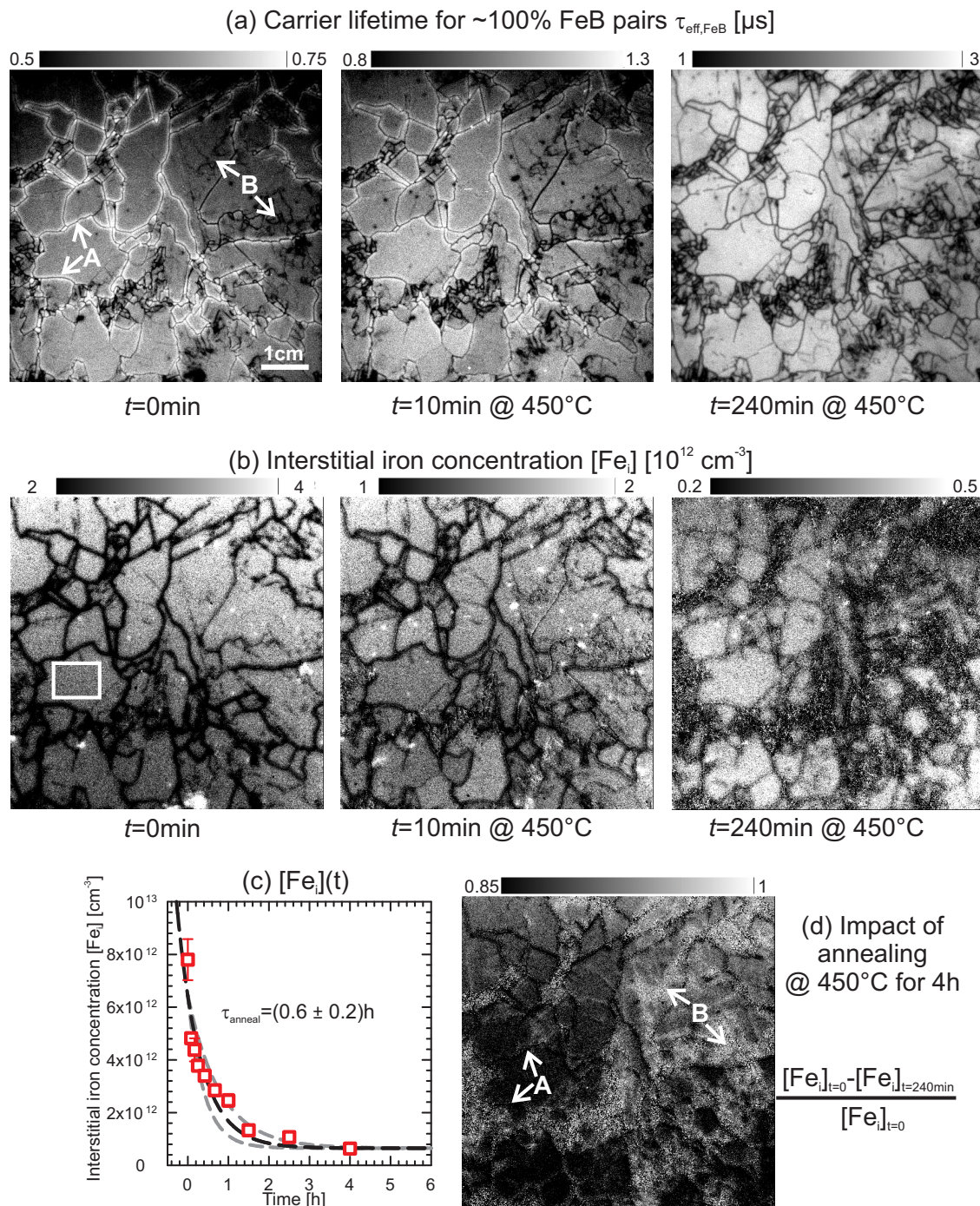


**Figure 4.6:** (a) Carrier lifetime for the associated state of the FeB pairs at  $t = 0$  before the annealing at  $450^\circ\text{C}$ , after 10 min of annealing, and after 4 h of annealing at  $450^\circ\text{C}$ . (b)  $\text{Fe}_i$  concentration images after different annealing times. (c) Time-dependent  $\text{Fe}_i$  concentration as a function of annealing time. The  $\text{Fe}_i$  concentration is averaged over the area inside a grain, marked in (b) with a white rectangle. (d) Impact of the annealing on the  $\text{Fe}_i$  concentration.

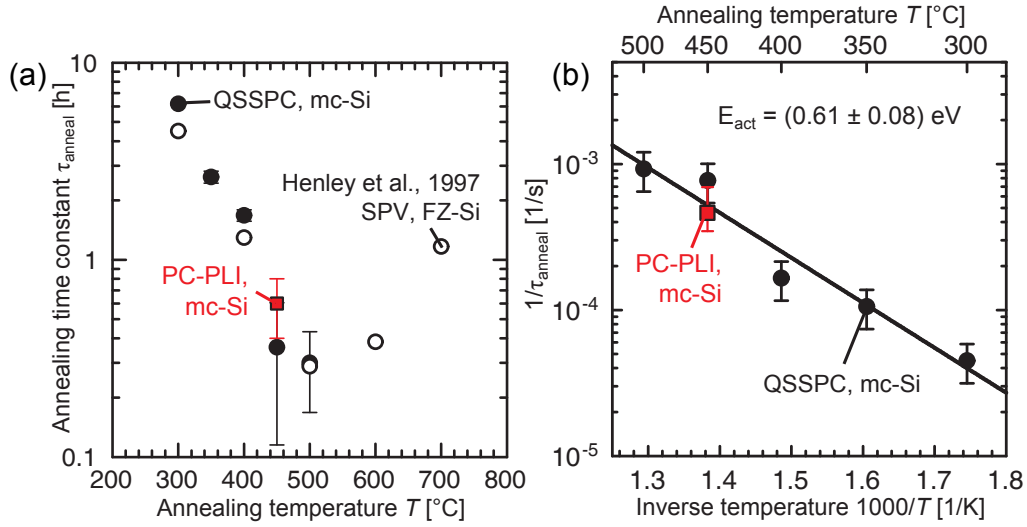


**Figure 4.7:** (a) Annealing time constants  $\tau_{\text{anneal}}$  as a function of temperature  $T$ . Comparison of our results with the data from Henley and Ramappa [147]. (b) Experimentally determined rates  $1/\tau_{\text{anneal}}$  of the internal gettering process as a function of the inverse temperature in an Arrhenius plot. The calculated activation energy  $E_{\text{act}}$  for the gettering process is determined to  $E_{\text{act}} = (0.61 \pm 0.08) \text{ eV}$ .

and the  $[\text{Fe}_i]$  image.

Figure 4.6 (d) shows the spatially resolved impact of the annealing on the  $\text{Fe}_i$  concentration. The change of the  $\text{Fe}_i$  concentration due to 4 h annealing is divided by the  $\text{Fe}_i$  content before the annealing. Thus, Fig. 4.6 (d) allows the spatially resolved comparison of the internal gettering efficiency. Noticeable is the different getter efficiency of the line type A and B. The clustered dislocations (type B) and the areas next to them appear to be the brightest in Fig. 4.6 (d) since the  $\text{Fe}_i$  concentration is reduced to a greater extent in the regions next to line type B.

However, despite the lower  $\text{Fe}_i$  concentration, the carrier lifetime in the surroundings of line type B is still lower as close to the lines of type A. We attribute the lower lifetime values to the higher dislocation density that provide with preferred recombination sites.

Figure 4.6 (c) shows the time dependence of the  $\text{Fe}_i$  concentration inside a particular grain (marked in Fig. 4.6 (b) with a white rectangle) as a function of annealing time. The  $\text{Fe}_i$  concentration was found to decay exponentially with a reduction of about one order of magnitude. The annealing time constant is determined to be  $\tau_{\text{ann}} = (0.6 \pm 0.2) \text{ h}$  and the final interstitial iron concentration after 4 h annealing is determined to be  $[\text{Fe}_i] = 5 \times 10^{11} \text{ cm}^{-3}$ .

In a parallel experiment, we investigated the long-term annealing as a function of temperature for mc-Si wafers with a resistivity of  $0.8 \text{ } \Omega\text{cm}$ . The interstitial iron concentration was analyzed for injection densities above the cross-over point using QSSPC measurements. The time constants are similar to the one found from Henley

and Ramappa [147] for the internal gettering rate of deliberately contaminated FZ-Si wafers. Figure 4.7 (a) compares all results as a function of temperature.

Since the annealing time constant strongly decreases with increasing temperature, we suggest a thermally activated mechanism for the  $\text{Fe}_i$  reduction. We found that the reduction of the  $\text{Fe}_i$  concentration by internal gettering has an activation energy of  $E_{\text{act}} = (0.61 \pm 0.08)$  eV by adjusting the data to the Arrhenius equation:

$$\frac{1}{\tau_{\text{anneal}}} = \nu \times \exp\left(\frac{-E_{\text{act}}}{k_B T}\right), \quad (4.10)$$

where  $\nu$  is the attempt frequency that is found to be  $\nu = (10 \pm 4) \text{ s}^{-1}$ . Figure 4.7 (b) shows the corresponding Arrhenius plot of the inverse annealing time constant as a function of the inverse annealing temperature. We suggest that the diffusion of the  $\text{Fe}_i$  to the gettering site is the rate-limiting process since the activation energy is close to the migration enthalpy of  $\text{Fe}_i$  in Si [119, 131].

For temperatures above  $500^\circ\text{C}$ , Henley and Ramappa [147] proposed a reduction of the precipitation and even a redissolution of pre-existing precipitates and release of previously gettered iron. As a consequence, they observed an increasing annealing time constant with temperature and a minimum at an annealing time constant of about  $500^\circ\text{C}$  [see Fig. 4.7 (a)].

### 4.3 Dynamic interstitial iron imaging

In this Section, a dynamic approach for measuring the interstitial iron concentration in B-doped Si using photoluminescence imaging is presented. The camera-based technique is based on the characteristic dependence of the dissociation rate of iron-boron pairs on the interstitial iron concentration [Eq. (4.9)]. The dissociation rate is determined by measuring the time-dependent photoluminescence signal after complete association of the iron-boron pairs in the sample.

#### 4.3.1 Principle of dynamic interstitial iron imaging

The basis of the dynamic interstitial iron imaging approach (dynamic  $\text{Fe}_i$ ) is the empirical investigation of Geerligs and Macdonald [134] who linked the dissociation rate with the interstitial iron concentration. If knowing the dissociation rate  $R_{\text{diss}}$  and the average photogeneration rate  $G_{\text{av}}$  [Eq. (2.38)], the interstitial iron concentration is easily calculated using Eq. (4.9):

$$[\text{Fe}_i] = G_{\text{av}} \sqrt{\frac{C_{\text{diss}}}{R_{\text{diss}}}}. \quad (4.11)$$

The dissociation rate  $R_{\text{diss}}$  can be obtained by linear regression of the derivative of the natural logarithm of the FeB pair concentration  $[\text{FeB}]_{\text{rel}}$  [Eq. (4.6)], normalized with respect to the total FeB concentration at  $t = 0$  [134]:

$$\frac{d[\ln([\text{FeB}]_{\text{rel}})]}{dt} \Big|_{t=0} = \frac{1}{[\text{FeB}]_{\text{rel}}(t=0)} \times \frac{d[\text{FeB}]_{\text{rel}}}{dt} \Big|_{t=0} = -R_{\text{diss}}. \quad (4.12)$$

Equation (4.12) is valid for  $t = 0$  or at least for  $t \ll (R_{\text{rep}} + R_{\text{diss}})^{-1}$ .

At low injection levels, the measured PL signal  $I_{\text{PL}}$  is proportional to the excess carrier density. Hence, for a constant photogeneration rate,  $I_{\text{PL}}$  is proportional to the carrier lifetime. Using this knowledge and Eq. (4.2), the relative FeB concentration  $[\text{FeB}]_{\text{PL,rel}}(t)$  can be calculated using only measured PL signals without requiring an additional calibration technique:

$$[\text{FeB}]_{\text{PL,rel}}(t) \propto \frac{1}{I_{\text{PL,Fe}_i}} - \frac{1}{I_{\text{PL,FeB}}(t)}, \quad (4.13)$$

with  $I_{\text{PL,Fe}_i}$  being the PL signal measured in the dissociated state of the FeB pairs and  $I_{\text{PL,FeB}}(t)$  being the time-dependent PL signal after FeB pair association during constant photogeneration. In order to ensure the validity of Eq. (4.13), the prefactor  $C_{\text{SRH}}$  of Eq. (4.2) is assumed to be independent of the injection density, which is a good approximation for low injection densities about two orders of magnitude below the characteristic cross-over point ( $\Delta n \leq 10^{12} \text{ cm}^{-3}$ ).

Using a PL setup, a quantity proportional to the integral of  $[\text{FeB}]_{\text{PL,rel}}$  over the camera integration time  $t_{\text{int}}$  is acquired. However, Eq. (4.12) can still be applied for the determination of  $R_{\text{diss}}$  if

$$t_{\text{int}} \ll (R_{\text{rep}} + R_{\text{diss}})^{-1}. \quad (4.14)$$

If Eq. (4.14) is fulfilled, the integral of  $[\text{FeB}]_{\text{PL,rel}}(t)$  over the camera integration time can be approximately written as  $[\text{FeB}]_{\text{PL,rel}} \cdot t_{\text{int}}$ . Thus, division of the measured quantity by the camera integration time  $t_{\text{int}}$  allows the determination of  $R_{\text{diss}}$ .

The PL measurements are performed at a constant photogeneration rate. For that reason, the injection density varies during the acquisition of  $I_{\text{PL,FeB}}(t)$ . As a consequence, an injection-dependent lifetime has an impact on  $I_{\text{PL,FeB}}(t)$ . However, the carrier lifetime in the presence of  $\text{Fe}_i$  is expected to be constant at low-level injection (see Fig. 4.1). Thus, no appreciable impact is expected due to the defect-related injection-dependent carrier lifetime. In the presence of another noticeable recombination path or at higher injection densities, the impact of an injection-dependent carrier lifetime has to be taken into account.

The dissociation of FeB pairs was shown to be recombination-enhanced [122]. Thus, the dissociation rate  $R_{\text{diss}}$  is related to the recombination rate of the injected excess carriers. This can also be derived from the empirical quadratic dependence of Geerligs and Macdonald [Eq. (4.9)] since the generation rate  $G$  equals the recombination rate in equilibrium. Geerligs and Macdonald [134] measured the dissociation rate for a sample with and without surface passivation and changed in this way the recombination per FeB pair. For the unpassivated sample, they found a reduced dissociation rate compared to the passivated sample. As a consequence, it can be concluded that for the application of the dynamic  $\text{Fe}_i$  technique, the recombination via the FeB pairs has to be the lifetime-limiting process. Otherwise, the empirical prefactor  $C_{\text{diss}}$  has to be adjusted.

Note that the dissociation rate depends on the actual generation (recombination) rate  $G$  and not on the average generation rate  $G_{\text{av}}$ .  $G$  and  $G_{\text{av}}$  are only equal if the injected carriers are homogeneously distributed throughout the sample. For high  $[\text{Fe}_i]$  and short excitation wavelengths, the excess carriers are located close to the surface directed to the excitation. In that case, the definition of  $G_{\text{av}}$  should be corrected for by using an effective thickness  $W_{\text{eff}}$  [see Eq. (2.35)]. If the physical thickness  $W$  is used instead of  $W_{\text{eff}}$ ,  $[\text{Fe}_i]_{\text{dyn}}$  would be underestimated. Fortunately, the expected uncertainty is supposed to be small for thin wafers. For a typical wafer thickness of  $W = 170 \mu\text{m}$ , the uncertainty for  $[\text{Fe}_i] = 10^{13} \text{ cm}^{-3}$  is below 20%.

### 4.3.2 Experimental

The procedure to establish the associated or dissociated state of the FeB pairs in the Si wafer was presented in Section 4.2.1. For the dynamic  $\text{Fe}_i$  approach, a sequence of PL images is acquired for the determination of  $[\text{FeB}]_{\text{PL,rel}}(t)$  after complete association

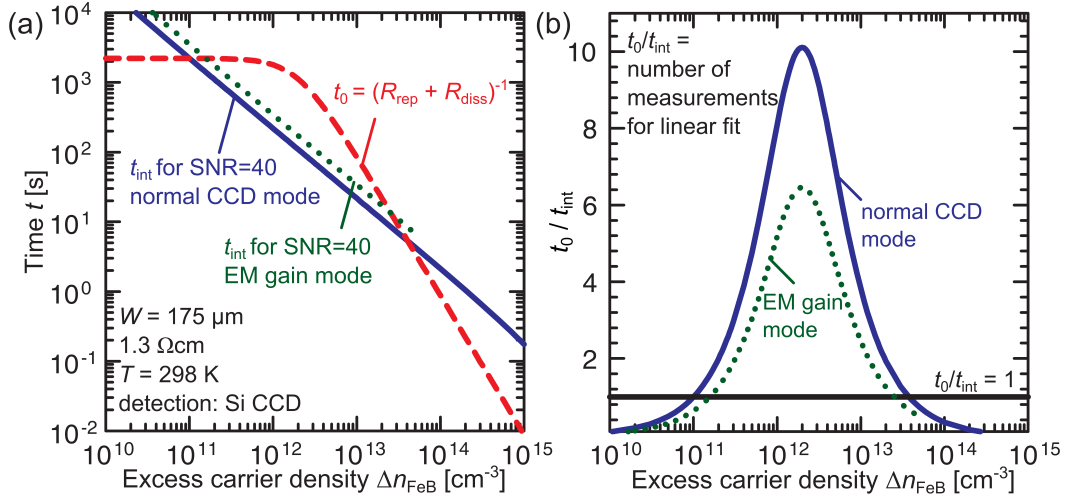


**Figure 4.8:** Optimal measurement condition for dynamic  $\text{Fe}_i$  imaging. (a) Comparison of the camera integration time  $t_{\text{int}}$  necessary to achieve a certain signal-to-noise ratio SNR with the time  $t_0 = (R_{\text{rep}} + R_{\text{diss}})^{-1}$  [time constant of Eq. (4.6)]. (b) The ratio  $t_0/t_{\text{int}}$  represents the number of data points that are maximal available for the linear regression if acquiring PL images with a SNR of 40.

of the  $\text{FeB}$  pairs to observe the impact of the impinging excitation light. The light source is off between each image acquisition. The period in the dark can be neglected in the evaluation since the  $\text{FeB}$  fraction that re-pairs during that time is negligible compared to the dissociated fraction. The average photogeneration rate for excess carriers  $G_{\text{av}}$  is calculated using Eq. (2.38).

The choice of the camera integration time  $t_{\text{int}}$  for the measurement of the dissociation rate  $R_{\text{diss}}$  is on the one hand controlled by an appropriate signal-to-noise ratio SNR but on the other hand should be chosen adequate to allow the determination of  $R_{\text{diss}}$  from Eq. (4.12). At least three data points are required in a time interval  $t \ll (R_{\text{rep}} + R_{\text{diss}})^{-1}$  to allow for a linear regression of the data.

Due to the specific dependence of the dissociation rate  $R_{\text{diss}}$  on the  $\text{Fe}_i$  concentration and the photogeneration rate, the sensitivity of the dynamic approach should not depend on  $[\text{Fe}_i]$  but only on the injection density of the PL measurement. This is a consequence of the linear dependence of the SRH recombination lifetime on the inverse impurity concentration [Eq. (1.16)]. To realize the same injection density for different  $\text{Fe}_i$  concentrations, the generation rate has to be scaled proportionally to the  $\text{Fe}_i$  concentration, leaving the dissociation rate as a function of the excess carrier density:

$$R_{\text{diss}} \propto \Delta n^2. \quad (4.15)$$

For that reason, we calculate the camera integration time  $t_{\text{int}}$  necessary to achieve a certain signal-to-noise ratio SNR [using the noise parameters of the available detectors (p. 136)] and the time constant of the dissociation process  $t_0 = (R_{\text{rep}} + R_{\text{diss}})^{-1}$  [Eq. (4.6)] as a function of the injection density  $\Delta n_{\text{FeB}}$ .  $t_{\text{int}}$  and  $t_0$  are compared in

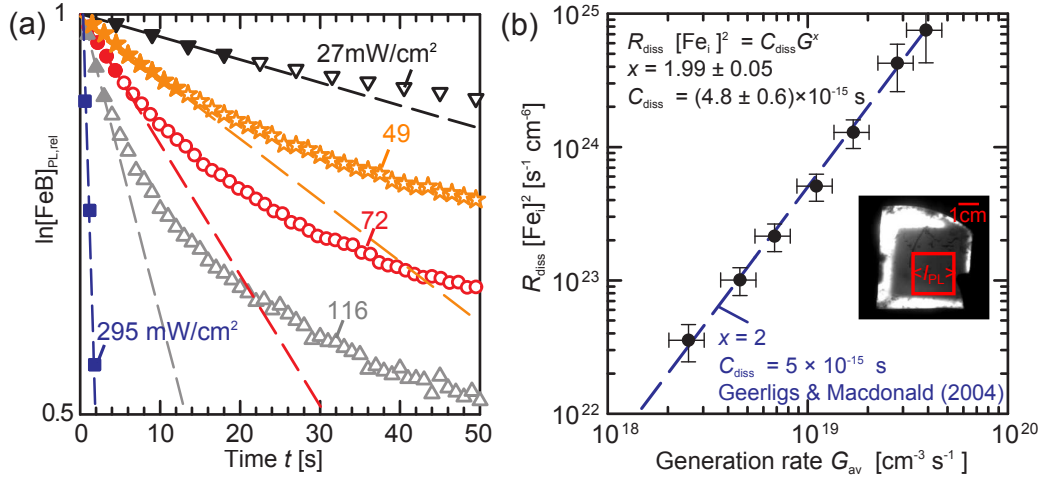


**Figure 4.9:** (a) Time dependence of the natural logarithm of  $[FeB]_{PL,rel}$  for different laser illumination intensities for a deliberately Fe-contaminated B-doped FZ-Si wafer with  $[Fe_i] = 2.5 \times 10^{12} \text{ cm}^{-3}$ . The filled symbols show the data points that are used for the linear regression (dashed lines). (b) Product of the measured  $R_{diss}$  of (a) and  $[Fe_i]^2$  as a function of the average generation rate  $G_{av}$ . The dashed blue line shows the dependence published in Ref. 134.

Fig. 4.8 (a).

The time interval for the complete PL sequence has to be smaller than  $t_0 = (R_{rep} + R_{diss})^{-1}$  to allow the correct determination of  $R_{diss}$  with Eq. (4.12). Otherwise, a linear regression is not possible since the fraction that is repaired again is notably increased. Hence, the ratio  $t_0(\Delta n)/t_{int}(\Delta n)$  specifies the number of measurements available for a linear regression with the slope being  $\sim R_{diss}$ . Figure 4.8 (b) shows the ratio  $t_0/t_{int}(\Delta n)$  and illustrates the best suitable injection density with the most data points available for the linear regression. As a consequence, the optimal measurement condition for a *p*-type Si wafer with a resistivity of 1.3  $\Omega\text{cm}$  at a temperature of 25°C is at an injection density of  $\sim 2 \times 10^{12} \text{ cm}^{-3}$ .

We found that the sensitivity of the dynamic  $Fe_i$  approach is not a function of the interstitial iron concentration but a function of the excess carrier density. Thus, basically arbitrary  $Fe_i$  concentrations are measurable using the dynamic  $Fe_i$  approach given that an appropriate excitation source is available that provides the required excess carrier density.

### 4.3.3 Verification on a deliberately Fe-contaminated FZ-Si wafer

In this Section, the results of Geerligs and Macdonald [134] [Eq. (4.9)] that form the basis of the dynamic  $Fe_i$  approach are verified. We measure the dissociation rate of FeB pairs at various illumination intensities for a deliberately Fe-contaminated SiN<sub>x</sub>-passivated FZ-Si wafer with a resistivity of 1  $\Omega\text{cm}$ , a thickness of 385  $\mu\text{m}$  and  $[Fe_i] = 2.5 \times 10^{12} \text{ cm}^{-3}$ . The iron (<sup>56</sup>Fe) was introduced by ion implantation using a

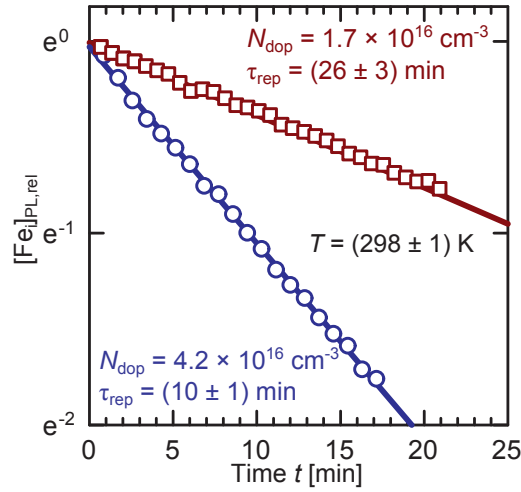


**Figure 4.10:** Natural logarithm of the relative  $Fe_i$  concentration  $[Fe_i]_{PL,rel}$  as a function of time for two wafers with different doping densities. The re-pairing time constant is obtained from a linear regression. The illumination intensity for both samples was set at  $4 \text{ mW/cm}^2$  ( $0.06 \text{ suns}$ ).

low-energy implanter ( $\sim 70 \text{ keV}$ ). After the implantation, the wafer was annealed at  $900^\circ\text{C}$  for 1 h to obtain a uniform iron distribution throughout the bulk. The actual  $Fe_i$  concentration was deduced from the implanted Fe dose. Details of the sample preparation have been published elsewhere [48].

The dissociation rate of FeB pairs  $R_{diss}$  is determined from  $[FeB]_{PL,rel}$  by linear regression of  $\ln([FeB]_{PL,rel})$  using Eq. (4.12). Figure 4.9 (a) shows  $\ln([FeB]_{PL,rel})$  as a function of time for different illumination intensities. The PL signal is averaged over an area of about  $2 \text{ cm}^2$  to increase the signal-to-noise ratio. The inset of Fig. 4.9 (b) shows a PL image of the investigated FZ-Si wafer. Clearly visible is the region with the implanted iron by the squared dark area as a result of the high recombination activity. The red square marks the area that is used for averaging the PL signal.

Figure 4.9 (b) presents the product of  $R_{diss}$ , as obtained from our PL measurements, and  $[Fe_i]^2$ , as calculated from the implanted dose, on a double logarithmic scale versus the measured photogeneration rate  $G_{av}$ . The dashed blue line shows the dependence published by Geerligs and Macdonald [134]. The excellent agreement further justifies the determination of the  $Fe_i$  concentration from the dissociation rate of FeB pairs.

An additional verification of the procedure for determining the dissociation rate is given by measuring the repairing rate using a similar approach. The repairing rate of FeB pairs  $\tau_{rep}$  is derived from PL measurements for two wafers with different dopant densities. One  $0.4 \text{ }\Omega\text{cm}$  mc-Si wafer and one  $0.9 \text{ }\Omega\text{cm}$  FZ-Si wafer are used for the measurement of  $\tau_{rep}$ . A PL sequence is acquired with the  $Fe_i$  being dissociated at the beginning of the measurement. The re-pairing has to be analyzed at a low illumination intensity to prevent FeB pair dissociation during the measurement. Hence, the illumination intensity for both samples is chosen to be  $\sim 4 \text{ mW/cm}^2$  ( $0.06 \text{ suns}$ ).

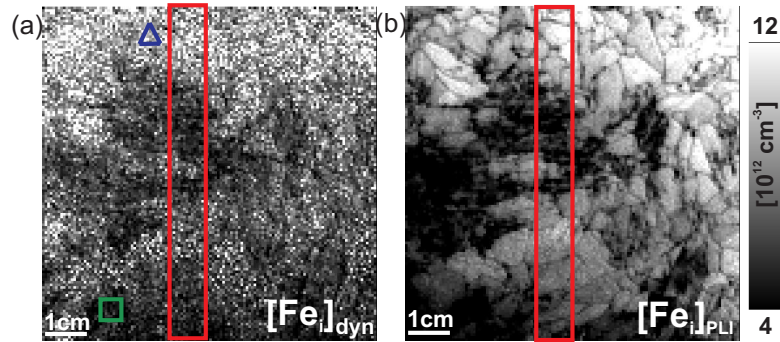


**Figure 4.11:** Spatially resolved interstitial iron concentration  $[Fe_i]$  for a wafer from the top region of an mc-Si ingot, determined from (a) the dissociation rate  $R_{diss}$  of FeB pairs ( $[Fe_i]_{dyn}$ ) and from (b) calibrated PL lifetime images ( $[Fe_i]_{PLI}$ ).

Figure 4.10 shows the relative concentration of mobile interstitial iron  $[Fe_i]_{PL,rel}$  as a function of time.  $[Fe_i]_{PL,rel}$  is calculated using Eq. (4.13) but inserting a time-dependent  $I_{PL,Fe_i}(t)$  and the actual value for  $I_{PL,FeB}$ . The association time constant is given by the slope of the time-dependent  $Fe_i$  concentration and is determined to be 26 min for the 0.9  $\Omega\text{cm}$  wafer and 10 min for the 0.4  $\Omega\text{cm}$  wafer. For comparison, the repairing time constant is calculated using the parameters published by Tan et al. [132] and found to be 24 min for the 0.9  $\Omega\text{cm}$  wafer and 10 min for the 0.4  $\Omega\text{cm}$  wafer. These values are in good agreement with the experimentally determined  $\tau_{rep}$  values of this work.

The doping dependence of the repairing rate can be used to determine the doping density from measurements of the re-pairing rate as Macdonald et al. [151] demonstrated on compensated Si. Lim et al. [152, 153] used this approach to measure the spatially-resolved dopant density of Si wafers with PL imaging.

#### 4.3.4 Application to an mc-Si wafer

The applicability of the dynamic  $Fe_i$  approach is demonstrated by investigating a solar-grade  $\text{SiN}_x$ -passivated mc-Si wafer with a resistivity of 0.4  $\Omega\text{cm}$  and a thickness of 170  $\mu\text{m}$ . The dynamically determined  $[Fe_i]_{dyn}$  image is shown in Fig. 4.11 (a). For comparison, Fig. 4.11 (b) shows the calculated interstitial iron concentration  $[Fe_i]_{PLI}$  from calibrated PL lifetime images. The PL information of 15 images is used for the linear regression [Eq. (4.12)] to determine  $R_{diss}$  with a camera integration time for each image of  $t_{int} = 1.5$  s and an illumination intensity of 34  $\text{mW}/\text{cm}^2$  (0.5 suns). Two measurements are averaged and a  $4 \times 4$  binning of the pixels is applied to increase the signal-to-noise ratio. Therefore, the total measurement time is 3 min.

For a better quantitative verification, a linescan is shown in Fig. 4.12 (a), averaged over 12 pixel rows, from the region marked with a red rectangle in Fig. 4.11. Figure 4.12 (b) exemplarily shows  $[FeB]_{PL,rel}(t)$  for two regions of the mc-Si wafer with different  $[Fe_i]$  that are marked in Fig. 4.11 with a green square and a blue triangle. A comparison

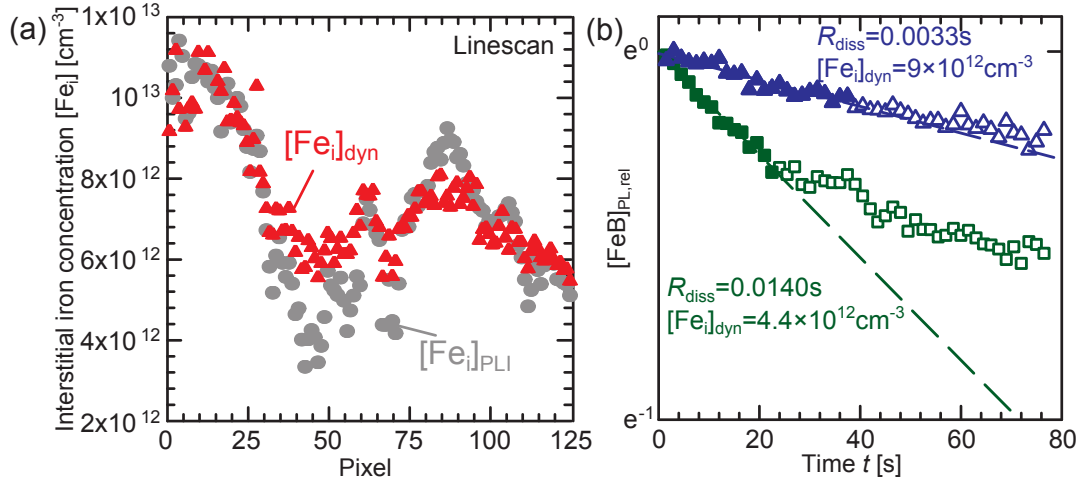


**Figure 4.12:** (a) Linescan of  $[Fe_i]_{dyn}$  and  $[Fe_i]_{PLI}$  averaged over 12 pixel rows that are marked in Fig. 4.11 with a red rectangle. (b) Time dependence of  $[FeB]_{rel,PL}(t)$  for two different regions of Fig. 4.11 (marked with a blue triangle and a green square). The dashed lines show the linear regressions of the filled data points for  $t < (R_{rep} + R_{diss})^{-1}$ .

of  $[Fe_i]_{dyn}$  and  $[Fe_i]_{PLI}$  in Figs. 4.11 and 4.12 (a) shows only deviations in the regions of low  $[Fe_i]$ .

It should be noted that averaging the time-dependent PL signal over two regions with strongly differing  $[Fe_i]$  will not result in the arithmetical mean of the dissociation rates  $R_{diss}$  of the two regions. The region with the higher  $R_{diss}$  (i.e. the area with lower  $[Fe_i]$ ) is overrated if averaging the PL signal over both regions due to the higher lifetime and injection density of that area. This behavior is reversed if the camera integration time  $t_{int}$  is larger than  $R_{diss}^{-1}$  for the area with low  $[Fe_i]$ . In that case, the region with the low  $Fe_i$  content has no impact on the decay of the averaged  $[FeB]_{PL,rel}$ .

A solution to this problem is the calibration of the image of  $[FeB]_{PL,rel}$  with the  $[Fe_i]_{dyn}$  image in a region of high (homogeneous)  $[Fe_i]$ . A positive side effect of this calibration would be an increased signal-to-noise ratio of the resulting  $[Fe_i]$  image.

The presented dynamic  $Fe_i$  approach is limited by the noise performance of the PL setup whereas the lifetime-based  $Fe_i$  approach is limited by the uncertainty of the recombination properties [see Fig. 4.1 (b)]. However, it is encouraging that the dynamic  $Fe_i$  approach is in good agreement with the lifetime-based  $Fe_i$  approach using the recombination properties listed in Tab. 4.1 and used in this work.

### 4.3.5 Summary

We introduced an alternative technique for the determination of the  $\text{Fe}_i$  concentration in B-doped Si wafers avoiding the necessity of measuring absolute values of the bulk lifetime. By merely detecting the time-dependent PL signal using a camera, the dissociation rate  $R_{\text{diss}}$  of FeB pairs is determined and utilized for the measurement of  $[\text{Fe}_i]$ . We found that the sensitivity of the dynamic  $\text{Fe}_i$  approach is not a function of the  $\text{Fe}_i$  concentration but a function of the excess carrier density. Thus, basically arbitrary  $\text{Fe}_i$  concentrations are measurable using the dynamic  $\text{Fe}_i$  approach given that an appropriate excitation source is available that provides the required excess carrier density. Our novel approach was verified by investigating a sample of known  $\text{Fe}_i$  concentration. Additionally, we generated the spatially resolved information of the  $\text{Fe}_i$  concentration of an mc-Si wafer.

The main advantages of the dynamic  $\text{Fe}_i$  approach over lifetime-based techniques are: i) a lifetime calibration is not required, ii) an exact knowledge of the doping density is not needed, iii) the dynamic technique is less sensitive to optical sample inhomogeneities and, iv) the dynamic  $\text{Fe}_i$  approach is independent of the recombination parameters of  $\text{Fe}_i$  and FeB. Our dynamic  $\text{Fe}_i$  approach should also be applicable to other techniques measuring quantities proportional to the excess carrier density, such as free carrier emission or photoconductance-based techniques.



# CHAPTER 5

---

## Summary

---

Within the scope of this work, the photoluminescence (PL) emission of silicon (Si) wafers was used to characterize their electrical quality. We realized two different approaches for PL-based carrier lifetime measurements. The first approach evaluates the PL emission under steady-state conditions of the generated excess carriers. The second approach analyzes the time-dependent PL emission for a modulated generation of excess carriers. Moreover, a new approach for determining the interstitial iron concentration in boron-doped Si was proposed and verified. The new approach is based on the measurement of the iron-boron dissociation rate from time-dependent PL measurements and is independent of absolute values of the carrier lifetime.

The steady-state lifetime approach was realized by implementing a photoconductance-based lifetime setup into a PL setup. The combination of both setups enables the calibration of the measured PL signal with a calibrated photoconductance (PC) measurement at identical excitation conditions.

We investigated if a single calibration procedure is sufficient to measure the recombination lifetime of wafers that differ in thickness, doping density and surface properties. The dependence of the PL emission on the doping density was found to be linear in the investigated doping range. Due to the increasing fraction of reabsorbed PL photons with wafer thickness, the calibration parameter does not scale linearly with thickness. However, the calibration can be linearly approximated for small thickness variations. The surface morphology was found to have a strong impact on the PL emission. We measured a four times higher PL emission for a textured surface compared to a planar surface. Even the unintentional surface roughness of an isotropically

etched multicrystalline silicon (mc-Si) wafer has led to an about two times higher calibration parameter than the polished surface of a float-zone Si wafer. Furthermore, we demonstrated that the PL calibration with a PC measurement is only valid for arbitrary injection and lifetime ranges if the charge carriers are homogeneously distributed as a function of the sample depth. As a consequence, we developed and verified a generalized calibration relation that takes the impact of an inhomogeneous carrier profile into account.

A second lifetime technique based on time-dependent PL measurements was realized by adapting the dynamic infrared lifetime mapping approach (dynamic ILM) of Ramspeck et al. [83]. We demonstrated that the ratio of three PL images (and one dark image), acquired at different times during a modulated excitation, is only a function of the camera integration time and the carrier lifetime. For that reason, it is possible to determine the carrier lifetime from the PL image ratio by comparison with a look-up table.

We demonstrated that the sensitivity of the dynamic PL approach is a function of the camera integration time and the effective carrier lifetime. We concluded that for each carrier lifetime an optimal camera integration time exists for minimizing the uncertainty in the measured dynamic carrier lifetime. The optimal camera integration time is about three times the effective carrier lifetime if considering the specific noise behavior of the used detector. The sensitivity analysis showed that lifetimes can be reliably measured with a systematic error of  $\sim 14\%$  down to  $20 \mu\text{s}$  for a measurement time of  $160 \text{ s}$  and an illumination intensity of  $1 \text{ sun}$ . For a dynamic lifetime approach, the impact of an injection-dependent lifetime has to be considered. We found from numerical simulation that for most relevant cases the difference between the measured dynamic lifetime and the actual steady-state lifetime is negligible. We showed that by an appropriate choice of the camera integration time, the impact of an injection-dependent lifetime can be significantly reduced.

Furthermore, we demonstrated the applicability of the dynamic PLI lifetime technique to thick Si bricks. An analytical expression for the dynamic image ratio was derived that takes the impact of surface recombination into account. We found that the exact knowledge of the sample thickness  $W$  and the surface recombination velocity  $S$  is not required for determining the bulk lifetime with dynamic PL lifetime imaging if  $S > 10^4 \text{ cm/s}$  and  $W > 0.3 \text{ cm}$ . Additionally, the accessible information depth of the PLI technique was analyzed and found to increase with increasing bulk lifetime. For a bulk lifetime of  $100 \mu\text{s}$ , the information depth is expected to be  $\sim 1 \text{ mm}$ .

We used PL-based lifetime measurements for the spatially-resolved determination of the interstitial iron ( $\text{Fe}_i$ ) concentration. Two approaches for reducing the  $\text{Fe}_i$  concentration in mc-Si were analyzed with respect to their efficiency. By adding copper and iron to the feedstock of directionally-solidified mc-Si ingots, co-precipitation of copper and iron was expected with the result of enhanced precipitation of the iron. However, we found that the presence of additional copper does not reduce the  $\text{Fe}_i$  content in our mc-Si ingots. Additionally, we studied the impact of long-term annealing at  $450^\circ\text{C}$  on

the  $\text{Fe}_i$  concentration of a deliberately-contaminated mc-Si wafer. We found that the overall  $\text{Fe}_i$  concentration is reduced by one order of magnitude after 4 h at 450°C due to internal gettering at crystallographic defects.

Additionally, we developed a novel technique for determining the  $\text{Fe}_i$  concentration in boron-doped Si wafers that avoids the necessity of measuring absolute values of the bulk lifetime. By merely detecting the time-dependent PL signal, the dissociation rate of FeB pairs is determined and used for the measurement of the interstitial iron concentration.



---

## Appendix: Camera noise analysis

---

In this Section, the main noise sources of the measured PL images are shortly presented and in part experimentally verified. Afterwards, the presented noise sources are combined to an analytical model for the accessible signal-to-noise ratio (SNR). The main noise sources that are considered are the photon shot noise, dark noise, and read-out noise. Within the scope of this work, the SNR model is used for assessing the sensitivity of the developed characterization techniques.

In this work, we investigate the noise properties of a Si CCD camera from Hamamatsu Photonics (model: C9100-13). An overview of the noise specifications can be found in Tab. A.1 for the normal CCD mode and the EM gain mode (with an electron multiplication amplifier). A more detailed description of the noise properties of CCD sensors can be found in Refs. 154–156. For comparison, we listed the noise data of the InGaAs CMOS camera (Xenics, model: Cheetah, data from Ref. 80) that is used for the dynamic PL lifetime imaging approach (Section 3.3).

**The photon shot noise**  $\sigma_s$  describes the variation of the emitted photons and obeys the Poisson statistics. Hence, the variance of a measured number of photons  $\Phi_{\text{ph}}$  is the number itself:

$$\sigma_s^2 = A_{\text{conv}}\Phi_{\text{ph}} = \Phi_S t_{\text{int}}, \quad (\text{A.1})$$

with  $A_{\text{conv}}$  being the conversion factor from detected photons into signal electrons of the detector.  $\Phi_S$  is the number of signal electrons per second and the camera integration time  $t_{\text{int}}$  describes the time span in which the detector collects signal electrons.

**Read-out noise**  $\sigma_{\text{ro}}$  results from the conversion of the collected charge carriers into a digital unit. For the Si CCD, the read-out noise is caused by an on-chip floating diffusion amplifier which converts the charges into a voltage. Read-out noise is prima-

rily caused by resetting the amplifier after the voltage conversion of the accumulated charges before the read-out of the next pixel.

For the verification of the noise specifications, found in the data sheet of the manufacturer, we determine the standard deviation of a signal measurement with a sealed camera opening. Figure A.1 (a) shows a normalized histogram of 3500 signal measurements in the dark for the two modes of the camera (EM gain and normal CCD).

For the histogram analysis, the photon shot noise and the dark current signal is negligible since the measurement is performed in the dark and within a short camera integration time. The read-out noise is determined by comparison with a Gaussian distribution curve. The result for the Si CCD in the normal CCD mode of  $\sigma_{\text{ro}} = A_{\text{conv}} \cdot \sigma_{\text{Gauss}} = 16.8 \text{ e}^-/\text{s}$  is comparable with the value of  $17 \text{ e}^-/\text{s}$  from the manufacturer. In the EM gain mode, the measured value of  $\sigma_{\text{ro}} = A_{\text{conv}} \cdot \sigma_{\text{Gauss}} = 215 \text{ e}^-/\text{s}$  differs strongly from the value of  $1 \text{ e}^-/\text{s}$  that was specified from the manufacturer. However, the SNR in the EM gain mode is not limited by the read-out noise for the signal range that is measured in this work. For that reason, the difference is not further investigated.

**Excess noise** has only to be considered if using a camera with an electron multiplication amplifier. The excess noise  $F$  results from fluctuations of the gain  $g$ . Since all signal electrons are amplified before the actual read-out, the excess noise has only an impact on the dark and the photon shot noise. The impact of the excess noise is considered by the product  $F^2 g^2$  with  $F = \sqrt{2}$  [155].

Figure A.1 (b) shows the verification of the detector linearity by measuring the electroluminescence signal of a forward-biased solar cell for both modes of the Si CCD camera. This graph is well-suited to determine the actual gain of the camera in the EM gain mode. The factor between the two slopes is 125. Considering the different conversion factors of the two modes, the actual amplification factor of the EM gain mode is  $g = 518$ .

**Dark noise**  $\sigma_{\text{d}}$  originates from the thermal generation of charge carriers in each pixel of the sensor. For the Si CCD the dark current is specified with only  $0.01 \text{ e}^-/\text{s}/\text{pixel}$ . This low value is achieved by cooling the sensor down to  $-65^\circ\text{C}$  using a multi-stage peltier element.

For verification, the thermally generated signal electrons are measured by acquiring the camera signal as a function of time avoiding the detection of photons by sealing the detector opening. Due to the low temperature of the sensor, a long time is required to measure an impact of dark current. The result of this measurement is shown in Fig. A.1 (c). Each data point is an average of four measurements. The slope equals the dark current  $I_{\text{d}}$  and is found to be  $(0.006 \pm 0.002) \text{ e}^-/\text{s}$ . Thus, our experimentally determined value is in agreement with the specification of the manufacturer. Since the generation of dark signal electrons is obeying the Poisson statistics, the dark noise

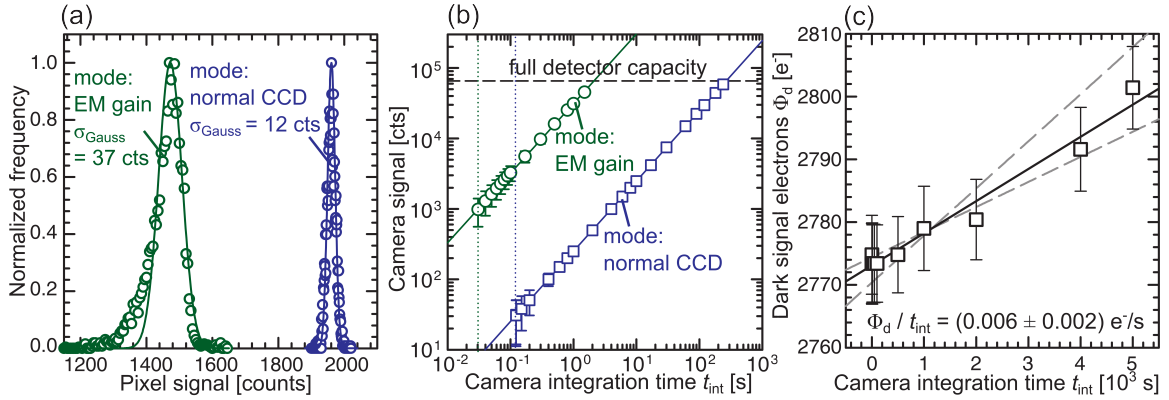


**Figure A.1:** (a) Normalized histogram of 3500 measurements of a single pixel with a sealed camera opening for the normal CCD and the EM gain mode. (b) Camera signal as a function of the integration time  $t_{\text{int}}$  for both available detector modes. (c) Camera signal as function of the integration time  $t_{\text{int}}$  with a sealed camera opening.

variance  $\sigma_d^2$  is given by the number of detected dark signal electrons  $\Phi_d$ :

$$\sigma_d^2 = \Phi_d = I_d t_{\text{int}}. \quad (\text{A.2})$$

**The total noise** variance  $\sigma_t^2$  of a single camera measurement is defined by the sum of the signal variances:

$$\sigma_t^2 = F^2 g^2 (\sigma_s^2 + \sigma_d^2) + \sigma_{\text{ro}}^2. \quad (\text{A.3})$$

Since the actual net signal of an optically excited Si wafer is determined by subtracting a measurement in the dark from a measurement with optical excitation, the read-out noise and the dark noise of the dark image has to be considered as well (hence, the factor two):

$$\sigma_t^2 = F^2 g^2 (\sigma_s^2 + 2\sigma_d^2) + 2\sigma_{\text{ro}}^2. \quad (\text{A.4})$$

The measured camera signal  $I_{\text{PL}}$  is given by

$$I_{\text{PL}} = \frac{\Phi_{\text{S,total}}}{A_{\text{conv}}} = \frac{\Phi_{\text{S}} t_{\text{int}} g}{A_{\text{conv}}}, \quad (\text{A.5})$$

where  $\Phi_{\text{S,total}}$  is the total number of signal electrons that are collected during the camera integration time  $t_{\text{int}}$ . The signal-to-noise ratio SNR of the acquired camera signal  $I_{\text{PL}}$  is defined as

$$\text{SNR} := \frac{I_{\text{PL}}}{v} \quad \text{with} \quad v := \frac{\sigma_t}{\sqrt{N}}, \quad (\text{A.6})$$

with the standard error or noise  $v$  calculated from the standard deviation  $\sigma_t$  of  $N$  measurements. Thus, the SNR can be expressed as a function of the single noise

components:

$$\begin{aligned} \text{SNR} &= \frac{\Phi_S g t_{\text{int}} \sqrt{N}}{\sigma_t} \\ &= \sqrt{N} \Phi_S g t_{\text{int}} \left( F^2 g^2 (\Phi_S + 2\Phi_{\text{dark}}) t_{\text{int}} + 2\sigma_{\text{ro}}^2 + F^2 g^2 2\sigma_{\text{temp}}^2 \right)^{-1/2}, \quad (\text{A.7}) \end{aligned}$$

where  $\sigma_{\text{temp}}^2$  is an additional noise source that is discovered especially for the InGaAs CMOS detector [80]. If using a camera mode without electron multiplication gain,  $F$  and  $g$  are set to one.

The analytical model for the SNR is verified by measurements of the SNR as a function of the camera integration time for both detectors that are used in this work. Measured and calculated SNR are shown in Fig. 2.9 and are in good agreement (see Section 2.2.3). The measured signal corresponds to an electroluminescence spectrum emitted from a solar cell operating at an applied voltage of 550 mV. Equal measurement conditions are used to allow a comparison of the two detectors. We used the same optics (lenses and filters), the same position of the solar cell image within the sensor and the same luminescence intensity for all data in Fig. 2.9.

From the analytical analysis of the SNR, it is found that the dark noise has no significant impact anymore on the noise performance of the Si CCD since the sensor is cooled to  $-65^\circ\text{C}$ . The Si CCD in the EM gain mode is clearly limited by the excess noise due to the EM amplification. As a consequence, the read-out noise has only a negligible impact in the EM gain mode. The Si CCD in the normal CCD mode is rather limited by the photon shot noise which can be deduced from the square root behavior as a function of the camera integration time (for  $t_{\text{int}} > 1$  s in Fig. 2.9) whereas for the InGaAs CMOS camera, read-out noise and sensor temperature fluctuations still have a non-negligible impact on the noise performance of the camera.

**Tabelle A.1:** Camera noise specifications for the signal-to-noise analysis

camera mode	Si CCD normal CCD	Si CCD EM gain	InGaAs CMOS
manufacturer	Hamamatsu	Hamamatsu	Xenics
dark current $I_d$ [ $\text{e}^-/\text{s}/\text{px}$ ]	0.01	0.01	220000
read-out noise $\sigma_{\text{ro}}$ [ $\text{e}^-/\text{px}$ ]	16.8	215	104
temperature noise $\sigma_{\text{temp}}$ [ $\text{e}^-/\text{px}$ ]	0	0	62
conversion factor $A_{\text{conv}}$ [ $\text{e}^-/\text{cts}$ ]	1.4	5.8	5.34

---

## References

---

- [1] *Photon* **4**, 42 (2012).
- [2] D. K. Schroder, *Semiconductor material and device characterization*, Wiley. (2006).
- [3] I. Uchida, Observation of the recombination radiation from silicon  $p$ - $n$  junction, *Japanese Journal of Applied Physics* **2**, 561 (1963).
- [4] T. Fuyuki, H. Kondo, Y. Kaji, T. Yamazaki, Y. Takahashi, and Y. Uraoka, One shot mapping of minority carrier diffusion length in polycrystalline silicon solar cells using electroluminescence, *Proceedings of the 31st Photovoltaic Specialists Conference, Lake Buena Vista, Florida*, p. 1343 (2005).
- [5] T. Fuyuki, H. Kondo, T. Yamazaki, Y. Takahashi, and Y. Uraoka, Photographic surveying of minority carrier diffusion length in polycrystalline silicon solar cells by electroluminescence, *Applied Physics Letters* **86**, 262108 (2005).
- [6] T. Trupke, R. Bardos, M. Schubert, and W. Warta, Photoluminescence imaging of silicon wafers, *Applied Physics Letters* **89**, 044107 (2006).
- [7] T. Trupke, R. A. Bardos, M. D. Abbott, P. Würfel, E. Pink, Y. Augarten, F. W. Chen, K. Fisher, J. E. Cotter, M. Kasemann, M. Rüdiger, S. Kontermann, M. C. Schubert, M. The, S. W. Glunz, W. Warta, D. Macdonald, J. Tan, A. Cuevas, J. Bauer, R. Gupta, O. Breitenstein, T. Buonassisi, G. Tarnowski, A. Lorenz, H. P. Hartmann, D. H. Neuhaus, and J. M. Fernandez, Progress with luminescence imaging for the characterisation of silicon wafers and solar cells, *Proceedings of the 22nd European Photovoltaic Solar Energy Conference, Milan, Italy*, p. 22 (2007).

- 
- [8] W. van Roosbroeck and W. Shockley, Photon-radiative recombination of electrons and holes in germanium, *Physical Review* **94**, 1558 (1954).
- [9] H. Schlangenotto, H. Maeder, and W. Gerlach, *Physica Status Solidi (a)* **21**, 357 (1974).
- [10] P. P. Altermatt, F. Geelhaar, T. Trupke, X. Dai, A. Neisser, and E. Daub, Injection dependence of spontaneous radiative recombination in c-Si: experiment, theoretical analysis, and simulation, *Proceedings of the 5th International Conference on Numerical Simulation of Optoelectronic Devices, Berlin, Germany*, p. 47 (2005).
- [11] P. P. Altermatt, F. Geelhaar, T. Trupke, X. Dai, A. Neisser, and E. Daub, Injection dependence of spontaneous radiative recombination in crystalline silicon: Experimental verification and theoretical analysis, *Applied Physics Letters* **88**, 261901 (2006).
- [12] J. Dziejwior and W. Schmid, Auger coefficients for highly doped and highly excited silicon, *Applied Physics Letters* **31**, 346 (1977).
- [13] A. Hangleiter and R. Häcker, Enhancement of band-to-band Auger recombination in crystalline silicon, *Physical Review Letters* **65**, 215 (1990).
- [14] P. P. Altermatt, J. Schmidt, G. Heiser, and A. G. Aberle, Assessment and parameterisation of Coulomb-enhanced Auger recombination coefficients in lowly injected crystalline silicon, *Journal of Applied Physics* **82**, 4938 (1997).
- [15] J. Schmidt, M. Kerr, and P. P. Altermatt, Coulomb-enhanced Auger recombination in crystalline silicon at intermediate and high-injection densities, *Journal of Applied Physics* **88**, 1494 (2000).
- [16] M. J. Kerr and A. Cuevas, General parameterization of Auger recombination in crystalline silicon, *Journal of Applied Physics* **91**, 2473 (2002).
- [17] A. Richter, F. Werner, A. Cuevas, J. Schmidt, and S. W. Glunz, Improved parameterization of Auger recombination in silicon, *Energy Procedia* **27**, 88 (2012).
- [18] A. Richter, S. W. Glunz, F. Werner, J. Schmidt, and A. Cuevas, Improved quantitative description of Auger recombination in crystalline silicon, *Physical Review B* **86**, 165202 (2012).
- [19] W. Shockley and W. T. Read, Statistics of the recombinations of holes and electrons, *Physical Review* **87**, 835 (1952).
- [20] R. N. Hall, Electron-hole recombination in germanium, *Physical Review* **87**, 387 (1952).

- 
- [21] D. Macdonald and A. Cuevas, Validity of simplified Shockley-Read-Hall statistics for modeling carrier lifetimes in crystalline silicon, *Physical Review B* **67**, 075203 (2003).
- [22] H. Feichtinger, J. Watzl, and A. Gschwandtner, Localization of the  $\text{Fe}^0$ -level in silicon, *Solid State Communications* **27**, 867 (1978).
- [23] G. Zoth and W. Bergholz, A fast, preparation-free method to detect iron in silicon, *Journal of Applied Physics* **11**, 6764 (1990).
- [24] J. Schmidt and A. G. Aberle, Accurate method for the determination of bulk minority-carrier lifetimes of mono- and multicrystalline silicon wafers, *Journal of Applied Physics* **81**, 6186 (1997).
- [25] B. Hoex, J. Schmidt, P. Pohl, M. C. M. van de Sanden, and W. M. M. Kessels, Silicon surface passivation by atomic layer deposited  $\text{Al}_2\text{O}_3$ , *Journal of Applied Physics* **104**, 044903 (2008).
- [26] J. Schmidt, A. Merkle, R. Brendel, B. Hoex, M. C. M. van de Sanden, and W. M. M. Kessels, Surface passivation of high-efficiency silicon solar cells by atomic-layer-deposited  $\text{Al}_2\text{O}_3$ , *Progress in Photovoltaics* **16**, 461 (2008).
- [27] A. B. Sproul, Dimensionless solution of the equation describing the effect of surface recombination on carrier decay in semiconductors, *Journal of Applied Physics* **76**, 2851 (1994).
- [28] A. Cuevas and R. A. Sinton, Prediction of the open-circuit voltage of solar cells from the steady-state photocon, *Progress in Photovoltaics* **5**, 79 (1997).
- [29] R. Sinton and A. Cuevas, Contactless determination of current-voltage characteristics and minority carrier lifetimes in semiconductors from quasi-steady-state photoconductance data, *Applied Physics Letters* **69**, 2510 (1996).
- [30] M. Bail, J. Kentsch, R. Brendel, and M. Schulz, Lifetime mapping of Si wafers by an infrared camera [for solar cell production], *Proceedings of the 28th IEEE Photovoltaic Specialists Conference, Anchorage, AK, USA*, p. 99 (2000).
- [31] P. Würfel, T. Trupke, T. Puzzer, E. Schäffer, W. Warta, and S. Glunz, Diffusion lengths of silicon solar cells from luminescence images, *Journal of Applied Physics* **101**, 123110 (2007).
- [32] J. Giesecke, M. Kasemann, M. C. Schubert, B. Michl, M. The, W. Warta, and P. Würfel, Determination of minority carrier diffusion lengths in silicon solar cells from photoluminescence images, *Proceedings of the 23rd European Photovoltaic Solar Energy Conference, Valencia, Spain*, p. 453 (2008).

- 
- [33] J. A. Giesecke, M. Kasemann, and W. Warta, Determination of local minority carrier diffusion lengths in crystalline silicon from luminescence images, *Journal of Applied Physics* **106**, 014907 (2009).
- [34] T. Trupke, B. Mitchell, J. W. Weber, and J. Nyhus, Bulk minority carrier lifetime from luminescence intensity ratios measured on silicon bricks, *Proceedings of the 25th European Photovoltaic Solar Energy Conference, Valencia, Spain*, p. 1307 (2010).
- [35] D. T. Stevenson and R. J. Keyes, Measurement of carrier lifetimes in germanium and silicon, *Journal of Applied Physics* **26**, 190 (1955).
- [36] E. Yablonovitch and T. Gmitter, Auger recombination in silicon at low carrier densities, *Applied Physics Letters* **49**, 587 (1986).
- [37] H. Nagel, C. Berge, and A. G. Aberle, Generalized analysis of quasi-steady-state and quasi-transient measurements of carrier lifetimes in semiconductors, *Journal of Applied Physics* **86**, 6218 (1999).
- [38] S. Deb and B. Nag, Measurement of carriers in semiconductors through microwave reflection, *Journal of Applied Physics* **33**, 1604 (1962).
- [39] M. Kunst and G. Beck, The study of charge carrier kinetics in semiconductors by microwave conductivity measurements, *Journal of Applied Physics* **60**, 3558 (1986).
- [40] M. Kunst and G. Beck, The study of charge carrier kinetics in semiconductors by microwave conductivity measurements II, *Journal of Applied Physics* **63**, 1093 (1988).
- [41] J. Schmidt, Measurement of differential and actual recombination parameters on crystalline silicon wafers, *IEEE Transactions on Electronic Devices* **46**, 2018 (1999).
- [42] D. B. M. Klaassen, A unified mobility model for device simulation - I. model equations and concentration dependence, *Solid-State Electronics* **35**, 953 (1992).
- [43] P. P. Altermatt, J. Schmidt, M. Kerr, G. Heiser, and A. G. Aberle, Exciton-enhanced Auger recombination in crystalline silicon under intermediate and high injection conditions, *Proceedings of the 16th European Photovoltaic Solar Energy Conference*, p. 243 (2000).
- [44] C. Berge, Vergleich transienter und quasistatischer Photoleitfähigkeitsmessungen an kristallinem Silicium, Diplomarbeit, Leibniz Universität Hannover (1998).
- [45] D. Macdonald and A. Cuevas, Trapping of minority carriers in multicrystalline silicon, *Applied Physics Letters* **74**, 1710 (1999).

- 
- [46] J. Schmidt, K. Bothe, and R. Hezel, Oxygen-related minority-carrier trapping centers in *p*-type Czochralski-grown silicon, *Applied Physics Letters* **80**, 4395 (2002).
- [47] J. A. Hornbeck and J. R. Haynes, Trapping of minority carriers in silicon. I. *p*-type silicon, *Physical Review* **97**, 311 (1955).
- [48] J. E. Birkholz, K. Bothe, D. Macdonald, and J. Schmidt, Electronic properties of iron-boron pairs in crystalline silicon by temperature- and injection-level-dependent lifetime measurements, *Journal of Applied Physics* **97**, 103708 (2005).
- [49] D. Macdonald, T. Roth, P. N. K. Deenapanray, T. Trupke, and R. A. Bardos, Doping dependence of the carrier lifetime crossover point upon dissociation of iron-boron pairs in crystalline silicon, *Applied Physics Letters* **89**, 142107 (2006).
- [50] P. Pohl, J. Schmidt, K. Bothe, and R. Brendel, Mapping of trap densities and energy levels in semiconductors using a lock-in infrared camera technique, *Applied Physics Letters* **87**, 142104 (2005).
- [51] M. Bail, M. Schulz, and R. Brendel, Space-charge region-dominated steady-state photoconductance in low-lifetime Si wafers, *Applied Physics Letters* **82**, 757 (2003).
- [52] D. H. Neuhaus, P. J. Cousins., and A. G. Aberle, Trapping and junction-related perturbations of the effective excess carrier lifetime, *Proceedings of the 3rd World Conference on Photovoltaic Energy Conversion, Osaka, Japan*, p. 91 (2003).
- [53] P. J. Cousins, D. H. Neuhaus, and J. E. Cotter, Experimental verification of the effect of depletion-region modulation on photoconductance lifetime measurements, *Journal of Applied Physics* **95**, 1854 (2004).
- [54] M. Garín, I. Martín, S. Bermejo, and R. Alcubilla, Fixed charge density in dielectrics deposited in *c*-Si using space charge region dominated lifetime measurements, *Journal of Applied Physics* **101**, 123716 (2007).
- [55] S. M. Sze and K. K. Ng, *Physics of semiconductor devices*, Wiley, Third Edition (2007).
- [56] P. Würfel, *Physics of solar cells*, Wiley (2005).
- [57] M. Planck, Über das Gesetz der Energieverteilung im Normalspectrum, *Annalen der Physik* **309**, 553 (1901).
- [58] P. Würfel, The chemical potential of radiation, *Journal of Physics C: Solid State Physics* **15**, 3967 (1982).

- 
- [59] K. Schick, E. Daub, S. Finkbeiner, and P. Würfel, Verification of a generalized Planck law for luminescence radiation from silicon solar cells, *Applied Physics A* **54**, 109 (1992).
- [60] P. Würfel, S. Finkbeiner, and E. Daub, Generalized Planck's radiation law for luminescence via indirect transitions, *Applied Physics A* **60**, 67 (1995).
- [61] F. Herrmann and P. Würfel, Light with nonzero chemical potential, *American Journal of Physics* **73**, 717 (2005).
- [62] T. Trupke, M. A. Green, P. Würfel, P. P. Altermatt, A. Wang, J. Zhao, and R. Corkish, Temperature dependence of the radiative recombination coefficient of intrinsic crystalline silicon, *Journal of Applied Physics* **94**, 4930 (2003).
- [63] M. A. Green and M. Keevers, Optical properties of intrinsic silicon at 300 K, *Progress in Photovoltaics* **3**, 189 (1995).
- [64] G. W. Hooft, The radiative recombination coefficient of GaAs from laser delay measurements and effective nonradiative carrier lifetimes, *Applied Physics Letters* **39**, 389 (1981).
- [65] E. Yablonovitch, Statistical ray optics, *Journal of the Optical Society of America* p. 899 (1982).
- [66] P. Campbell, Light trapping in textured solar cells, *Solar Energy Materials* **21**, 165 (1990).
- [67] C. Schinke, D. Hinken, J. Schmidt, K. Bothe, and R. Brendel, Modeling the spectral luminescence emission of silicon solar cells and wafers, *IEEE Journal of Photovoltaics* **3**, 1038 (2013).
- [68] J. Schmidt, *Untersuchungen zur Ladungsträgerrekombination an den Oberflächen und im Volumen von kristallinen Silicium-Solarzellen*, PhD thesis, Leibniz Universität Hannover (1998).
- [69] K. Ramspeck, *Characterization techniques for silicon solar cells and material using an infrared-camera based approach*, PhD thesis, Leibniz Universität Hannover (2009).
- [70] K. L. Luke and L.-P. Cheng, Analysis of the interaction of a laser pulse with a silicon wafer: Determination of bulk lifetime and surface recombination velocity, *Journal of Applied Physics* **61**, 2282 (1987).
- [71] G. S. Kousik, Z. G. Ling, and P. K. Ajmera, Nondestructive technique to measure bulk lifetime and surface recombination velocities at the two surfaces by infrared absorption due to pulsed optical excitation, *Journal of Applied Physics* **72**, 141 (1992).

- 
- [72] G. Duggan and G. B. Scott, The efficiency of photoluminescence of thin epitaxial semiconductors, *Journal of Applied Physics* **52**, 407 (1981).
- [73] S. Bowden and R. Sinton, Determining lifetime in silicon blocks and wafers with accurate expressions for carrier density, *Journal of Applied Physics* **102**, 124501 (2007).
- [74] T. Trupke, J. Nyhus, R. A. Sinton, and J. W. Weber, Photoluminescence imaging on silicon bricks, *Proceedings of the 24th European Photovoltaic Solar Energy Conference, Hamburg, Germany*, p. 1029 (2009).
- [75] M. Bigas, E. Cabruja, J. Forest, and J. Salvi, Review of CMOS image sensors, *Microelectronics Journal* **37**, 433 (2006).
- [76] P. Fiorentin, P. Iacomussi, and G. Rossi, Characterization and calibration of a CCD detector for light engineering, *IEEE Transactions of Instrumentation and Measurement* **54**, 171 (2005).
- [77] W. Bludau, A. Onton, and W. Heinke, Temperature dependence of the band gap of silicon, *Journal of Applied Physics* **45**, 1846 (1974).
- [78] K. S. Bindra, R. Chari, V. Shukla, A. Singh, S. Ida, and S. M. Oak, Two-photon absorption and nonlinear refraction in commercial colour glass filters, *Journal of Optics A: Pure and Applied Optics* **1**, 73 (1999).
- [79] D. Hinken, Ortsaufgelöste Charakterisierung von Silizium-Solarzellen durch Elektrolumineszenz, Diplomarbeit, Leibniz Universität Hannover (2007).
- [80] C. Schinke, Spektralanalyse der Elektrolumineszenzemission von Siliziumsolarzellen, Diplomarbeit, Leibniz Universität Hannover (2010).
- [81] N. Schüler, T. Hahn, K. Dornich, J. R. Niklas, and B. Gründig-Wendrock, Theoretical and experimental comparison of contactless lifetime measurement methods for thick silicon samples, *Solar Energy Materials & Solar Cells* **94**, 1076 (2010).
- [82] J. S. Swirhun, R. A. Sinton, M. K. Forsyth, and T. Mankad, Contactless measurement of minority carrier lifetime in silicon ingots and bricks, *Progress in Photovoltaics* **19**, 313 (2011).
- [83] K. Ramspeck, S. Reissenweber, J. Schmidt, K. Bothe, and R. Brendel, Dynamic carrier lifetime imaging of silicon wafers using an infrared camera-based approach, *Applied Physics Letters* **93**, 102104 (2008).
- [84] R. A. Bardos, T. Trupke, M. C. Schubert, and T. Roth, Trapping artifacts in quasi-steady-state photoluminescence and photoconductance lifetime measurements on silicon wafers, *Applied Physics Letters* **88**, 053504 (2006).

- [85] R. A. Sinton, H. Tathgar, S. Bowden, and A. Cuevas, On the problem of determining the bulk lifetime of unpassivated silicon wafers, *Proceedings of the 14th NREL Workshop on Crystalline Silicon Solar Cell Materials & Modules, Vail, USA*, p. 192 (2004).
- [86] K. Bothe, R. Krain, R. Falster, and R. Sinton, Determination of the bulk lifetime of bare multicrystalline silicon wafers, *Progress in Photovoltaics* **18**, 204 (2010).
- [87] J. R. Haynes and H. B. Briggs, *Physical Review* **86**, 647 (1952).
- [88] J. R. Haynes and W. C. Westphal, Radiation resulting from recombination of holes and electrons in silicon, *Physical Review* **101**, 1676 (1956).
- [89] K. Penner, Electroluminescence from silicon devices - a tool for device and material characterization, *Journal de Physique* **C4**, 797 (1988).
- [90] G. Bohnert, R. Häcker, and A. Hangleiter, Position resolved carrier lifetime measurements in silicon power devices by time resolved photoluminescence spectroscopy, *Journal de Physique* **C4**, 617 (1988).
- [91] I. Tarasov, S. Ostapenko, V. Feifer, S. McHugo, S. V. Kovesnikov, J. Weber, C. Haessler, and E.-U. Reisner, Defect diagnostics using scanning photoluminescence in multicrystalline silicon, *Physica B* **273-274**, 549 (1999).
- [92] T. Trupke, J. Zhao, A. Wang, R. Corkish, and M. A. Green, Very efficient light emission from bulk crystalline silicon, *Applied Physics Letters* **82**, 2996 (2003).
- [93] T. Trupke, R. A. Bardos, F. Hudert, P. Würfel, J. Zhao, A. Wang, and M. A. Green, Effective excess carrier lifetimes exceeding 100 milliseconds in float zone silicon determined from photoluminescence, *Proceedings of the 19th European Photovoltaic Solar Energy Conference, Paris, France*, p. 758 (2004).
- [94] T. Trupke and R. A. Bardos, Photoluminescence: A surprisingly sensitive lifetime technique, *Proceedings of the 31st IEEE photovoltaic specialists conference, Orlando, USA*, p. 903 (2005).
- [95] T. Trupke, R. A. Bardos, and M. D. Abbott, Self-consistent calibration of photoluminescence and photoconductance lifetime measurements, *Applied Physics Letters* **87**, 184102 (2005).
- [96] R. Brüggemann and S. Reynolds, Modulated photoluminescence studies for lifetime determination in amorphous-silicon passivated crystalline-silicon wafers, *Journal of Non-Crystalline Solids* **352**, 1888 (2006).
- [97] M. Abbott, J. Cotter, F. Chen, T. Trupke, R. Bardos, and K. Fisher, Application of photoluminescence characterization to the development and manufacturing of high-efficiency silicon solar cells, *Journal of Applied Physics* **100**, 114514 (2006).

- [98] H. Sugimoto and M. Tajima, Photoluminescence imaging of multicrystalline Si wafers during HF etching, *Japanese Journal of Applied Physics* **46**, L339 (2007).
- [99] M. The, M. C. Schubert, and W. Warta, Quantitative lifetime measurements with photoluminescence imaging, *Proceedings of the 22nd European Photovoltaic Solar Energy Conference, Milan, Italy*, p. 354 (2007).
- [100] D. Macdonald, J. Tan, R. A. Bardos, and T. Trupke, Impurities in solar-grade silicon and their characterisation, *Proceedings of the 22nd European Photovoltaic Conference, Milan, Italy*, p. 820 (2007).
- [101] D. Macdonald, J. Tan, and T. Trupke, Imaging interstitial iron concentrations in boron-doped crystalline silicon using photoluminescence, *Journal of Applied Physics* **103**, 073710 (2008).
- [102] T. Trupke, Influence of photon reabsorption on quasi-steady-state photoluminescence measurements on crystalline silicon, *Journal of Applied Physics* **100**, 063531 (2006).
- [103] W. Kern and P. A. Puotinen, Cleaning solutions based on hydrogen peroxide for use in silicon semiconductor technology, *RCA Review* **31**, 187 (1970).
- [104] J. A. Giesecke, M. C. Schubert, B. Michl, F. Schindler, and W. Warta, Minority carrier lifetime imaging of silicon wafers calibrated by quasi-steady-state photoluminescence, *Solar Energy Materials & Solar Cells* **95**, 1011 (2011).
- [105] Z. Hameiri, T. Trupke, N. Gao, R. A. Sinton, and J. W. Weber, Effective bulk doping concentration of diffused and undiffused silicon wafers obtained from combined photoconductance and photoluminescence measurements, *Progress in Photovoltaics* (2012). DOI: 10.1002/pip.2184.
- [106] F. M. Smits, Measurement of sheet resistivities with the four-point probe, *The Bell System Technical Journal* **37**, 711 (1958).
- [107] A. Cuevas, M. Stocks, D. Macdonald, and R. Sinton, Applications of the quasi-steady-state photoconductance technique, *Proceedings of the 2nd World Photovoltaic Solar Energy Conference, Vienna, Austria*, p. 1236 (1998).
- [108] D. Sautter and H. Weinerth, *Lexikon Elektrotechnik und Mikroelektronik*, Springer (1993).
- [109] O. Geschke, H. Klank, and P. Telleman, *Microsystem Engineering of Lab-on-a-Chip Devices*, Wiley (2004).
- [110] K. Ramspeck, K. Bothe, J. Schmidt, and R. Brendel, Combined dynamic and steady-state infrared camera based carrier lifetime imaging of silicon wafers, *Journal of Applied Physics* **106**, 114506 (2009).

- 
- [111] M. Kunst, G. Müller, R. Schmidt, and H. Wetzels, Surface and volume decay processes in semiconductors studied by contactless transient photoconductivity measurements, *Applied Physics A* **46**, 77 (1988).
- [112] A. B. Sproul, M. A. Green, and A. W. Stephens, Accurate determination of minority carrier- and lattice scattering-mobility in silicon from photoconductance decay, *Journal of Applied Physics* **92**, 4161 (1992).
- [113] P. Pohl, *Infrared camera-based imaging techniques for solar-grade silicon*, PhD thesis, Leibniz Universität Hannover (2007).
- [114] D. K. Schroder, R. N. Thomas, and J. C. Swartz, Free carrier absorption in silicon, *IEEE Journal of Solid-State Circuits* **13**, 180 (1978).
- [115] A. A. Istratov, H. Hieslmair, and E. R. Weber, Iron contamination in silicon technology, *Applied Physics A* **70**, 489 (2000).
- [116] M. Kittler, W. Seifert, K. Schmalz, and K. Tittelbach-Helmrich, Comparison of EBIC and DLTS measurements on boron-doped Cz silicon contaminated with iron, *Physica Status Solidi (a)* **96**, K133 (1986).
- [117] D. H. Macdonald, L. J. Geerligs, and A. Azzizi, Iron detection in crystalline silicon by carrier lifetime measurements for arbitrary injection and doping, *Journal of Applied Physics* **95**, 1021 (2004).
- [118] J. Schmidt and D. Macdonald, Recombination activity of iron-gallium and iron-indium pairs in silicon, *Journal of Applied Physics* **97**, 113712 (2005).
- [119] A. A. Istratov, H. Hieslmair, and E. R. Weber, Iron and its complexes in silicon, *Applied Physics A* **69**, 13 (1999).
- [120] A. A. Istratov, H. Hieslmair, and E. R. Weber, What do we know about iron in silicon after 45 yr of research, *Physica B* **273-274**, 412 (1999).
- [121] H. Lemke, Dotierungseigenschaften von Eisen in Silizium, *Physica Status Solidi (a)* **64**, 215 (1981).
- [122] L. C. Kimerling and J. L. Benton, Electronically controlled reactions of interstitial iron in silicon, *Physica B & C* **116B**, 197 (1983).
- [123] J. Lagowski, P. Edelman, A. M. Kontkietwicz, O. Milic, W. Henley, M. Dexter, L. Jastrzebski, and A. M. Hoff, Iron detection in the part per quadrillion range in silicon using surface photovoltage and photodissociation of iron-boron pairs, *Applied Physics Letters* **63**, 3043 (1993).
- [124] J. Lagowski, P. Edelman, M. Dexter, and W. Henley, Non-contact mapping of heavy metal contamination for silicon IC fabrication, *Semiconductor Science and Technology* **7**, A185 (1992).

- [125] O. Palais, S. Martinuzzi, and J. J. Simon, Minority carrier lifetime and metallic impurity mapping in silicon wafers, *Materials Science in Semiconductor Processing* **4**, 27 (2001).
- [126] O. Palais, E. Yakimow, and S. Martinuzzi, Minority carrier lifetime scan maps applied to iron concentration mapping in silicon wafers, *Materials Science and Engineering* **B91-92**, 216 (2002).
- [127] J. Henze, P. Pohl, C. Schmiga, M. Dhamrin, T. Saitoh, I. Yamaga, and J. Schmidt, Millisecond area-averaged lifetimes in gallium-doped multicrystalline silicon, *Proceedings of the 20th European Photovoltaic Solar Energy Conference, Barcelona, Spain*, p. 769 (2005).
- [128] S. Rein and S. W. Glunz, Electronic properties of interstitial iron and iron-boron pairs determined by means of advanced lifetime spectroscopy, *Journal of Applied Physics* **98**, 113711 (2005).
- [129] H. Reiss, C. S. Fuller, and F. J. Morin, Chemical interactions among defects in germanium and silicon, *The Bell System Technical Journal* **35**, 535 (1956).
- [130] D. Macdonald, T. Roth, P. N. K. Deenapanray, K. Bothe, P. Pohl, and J. Schmidt, Formation rates of iron-acceptor pairs in crystalline silicon, *Journal of Applied Physics* **98**, 083509 (2005).
- [131] E. R. Weber, Transition metals in silicon, *Applied Physics A* **30**, 1 (1983).
- [132] J. Tan, D. Macdonald, F. Rougieux, and A. Cuevas, Accurate measurement of the formation rate of iron-boron pairs in silicon, *Semiconductor Science and Technology* **26**, 055019 (2011).
- [133] K. Graff and H. Pieper, The properties of iron in silicon, *Journal of Electrochemical Society* **128**, 669 (1981).
- [134] L. J. Geerligs and D. Macdonald, Dynamics of light-induced FeB pair dissociation in crystalline silicon, *Applied Physics Letters* **85**, 5227 (2004).
- [135] M. C. Schubert, M. J. Kerler, and W. Warta, Influence of heterogeneous profiles in carrier density measurements with respect to iron concentration measurements in silicon, *Journal of Applied Physics* **105**, 114903 (2009).
- [136] A. A. Istratov, T. Buonassisi, R. J. Macdonald, A. R. Smith, R. Schindler, J. A. Rand, J. P. Kalejs, and E. R. Weber, Metal content of multicrystalline silicon for solar cells and its impact on minority carrier diffusion length, *Journal of Applied Physics* **94**, 6552 (2003).
- [137] D. Macdonald, A. Cuevas, A. Kinomura, Y. Nakano, and L. J. Geerligs, Transition metal profiles in a multicrystalline silicon ingot, *Journal of Applied Physics* **97**, 033523 (2005).

- [138] T. U. Naerland, L. Arnberg, and A. Holt, Origin of the low carrier lifetime edge zone in multicrystalline PV silicon, *Progress in Photovoltaics* **17**, 289 (2009).
- [139] P. S. Plekhanov, R. Gafiteanu, U. M. Gösele, and T. Y. Tan, Modeling of gettering of precipitated impurities from Si for carrier lifetime improvement in solar cell applications, *Journal of Applied Physics* **86**, 2453 (1999).
- [140] T. Buonassisi, A. A. Istratov, M. A. Marcus, B. Lai, Z. Cai, S. M. Heald, and E. R. Weber, Engineering metal-impurity nanodefects for low-cost solar cells, *Nature materials* **4**, 676 (2005).
- [141] T. Buonassisi, M. Heuer, A. Istratov, M. Pickett, M. Marcus, B. Lai, Z. Cai, S. Heald, and E. Weber, Transition metal co-precipitation mechanisms in silicon, *Acta Materialia* **55**, 6119 (2007).
- [142] S. Riepe, I. E. Reis, and W. Koch, Solar silicon material research network SolarFocus (Solarsilizium Forschungscluster), *Proceedings of the 23rd European Photovoltaic Solar Energy Conference, Valencia, Spain*, p. 1410 (2008).
- [143] R. Kvande, L. J. Geerligs, G. Coletti, L. Arnberg, M. D. Sabatino, E. J. Ovreid, and C. C. Swanson, Distribution of iron in multicrystalline silicon ingots, *Journal of Applied Physics* **104**, 064905 (2008).
- [144] D. Macdonald, T. Roth, L. J. Geerligs, and A. Cuevas, Behaviour of natural and implanted iron during annealing of multicrystalline silicon wafers, *Solid State Phenomena* **108-109**, 519 (2005).
- [145] T. Buonassisi, M. D. Pickett, and R. Sweeney, Reducing the concentration of interstitial iron in crystalline silicon solar cells via low ( $\leq 500^\circ\text{C}$ ) temperature annealing, *Proceedings of the 17th NREL Workshop on Crystalline Silicon Solar Cells & Modules, Vail, USA*, p. 218 (2007).
- [146] M. D. Pickett and T. Buonassisi, Iron point defect reduction in multicrystalline silicon solar cells, *Applied Physics Letters* **92**, 122103 (2008).
- [147] W. B. Henley and D. A. Ramappa, Iron precipitation in float zone grown silicon, *Journal of Applied Physics* **82**, 589 (1997).
- [148] L. L. Kazmerski, P. J. Ireland, and T. F. Ciszek, Evidence for the segregation of impurities to grain boundaries in multigrained silicon using Auger electron spectroscopy and secondary ion mass spectroscopy, *Applied Physics Letters* **63**, 323 (1980).
- [149] T. Buonassisi, A. A. Istratov, M. D. Pickett, M. A. Marcus, T. F. Ciszek, and E. R. Weber, Metal precipitation at grain boundaries in silicon: Dependence on grain boundary character and dislocation decoration, *Applied Physics Letters* **89**, 042102 (2006).

- 
- [150] M. D. Sabatino and G. Stokkan, Defect generation, advanced crystallization, and characterization methods for high-quality solar-cell silicon, *Physica Status Solidi (a)* **210**, 641 (2013).
- [151] D. Macdonald, A. Cuevas, and L. J. Geerligs, Measuring dopant concentrations in compensated *p*-type crystalline silicon via iron-acceptor pairing, *Applied Physics Letters* **92**, 202119 (2008).
- [152] S. Y. Lim and D. Macdonald, Measuring dopant concentrations in *p*-type silicon using iron-acceptor pairing monitored by band-to-band photoluminescence, *Solar Energy Materials & Solar Cells* **95**, 2485 (2011).
- [153] S. Y. Lim, P. Phang, T. Trupke, A. Cuevas, and D. Macdonald, Dopant concentration imaging in crystalline silicon wafers by band-to-band photoluminescence, *Journal of Applied Physics* **110**, 113712 (2011).
- [154] J. R. Janesick, *Scientific Charge Coupled Devices*, SPIE Press (2001).
- [155] M. S. Robbins, The noise performance of electron multiplying charge-coupled devices, *IEEE Transactions on Electron Devices* **50**, 1227 (2003).
- [156] J. Hynccek and T. Nishiwaki, Excess noise and other important characteristics of low light level imaging using charge multiplying CCDs, *IEEE Transactions on Electronic Devices* **50**, 239 (2003).



# List of publications

Publications arising from the work in this thesis:

## Refereed papers as first author

1. S. Herlufsen, J. Schmidt, D. Hinken, K. Bothe, and R. Brendel, Photoconductance-calibrated photoluminescence lifetime imaging of crystalline silicon, *Physica Status Solidi (RRL)* **2**, 245 (2008).
2. S. Herlufsen, K. Ramspeck, D. Hinken, A. Schmidt, J. Müller, K. Bothe, J. Schmidt and R. Brendel, Dynamic photoluminescence lifetime imaging for the characterisation of silicon wafers, *Physica Status Solidi (RRL)* **5**, 25 (2011).
3. S. Herlufsen, D. Macdonald, K. Bothe, and J. Schmidt, Imaging of the interstitial iron concentration by measuring the dissociation rate of iron-boron pairs, *Physica Status Solidi (RRL)* **6**, 1 (2012).
4. S. Herlufsen, K. Bothe, J. Schmidt, R. Brendel, and S. Siegmund, Dynamic photoluminescence lifetime imaging of multicrystalline silicon bricks, *Solar Energy Materials & Solar Cells* **106**, 42 (2012).
5. S. Herlufsen, D. Hinken, M. Offer, J. Schmidt, and K. Bothe, Validity of calibrated photoluminescence lifetime measurements of crystalline silicon wafers for arbitrary lifetime and injection ranges, *IEEE Journal of Photovoltaics* **3**, 381 (2013).

## Refereed papers as coauthor

1. R. Krain, S. Herlufsen, and J. Schmidt, Internal gettering of iron in multicrystalline silicon at low temperature, *Applied Physics Letters* **93**, 152108 (2008).
2. D. Hinken, K. Bothe, K. Ramspeck, S. Herlufsen, and R. Brendel, Determination of the effective diffusion length of silicon solar cells from photoluminescence, *Journal of Applied Physics* **105**, 104516 (2009).
3. K. Bothe, K. Ramspeck, D. Hinken, C. Schinke, J. Schmidt, S. Herlufsen, R. Brendel, J. Bauer, J.-M. Wagner, N. Zakharov, and O. Breitenstein, Luminescence emission from forward- and reverse-biased multicrystalline silicon solar cells, *Journal of Applied Physics* **106**, 104510 (2009).
4. D. Hinken, C. Schinke, S. Herlufsen, A. Schmidt, K. Bothe, and R. Brendel, Experimental setup for camera-based measurements of electrically and optically stimulated luminescence of silicon solar cells and wafers, *Review of Scientific Instruments* **82**, 033706 (2011).

5. J. Müller, K. Bothe, S. Herlufsen, H. Hannebauer, R. Ferré, and R. Brendel, Reverse saturation current density imaging of highly doped regions in silicon: A photoluminescence approach, *Solar Energy Materials & Solar Cells* **106**, 76 (2012).
6. J. Müller, K. Bothe, S. Herlufsen, T. Ohrdes, and R. Brendel, Reverse saturation current density imaging of highly doped regions in silicon employing photoluminescence measurements, *IEEE Journal of Photovoltaics* **2**, 473 (2012).

### **Refereed papers presented at international conferences as first author**

1. S. Herlufsen, J. Schmidt, D. Hinken, K. Bothe, and R. Brendel, Camera-based photoluminescence lifetime imaging of crystalline silicon wafers, *Proceedings of the 24th European Photovoltaic Solar Energy Conference*, p. 913 (2009).
2. S. Herlufsen, K. Ramspeck, D. Hinken, A. Schmidt, J. Müller, K. Bothe, J. Schmidt, and R. Brendel, Dynamic lifetime imaging based on photoluminescence measurements, *Proceedings of the 25th European Photovoltaic Solar Energy Conference*, p. 2369 (2010).
3. S. Herlufsen, D. Macdonald, K. Bothe, and J. Schmidt, Imaging of the interstitial iron concentration in boron-doped c-Si based on time-dependent photoluminescence imaging, *Proceedings of the 27th European Photovoltaic Solar Energy Conference*, p. 990 (2012).

### **Refereed papers presented at international conferences as coauthor**

1. R. Krain, S. Herlufsen, and J. Schmidt, Low-temperature gettering of iron in mono- and multicrystalline silicon, *Proceedings of the 24th European Photovoltaic Solar Energy Conference*, p. 965 (2009).
2. K. Bothe, D. Hinken, K. Ramspeck, S. Herlufsen, J. Schmidt, R. Brendel, J.-M. Wagner, N. Zakharov, and O. Breitenstein, Imaging and analysis of pre-breakdown sites in multicrystalline silicon solar cells, *Proceedings of the 24th European Photovoltaic Solar Energy Conference*, p. 918 (2009).
3. D. Hinken, K. Bothe, K. Ramspeck, S. Herlufsen, and R. Brendel, Determination of the emitter saturation current density of silicon solar cells using photoluminescence and quantum efficiency analysis, *Proceedings of the 24th European Photovoltaic Solar Energy Conference*, p. 1082 (2009).

4. R. Ferré, N.-P. Harder, W. Mühleisen, S. Herlufsen, C. Ulzhöfer, M. C. Schubert, R. Wade, V. Mertens, and R. Brendel, Bulk lifetime enhancement by firing steps in back contacted multicrystalline silicon solar cells, *Proceedings of the 25th European Photovoltaic Solar Energy Conference*, p. 1438 (2010).
5. R. Krain, S. Beljakova, S. Herlufsen, M. Krieger, and J. Schmidt, Classification of defective regions in *p*-type multicrystalline silicon by comparing luminescence images measured under different conditions, *Proceedings of the 3rd International Conference on Crystalline Silicon Photovoltaics: Energy Procedia*, vol. 38, p. 101 (2013).



# Acknowledgment

Abschließend möchte ich mich bei den Menschen bedanken, die wesentlich zum Gelingen dieser Arbeit beigetragen haben, insbesondere bei:

Prof. Dr. Jan Schmidt, Dr. Karsten Bothe und Prof. Dr. Rolf Brendel für die gute wissenschaftliche Betreuung, sowie für den steten Strom an Motivation und Begeisterung für unsere Arbeit.

Prof. Dr. Michael Oestreich für die Übernahme des Korreferates, Prof. Dr. Daniel Macdonald für die Übernahme des externen Korreferates, sowie bei Prof. Dr. Holger Frahm für die Übernahme des Prüfungsvorsitzes bei meiner Disputation.

meinen Kollegen aus der Charakterisierungsgruppe, besonders bei Ingo Ahrens, Dr. David Hinken, Rafael Krain, Dr. Bianca Lim, Susanne Mau, Ashley Milsted, Jens Müller, Dr. Matthias Offer, Carsten Schinke, Arne Schmidt, Dominic Walter und Martin Wolf, für ein gutes Arbeitsklima und Unterstützung bei vielen technischen und physikalischen Fragen.

Auch bei den vielen hier ungenannten Kollegen des ISFHs sowie bei meinen zahlreichen Mitdoktoranden möchte ich mich an dieser Stelle für die stets freundliche und entspannte Arbeitsatmosphäre bedanken.

Ohne meine Freunde, Familie und meinen lieben Hendrik wären die letzten Jahre sicherlich nicht so lustig und entspannt verlaufen. Vielen Dank für Eure Unterstützung.



# Curriculum vitae

---

<b>Name</b>	Sandra Herlufsen
<b>Anschrift</b>	Kaiserstraße 49, 31785 Hameln
<b>Geburtsdatum</b>	26. Oktober 1979
<b>Nationalität</b>	deutsch
<b>Familienstand</b>	ledig

## Ausbildung

---

<b>Februar 1998 - Juni 2001</b>	Abendgymnasium in Bremerhaven Abschluss der allgemeinen Hochschulreife im Juni 2001
<b>Oktober 2001 - September 2007</b>	Universität Bremen Studium der Physik Diplomprüfung im September 2007
<b>Juli 2005 - Januar 2006</b>	University of Adelaide, Australien Auslandssemester

## Anstellung

---

<b>seit November 2007</b>	Institut für Solarenergieforschung GmbH (ISFH) Hameln/Emmerthal Wissenschaftliche Mitarbeiterin im Bereich Materialforschung und Charakterisierung
---------------------------	---